Selectivity in histone deacetylase inhibition: A biophysical approach

Vom Fachbereich Chemie
der Technischen Universität Darmstadt

zur Erlangung des akademischen Grades eines
Doctor rerum naturalium (Dr. rer. nat.)

genehmigte

Dissertation

vorgelegt von
Christian Stephan Meyners, M.Sc.
aus Norden

Referent:	Prof. Dr. Harald Kolmar
Korreferenten:	Prof. Dr. Franz-Josef Meyer-Almes (Hochschule Darmstadt)
	Prof. Dr. Elmar Jaenicke (Johannes Gutenberg-Universität Mainz)
Tag der Einreichung:	11. Mai 2017
Tag der mündlichen Prüfung:	03. Juli 2017

Darmstadt 2017

D17

Die vorliegende Arbeit wurde im Arbeitskreis von Prof. Dr. Franz-Josef Meyer-Almes an der Hochschule Darmstadt im Fachbereich Chemie- und Biotechnologie in Kooperation mit Prof. Dr. Harald Kolmar am Clemens-Schöpf-Institut für Organische Chemie und Biochemie der Technischen Universität Darmstadt von April 2014 bis Mai 2017 angefertigt.

Research Articles

Kinetic method for the large-scale analysis of the binding mechanism of histone deacetylase inhibitors. Meyners C, Baud MGJ, Fuchter MJ, Meyer-Almes F-J. *Anal. Biochem.* (2014) 460: 39–46

A fluorescence lifetime-based binding assay for acetylpolyamine amidohydrolases from *Pseudomonas aeruginosa* using a [1,3]dioxolo[4,5-*f*]benzodioxole (DBD) ligand probe. Meyners C, Wawrzinek R, Krämer A, Hinz S, Wessig P, Meyer-Almes F-J. *Anal. Bioanal. Chem.* (2014) 406: 4889–4897

Potent and selective non-hydroxamate histone deacetylase 8 inhibitors. Kleinschek A, Meyners C, di Giorgio E, Brancolini C, Meyer-Almes F-J. *ChemMedChem* (2016) 11: 2598–2606

A fluorescence lifetime-based binding assay for class IIa histone deacetylases. Meyners C, Mertens M, Wessig P, Meyer-Almes F-J. *Chem. Eur. J.* (2017) 23: 3107–3116

Perflourinated hydroxamic acids are potent and selective inhibitors of HDAC-like enzymes from *Pseudomonas aeruginosa*. Meyners C, Wolff B, Kleinschek A, Krämer A, Meyer-Almes F-J. *Bioorg. Med. Chem. Lett.* (2017) 27: 1508–1512

The thermodynamic signature of ligand binding to histone deacetylase-like amidohydrolases is most sensitive to the flexibility in the L2-loop lining the active site pocket. Meyners C, Krämer A, Yildiz Ö, Meyer-Almes F-J. BBA - General subjects (2017)
DOI: http://dx.doi.org/10.1016/j.bbagen.2017.04.001

Conference Contributions

Selected talk and poster: EBSA 2015 10th European Biophysics Congress, Dresden, Germany July 18 to 22, 2015 *Isoform selective inhibition of histone deacetylase-like amidohydrolases*

Selected talk: BφDD 2016 3rd NovAliX Conference Biophysics in Drug Discovery 2016, Strasbourg, France June 7 to 10, 2016 *Combining binding thermodynamics and kinetic binding mechanisms to assess the selectivity of inhibitors of histone deacetylase-like amidohydrolases*

Patents

Meyer-Almes F.-J., Haus P., Kleinschek A., Meyners C., Selective HDAC8 inhibitors and their uses, PCT/EP2016/076615 (pending)

Table of content

1. Abstract

1.1. Zusammenfassung

Die Entwicklung von selektiven und sicheren Wirkstoffen ist eine wichtige Aufgabe in der pharmazeutischen Forschung und in den letzten 25 Jahren sind biophysikalische Methoden zur Charakterisierung von Protein-Ligand Wechselwirkungen zu einem wichtigen Hilfsmittel entwickelt worden. Zum einem erlauben diese Methoden eine Verifizierung von in Hochdurchsatzverfahren identifizierten Molekülen und zum anderen ergänzen sie traditionelle Ansätze zum Wirkstoffdesign, durch tiefe Einblicke in die Thermodynamik, Kinetik und den Mechanismus der Interaktion. Basierend auf diesen Informationen wurden Rationalen entwickelt, die zur Identifizierung von vielversprechenden Leitstrukturen genutzt werden können.
Histondeacetylasen (HDACs) sind eine Familie von Proteinen, die intensiv als therapeutische Ziele für die Behandlung von verschiedenen Krankheiten, unter anderem Krebs, neurodegenerativen Krankheiten und parasitäreren Infektionen untersucht werden. Sie katalysieren die Deacetylierung der ε-Aminofunktion von Lysinen von Histonen und anderen Proteinen, wodurch sie wichtige Funktionen in der epigenetischen Regulation ausüben. Mit SAHA, FK228, PXD101 und LBH589 wurden vier Histondeacetylase-Inhibitoren zur Behandlung von verschiedenen Tumorerkrankungen zugelassen. Diese verursachen zahlreiche Nebenwirkungen. SAHA, PXD101 und LBH589 sind unspezifische Inhibitoren, die nahezu alle Isotypen der HDACs hemmen. Durch eine Entwicklung von selektiven Inhibitoren sollen Nebenwirkungen minimiert werden und gleichzeitig eine spezifischere Therapie ermöglicht werden. Die vorliegende Arbeit beschäftigt sich mit der Frage, inwieweit Informationen aus der Analyse der Thermodynamik, Kinetik und Bindemechanismen genutzt werden können, um die Selektivität von Inhibitoren der HDAC-Familie zu beschreiben. Die im Rahmen dieser Doktorarbeit erzielten Ergebnisse sind im kumulativen Teil, bestehend aus fünf in begutachteten Zeitschriften publizierten Artikeln und einer zur Begutachtung eingereichten Publikation, dargestellt. Sie liefern zum einen Beiträge zur Methodik der Identifizierung und biophysikalischen Charakterisierung von Histondeacetylase-Inhibitoren, und zum anderen tragen sie zum tiefen Verständnis der molekularen Grundlagen der Inhibition von HDACs im Speziellen und von Protein-Ligand-Wechselwirkungen im Allgemeinen bei.

Der erste Teil dieser Arbeit beinhaltet Methodenentwicklungen zur Identifizierung und biophysikalischen Charakterisierung von Histondeacetylase-Inhibitoren. In einer Kooperation mit der Arbeitsgruppe von Herrn Prof. Wessig von der Universität Potsdam wurden Liganden entwickelt, deren Fluoreszenzlebensdauer sich bei der Bindung an HDACs ändert. Über eine Verdrängungsreaktion kann die Bindung von Histondeacetylase-Inhibitoren bestimmt werden. Ein daraus entwickelter kompetitiver

Bindeassay ist für Anwendungen im Hochdurchsatz-Screening und zur Bestimmung von Bindekonstanten hervorragend einsetzbar. Ferner eignet sich der erstellte Assay auch für Anwendungen mit Klasse IIa HDACs, womit der erste Bindeassay für diese Klasse entwickelt werden konnte.
Zur Ermittlung von kinetischen Parametern und des Mechanismus der Bindung von Inhibitoren an HDACs wurde ein bestehender fluoreszenzspektroskopischer Bindeassay modifiziert, sodass zeitaufgelöst die Bindung von nichtfluoreszenten Liganden gemessen werden kann. Die ermittelten Kinetiken wurden mit einer globalen Fitanalyse analysiert. Mit dieser Methodik wurden die Reaktionsmechanismen für die Bindung von vier verschiedenen Liganden an die humanen HDACs 1, 6 und 8 sowie an eine bakterielle Histondeacetylase-ähnliche Amidohydrolase ermittelt.

Im zweiten Teil dieser Arbeit wurde am Beispiel der Histondeacetylase-ähnlichen Amidohydrolase aus *Pseudomonas aeruginosa*, $HDAH_{pa}$, evaluiert, welche strukturellen Eigenschaften von Histondeacetylase-Inhibitoren die Selektivität beeinflussen und inwiefern mechanistische und thermodynamische Parameter zur Bewertung der Selektivität verwendet werden können. Hierzu wurden die Reaktionsmechanismen und die thermodynamische Signatur von strukturverwandten Inhibitoren des bekannten Histondeacetylase-Inhibitor *N*-Hydroxy-*N'*-phenyloctandiamid (SAHA) bestimmt, und deren Selektivität gegen die humanen HDACs 1–8 ermittelt. Im Allgemeinen zeigen SAHA und andere Liganden mit Hydroxamsäuren als zinkbindende Gruppe eine gute Selektivität gegenüber HDACs der Klasse IIa. Demgegenüber besitzt SATFMK, bei dem die Hydroxamsäurefunktion gegen eine Trifluormethylcarbonylgruppe ausgetauscht ist, eine gute bis sehr gute Selektivität gegen die HDACs 1–3 und 6, aber eine geringere Selektivität gegenüber HDACs der Klasse IIa und HDAC8. Mit einer mindestens 1000fachen Selektivität gegenüber den humanen HDACs konnte die höchste Selektivität für $HDAH_{pa}$ beim Liganden PFSAHA beobachtet werden. Dieser besitzt eine im Vergleich zu SAHA und SATFMK sterisch anspruchsvollere perfluorierte Alkylkette. Ferner wurde in einer weiteren Studie festgestellt, dass die hohe Selektivität von PFSAHA bei einer Variation der Kopfgruppe in vielen Fällen erhalten bleibt und durch Methylierung oder Chlorierung noch gesteigert werden kann.
Überraschenderweise, ergab eine Analyse der Bindemechanismen, dass PFSAHA und SATFMK je an andere Proteinkonformationen binden als die übrigen Liganden. Diese Ergebnisse unterstützen die These, dass selektive Liganden anhand ihres Bindemechanismus identifiziert werden können.
Zur Vertiefung des Verständnisses der molekularen Erkennung von Inhibitoren durch $HDAH_{pa}$ wurden die Bindungsreaktionen mittels isothermer Titrationskalorimetrie untersucht. Die Bestimmung der thermodynamischen Parameter zeigte, dass die Bindung von PFSAHA an $HDAH_{pa}$ mit einer unvorteilhaften Entropieänderung ausschließlich über enthalpische Beiträge erfolgt, während bei SATFMK die enthalpischen und entropischen Beiträge ausgeglichen sind. Dies deutet in der Tat darauf

hin, dass der enthalpische Beitrag bei selektiven Liganden höher ausgeprägt ist. Dennoch hat sich gezeigt, dass der enthalpische Beitrag zur Bindungsreaktion nur bedingt zur Vorhersage der Selektivität von Histondeacetylase-Inhibitoren geeignet ist. Erst eine neu definierte enthalpiegewichtete Bindekonstante zeigt eine gute Korrelation zur bestimmten Selektivität der Histondeacetylase-Inhibitoren. Allerdings müssen die Anwendbarkeit und Übertragbarkeit dieses empirischen Parameters für andere Proteintargets noch evaluiert werden. In einer weiteren Studie wurde die Bindung von PFSAHA und SATFMK an $HDAH_{pa}$ und eine zu $HDAH_{pa}$ homologe Histondeacetylase-ähnlichen Amidohydrolase aus *Bordetella/Alcaligenes* durch Proteinkristallographie und isothermer Titrationskalorimetrie detaillierter untersucht. Es konnte ermittelt werden, dass die Flexibilität und die Zugänglichkeit der Bindetasche einen wesentlichen Einfluss auf die Thermodynamik und den Mechanismus der Bindung hat. Bei einer besseren Zugänglichkeit und einer erhöhten Flexibilität erfolgt die Bindung in einer apparenten Einschritt-Reaktion und mit einem höheren enthalpischen Beitrag zur Bindungsreaktion. Dieser wird allerdings durch Enthalpie-Entropie-Kompensation ausgeglichen, sodass es zu keiner Veränderung der Affinität kommt. Diese Ergebnisse erscheinen außerordentlich wichtig für die Entwicklung von Histondeacetylase-Inhibitoren, da HDACs mit vielen Proteinen interagieren und es wahrscheinlich ist, dass dies die Flexibilität der HDACs und damit die Ligandenbindung beeinflusst. Zusammenfassend zeigen diese Studien, dass eine bloße Betrachtung der Thermodynamik für die Identifizierung von selektiven Liganden im Allgemeinen nicht ausreicht, aber besonders in Verbindung mit mechanistischen Untersuchungen wertvolle Informationen über die potentielle Selektivität von Wirkstoffen liefert und vorhandene Parameter zur frühen Identifikation der Wirkstoffkandidaten mit der höchsten Erfolgswahrscheinlichkeit ergänzt.

1.2. Abstract

The development of selective and save compounds is an important task in drug discovery and during the past 25 years biophysical methods for the characterization of protein-ligand interactions have been developed to a valuable tool. On the one hand these methods allow to validate screening hits and on the other hand they complement traditional approaches in drug discovery by providing deep insights into the thermodynamics, kinetics and the mechanism of molecular interactions. Based on these information, approaches were developed which allow to identify promising lead structures for further development.

Histone deacetylases (HDACs) are a protein family which are investigated as therapeutic targets for the treatment of different diseases like cancer neurodegenerative disorders and parasitic infections. By catalyzing the deacetylation of the ε-amino function of lysines of histones and other proteins they fulfill an important function for the epigenetic regulation. With SAHA, FK228, PXD101 and LBH589 four HDAC inhibitors were approved for the treatment of different cancers. They cause several

unwanted side effects. SAHA, PXD101 and LBH589 are unselective inhibitors which inhibit most HDAC isotypes. In order to minimize unwanted side effects and to provide a more specific therapy isotype selective inhibitors are developed. The present work deals with the question how information from an analysis of the thermodynamics, kinetics and binding mechanisms can be exploited to characterize the selectivity of inhibitors of the HDAC family. The generated results of this doctoral thesis are provided in the cumulative part which consists of five articles published in peer reviewed journals and one article submitted for peer review. One the one hand they extend the methodology on the identification and biophysical characterization of HDAC inhibitors and on the other hand they contribute to the deep comprehension of the molecular basis of the inhibition of HDACs and of protein-ligand interactions.

The first part of this work covers methods developed for the identification and biophysical characterization of HDAC inhibitors. In a cooperation with the research group of Prof. Wessig at the University of Potsdam ligands were generated whose fluorescence lifetime change upon binding to histone deacetylases. By a displacement of the ligands from the active site the binding of HDAC inhibitors can be monitored. A developed competitive binding assay is outstandingly suited for high throughput screening applications and the determination of binding constants. Furthermore, the developed assay is also applicable for class IIa HDACs resulting in the first binding assay for this HDAC class.
For the determination of kinetic parameters and the binding mechanism of the binding inhibitors to histone deacetylases an established fluorescence spectroscopic binding assay was modified, so that a time-resolved monitoring of the binding of nonfluorescent ligands is allowed. The determined kinetic traces were subjected to a global fit analysis. With this method the reaction mechanisms of the binding of four ligands to the human histone deacetylases 1, 6 and 8 as well as to a bacterial histone deacetylase-like amidohydrolase were evaluated.

In the second part of this work it was evaluated on the basis of a histone deacetylase-like amidohydrolase from *Pseudomonas aeruginosa*, $HDAH_{pa}$, which structural elements of HDAC inhibitors affect the selectivity and how mechanistic and thermodynamic parameters can be applied to assess the selectivity. Therefore, the reaction mechanisms and the thermodynamic signature of structurally related inhibitors of the known HDAC inhibitor *N*-hydroxy-*N*′-phenyloctanediamide (SAHA) were determined and evaluated for their selectivity against the human histone deacetylases 1–8. Generally, SAHA and other compounds with a hydroxamic acid as zinc binding moiety exhibit a good selectivity against class IIa HDACs. In contrast, the compound SATFMK, where the hydroxamic acid moiety is exchanged by a trifluoromethyl ketone moiety, exhibits a good to very good selectivity against the HDACs 1–3 and 6 but a lower selectivity against class IIa HDACs and HDAC8. With an at least 1000-

fold selectivity over human HDACs the highest selectivity was determined for the compound PFSAHA. This compound exhibits, compared to SAHA and SATFMK, a sterically more demanding perflourinated spacer. Furthermore, it was determined in another study that upon an exchange of the cap group the high selectivity is preserved in most cases and can be improved by methylation and chlorination.

Surprisingly, an analysis of the determined binding mechanisms suggests that PFSAHA and SATFMK bind each to other protein conformations as the other ligands. These results support the assumption that selective ligands can be identified on the basis of their binding mechanism.

In order to deepen the knowledge about the molecular recognition of inhibitors by $HDAH_{pa}$ the binding reactions were studied by isothermal titration calorimetry. The determination of the thermodynamic parameters revealed that the binding of PFSAHA to $HDAH_{pa}$ occurs with unfavorable entropic contributions and is solely enthallpically driven, while for the binding of SATFMK the entropic and enthalpic contributions are balanced. This indicates indeed that for selective binders the enthalpic contributions are more pronounced. However, the enthalpic contributions to binding are of limited suitability for the prediction of the selectivity of HDAC inhibitors. Only a newly defined enthalpy weighted binding constant exhibits a good correlation to the determined selectivity of the HDAC inhibitors. Certainly, the applicability and transferability to other protein targets have yet to be evaluated. In a further study, the binding of PFSAHA and SATFMK to $HDAH_{pa}$ and a to $HDAH_{pa}$ homologous histone deacetylase-like amidohydrolase from *Bordetella/Alcaligenes* were investigated in more detail by protein crystallography and isothermal titration calorimetry. It was shown, that the thermodynamic signature and the mechanism of the binding reaction is largely influenced by flexibility and accessibility of the active site. With a better accessibility and a higher flexibility the binding occurs in an apparent one-step reaction and with more favorable enthalpic contributions to binding. But these are balanced by enthalpy-entropy compensation resulting in an unchanged binding affinity. These findings seem to be exceptionally important for the development of HDAC inhibitors, since HDACs interact with several proteins and it is likely that these interactions alter the flexibility of the HDACs and with it the recognition of ligands. Taken together these studies indicate that generally a solely consideration of thermodynamic signatures is insufficient for the identification of selective compounds, but especially in combination with mechanistic investigations useful information about the potential selectivity of compounds are provided, which supplement existing parameters for the early identification of leads with a high probability of success.

2. Introduction

2.1. Biophysical characterization of protein-ligand interactions

The rational development of save and selective compounds is a major task in drug discovery and during the past 25 years biophysical methods evolved to be key technologies for the characterization of proteins and protein-ligand interactions.[1] Biophysical methods are nowadays successfully applied for the quality control of protein preparations and for the validation of hits and identification of false-positives from screening campaigns.[2] Furthermore, biophysical parameters like thermodynamic signatures, residence times and binding mechanisms emerged to complement traditional parameters as the activity towards the target, the drug-likeness and lead-likeness to develop a rational basis for the selection of promising candidates for further optimization.[1,3–7] Especially, methods like X-ray crystallography, nuclear magnetic resonance spectroscopy (NMR), isothermal titration calorimetry and binding assays allow insights into the structure, molecular mechanism, thermodynamics and kinetics of the binding reaction.[1,2,8]

Not surprisingly, the first biophysical methods which were integrated into drug discovery processes were structure based methods like X-ray crystallography and NMR spectroscopy as they allowed a detailed molecular view of protein-ligand interactions.[1,8,9] An advantage of these methods is the reliable identification of unique structural elements like subpockets, which can be exploited to generate selective ligands and in combination with computational methods they evolved to be the basis for structure based drug design approaches. Today, these methods are also successfully implemented into screening procedures, especially for fragment based drug design. As for most methods, structural techniques are more powerful if they are combined with other methods like binding and activity assays to obtain information about the affinity of the interaction.[8]

Binding constants and thermodynamic signatures

A classical parameter to describe the activity of compounds towards a target is the determination of IC_{50}- and EC_{50}-values, which reflect the compound concentration at which the inhibition (IC_{50}) or more general the effect (EC_{50}) is half maximal. As these values are dependent on the used test parameters and are especially sensitive to the concentrations of the reactants, the equilibrium dissociation constant, K_d, of the protein-compound complex is a more reliable parameter to compare different compounds. This value defines how willingly the protein-compound complex dissociates and the lower a K_d-value of a molecular interaction is the higher is the affinity. Physically, the K_d-value of a molecular interaction depends on the change of the Gibbs energy at standard conditions (ΔG^0), which denotes the difference between the energy of the complex and the energy of the free binding partners and defines

the distribution between the bound and unbound state at equilibrium conditions. The change of the Gibbs energy is furthermore composed of enthalpic (ΔH^0) and entropic (ΔS^0) contributions to binding and as for the K_d-value it applies the lower (more negative) the value for ΔG^0 is the higher is the affinity.

$$\Delta G^0 = R \times T \times \ln K_d = \Delta H^0 - T \times \Delta S^0 \quad (1)$$

with R = universal gas constant, T = thermodynamic temperature

Optimizing the change in Gibbs energy upon complex formation towards more negative values results consequently in a lower K_d-value and an increased affinity towards the target. This approach has been highlighted by Bissantz *et al.* as the only reasonable way for optimizing compounds as other approaches are very dependent on the system under investigation.[10] Furthermore, K_d-values are easily determined and the most useful parameter to establish structure-activity relationships.

Improvements in the K_d-value are often achieved by the addition of hydrophobic moieties like methyl or ethyl groups to the ligand.[7,11] According to Ladbury *et al.* this approach has serious drawbacks since the gain in affinity through hydrophobic moieties mostly results from greater entropic contributions, which are believed to negatively impact the selectivity of the ligand.[11] In general, entropic contributions to binding result from a change in the degree of freedom of the system upon binding.[12,13] While unfavorable entropic contributions result mainly from a fixation of the ligand and from a structuring or decreased flexibility of the target-ligand complex, favorable contributions are gained through the release of structured water clusters from the binding pocket and a desolvation of hydrophobic moieties of the ligand or target molecule.[12–14] These effects are often observed for hydrophobic interactions and therefore also referred to as hydrophobic effect.

Favorable enthalpic contributions to binding result from polar interactions like hydrogen bonding and chelation of metal ions but also from van-der-Waals interactions and an optimal geometric fit of the ligand into the binding pocket.[11,13,14] According to Ladbury *et al.* and Freire *et al.* favorable enthalpic contributions are more specific since the geometry of the binding site and the possible positions of hydrogen bonds are dependent on the target.[15] On the other hand the optimization of the enthalpic contributions is extraordinary hard, especially without structural information of the target as these types of interactions follow strict geometric rules and the distances and angles of the interacting groups have to be accurately adjusted.[11,16] Polar groups which are wrongly positioned have are large negative effect on the binding enthalpy if they are desolvated upon binding but not able to reestablish a polar interaction in the bound state. Furthermore, it is often observed that generated favorable enthalpic contributions are compensated by unfavorable entropic contributions due to a decrease in the degree of freedom caused by a strong fixation of the ligand and/or the binding pocket.[12,13,16] In order to overcome these difficulties Ladbury *et al.* and Freire *et al.* suggest to include a thermodynamic characterization of the binding reaction in early stages of drug development

processes and to select leads for further optimization, which already possess favorable enthalpic contributions.[11,13,17] On the other hand the thermodynamics of protein-ligand interactions are very complex and the value of enthalpy based ligand optimization without knowing about the molecular or structural basis is questionable.[16,18]

Binding kinetics and residence time

Another aspect which has to be considered for the selection of lead structures is their behavior in non-equilibrium systems like the human body. Equilibrium data as K_d-values and thermodynamic signatures are not suitable to predict the time dependency of the binding degree but since a compound is only active while it is bound to its target, this information is crucial.[19] The behavior of a compound at dynamic conditions is defined by its kinetic rate constants and compounds with similar affinities can exhibit large differences in their binding kinetics. In certain circumstances unfavorable kinetic rate constants could hamper the activity *in vivo* although the ligand exhibits a high affinity *in vitro*.[20] Optimization of the binding kinetics is therefore an important task during compound development.[21–23]

Copeland and Tummino started to tackle this task with the introduction of the "residence time concept" which focuses on the optimization of the dissociation rate of a compound.[19,24] Slower dissociation rates are thereby believed to result in an increased target occupancy after most of the unbound ligand has been washed out. In the best case this would allow to increase the intervals between the application of the compound, which could reduce unwanted side effects through a temporal discrimination to unspecific binding.[24,25] Focusing on dissociation rates results often in a negligence of the association rates but computational simulations indicate that also a high affinity binder has to possess a considerable association rate to exhibit a effect *in vivo* at therapeutic relevant concentrations. [20] Furthermore, besides its binding kinetics the *in vivo* effect of a compound is also dependent on its pharmacokinetics and it was elucidated that in several cases the plasma half life is indeed the rate limiting step.[20] Taken together these findings suggest that the binding kinetics of a compound should be balanced in order to achieve a high efficacy *in vivo*.[26]

Binding mechanisms

Besides association and dissociation rates, kinetic studies of a binding reaction are useful to gain insights into the molecular binding mechanism. On the one hand mechanistic studies help to understand the molecular basics of the binding reaction but furthermore they can be used to stratify ligands and to identify compounds with unique mechanistic characteristics, which can serve as good

starting points for the development of selective and save compounds with an optimized therapeutic index.[27]

The simplest kinetic model to describe a binding reaction is a one step association and dissociation mechanism. Thereby, the complex formation is determined by a single exponential kinetic and at pseudo first order conditions the observed rate constants, k_{obs}, possess a linear dependency on the concentration of the varied binding partner. From the slope and the y axis intercept it is possible to determine the association rate constant, k_{on} and the dissociation rate constant, k_{off}.[24]

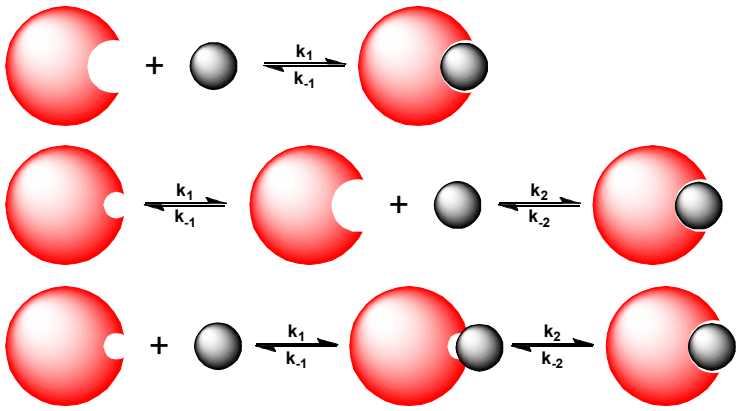

Figure 1: Schematic representation of an one step (top), a conformational selection (middle) and an induced fit (bottom) binding reaction.

In practice, binding reaction often occur with more complex mechanisms which involve several unimolecular isomerization steps. Two prominent models which have been proposed are the induced fit model and the conformational selection model (Figure 1). The induced fit model was introduced in 1958 by Koshland and it describes a two step binding reaction, where the initial ligand-protein complex isomerizes unimolecular into a thermodynamically more stable complex.[28] In contrast the conformational selection mechanism assumes that the protein exists in at least two different conformations of which one is accessible to the binding reaction.[29–31] Besides these simple models several combinations and extensions of both mechanisms can be formulated to describe more complex binding reactions. For the discrimination between these more complex models determining the concentration dependence of the observed rate constants is not sufficient and other parameters have to be integrated into a global fit approach.[32] Although, a controversial debate about the generalization of both formalisms is present in the literature, experimental data indeed indicates that both mechanisms occur.[29,33–35] The conformational selection approach has been recently used for the development of allosteric kinase inhibitors, which lock the protein in an inactive conformation.[36] Induced fit mechanisms were formulated especially for the binding into dynamic subpockets and for the enclosure of ligand between flexible loop regions.[22,37]

2.2. Human histone deacetylases

The acetylation of the ε-amino function of lysine residues is an often observed post-translational modification of proteins. First described by Phillips and Allfrey *et al.* in 1963/64 the subsequent research focused mainly on histones and other epigenetically relevant proteins.[38–41] But during the last 20 years and especially with the arise of proteomic methods it appeared that proteins of many cell physiological areas can be acetylated and that this modification seems as abundant as phosphorylations.[42–45] Interestingly, more recent studies indicate that protein acetylation also frequently occurs in bacteria like *Escherichia coli*, *Salmonella enterica* and *Pseudomonas aeruginosa*, which is in contrast to the general assumption that simpler life-forms are mostly not capable of post-translational protein modifications.[42,46–51] The acetylation of lysine residues itself is catalyzed by histone acetyltransferases (HATs), whereas the deacetylation is catalyzed by histone deacetylases (HDACs).

Based on their sequence phylogeny the 18 isotypes of the human HDACs are divided into four classes. The classes I (HDAC1, 2, 3 and 8), II (IIa: HDAC4, 5, 7 and 9; IIb: HDAC6 and 10) and IV (HDAC11) are Zn^{2+}dependent in contrast class III HDACs (SIRT 1–7) require NAD^{+} as a cofactor.[52] For class I, IIb and IV HDACs the active site is highly conserved and consists of two lateral histidines and a tyrosine, that are located at the bottom of the active site pocket next to the catalytic Zn^{2+} ion, which is coordinated by two aspartic acids and a further histidine.[53–54] In class IIa HDACs the tyrosine is replaced by a histidine, which turns these proteins essentially inactive towards acetylated substrates. The catalytic activity can be restored by replacement of the histidine by tyrosine.[55] The two histidines have also be found to be crucial for the deacetylation mechanism as indicated by site directed mutagenesis studies with HDAC8 and bacterial HDAC homologues.[56–59] Both histidines form charge relay systems through hydrogen bonding with aspertate residues and this is believed to affect the pK_a of the histidines.[59,60,61] Besides the active site the secondary and tertiary structures of the deacetylase domains are highly conserved as well. The core consists of eight parallel beta strands, which are surrounded by alpha helices and disordered loop regions (Figure 2). The catalytic zinc ion is located at the bottom of a pocket, which is connected to the protein surface through a narrow channel and the entrance is formed by six loops. Furthermore, the deacetylase domain exhibits two binding sites for monovalent cations like potassium or sodium ions, which are able to influence the deacetylase activity.[56]

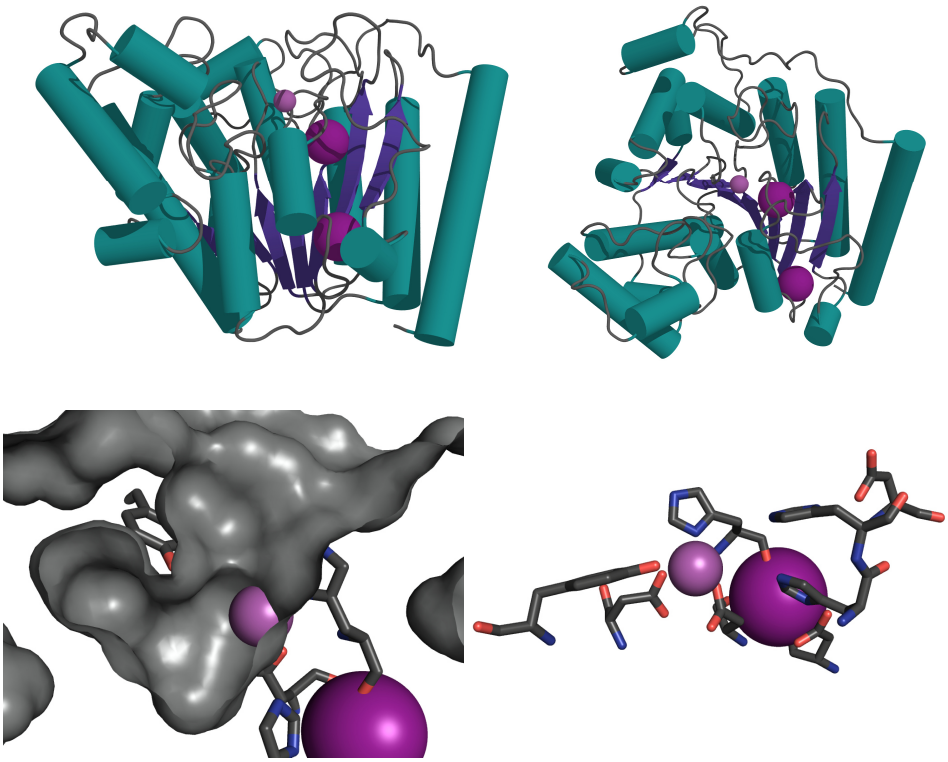

Figure 2: (top panel) General structure of Zn^{2+} dependent histone deacetylases based on the crystal structure of HDAC8 (3F07). Beta sheets are colored in blue, alpha helices in teal and loops in grey. The magenta sphere represents the catalytic zinc ion whereas the structural potassium ions are colored in purple. (bottom, left) Cut-open view of the surface of the active site pocket. (bottom, right) Close up view of the active site of HDAC8.

Based on the crystal structure of a histone decatylase like protein (HDLP) from *Aquifex aeolicus* the first detailed reaction mechanism was proposed by Finnin and colleagues.[53] They suggested a general acid-base catalytic pair mechanism, where the histidine corresponding to H143 in HDAC8 is protonated and the histidine corresponding to H142 in HDAC8 acts as a base and abstracts a proton from the reactive zinc bound water. The proton of the H143 corresponding histidine acts as an acid and is used to facilitate the second amide bond cleavage.[53]

Vanommeslaeghe *et al.* suggested a different mechanism, which was based on computational methods and the crystal structure of HDLP.[61] They proposed that the H142 corresponding histidine deprotonates a water molecule resulting in a protonated histidine and a hydroxide ion, which is bound between the zinc ion and the tyrosine. During the deacetylation the proton of the H142 corresponding histidine is transferred to the H143 corresponding histidine and used further to facilitate the second amide bond cleavage.[61]

As a third mechanism a proton-shuttle mechanism was formulated by Zhang and colleagues based on computational methods and crystal structures of HDLP and HDAC8.[60,62] The authors suggested that both histidines are in a non-protonated state upon substrate binding and that the H143 corresponding histidine acts as a base as well as an acid catalyst during the deacetylation. Although this mechanism was initially contested by Chen *et al.* the key role of the H143 corresponding histidine is supported by

a recently published experimental study with HDAC8, which proposed a single residue acid-base catalysis for the H143 corresponding histidine as well.[59,63] But also the mechanism proposed by Finnin and colleagues got recent support by a comprehensive crystallographic study with HDAC6 indicating that indeed both mechanisms occur (Figure 3).[64]

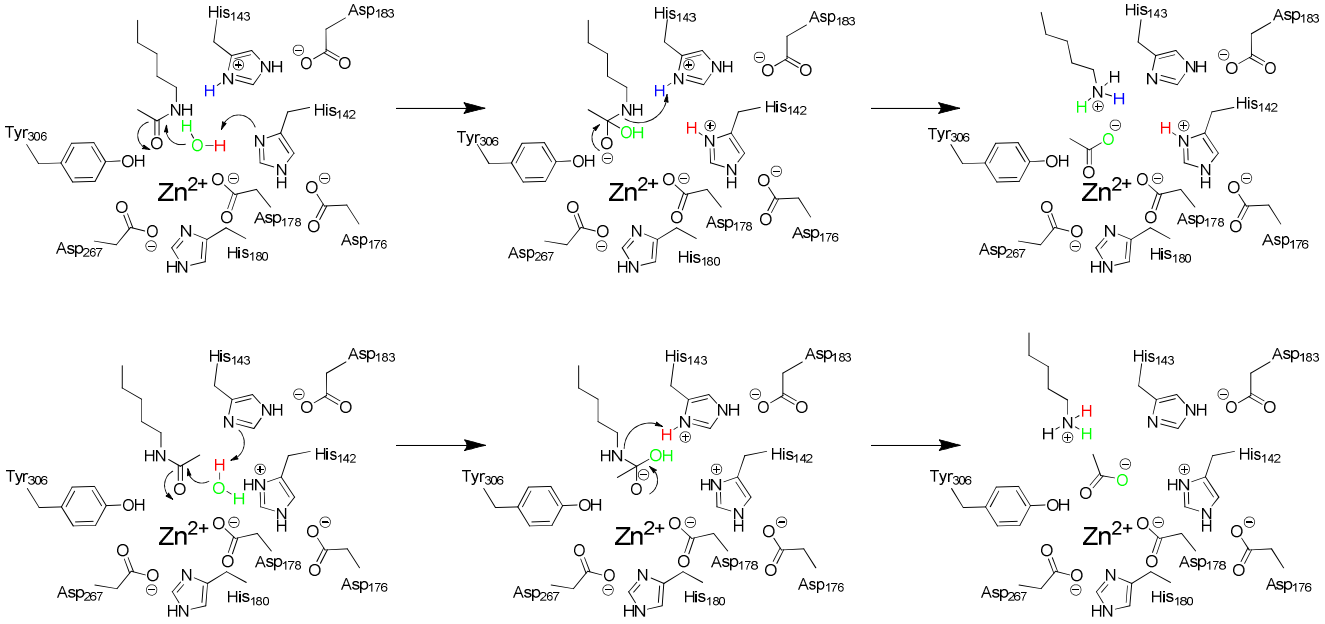

Figure 3: (top) General acid-base catalytic pair mechanism as proposed by Finnin and colleagues. (bottom) Proton-shuttle or single residue acid-base mechanism as proposed by Fierke and coworkers. Numbering of the amino acids is based on HDAC8.

Although, the general organization of the deacetylase domains is highly conserved among the human HDACs, small differences especially in the loops regions can be observed, which effects the function and regulation of the isotypes.[65,66] Class I HDACs are homologous to the yeast HDAC Rpd3, ubiquitously expressed and are mainly localized in the nucleus of the cell.[52] They are mostly recognized for their ability to control the gene expression epigenetically by deacetylation of acetylated histones.[54] But during the last decade also a number of non-histone proteins like p53, ERRα and CREB have been found to be substrates of class I HDACs.[67–70] While HDAC8 is solely active, HDAC1–3 are recruited to large multi protein complexes for their function and possess a longer C-terminal tail.[70–73] Recently, the structure of HDAC3 in complex with the deacetylase activating domain (DAD) of the nuclear receptor corepressor 2 (N-CoR2) has been solved.[74] Unexpectedly, the authors found inositol 1,4,5,6-tetrakisphosphate (Ins(1,4,5,6)P_4) to be bound in a basic pocket between both proteins and further studies indeed indicated that Ins(1,4,5,6)P_4 is needed for the activation of HDAC3 (Figure 4).[74,75] A multiple sequence alignment revealed that the amino acids responsible for the binding of Ins(1,4,5,6)P_4 are conserved among HDAC1, 2 and 3 but are absent in HDAC8.[74] Furthermore, a second multiple sequence alignment indicated that the Ins(1,4,5,6)P_4 binding amino acids of the DAD are conserved among other HDAC activating proteins like the REST corepressors 1–3, the nuclear receptor corepressor 1 and the metastasis-associated proteins MTA1–3.

Elucidation of the structure of the HDAC1:MTA1 complex revealed indeed a similar binding pocket for Ins(1,4,5,6)P_4 and a similar activation behavior was observed as for the HDAC3:DAD complex.[75,76]

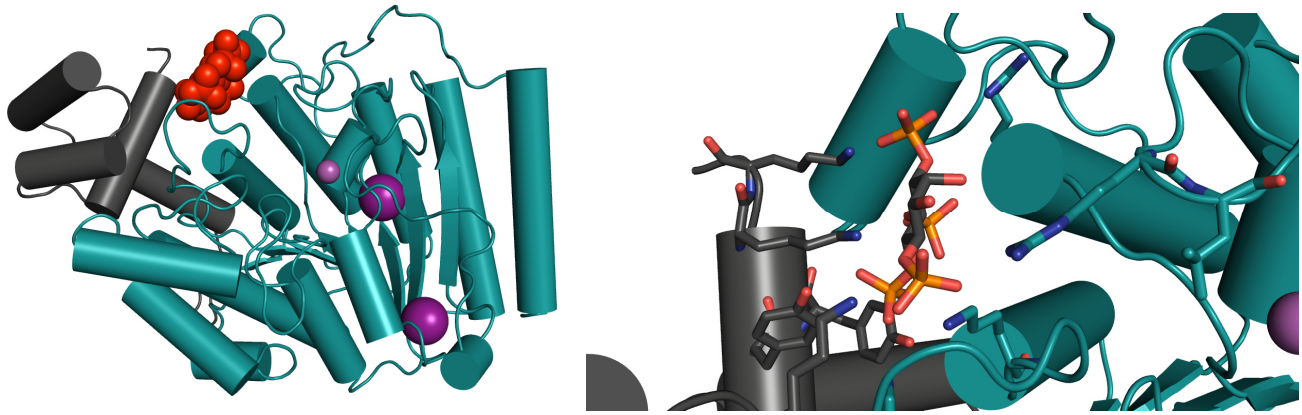

Figure 4: (left) Structure of the HDAC3(teal):DAD(grey) complex (4A69) bound to Ins(1,4,5,6)P_4 (red). The catalytic zinc ion is represented by the magenta sphere and the structural potassium ions are colored in purple. (right) Close up view of the inositolphosphate binding site of the HDAC3:DAD complex.

HDACs of the class II are subdivided into class IIa and class IIb and are homologous to the yeast HDAC Hda1.[77,78] While HDAC10 is mostly localized in the nucleus, HDAC6 is a mainly cytosolic protein and it is also the only HDAC with two active deacetylase domains.[64,78–80] Prominent substrates are α-tubulin, HSP90 and cortactin, through which HDAC6 influences cell migration and angiogenesis.[81–83]

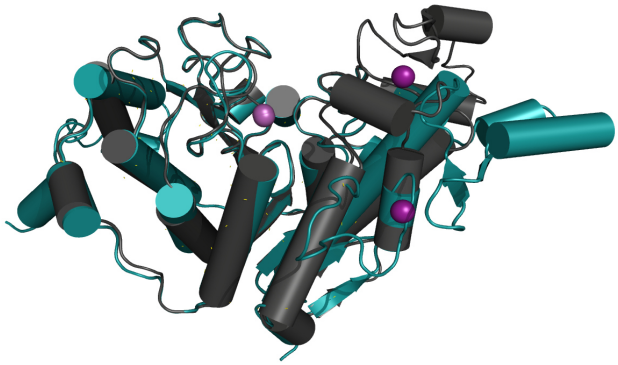

Figure 5: Overlay of the deacetylase domain of HDAC4 in the open (teal, 2VQJ) and closed (grey, 5A2S) state. The catalytic zinc ion is indicated as magenta sphere, whereas the structural zinc ion is colored in purple.

Furthermore, HDAC6 is required for the binding and transport of protein aggregates as it possesses a ubiquitin binding domain which binds to unanchored ubiquitin of protein aggregates.[84]

HDACs of the class IIa exhibit a large N-terminal domain through which they interact with transcription factors like RelB and the myocyte enhancer factors 2 A–D.[78,85–90] They are tissue dependently expressed and shuttle between the cytoplasm and the nucleus in a highly regulated way.[85,91–93] As aforementioned class IIa HDACs are inactive towards classic HDAC substrates through a tyrosine to histidine exchange in the active site but they are able to recruit class I HDAC containing multi protein complexes.[55,85,94,95] The main differences to other HDACs are localized in the L1 and L2 loops as crystal structures revealed a second zinc binding site. This structural zinc is either bound between two histidines and two cysteines resulting in an open protein conformation or between one histidine and three cysteines, which results in a closed conformation (Figure 5).[55] For HDAC4 it was observed that two of the zinc binding cysteines can form a intramolecular disulfide bond

in response to reactive oxygen species, which induces a shuttling of HDAC4 from the nucleus to the cytoplasm. The disulfide bond can be reduced by thioredoxin 1.[96] Interestingly, studies of the interaction between HDAC4 and N-CoR2 revealed that the structural zinc binding site is very important for the binding reaction and furthermore, it was shown that the binding depends on conserved motifs, which are unique for N-CoR1 and N-CoR2.[94,95]

2.3. Prokaryotic histone deacetylase-like amidohydrolases

Most so far identified prokaryotic proteins of the histone deacetylase family are acetylpolyamine deacetylases (APAHs), acetoin utilization proteins, histone deacetylase-like proteins (HDLPs), histone deacetylase-like amidohydrolases (HDAHs) and sirtuin homologue deacetylases.[53,97–100] In general, APAHs catalyze the deacetylation of acetylated polyamines and acetoin utilization proteins are part of the acetoin metabolism.[97] Proven APAHs were for example identified for *Mycoplana ramosa* and *Pseudomonas aeruginosa*.[100,101] Although, the exact functions and substrates of HDLPs and HDAHs are not known yet, preliminary results indicate that they act on acetylated proteins rather than on acetylated polyamines.[53,58,99] For instance, it has been shown that the HDAC6 homologous HDAH from *Pseudomonas aeruginosa* ($HDAH_{pa}$) is indeed unable to deacetylate polyamines *in vitro*.[58] Another HDAC6 homologous HDAH from *Bordetella/Alcaligenes* ($HDAH_{bo}$) is able to catalyze polyamine deacetylation, but the determined activity is relatively low compared to proven APAHs from *Mycoplana ramosa* and *Pseudomonas aeruginosa*.[99–101] Furthermore, $HDAH_{bo}$ was found to be inhibited by known HDAC inhibitors and to be active on acetylated histones and synthetic HDAC substrates.[99] Therefore, HDAHs and HDLP have been used as model system for human

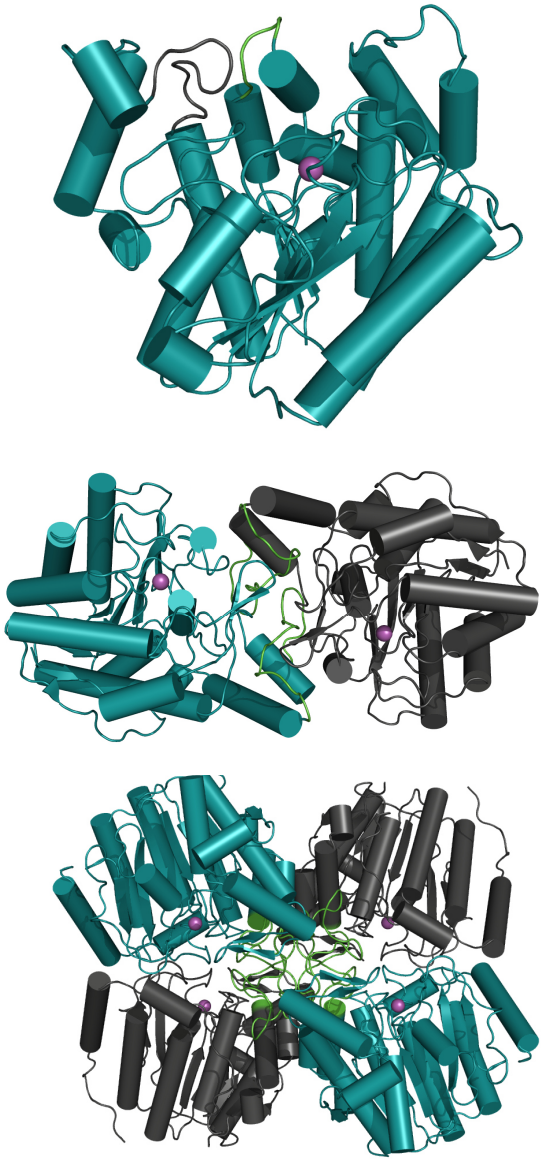

Figure 6: Structure of HDLP (top, 1C3S), APAH from Mycoplana ramosa (middle, 3Q9B) and $HDAH_{pa}$ (bottom, 5G10). The loops (L2 (green) for APAH, L1 (green) for $HDAH_{pa}$ and for comparison L1 (green) and L2 (grey) for HDLP) responsible for dimerization and tetramerization are highlighted. The catalytic zinc ion is indicated as magenta sphere.

HDACs. $HDAH_{bo}$ was used for the development of binding assays and HDLP from *Aquifex aeolicus*, which is homologue to HDAC1 was the first crystallized HDAC isotype and served as template for the elucidation of the molecular mechanisms of inhibition and catalysis of HDACs.[53,102–105] The determined secondary and tertiary structure of HDLP exhibits the same open α/β folds, which were later found to be conserved among the Zn^{2+} dependent HDACs (Figure 6).[66] The same core structure was also determined for the APAH from *Mycoplana ramosa* and for $HDAH_{bo}$ and $HDAH_{pa}$.[58,100,102] Interestingly, HDAHs as well as APAHs exhibit an elongated loop compared to HDLP and other class I and IIb HDACs, which impacts the quaternary structure(Figure 6). APAHs form a "head-to-head" dimer through an elongated L2 loop.[100] In contrast, HDAHs possess an elongated L1 loop which causes not only a "head-to-head" dimerization but furthermore a tertamerization occurs as a dimer of two dimers is formed.[58] For APAHs as well as for HDAHs the dimerization alters the entrance and the shape of the active site, which is believed to affect the specificity of substrate and inhibitor recognition (Figure 7).[58,100]

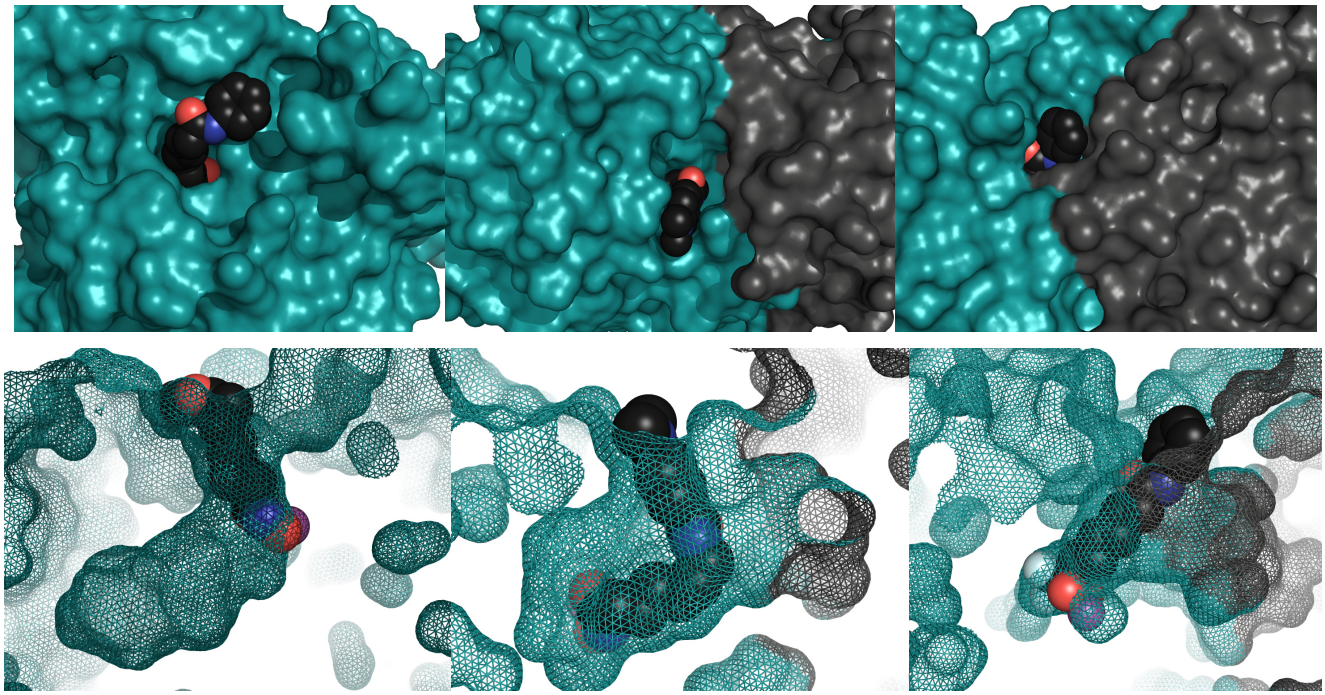

Figure 7: Surface representation of the entrance (top panel) and shape (bottom panel) of the active site of HDLP bound to SAHA (left, 1C3S), APAH dimer from *Mycoplana ramosa* bound to M344 (middle, 3Q9B) and $HDAH_{pa}$ dimer bound to SATFMK (right, 5G10). The catalytic zinc ion is indicated as magenta sphere.

2.4. Biophysics for inhibitors binding to histone deacetylases

Through their important functions in the epigenetic regulation of gene expression human HDACs have been identified as protein targets for the treatment of different types of cancer.[106–109] Four HDAC inhibitors have been approved by the United States Food and Drug Administration between 2006 and 2015 for the treatment of cutaneous and peripheral T-cell lymphoma and multiple myeloma and several more are in clinical trials (Figure 8).[110] Besides cancer HDAC are evaluated as targets for a broad range of different disorders ranging from neurodegenerative diseases like Parkinson's disease and Huntington's chorea over diabetes type 2 and disadvantages resulting from physical inactivity to parasitic infections.[109,111–117] While unwanted side effects of HDAC inhibitors like fatigue, nausea and thrombocytopenia are more or less tolerated for the treatment of cancer, they have to be reduced for other therapeutic approaches, especially if nonhuman HDACs are targeted.[108,118] Three of the four approved HDAC inhibitors SAHA, PXD101, LBH589 and FK228 exhibit a characteristic structure which consists of a zinc binding group, an aliphatic spacer and a capping group which is connected to the spacer through a polar connection unit. They were found to be rather unselective and huge efforts are undertaken to develop better and isotype selective HDAC inhibitors in order to reduce unwanted side effects.[119]

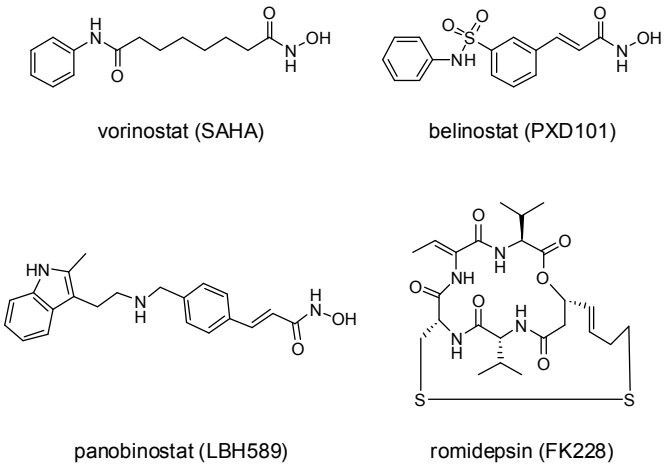

Figure 8: Approved cancer drugs.

As stated above the biophysical characterization of protein-ligand interactions is a valuable tool for the identification and selection of selective ligands. For HDACs and HDAC-like proteins especially crystallographic studies were carried out and indeed all Zn^{2+} dependent human HDACs except for HDAC5, 9, 10 and 11 have been crystallized.[119,120] Based on the structure of the class I homologue HDLP it was possible to develop a HDAC1/2 selective ligand. Therefore, the aminophenyl moiety of the known HDAC1, 2, 3 and 11 selective Inhibitor MS-275 was extended with a thienyl moiety to occupy the larger foot pocket.[121,122] The resulting ligand inhibits HDAC1 and 2 with IC_{50}-values of 20 and 100 nM and is inactive against HDAC3 up to concentrations of 20 μM.[122] This concept was also applied by Bressi *et al.*, Lauffer *et al.* and Wagner *et al.* who crystallized HDAC2 in complex with different *N*-(2-aminophenyl)-benzamide based inhibitors (Figure 9).[123–125] Bressi *et al.* explored the foot pocket in more detail and found a strong preference for phenyl, 4-fluorophenyl and 2- or 3-furanyl extensions, which inhibit HDAC2 with IC_{50}-values between 27 and 43 nM. Furthermore, they

elucidated that inhibitors with a *N*-(2-aminophenyl)-benzamide based scaffold are slow and tight-binding inhibitors since the IC_{50}-values decrease up to 42-fold upon longer incubation times.[125] The slow binding characteristics of benzamide based inhibitors were further exploited by Wagner *et al.* to achieve a temporal discrimination between HDAC1 and 2.[123] Especially, the developed compounds BRD4884 and BRD6688 possess useful kinetic profiles. BRD4884 allows a specific engagement of HDAC1 as the slow association rate for HDAC2 prevents an effective binding at dynamic conditions. In contrast, the compound BRD6688 exhibits a six times longer residence time for HDAC2 compared to HDAC1 which results in a longer lasting inhibition of HDAC2.[123] Kinetic and structural insights into the binding of MS-275, SAHA, Trichostatin A (TSA) and two extended *N*-(2-aminophenyl)-benzamide based inhibitors to HDAC1 and 2 were also provided by Lauffer *et al.* who performed kinetic studies to determine association rate constant and the residence time using a reporter displacement assay developed by Neumann and colleagues.[124,126] Unfortunately, the detailed assay principles and the chemical structure of the used probe are not published. For TSA and SAHA the binding kinetics were found to be fast. In contrast MS-275 and the extended benzamide based compounds were found to be slow binders with similar association rates between $1.44x10^2$ and $4.4x10^2$ $M^{-1}s^{-1}$. The extended benzamide based compounds exhibit slower dissociation rates than MS-275 resulting in an increased affinity and residence times in the order of 20–38 hours. Furthermore, they crystallized HDAC2 in complex with the hydroxamic acid SAHA and a benzamide based compound. The crystal structures revealed that the pocket responsible for the incorporation of the extended benzamide scaffold is opened upon ligand binding through a rotation of leucine 144 (Figure 10).[124]

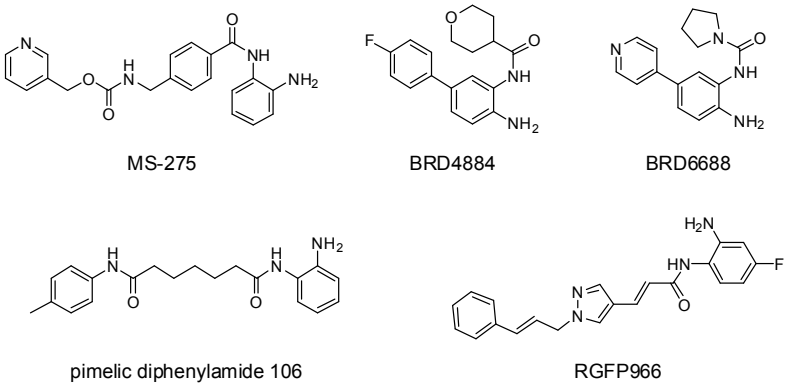

Figure 9: *N*-(2-aminophenyl)-benzamide based HDAC inhibitors.

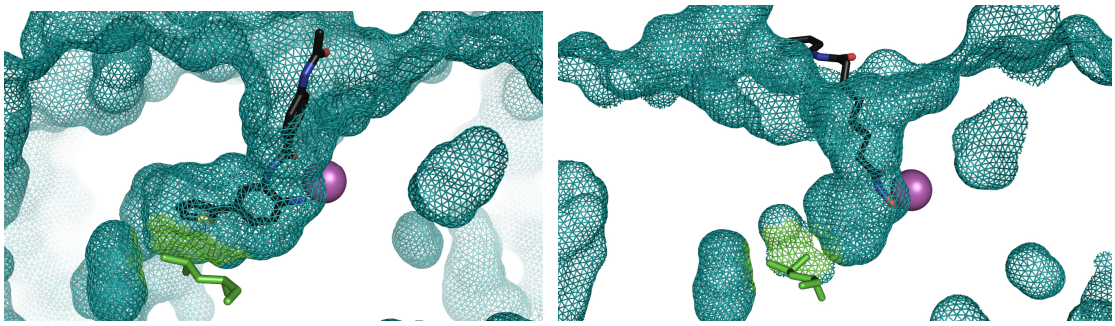

Figure 10: Surface representation of the active site of HDAC2 bound to a *N*-(2-aminophenyl)-benzamide based inhibitor (left, 4LY1) and SAHA (right, 4LXZ). The catalytic zinc ion is represented by the magenta sphere. Leucine 144 which undergoes a conformational switch upon binding of the *N*-(2-aminophenyl)-benzamide based inhibitor is highlighted in green.

The authors of the conducted kinetic studies assumed a one step binding reaction for the inhibition of HDAC1 and 2 and indeed a mechanistic study with the related compound pimelic diphenylamide 106 revealed a one step binding mechanism for HDAC1 and 2.[127] Interestingly, the authors found that binding of this compound to HDAC3 occurs with a two step induced fit mechanism. Furthermore, the determined inhibition constants revealed an about ten times stronger binding to HDAC3 compared to HDAC1.[127] The scaffold of this inhibitor was therefore used to design the HDAC3 selective ligand RGFP966 which inhibits HDAC3 with an IC_{50}-value of 80 nM and shows a 200-fold selectivity over other HDAC isotypes (Figure 9).[128]

As described above the structure of the foot pocket of class I HDACs 1, 2 and 3 is crucial for the observed selectivity of *N*-(2-aminophenyl)-benzamide based inhibitors. For HDAC8 this pocket is partially occupied as the leucine, which is responsible for the opening of the foot pocket is exchanged by a tryptophane.[124,129,130] The resulting differences in the structure of the foot pocket were exploited by Whitehead *et al.* to generate HDAC8 selective ligands with a (*R*)-α-amino-ketone moiety. The two developed compounds **1** and **2** inhibit HDAC8 with IC_{50}-values of 0.09 and 0.2 μM and achieved a 18- to 150-fold selectivity over HDAC1, 2 and 6. Especially, the high selectivity of the less affine binder **2** is comparable to the gold standard PCI-34051, which inhibits HDAC8 with an IC_{50}-value of 10 nM and exhibits a 200-fold selectivity over other HDAC isotypes (Figure 11).[130,131]

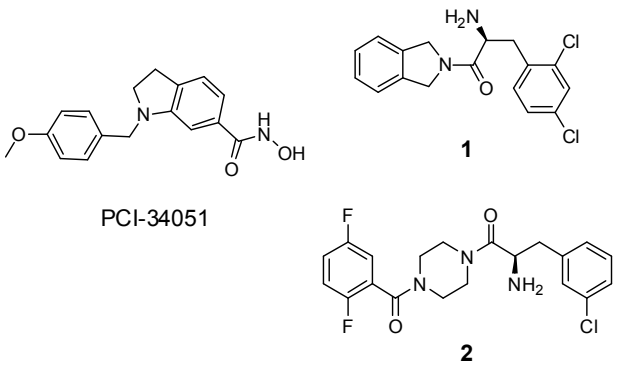

Figure 11: HDAC8 selective inhibitors

Besides the structure based design, HDAC8 was also used to investigate the thermodynamics, kinetics and the mechanism of the binding of selected compounds. The research group of Srivastava elucidated the kinetic binding mechanism and the thermodynamics for the binding of SAHA and TSA.[132] For

the determination of the kinetic properties it was exploited that binding of both compounds results in a binding specific quenching of the intrinsic tryptophane fluorescence. Using stopped-flow experiments it was determined that binding of both compounds to HDAC8 occurs in fast binding reactions via a two step induced fit mechanism. The thermodynamic characterization by isothermal titration calorimetry of the binding reactions revealed higher enthalpic contributions for the binding of SAHA than for binding of TSA. The authors postulated that these result from an additional hydrogen bond and concluded that SAHA establishes overall more specific interactions.[132] The determined binding enthalpies were corrected in a second study as it was elucidated that protonation effects had to be included into the analysis. By performing isothermal titration calorimetry experiments in different buffers it was determined that binding of TSA and SAHA is mainly entropy driven.[133]

Quite similar to the binding of SAHA and TSA to HDAC8 the binding of (*E*)-3-(Furan-2-yl)-*N*-hydroxyacrylamide (FAHA) to $HDAH_{bo}$ results in a reduced intrinsic tryptophane fluorescence.[103] By performing stopped-flow experiments the research group of Meyer-Almes elucidated an induced fit mechanism for the binding reaction, but in contrast to HDAC8 the reaction requires three steps.[134] The authors proposed that the initial binding of FAHA occurs at that the surface of $HDAH_{bo}$ in a rapid equilibrium. From there the inhibitor relocates to the active site and a second transient complex is formed, which finally isomerizes into a more stable complex.[134] The strong quenching properties of FAHA were further exploited to develop a reporter displacement assay, which was used to determine the binding constants of unlabeled inhibitors.[103] Another reporter displacement assay, that was developed by the same group was based on hydroxamic acid probes, which were conjugated to a dansyl moiety.[104] Upon binding of the dansyl conjugates a Förster resonance energy transfer between the intrinsic tryptophanes of $HDAH_{bo}$ and the dansyl moiety occurred and was exploited to determine the binding degree of the probes and the respective binding constants of the probes and of unlabeled compounds. Furthermore, the thermodynamic signatures of the probes and unlabeled compounds were determined by investigating the temperature dependence of the binding constants. Interestingly, it was found that higher enthalpic contributions to the binding resulted in an increased selectivity against HDAC1.[104]

Most biophysical studies on HDACs have been performed with isolated proteins, but as the function of several human HDACs is dependent on the binding to other proteins the influence of these interactions has to be considered for the development of selective ligands.[135] Bantscheff *et al.* started to evaluate the influence of complex formation on the affinity of selected ligands by a mass spectrometry based approach.[136] They elucidated that two ligands exhibited indeed a preference for HDAC3 containing complexes while being inactive towards HDAC1/2 containing SIN3 complexes.[136] One parameter,

that is likely affected by the binding to other proteins is the flexibility of the binding pocket as indicated by computational simulations for HDAC3, which propose a structural stabilization of the loops surrounding the active site by binding of the DAD.[137,138] Besides HDAC3, changes in the structural changes upon complex formation are also proposed for class IIa HDACs, since they are able to switch between an open and a closed state.[55] The closed state is thereby believed to be the active conformation, which is accessible to protein-protein interactions. Bottomley *et al.* developed the ligand **3**, that locks HDAC4 in the open state and successfully inhibits complex formation with the N-CoR:HDAC3 complex (Figure 12).[55] The applicability of this approach was also demonstrated by Issacs *et al.* who identified tasquinimod as an allosteric inhibitor of HDAC4 which binds with a K_d-value of 10–30 nM and prohibits binding to N-CoR2.[139] The authors proposed that binding of tasquinimod occurs in proximity to the structural zinc binding domian and locks HDAC4 in the open state.[139] Besides the open state, also the closed state of class IIa HDACs can be targeted to develop class selective ligands. Dominguez *et al.* used therefore the crystal structure of HDAC4 to design and optimize ligands based on the structure of **4** developed by Tessier and colleagues.[140-142] Interestingly, they used a cyclopropane core to achieve a geometrical preforming of the ligand. This strategy allowed to develop ligands like **5**, which inhibit class IIa HDACs with IC_{50}-values in the two digit nanomolar range and exhibit at least 28-fold selectivity over other HDAC isotypes.[142] Another class IIa selective ligand was identified by Lobera *et al.* by a high throughput screening with HDAC9.[143] The determined inhibitory constants for the hit compound TMP-269 for class IIa HDACs were 19 and 126 nM, resulting in an at least 18-fold selectivity over other HDAC isotypes. TMP-269 possesses a trifluoromethyloxadiazole moiety, which was found to be a nonchelating zinc binding group.[143]

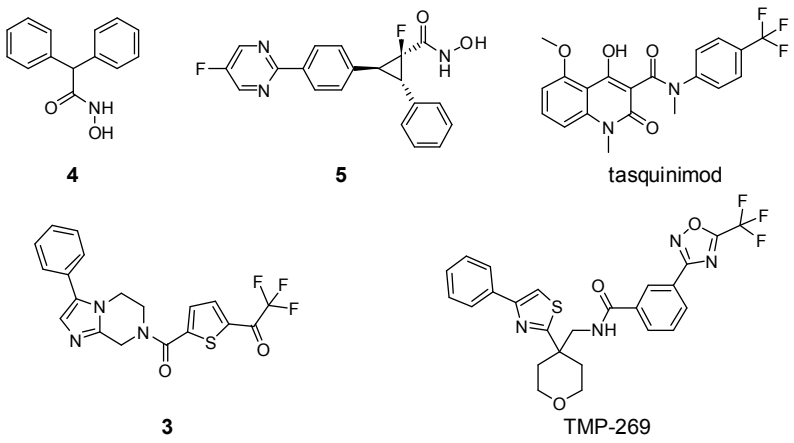

Figure 12: HDAC class IIa selective inhibitors

2.5. Objectives of the work

Human HDACs have emerged to be proven protein targets for the treatment of cancer and are evaluated as targets for a broad range of other diseases.[110,113,144] With SAHA, PXD101, LBH589 and FK228 four compounds were approved by the United States Food and Drug Administration for the treatment of different types of cancers.[145] They cause severe side effects like fatigue, nausea, anemia thrombocytopenia and leukopenia and most of these compounds were found to be pan

inhibitors.[108,118] Although several strategies were exploited for the development of selective inhibitors and indeed some success is visible, most compounds are if at all only class selective.[119,120] Furthermore, most compounds are from a narrow chemical space and are based on the traditional design concept. Several investigated compounds and also three of the approved drugs are hydroxamic acids which has serious drawbacks for the application of these compounds for not life threatening diseases since hydromxamic acids were found to be potentially mutagenic and are prone to unspecific reactions with other metal-dependent proteins.[143,146] For the identification of novel HDAC inhibitors with other chemical entities high throughput screening of diverse compound libraries would be useful. A necessary condition for conducting a high throughput campaign is the availability of suitable assays. For HDACs, most assays are activity based and require the deacetylation of a synthetic peptide.[147] The deacetylated peptide is then converted into a fluorescent product by the addition of trypsin and luciferase if a luminogenic assay is conducted.[148-150] Although these assays have been applied for screening they have some drawbacks as multi enzyme reactions and activity based assays are prone to errors which might result in a high false-positive rate.[143,151,152] Other approaches used labeled inhibitors as probes for the development of binding assays to determine binding constants, which are better suited than IC_{50}-values for the establishment of structure-activity relationships. Simultaneously, Riester *et al.* and Mazitschek *et al.* developed a binding assay for HDACs by fusing a fluorescent moiety to an unselective HDAC inhibitor.[105,153] Mazitschek *et al.* monitored the binding of HDACs via changes in the fluorescence polarization of the probe.[153] The assay developed by Riester *et al.* was able to use changes in the fluorescence anisotropy as well as in the fluorescence life-time of the probe as a readout resulting in a dual parameter assay, which was well suited for screening applications.[105,152]

Following up on their work, one part of this work is focused on the expansion of the methodology for the screening for HDAC inhibitors and the determination of their binding constants. Therefore, suitable binding assays are developed and evaluated for their applicability for high throughput screening. In order to reduce the false-positive rate and the subsequent efforts for compound logistics and retesting the robust readout fluorescence life-time is chosen.

To facilitate the drug discovery process for novel HDAC inhibitors further, the second part of this work evaluates whether a biophysical characterization of HDAC inhibitors can be used to estimate the selectivity of HDAC inhibitors. Since biophysical binding characteristics, like thermodynamic signatures, binding kinetics and mechanisms were successfully applied for other systems and used to develop a rational approach for the selection of promising lead structures, these parameters are determined and evaluated for their impact on the selectivity. For this propose closely to human HDACs related bacterial HDAHs are used as model systems. To gain further insights into the binding reaction the influence of the accessibility and flexibility on the thermodynamics are evaluated and it is

investigated how the thermodynamics, kinetics and mechanisms of the binding of HDAC inhibitors can be combined to identify and stratify selective compounds.

3. References

1. Renaud J-P, Chung C, Danielson UH, Egner U, Hennig M, Hubbard RE, Nar H: **Biophysics in drug discovery: impact, challenges and opportunities.** *Nat. Rev. Drug Discovery* (2016) **15**(10):679–698.

2. Folmer RH. **Integrating biophysics with HTS-driven drug discovery projects.** *Drug Discovery Today* (2016) **21**(3):491–498.

3. Chuprina A, Lukin O, Demoiseaux R, Buzko A, Shivanyuk A. **Drug-and lead-likeness, target class, and molecular diversity analysis of 7.9 million commercially available organic compounds provided by 29 suppliers.** *J. Chem. Inf. Model.* (2010) **50**(4):470–479.

4. Lipinski CA. **Rule of five in 2015 and beyond: Target and ligand structural limitations, ligand chemistry structure and drug discovery project decisions.** *Adv. Drug Delivery Rev.* (2016) **101**:34–41.

5. Muegge I. **Selection criteria for drug-like compounds.** *Med. Res. Rev.* (2003) **23**(3):302–321.

6. Hefti FF. **Requirements for a lead compound to become a clinical candidate.** *BMC Neurosci.* (2008) **9**(Suppl 3):S7.

7. Claveria-Gimeno R, Vega S, Abian O, Velazquez-Campoy A. **A Look at Ligand Binding Thermodynamics in Drug Discovery.** *Expert Opin. Drug Discovery* (2017).

8. Zheng H, Handing KB, Zimmerman MD, Shabalin IG, Almo SC, Minor W. **X-ray crystallography over the past decade for novel drug discovery-where are we heading next?** *Expert Opin. Drug Discovery* (2015) **10**(9):975–989.

9. Whittle PJ, Blundell TL. **Protein structure-based drug design.** *Annu. Rev. Biophys. Biomol. Struct.* (1994) **23**(1):349–375.

10. Bissantz C, Kuhn B, Stahl M. **A medicinal chemist's guide to molecular interactions.** *J. Med. Chem.* (2010) **53**(14):5061–5084.

11. Ladbury JE, Klebe G, Freire E. **Adding calorimetric data to decision making in lead discovery: a hot tip.** *Nat. Rev. Drug Discovery.* (2009) **9**(1):23–27.

12. Bronowska AK. **Thermodynamics of Ligand-Protein Interactions: Implications for Molecular Design, Thermodynamics Interaction Studies - Solids, Liquids and Gases, JC Moreno-Pirajan (Ed.)** *InTech* (2011).

13. Chaires JB. **Calorimetry and thermodynamics in drug design.** *Annu. Rev. Biophys.* (2008) **37**:135–151.

14. Kawasaki Y, Freire E. **Finding a better path to drug selectivity.** *Drug Discovery Today* (2011) **16**(21):985–90.

15. Freire E. **Do enthalpy and entropy distinguish first in class from best in class?** *Drug Discovery Today.* (2008) **13**(19-20):869–874.

16. Klebe G. **Applying thermodynamic profiling in lead finding and optimization.** *Nat. Rev. Drug Discovery* (2015) **14**(2):95–110.

17. Schön A, Freire E. **Enthalpy screen of drug candidates.** *Anal. Biochem.* (2016) **513**:1–6.

18. Geschwindner S, Ulander J, Johansson P. **Ligand binding thermodynamics in drug discovery: still a hot tip?** *J. Med. Chem.* (2015) **58**(16):6321–6335.

19. Copeland RA, Pompliano DL, Meek TD. **Drug-target residence time and its implications for lead optimization.** *Nat. Rev. Drug Discovery* (2006) **5**(9):730–739.

20. Dahl G, Åkerud T. **Pharmacokinetics and the drug-target residence time concept.** *Drug Discovery Today* (2013) **18**(15-16):697–707

21. Cusack KP, Wang Y, Hoemann MZ, Marjanovic J, Heym RG, Vasudevan A. **Design strategies to address kinetics of drug binding and residence time.** *Bioorg. Med. Chem. Lett.* (2015) **25**(10):2019–2027.

22. Forster M, Chaikuad A, Bauer SM, Holstein J, Robers MB, Corona CR, Gehringer M, Pfaffenrot E, Ghoreschi K, Knapp S, et al.. **Selective JAK3 Inhibitors with a Covalent Reversible Binding Mode Targeting a New Induced Fit Binding Pocket.** *Cell Chem. Biol.* (2016) **23**(11):1335–1340.

23. Bradshaw JM, McFarland JM, Paavilainen VO, Bisconte A, Tam D, Phan VT, Romanov S, Finkle D, Shu J, Patel V, et al.. **Prolonged and tunable residence time using reversible covalent kinase inhibitors.** *Nat. Chem. Biol.* (2015) **11**(7):525–531

24. Tummino PJ, Copeland RA. **Residence Time of Receptor- Ligand Complexes and Its Effect on Biological Function.** *Biochemistry* (2008) **47**(20):5481–5492.

25. Lu H, Tonge PJ. **Drug-target residence time: critical information for lead optimization.** *Curr. Opin. Chem. Biol.* (2010) **14**(4):467–474.

26. Copeland RA. **The drug-target residence time model: a 10-year retrospective.** *Nat. Rev. Drug Discovery* (2016) **15**(2):87–95;

27. Swinney DC. **Kinetic Binding Mechanisms: Their Contribution to an Optimal Therapeutic Index.** *Label-Free Technologies for Drug Discovery*. (2011) 283–302.

28. Koshland D. **Enzyme flexibility and enzyme action.** *J. Cell. Comp. Physiol.* (1959) **54**(S1):245–58.

29. Changeux J-P, Edelstein S. **Conformational selection or induced fit? 50 years of debate resolved.** *F1000 Biol. Rep.* (2011) **3**:19.

30. Vogt AD, Di Cera E. **Conformational selection or induced fit? A critical appraisal of the kinetic mechanism.** *Biochemistry.* (2012) **51**(30):5894–5902.

31. Vogt AD, Pozzi N, Chen Z, Di Cera E. **Essential role of conformational selection in ligand binding.** *Biophys. Chem.* (2014) **186**:13–21

32. Meyer-Almes F-J. **Discrimination between conformational selection and induced fit protein-ligand binding using Integrated Global Fit analysis.** *Eur. Biophys. J.* (2016) **45**(3):245–257.

33. Clore GM. **Interplay between conformational selection and induced fit in multidomain protein-ligand binding probed by paramagnetic relaxation enhancement.** *Biophys. Chem.* (2014) **186**:3–12

34. Agafonov RV, Wilson C, Otten R, Buosi V, Kern D. **Energetic dissection of Gleevec's selectivity toward human tyrosine kinases.** *Nat. Struct. Mol. Biol.* (2014) **21**(10):848–853.

35. Dosnon M, Bonetti D, Morrone A, Erales J, Di Silvio E, Longhi S, Gianni S. **Demonstration of a folding after binding mechanism in the recognition between the measles virus NTAIL and X domains.** *ACS Chem. Biol.* (2014) **10**(3):795–802.

36. Badireddy S, Yunfeng G, Ritchie M, Akamine P, Wu J, Kim CW, Taylor SS, Qingsong L, Swaminathan K, Anand GS. **Cyclic AMP analog blocks kinase activation by stabilizing inactive conformation: conformational selection highlights a new concept in allosteric inhibitor design.** *Mol. Cell. Proteomics* (2011) **10**(3):M110.004390.

37. Cheng W-C, Chen Y-F, Wang H-J, Hsu K-C, Lin S-C, Chen T-J, Yang J-M, Wang W-C. **Structures of Helicobacter pylori shikimate kinase reveal a selective inhibitor-induced-fit mechanism.** *PLoS One* (2012) **7**(3):e33481.

38. Phillips D. **The presence of acetyl groups in histones.** *Biochem. J.* (1963) **87**(2):258–263.

39. ALLFREY VG, FAULKNER R, MIRSKY AE. **ACETYLATION AND METHYLATION OF HISTONES AND THEIR POSSIBLE ROLE IN THE REGULATION OF RNA SYNTHESIS.** *Proc. Natl. Acad. Sci. U.S.A.* (1964) **51**:786–794.

40. Grunstein M. **Histone acetylation in chromatin structure and transcription.** *Nature* (1997) **389**(6649):349–352.

41. Turner BM. *Histone acetylation and an epigenetic code*. *Bioessays* (2000) **22**(9):836–845.

42. Hu LI, Lima BP, Wolfe AJ. **Bacterial protein acetylation: the dawning of a new age.** *Mol. Microbiol.* (2010) **77**(1):15–21.

43. Zhao S, Xu W, Jiang W, Yu W, Lin Y, Zhang T, Yao J, Zhou L, Zeng Y, Li H et al.. **Regulation of cellular metabolism by protein lysine acetylation.** *Science* (2010) **327**(5968):1000–1004.

44. Kouzarides T. **Acetylation: a regulatory modification to rival phosphorylation?** *EMBO J.* (2000) **19**(6):1176–1179.

45. Kim SC, Sprung R, Chen Y, Xu Y, Ball H, Pei J, Cheng T, Kho Y, Xiao H, Xiao L et al.. **Substrate and functional diversity of lysine acetylation revealed by a proteomics survey.** *Mol. Cell* (2006) **23**(4):607–618.

46. Jones JD, O'Connor CD. **Protein acetylation in prokaryotes.** *Proteomics* (2011) **11**(15):3012–3022.

47. Bernal V, Castaño-Cerezo S, Gallego-Jara J, Écija-Conesa A, de Diego T, Iborra JL, Cánovas M. **Regulation of bacterial physiology by lysine acetylation of proteins.** *New Biotechnol.* (2014) **31**(6):586–595

48. Pan J, Ye Z, Cheng Z, Peng X, Wen L, Zhao F. **Systematic analysis of the lysine acetylome in Vibrio parahaemolyticus.** *J. Proteome Res.* (2014) **13**(7):3297–3202

49. Ouidir T, Cosette P, Jouenne T, Hardouin J. **Proteomic profiling of lysine acetylation in Pseudomonas aeruginosa reveals the diversity of acetylated proteins.** *Proteomics* (2015) **15**(13):2152–2157.

50. Yu BJ, Kim JA, Moon JH, Ryu SE, Pan J-G. **The diversity of lysine-acetylated proteins in Escherichia coli.** *J. Microbiol. Biotechnol.* (2008) **18**(9):1529–1536.

51. Cain JA, Solis N, Cordwell SJ. **Beyond gene expression: The impact of protein post-translational modifications in bacteria.** *J. Proteomics* (2014) **97**:265–286.

52. Yang X-J, Seto E. **The Rpd3/Hda1 family of lysine deacetylases: from bacteria and yeast to mice and men.** *Nat. Rev. Mol. Cell Biol.* (2008) **9**(3):206–218.

53. Finnin MS, Donigian JR, Cohen A, Richon VM, Rifkind RA, Marks PA, Breslow R, Pavletich NP. **Structures of a histone deacetylase homologue bound to the TSA and SAHA inhibitors.** *Nature* (1999) **401**(6749):188–193.

54. Marks PA, Miller T, Richon VM. **Histone deacetylases.** *Curr. Opin. Pharmacol.* (2003) **3**(4):344–351.

55. Bottomley MJ, Surdo PL, Di Giovine P, Cirillo A, Scarpelli R, Ferrigno F, Jones P, Neddermann P, De Francesco R, Steinkühler C, et al.. **Structural and functional analysis of the human HDAC4 catalytic domain reveals a regulatory structural zinc-binding domain.** *J. Biol. Chem.* (2008) **283**(39):26694–26704.

56. Gantt SL, Joseph CG, Fierke CA. **Activation and inhibition of histone deacetylase 8 by monovalent cations.** *J. Biol. Chem.* (2010) **285**(9):6036–6043.

57. Dowling DP, Gantt SL, Gattis SG, Fierke CA, Christianson DW. **Structural Studies of Human Histone Deacetylase 8 and Its Site-Specific Variants Complexed with Substrate and Inhibitors.** *Biochemistry* (2008) **47**(51):13554–13563.

58. Kräḿer A, Wagner T, Yildiz O, Meyer-Almes F-J. **Crystal Structure of a Histone Deacetylase Homologue from Pseudomonas aeruginosa.** *Biochemistry* (2016) **55**(49):6858–6868.

59. Gantt SML, Decroos C, Lee MS, Gullett LE, Bowman CM, Christianson DW, Fierke CA. **General Base-General Acid Catalysis in Human Histone Deacetylase 8.** *Biochemistry* **(**2016) **55**(5):820–832.

60. Corminboeuf C, Hu P, Tuckerman ME, Zhang Y. **Unexpected deacetylation mechanism suggested by a density functional theory QM/MM study of histone-deacetylase-like protein.** *J. Am. Chem. Soc.* (2006) **128**(14):4530–4531.

61. Vanommeslaeghe K, De Proft F, Loverix S, Tourwe D, Geerlings P. **Theoretical study revealing the functioning of a novel combination of catalytic motifs in histone deacetylase.** *Bioorg. Med. Chem.* (2005) **13**(12):3987–3992.

62. Wu R, Wang S, Zhou N, Cao Z, Zhang Y. **A proton-shuttle reaction mechanism for histone deacetylase 8 and the catalytic role of metal ions.** *J. Am. Chem. Soc.* (2010) **132**(27):9471–9479.

63. Chen K, Zhang X, Wu Y-D, Wiest O. **Inhibition and mechanism of HDAC8 revisited.** *J. Am. Chem. Soc.* (2014) **136**(33):11636–11643.

64. Hai Y, Christianson DW. **Histone deacetylase 6 structure and molecular basis of catalysis and inhibition.** *Nat. Chem. Biol.* (2016) **12**(9):741–747

65. Marmorstein R. **Structure of histone deacetylases: insights into substrate recognition and catalysis.** *Structure* (2001) **9**(12):1127–1133.

66. Lombardi PM, Cole KE, Dowling DP, Christianson DW. **Structure, mechanism, and inhibition of histone deacetylases and related metalloenzymes.** *Curr. Opin. Struct. Biol.* (2011) **21**(6):735–743.

67. Wolfson NA, Pitcairn CA, Fierke CA. **HDAC8 substrates: Histones and beyond.** *Biopolymers* (2013) **99**(2):112–126.

68. Chakrabarti A, Oehme I, Witt O, Oliveira G, Sippl W, Romier C, Pierce RJ, Jung M. **HDAC8: a multifaceted target for therapeutic interventions.** *Trends Pharmacol. Sci.* (2015) **36**(7):481–492.

69. Juan L-J, Shia W-J, Chen M-H, Yang W-M, Seto E, Lin Y-S, Wu C-W. **Histone deacetylases specifically down-regulate p53-dependent gene activation.** *J. Biol. Chem.* (2000) **275**(27):20436–20443.

70. Moser MA, Hagelkruys A, Seiser C. **Transcription and beyond: the role of mammalian class I lysine deacetylases.** *Chromosoma* (2014) **123**(1-2):67–78.

71. Nagy L, Kao H-Y, Chakravarti D, Lin RJ, Hassig CA, Ayer DE, Schreiber SL, Evans RM. **Nuclear receptor repression mediated by a complex containing SMRT, mSin3A, and histone deacetylase.** *Cell* (1997) **89**(3):373–380.

72. You A, Tong JK, Grozinger CM, Schreiber SL. **CoREST is an integral component of the CoREST-human histone deacetylase complex.** *Proc. Natl. Acad. Sci. U.S.A.* (2001) **98**(4):1454–1458.

73. Guenther MG, Barak O, Lazar MA. **The SMRT and N-CoR corepressors are activating cofactors for histone deacetylase 3.** *Mol Cell. Biol.* (2001) **21**(18):6091–6101.

74. Watson PJ, Fairall L, Santos GM, Schwabe JW. **Structure of HDAC3 bound to co-repressor and inositol tetraphosphate**. *Nature* (2012) **481**(7381):335–340.

75. Watson PJ, Millard CJ, Riley AM, Robertson NS, Wright LC, Godage HY, Cowley SM, Jamieson AG, Potter BV, Schwabe JW. **Insights into the activation mechanism of class I HDAC complexes by inositol phosphates.** *Nat. Commun.* (2016) **7**:11262.

76. Millard CJ, Watson PJ, Celardo I, Gordiyenko Y, Cowley SM, Robinson CV, Fairall L, Schwabe JW. **Class I HDACs share a common mechanism of regulation by inositol phosphates.** *Mol. Cell* (2013) **51**(1):57–67.

77. Grozinger CM, Hassig CA, Schreiber SL. **Three proteins define a class of human histone deacetylases related to yeast Hda1p.** *Proc. Natl. Acad. Sci. U.S.A.* (1999) **96**(9):4868–4873.

78. Gregoretti I, Lee Y-M, Goodson HV. **Molecular evolution of the histone deacetylase family: functional implications of phylogenetic analysis.** *J. Mol. Biol.* (2004) **338**(1):17–31.

79. Guardiola AR, Yao T-P. **Molecular cloning and characterization of a novel histone deacetylase HDAC10.** *J. Biol. Chem.* (2002) **277**(5):3350–3356.

80. Miyake Y, Keusch JJ, Wang L, Saito M, Hess D, Wang X, Melancon BJ, Helquist P, Gut H, Matthias P. **Structural insights into HDAC6 tubulin deacetylation and its selective inhibition.** *Nat. Chem. Biol.* (2016) **12**(9):748–754.

81. Kaluza D, Kroll J, Gesierich S, Yao T-P, Boon RA, Hergenreider E, Tjwa M, Rössig L, Seto E, Augustin HG, et al.. **Class IIb HDAC6 regulates endothelial cell migration and angiogenesis by deacetylation of cortactin.** *EMBO J.* (2011) **30**(20):4142–4156.

82. Li D, Xie S, Ren Y, Huo L, Gao J, Cui D, Liu M, Zhou J. **Microtubule-associated deacetylase HDAC6 promotes angiogenesis by regulating cell migration in an EB1-dependent manner.** *Protein Cell* (2011) **2**(2):150–160.

83. Boyault C, Sadoul K, Pabion M, Khochbin S. **HDAC6, at the crossroads between cytoskeleton and cell signaling by acetylation and ubiquitination.** *Oncogene* (2007) **26**(37):5468–5476.

84. Ouyang H, Ali YO, Ravichandran M, Dong A, Qiu W, MacKenzie F, Dhe-Paganon S, Arrowsmith CH, Zhai RG. **Protein aggregates are recruited to aggresome by histone deacetylase 6 via unanchored ubiquitin C termini.** *J. Biol. Chem.* (2012) **287**(4):2317–2327.

85. Lahm A, Paolini C, Pallaoro M, Nardi M, Jones P, Neddermann P, Sambucini S, Bottomley M, Surdo PL, Carfi A, et al.. **Unraveling the hidden catalytic activity of vertebrate class IIa histone deacetylases.** *Proc. Natl. Acad. Sci. U.S.A.* (2007) **104**(44):17335–17340.

86. Clocchiatti A, Di Giorgio E, Viviani G, Streuli C, Sgorbissa A, Picco R, Cutano V, Brancolini C. **The MEF2-HDAC axis controls proliferation of mammary epithelial cells and acini formation in vitro.** *J. Cell. Sci.* (2015) **128**(21):3961–3976.

87. Clocchiatti A, Di Giorgio E, Demarchi F, Brancolini C. **Beside the MEF2 axis: unconventional functions of HDAC4.** *Cell. Signalling* (2013) **25**(1):269–276.

88. Nebbioso A, Manzo F, Miceli M, Conte M, Manente L, Baldi A, De Luca A, Rotili D, Valente S, Mai A, et al.. **Selective class II HDAC inhibitors impair myogenesis by modulating the stability and activity of HDAC-MEF2 complexes.** *EMBO Rep.* (2009) **10**(7):776–782.

89. Clocchiatti A, Di Giorgio E, Ingrao S, Meyer-Almes F-J, Tripodo C, Brancolini C. **Class IIa HDACs repressive activities on MEF2-depedent transcription are associated with poor prognosis of ER+ breast tumors.** *FASEB J.* (2013) **27**(3):942–954.

90. Vallabhapurapu SD, Noothi SK, Pullum DA, Lawrie CH, Pallapati R, Potluri V, Kuntzen C, Khan S, Plas DR, Orlowski RZ, et al.. **Transcriptional repression by the HDAC4-RelB-p52 complex regulates multiple myeloma survival and growth.** *Nat. Commun.* (2015) **6**:8428.

91. Martin M, Kettmann R, Dequiedt F. **Class IIa histone deacetylases: conducting development and differentiation.** *Int. J. Dev. Biol.* (2009) **53**(2):291–301.

92. Soriano FX, Chawla S, Skehel P, Hardingham GE. **SMRT-mediated co-shuttling enables export of class IIa HDACs independent of their CaM kinase phosphorylation sites.** *J. Neurochem.* (2013) **124**(1):26–35.

93. Di Giorgio E, Brancolini C. **Regulation of class IIa HDAC activities: it is not only matter of subcellular localization.** *Epigenomics* (2016) **8**(2):251–269.

94. Hudson GM, Watson PJ, Fairall L, Jamieson AG, Schwabe JW. **Insights into the Recruitment of Class IIa histone deacetylases (HDACs) to the SMRT/NCoR transcriptional repression complex.** *J. Biol. Chem.* (2015) **290**(29):18237–18244.

95. Kim GS, Jung H-E, Kim J-S, Lee YC. **Mutagenesis Study Reveals the Rim of Catalytic Entry Site of HDAC4 and-5 as the Major Binding Surface of SMRT Corepressor.** *PloS one (*2015) **10**(7):e0132680.

96. Ago T, Liu T, Zhai P, Chen W, Li H, Molkentin JD, Vatner SF, Sadoshima J. **A redox-dependent pathway for regulating class II HDACs and cardiac hypertrophy.** *Cell* (2008) **133**(6):978–993.

97. Grundy FJ, Waters DA, Takova TY, Henkin TM. **Identification of genes involved in utilization of acetate and acetoin in Bacillus subtilis.** *Mol. Microbiol.* (1993) **10**(2):259–271.

98. Buck SW, Gallo CM, Smith JS. **Diversity in the Sir2 family of protein deacetylases.** *J. Leukocyte Biol.* (2004) **75**(6):939–950.

99. Hildmann C, Ninkovic M, Dietrich R, Wegener D, Riester D, Zimmermann T, Birch OM, Bernegger C, Loidl P, Schwienhorst A. **A new amidohydrolase from Bordetella or Alcaligenes strain FB188 with similarities to histone deacetylases.** *J. Bacteriol.* (2004)**186**(8):2328–2339.

100. Lombardi PM, Angell HD, Whittington DA, Flynn EF, Rajashankar KR, Christianson DW. **Structure of prokaryotic polyamine deacetylase reveals evolutionary functional relationships with eukaryotic histone deacetylases.** *Biochemistry* (2011) **50**(11):1808–1817.

101. Krämer A, Herzer J, Overhage J, Meyer-Almes F-J. **Substrate specificity and function of acetylpolyamine amidohydrolases from Pseudomonas aeruginosa.** *BMC Biochem.* (2016) **17**:4.

102. Nielsen TK, Hildmann C, Dickmanns A, Schwienhorst A, Ficner R. **Crystal structure of a bacterial class 2 histone deacetylase homologue.** *J. Mol. Biol.* (2005) **354**(1):107–120.

103. Riester D, Hildmann C, Schwienhorst A, Meyer-Almes F-J. **Histone deacetylase inhibitor assay based on fluorescence resonance energy transfer.** *Anal. Biochem.* (2007) **362**(1):136–141.

104. Meyners C, Baud MG, Fuchter MJ, Meyer-Almes F-J. **Thermodynamics of ligand binding to histone deacetylase like amidohydrolase from Bordetella/Alcaligenes.** *J. Mol. Recognit.* (2014) **27**(3):160–172.

105. Riester D, Hildmann C, Haus P, Galetovic A, Schober A, Schwienhorst A, Meyer-Almes F-J. **Non-isotopic dual parameter competition assay suitable for high-throughput screening of histone deacetylases.** *Bioorg. Med. Chem. Lett.* (2009) **19**(13):3651–3656.

106. Yoshida M, Furumai R, Nishiyama M, Komatsu Y, Nishino N, Horinouchi S. **Histone deacetylase as a new target for cancer chemotherapy.** *Cancer Chemother. Pharmacol.* (2001) **48**(1):20–26.

107. Johnstone RW. **Histone-deacetylase inhibitors: novel drugs for the treatment of cancer.** *Nat. Rev. Drug Discovery* (2002) **1**(4):287–299.

108. Marks PA, Breslow R. **Dimethyl sulfoxide to vorinostat: development of this histone deacetylase inhibitor as an anticancer drug.** *Nat. Biotechnol.* (2007) **25**(1):84–90.

109. Qiu X, Xiao X, Li N, Li Y. **Histone deacetylases inhibitors (HDACis) as novel therapeutic application in various clinical diseases.** *Prog. Neuro-Psychopharmacol. Biol. Psychiatry* (2017) **72**:60–72.

110. Yoon S, Eom GH. **HDAC and HDAC inhibitor: from cancer to cardiovascular diseases.** *Chonnam Med. J.* (2016) **52**(1):1–11.

111. Sharma S, Taliyan R. **Histone deacetylase inhibitors: Future therapeutics for insulin resistance and type 2 diabetes.** *Pharmacol. Res.* (2016) **113**:320–326.

112. Jia H, Kast RJ, Steffan JS, Thomas EA. **Selective histone deacetylase (HDAC) inhibition imparts beneficial effects in Huntington's disease mice: implications for the ubiquitin-proteasomal and autophagy systems.** *Hum. Mol. Genet.* (2012) **21**(24):5280–5293.

113. Chuang D-M, Leng Y, Marinova Z, Kim H-J, Chiu C-T. **Multiple roles of HDAC inhibition in neurodegenerative conditions.** *Trends Neurosci.* (2009) **32**(11):591–601.

114. Mielcarek M, Landles C, Weiss A, Bradaia A, Seredenina T, Inuabasi L, Osborne GF, Wadel K, Touller C, Butler R, et al.. **HDAC4 reduction: a novel therapeutic strategy to target cytoplasmic huntingtin and ameliorate neurodegeneration.** *PLoS Biol.* (2013) **11**(11):e1001717.

115. Yue F, Li W, Zou J, Chen Q, Xu G, Huang H, Xu Z, Zhang S, Gallinari P, Wang F, et al.. **Blocking the association of HDAC4 with MAP1S accelerates autophagy clearance of mutant Huntingtin.** *Aging* (2015) **7**(10):839–853.

116. Andrews KT, Haque A, Jones MK. **HDAC inhibitors in parasitic diseases.** *Immunol. Cell Biol.* (2011) **90**(1):66–77.

117. Chua MJ, Arnold MS, Xu W, Lancelot J, Lamotte S, Späth G, Prina E, Pierce RJ, Fairlie DP, Skinner-Adams TS, et al.. **Effect of clinically approved HDAC inhibitors on plasmodium, Leishmania and Schistosoma parasite growth.** *Int. J. Parasitol. Drugs Drug Resist.* (2017) **7**(1):42–50

118. Marks P, Xu W-S. **Histone deacetylase inhibitors: Potential in cancer therapy.** *J. Cell. Biochem.* (2009) **107**(4):600–608.

119. Roche J, Bertrand P. **Inside HDACs with more selective HDAC inhibitors.** *Eur. J. Med. Chem.* (2016) **121**:451–483

120. Micelli C, Rastelli G. **Histone deacetylases: structural determinants of inhibitor selectivity.** *Drug Discovery Today* (2015) **20**(6):718–735.

121. Saito A, Yamashita T, Mariko Y, Nosaka Y, Tsuchiya K, Ando T, Suzuki T, Tsuruo T, Nakanishi O. **A synthetic inhibitor of histone deacetylase, MS-27-275, with marked in vivo antitumor activity against human tumors.** *Proc. Natl. Acad. Sci. U.S.A.* (1999) **96**(8):4592–4597.

122. Moradei OM, Mallais TC, Frechette S, Paquin I, Tessier PE, Leit SM, Fournel M, Bonfils C, Trachy-Bourget M-C, Liu J, et al.. **Novel aminophenyl benzamide-type histone deacetylase inhibitors with enhanced potency and selectivity.** *J. Med. Chem.* (2007) **50**(23):5543–5546.

123. Wagner F, Zhang Y-L, Fass D, Joseph N, Gale J, Weiwer M, McCarren P, Fisher S, Kaya T, Zhao W-N, et al.. **Kinetically selective inhibitors of histone deacetylase 2 (HDAC2) as cognition enhancers.** *Chem. Sci.* (2015) **6**(1):804–815.

124. Lauffer BE, Mintzer R, Fong R, Mukund S, Tam C, Zilberleyb I, Flicke B, Ritscher A, Fedorowicz G, Vallero R, et al.. **Histone deacetylase (HDAC) inhibitor kinetic rate constants correlate with cellular histone acetylation but not transcription and cell viability.** *J. Biol. Chem.* (2013) **288**(37):26926–26943

125. Bressi JC, Jennings AJ, Skene R, Wu Y, Melkus R, De Jong R, O'Connell S, Grimshaw CE, Navre M, Gangloff AR. **Exploration of the HDAC2 foot pocket: Synthesis and SAR of substituted N-(2-aminophenyl) benzamides.** *Bioorg. Med. Chem. Lett.* (2010) **20**(10):3142–3145.

126. Neumann L, von König K, Ullmann D. **HTS reporter displacement assay for fragment screening and fragment evolution toward leads with optimized binding kinetics, binding selectivity, and thermodynamic signature.** *Methods Enzymol.* (2010) **493**:299–320.

127. Chou CJ, Herman D, Gottesfeld JM. **Pimelic diphenylamide 106 is a slow, tight-binding inhibitor of class I histone deacetylases.** *J Biol. Chem.* (2008) **283**(51):35402–35409.

128. Malvaez M, McQuown SC, Rogge GA, Astarabadi M, Jacques V, Carreiro S, Rusche JR, Wood MA. **HDAC3-selective inhibitor enhances extinction of cocaine-seeking behavior in a persistent manner.** *Proc. Natl. Acad. Sci. U.S.A.* (2013) **110**(7):2647–2652.

129. Somoza JR, Skene RJ, Katz BA, Mol C, Ho JD, Jennings AJ, Luong C, Arvai A, Buggy JJ, Chi E, et al.. **Structural snapshots of human HDAC8 provide insights into the class I histone deacetylases.** *Structure* (2004) 12(7):1325–1334.

130. Whitehead L, Dobler MR, Radetich B, Zhu Y, Atadja PW, Claiborne T, Grob JE, McRiner A, Pancost MR, Patnaik A, et al.. **Human HDAC isoform selectivity achieved via exploitation of the acetate release channel with structurally unique small molecule inhibitors.** *Bioorg. Med. Chem.* (2011) **19**(15):4626–4634.

131. Balasubramanian S, Ramos J, Luo W, Sirisawad M, Verner E, Buggy J. **A novel histone deacetylase 8 (HDAC8)-specific inhibitor PCI-34051 induces apoptosis in T-cell lymphomas.** *Leukemia* (2008) **22**(5):1026–1034.

132. Singh RK, Lall N, Leedahl TS, McGillivray A, Mandal T, Haldar M, Mallik S, Cook G, Srivastava D. K**inetic and Thermodynamic Rationale for Suberoylanilide Hydroxamic Acid Being a Preferential Human Histone Deacetylase 8 Inhibitor As Compared to the Structurally Similar Ligand, Trichostatin A.** *Biochemistry* (2013) **52**(45):8139–8149.

133. Singh RK, Suzuki T, Mandal T, Balsubramanian N, Haldar M, Mueller DJ, Strode JA, Cook G, Mallik S, Srivastava D. **Thermodynamics of binding of structurally similar ligands to histone deacetylase 8 sheds light on challenges in the rational design of potent and isozyme-selective inhibitors of the enzyme.** *Biochemistry* (2014) **53**(48):7445–7458.

134. Sykora J, Meyer-Almes F-J. **Mechanism of Binding of the Inhibitor (E)-3-(Furan-2-yl)-N-hydroxyacrylamide to a Histone Deacetylase-like Amidohydrolase.** *Biochemistry* (2010) **49**(7):1418–1424.

135. Millard CJ, Watson PJ, Fairall L, Schwabe JW. **Targeting Class I Histone Deacetylases in a "Complex" Environment.** *Trends Pharmacol. Sci.* (2017) **38**(4):363–377.

136. Bantscheff M, Hopf C, Savitski MM, Dittmann A, Grandi P, Michon A-M, Schlegl J, Abraham Y, Becher I, Bergamini G, et al.. **Chemoproteomics profiling of HDAC inhibitors reveals selective targeting of HDAC complexes.** *Nat. Biotechnol.* (2011) **29**(3):255–265.

137. Arrar M, Turnham R, Pierce L, de Oliveira CAF, McCammon JA. **Structural insight into the separate roles of inositol tetraphosphate and deacetylase-activating domain in activation of histone deacetylase 3.** *Protein Sci.* (2013) **22**(1):83–92.

138. Deschamps N, Simões-Pires CA, Carrupt P-A, Nurisso A. **How the flexibility of human histone deacetylases influences ligand binding: an overview.** *Drug Discovery Today*. (2015) **20**(6):736–742.

139. Isaacs JT, Antony L, Dalrymple SL, Brennen WN, Gerber S, Hammers H, Wissing M, Kachhap S, Luo J, Xing L, et al.. **Tasquinimod is an allosteric modulator of HDAC4 survival signaling within the compromised cancer microenvironment.** *Cancer Res*. (2013) **73**(4):1386–1399.

140. Tessier P, Smil DV, Wahhab A, Leit S, Rahil J, Li Z, Déziel R, Besterman JM. **Diphenylmethylene hydroxamic acids as selective class IIa histone deacetylase inhibitors.** *Bioorg. Med. Chem. Lett.* (2009) **19**(19):5684–5688.

141. Bürli RW, Luckhurst CA, Aziz O, Matthews KL, Yates D, Lyons KA, Beconi M, McAllister G, Breccia P, Stott AJ, et al.. **Design, synthesis, and biological evaluation of potent and selective class IIa histone deacetylase (HDAC) inhibitors as a potential therapy for Huntington's disease.** *J. Med. Chem.* (2013) **56**(24):9934–9954.

142. Luckhurst CA, Breccia P, Stott AJ, Aziz O, Birch HL, Bürli RW, Hughes SJ, Jarvis RE, Lamers M, Leonard PM, et al.. **Potent, selective, and CNS-penetrant tetrasubstituted cyclopropane class IIa histone deacetylase (HDAC) inhibitors.** *ACS Med. Chem. Lett.* (2015) **7**(1):34–39.

143. Lobera M, Madauss KP, Pohlhaus DT, Wright QG, Trocha M, Schmidt DR, Baloglu E, Trump RP, Head MS, Hofmann GA, et al.. **Selective class IIa histone deacetylase inhibition via a nonchelating zinc-binding group.** *Nat. Chem. Biol.* (2013) **9**(5):319–325.

144. Li Y, Seto E. **HDACs and HDAC inhibitors in cancer development and therapy.** *Cold Spring Harb. Perspect. Med.* (2016) **6**(10):a026831.

145. Zhang L, Han Y, Jiang Q, Wang C, Chen X, Li X, Xu F, Jiang Y, Wang Q, Xu W. **Trend of histone deacetylase inhibitors in cancer therapy: isoform selectivity or multitargeted strategy.** *Med. Res. Rev.* (2015) **35**(1):63–84.

146. Shen S, Kozikowski AP. **Why Hydroxamates May Not Be the Best Histone Deacetylase Inhibitors—What Some May Have Forgotten or Would Rather Forget?** *ChemMedChem* (2015) **11**(1):15–21.

147. Howitz KT. **Screening and profiling assays for HDACs and sirtuins.** *Drug Discovery Today Technol.* (2015) **18**:38–48.

148. Wegener D, Hildmann C, Riester D, Schwienhorst A. **Improved fluorogenic histone deacetylase assay for high-throughput-screening applications.** *Anal. Biochem.* (2003) **321**(2):202–208.

149. Wegener D, Wirsching F, Riester D, Schwienhorst A. **A fluorogenic histone deacetylase assay well suited for high-throughput activity screening.** *Chem. Biol.* (2003) **10**(1):61–68.

150. Halley F, Reinshagen J, Ellinger B, Wolf M, Niles AL, Evans NJ, Kirkland TA, Wagner JM, Jung M, Gribbon P, et al.. **A Bioluminogenic HDAC Activity Assay Validation and Screening.** *J. Biomol. Screening* (2011) **16**(10):1227–35.

151. Hsu C-W, Shou D, Huang R, Khuc T, Dai S, Zheng W, Klumpp-Thomas C, Xia M. **Identification of HDAC Inhibitors Using a Cell-Based HDAC I/II Assay.** *J. Biomol. Screening* (2016) **21**(6):643–652.

152. Haus P, Korbus M, Schröder M, Meyer-Almes F-J. **Identification of selective class II histone deacetylase inhibitors using a novel dual-parameter binding assay based on fluorescence anisotropy and lifetime.** *J. Biomol. Screening* (2011) **16**(10):1206–1216.

153. Mazitschek R, Patel V, Wirth DF, Clardy J. **Development of a fluorescence polarization based assay for histone deacetylase ligand discovery.** *Bioorg. Med. Chem. Lett.* (2008) **18**(9):2809–2812.

4. Cumulative Part

This chapter contains the following five articles which were published in peer-reviewed journals and one article that was submitted for publication:

A fluorescence lifetime-based binding assay for acetylpolyamine amidohydrolases from *Pseudomonas aeruginosa* using a [1,3]dioxolo[4,5-*f*]benzodioxole (DBD) ligand probe. Meyners C, Wawrzinek R, Krämer A, Hinz S, Wessig P, Meyer-Almes F-J. *Anal. Bioanal. Chem.* (2014) 406: 4889–4897

A fluorescence lifetime-based binding assay for class IIa histone deacetylases. Meyners C, Mertens M, Wessig P, Meyer-Almes F-J. *Chem. Eur. J.* (2017) 23: 3107–3116

Kinetic method for the large-scale analysis of the binding mechanism of histone deacetylase inhibitors. Meyners C, Baud MGJ, Fuchter MJ, Meyer-Almes F-J. *Anal. Biochem.* (2014) 460: 39–46

Impact of binding mechanism on selective inhibition of histone deacetylase isoforms. Meyners C, Meyer-Almes F-J. Submitted for publication in *Chemical Biology and Drug Design*

Perflourinated hydroxamic acids are potent and selective inhibitors of HDAC-like enzymes from *Pseudomonas aeruginosa*. Meyners C, Wolff B, Kleinschek A, Krämer A, Meyer-Almes F-J. *Bioorg. Med. Chem. Lett.* (2017) 27: 1508–1512

The thermodynamic signature of ligand binding to histone deacetylase-like amidohydrolases is most sensitive to the flexibility in the L2-loop lining the active site pocket. Meyners C, Krämer A, Yildiz Ö, Meyer-Almes F-J. *BBA - General subjects* (2017)
DOI: http://dx.doi.org/10.1016/j.bbagen.2017.04.001

4.1. Fluorescence life-time based binding assay for histone deacetylases

Title:

A fluorescence lifetime-based binding assay for acetylpolyamine amidohydrolases from *Pseudomonas aeruginosa* using a [1,3]dioxolo[4,5-*f*]benzodioxole (DBD) ligand probe.

Authors:

Christian Meyners, Robert Wawrzinek, Andreas Krämer, Steffen Hinz, Pablo Wessig, Franz-Josef Meyer-Almes

Bibliographic Data:

Analytical and Bioanalytical Chemistry

Volume 406, Issue 20, Pages 4889–4897, August, 2014. DOI: 10.1007/s00216-014-7886-5

First published online: May 29, 2014

Abstract:

High-throughput assays for drug screening applications have to fulfill particular specifications. Besides the capability to identify even compounds with low potency, one of the major issues is to minimize the number of false-positive hits in a screening campaign in order to reduce the logistic effort for the subsequent cherry picking and confirmation procedure. In this respect, fluorescence lifetime (FLT) appears as an ideal readout parameter that is supposed to be robust against autofluorescent and light-absorbing compounds, the most common source of systematic false positives. The extraordinary fluorescence features of the recently discovered [1,3]dioxolo[4,5-*f*][1,3] benzodioxole dyes were exploited to develop an FLT-based binding assay with exceptionally robust readout. The assay setup was comprehensively validated and shown to comply not only with all requirements for a powerful high-throughput screening assay but also to be suitable to determine accurate binding constants for inhibitors against enzymes of the histone deacetylase family. Using the described binding assay, the first inhibitors against three members of this enzyme family from *Pseudomonas aeruginosa* were identified. The compounds were characterized in terms of potency and selectivity profile. The novel ligand probe should also be applicable to other homologues of the histone deacetylase family that are inhibited by *N*-hydroxy-*N*′-phenyloctandiamide.

Contributions by C. Meyners:

- Developed and executed the fluorescence lifetime binding assay
- Analyzed the generated data

Anal Bioanal Chem (2014) 406:4889–4897
DOI 10.1007/s00216-014-7886-5

RESEARCH PAPER

A fluorescence lifetime-based binding assay for acetylpolyamine amidohydrolases from *Pseudomonas aeruginosa* using a [1,3]dioxolo[4,5-*f*][1,3]benzodioxole (DBD) ligand probe

Christian Meyners · Robert Wawrzinek · Andreas Krämer · Steffen Hinz · Pablo Wessig · Franz-Josef Meyer-Almes

Received: 14 March 2014 / Revised: 9 April 2014 / Accepted: 12 May 2014 / Published online: 29 May 2014

Abstract High-throughput assays for drug screening applications have to fulfill particular specifications. Besides the capability to identify even compounds with low potency, one of the major issues is to minimize the number of false-positive hits in a screening campaign in order to reduce the logistic effort for the subsequent cherry picking and confirmation procedure. In this respect, fluorescence lifetime (FLT) appears as an ideal readout parameter that is supposed to be robust against autofluorescent and light-absorbing compounds, the most common source of systematic false positives. The extraordinary fluorescence features of the recently discovered [1,3]dioxolo[4,5-*f*][1,3] benzodioxole dyes were exploited to develop an FLT-based binding assay with exceptionally robust readout. The assay setup was comprehensively validated and shown to comply not only with all requirements for a powerful high-throughput screening assay but also to be suitable to determine accurate binding constants for inhibitors against enzymes of the histone deacetylase family. Using the described binding assay, the first inhibitors against three members of this enzyme family from *Pseudomonas aeruginosa* were identified. The compounds were characterized in terms of potency and selectivity profile. The novel ligand probe should also be applicable to other homologues of the histone deacetylase family that are inhibited by *N*-hydroxy-*N*′-phenyloctandiamide.

Electronic supplementary material The online version of this article (doi:10.1007/s00216-014-7886-5) contains supplementary material, which is available to authorized users.

C. Meyners · A. Krämer · S. Hinz · F.-J. Meyer-Almes (✉)
Department of Chemical Engineering and Biotechnology, University of Applied Sciences Darmstadt, Schnittspahnstr. 12, 64287 Darmstadt, Germany
e-mail: franz-josef.meyer-almes@h-da.de

R. Wawrzinek · P. Wessig
Institut für Chemie, Universität Potsdam, 14476 Potsdam, Germany

Keywords Histone deacetylases · Acetylpolyamine amidohydrolases · Fluorescence life time · Binding assay · *Pseudomonas aeruginosa*

Introduction

Enzymes of the histone deacetylase family (HDACs) are physiologically highly relevant targets in different indication areas [1–3]. Recently, three acetylpolyamine amidohydrolases (APAHs) of *Pseudomonas aeruginosa* have been predicted from the sequenced genome [4] which contains the highly conserved deacetylase binding domain with Zn^{2+} ion at the bottom of the binding pocket. As shown for other microorganisms, APAHs are involved in the polyamine metabolism [5] and polyamines were reported to interfere with biofilm formation [6, 7], the major success strategy of the notorious hospital pathogen *P. aeruginosa.*

Considering the large and still growing pharmacological interest in protein targets from the histone deacetylase family, there is an urgent need for the development of suitable assay systems which are capable of high-throughput screening (HTS) of large compound collections to enable the identification of novel HDAC and APAH inhibitors. Such an HTS assay has to comply with a number of particular specifications: The assay protocol has to be simple to avoid error propagation due to too many handling steps. This is usually achieved by a homogeneous mix-and-measure procedure without any separation step. Further requirements include the ability for miniaturization and parallelization on a microtiter plate format to achieve the desired throughput. Of course, the reagents must be chemically stable over the course of the screening campaign. The assay must certainly be capable to identify also compounds with weak potencies but innovative chemical structures that bear the potential to be subsequently

developed to novel drug candidates in a medicinal chemistry effort. A major issue of HTS assays is the number of statistical and systematic false-positive hits. High false-positive hit rates are very undesirable due to the enormous logistic effort to confirm and follow up too many false positives. To reduce the number of statistical error, a screening assay must have a very high performance which is usually measured in terms of the Z' factor which has been introduced by Zhang et al. [8].

A major source for systematic false-positive hits in fluorescence-based assays is autofluorescence, inner filter effect, or light scattering of test compounds. Many types of fluorescence readouts, e.g., simple fluorescence intensity (FI) [9], fluorescence polarization (FP) [10], Foerster resonance energy transfer (FRET) [11, 12], time-gated fluorescence relying on rare-earth chelate probes (TRF) [13], or, more recently, fluorescence lifetime (FLT) [14–16], were employed in screening assays to minimize the number of false positives. Possible assay interferences of luminescent readouts for high-throughput screening assays have been comprehensively discussed by Comley [17]. FI, FP, and FRET are prone to autofluorescent and light-absorbing compounds and usually produce many false-positive or negative hits. TRF refers to the prolonged luminescence lifetime of rare-earth chelates and combines resonance energy transfer with time gating of the luminescence decay. This allows a much better discrimination against autofluorescent compounds. A major drawback of the TRF-assay format is the high cost of the rare-earth chelates to be conjugated to one binding partner. In contrast to many other employed assay readouts, FLT is an intrinsic property of a fluorophor and should be independent of the concentration of the fluorescent probe as well as absorbing and autofluorescent screening compounds. However, there are only rare reports about the application of FLT in HTS assays because of the lack of suitable FLT probes [18, 14]. In practice, the fluorescent probe must fulfill the following requirements to ensure a robust readout: firstly, the FLT and the FLT change upon binding should be as big as possible to discriminate against autofluorescent compounds with typical FLTs of less than 2 ns; secondly, the excitation and emission wavelength should be far in the long wavelength region and exhibit a large stokes shift to enable efficient spectral discrimination against fluorescent contaminants.

Here, the development of an efficient FLT-based binding assay is described on the example of APAHs, members of the pharmacologically most important histone deacetylase family. In the past, several assays formats have been used to probe the enzyme activity of APAHs: Typical assays were based on mass spectrometry [19], an acetate release assay (catalog no. 148261; Roche Diagnostics, Mannheim, Germany) [20], or a colorimetric assay that quantifies putrescine generation via an enzyme cascade using a diamine oxidase and horseradish peroxidase [21]. Occasionally, the capability of many APAHs to also deacetylate the fluorogenic HDAC substrate Boc-Lys(Ac)-7-amino-4-methyl coumarin (AMC) or its trifluoroacetyl derivative has been exploited experimentally [20]. Mass spectrometry assays have the intrinsic disadvantage of a considerable instrumental effort. Throughput and quantification is often an issue. The other three assay formats rely on more or less complex enzyme cascades with several possible error sources. Test compound can possibly interact with every cascade enzyme pretending false-positive results. The acetate standard assay is rather unspecific and insensitive against acetate concentrations below 1 mM. The alternative assay with the diamine oxidase/horseradish peroxidase cascade is a little bit less prone to absorbing test compounds because absorption is measured at bigger wavelengths (498 nm). Since the transmission of the signal is based on the generation of hydrogen peroxide, the signal will be influenced by the redox potential of screening compounds. The lysine deacetylation assay measures the fluorescence of released 4-methyl-7-amino-coumarin in the near UV range and is more sensitive to deacetylation than the colorimetric (absorbance) assays. But the obvious disadvantage of this type of assay in screening applications is its susceptibility to auto fluorescent or adsorbing compounds and the involvement of trypsin to generate the fluorescence signal which leads to great quantities of false-positive hits.

The drawbacks of all these assay formats have been largely overcome in the described FLT-based binding assay which exploits the particular fluorescence characteristics of the recently discovered class of [1,3]dioxolo[4,5-*f*-][1,3]benzodioxole (DBD) dyes [22] and enables both, a spectral and a temporal discrimination of the probe signal thereby suppressing interferences with optical compound perturbances. In this study a DBD-conjugate probe was synthesized which reversibly bound to all APAHs of *P. aeruginosa* showing a substantial difference in FLT up to 7.2 ns upon binding. Based on this finding, a robust competitive binding assay for APAHs and structurally related histone deacetylase homologues was developed and validated. The assay was also shown to determine accurate binding constants for APAH ligands.

Material and methods

Reagents

Chemicals and solvents were purchased from Sigma-Aldrich (USA), Merck (Germany), Roth (Germany), VWR (Germany), Alfa Aesar (USA), Fisher Scientific (Germany), and *N*-hydroxy-*N*′-phenyloctandiamide (SAHA) was purchased from Cayman Chemical (USA) and Boc-Lys(Ac)-AMC and Boc-Lys(trifluoacetyl)-AMC from Bachem (Switzerland). MB265, MB275, PDF299, and PCI34051 were a kind gift from Dr. Matthew Fuchter (Imperial College,

London). 2,2,3,3,4,4,5,5,6,6,7,7-Dodecafluorooctanedioic acid hydroxyamide phenyl-amide (Lu210) was synthesized according to Meyer-Almes et al. [23], and 9,9,9-trifluoro-8-oxo-N-phenylnonanamide (SATFMK) according to Zard et al. [24]. The assay buffer consisted of 50 mM sodium chloride, 20 mM Tris–HCl, and 0.001 % Pluronic F-127 at pH 8.0.

Protein expression and purification of APAHs

The gene *pa0321* was codon optimized and ordered from GenScript (USA). The gene was embedded in a pUC57 plasmid and subsequently cloned into the pET21-CPD vector (sequence see Electronic supplementary material). The *pa1409* and *pa3774* genes were kindly provided by Andreas Schwienhorst (University of Goettingen, Germany) in pQEB-MCS vector and also cloned into the pET21a(+)-CPD vector. All three APAHs were recombinant expressed in the *E. coli* strain BL21 (DE3) using the CPD expression technique. In this approach, the enzyme is fused to a C-terminal cysteine protease domain (CPD) followed by a His_{10}-tag [25]. In the major step the CPD is induced by phytic acid which cuts the target enzyme and releases it free of tag into the supernatant. Bacteria cultures were grown at 37 °C to an optical density of 0.8–1.0 at 600 nm and the protein expression was induced by addition of 1 mM isopropyl-β-D-thiogalactopyranoside. The cells were further cultivated overnight at room temperature and harvested the next day by centrifugation (15 min, 17.000×*g*, 4 °C). The pellet was resuspended in lysis buffer containing 20 mM Tris–HCl pH 8.0, 50 mM NaCl, 10 mM imidazole (3 ml/g pellet), and subsequently disintegrated by sonication. Cell fragments were separated by centrifugation (30 min, 26,000×*g*, 4 °C) and the supernatant was loaded onto an immobilized metal affinity chromatography (IMAC) [26] using a sepharose resin (Chelating Sepharose™ Fast Flow, GE Healtcare, Uppsala, Sweden) which was equilibrated with lysis buffer and saturated with 100 mM $NiCl_2$. The APAH enzymes were eluted from the resin after 1 h of incubation with 50 μM phytic acid (dissolved in lysis buffer) and further purified by gelfiltration using a Superdex 200 16/60 column (GE Healthcare, USA). The column was equilibrated with lysis buffer supplemented by 2 mM TCEP. The concentration of the highly purified protein was determined by using the bicinchoninic acid (BCA) assay (Pierce Biotechnology, USA) [27].

Binding assay and calculation of K_d values

The binding of the APAHs to the DBD ligand was analyzed from a titration of 50 nM **8** with increasing concentrations of the respective enzyme. If not stated otherwise, all binding and competition reactions were carried out in the assay buffer. The assay was performed in black 96-well half area microtiter plates (Greiner, Germany) in a total final volume of 60 μl. The fluorescence decay was measured on a LF502 nanoscan instrument from Berthold Detection Systems GmbH (Pforzheim, Germany) behind a 630 nm bandpass filter with passband width 50 nm after pulse excitation at 456 nm. Binding of the DBD ligand resulted in an increased FLT. For each sample, the fluorescence decay was measured over a period of 50 ns. This signal was normalized and transformed into binding degrees (B.D.) according to

$$\text{B.D.} = \frac{A - A_{\min}}{A_{\max} - A_{\min}} \tag{1}$$

where A denotes the FLT in the presence of a certain enzyme concentration of interest, $A_{\min}$ denotes the FLT in the absence of enzyme, and $A_{\max}$ denotes the FLT in the presence of saturating enzyme concentrations.

The binding of the DBD ligand, L, to enzyme, E, was interpreted as simple bimolecular interaction (E+L=EL). Initial concentrations are marked by the subscript 0. All the other concentrations refer to the chemical equilibrium state. Then, the binding degree B.D. can be described by the following equation

$$\text{B.D.} = \frac{[\text{EL}]}{[\text{L}]_0} = \frac{1}{2[\text{L}]_0}\left([\text{E}]_0 + [\text{L}]_0 + K_d - \sqrt{\left([\text{E}]_0 + [\text{L}]_0 + K_d\right)^2 - 4[\text{L}]_0[\text{E}]_0}\right) \tag{2}$$

where [EL] is the equilibrium concentration of the enzyme-ligand complex and K_d is the dissociation constant of the equilibrium between bound and free ligand probe. The dissociation constant was obtained from a fit of the data to Eq. 2.

Calculation of inhibitor binding constant K_i

The enzyme concentration was chosen such that there was a sufficient measuring window for accurate fitting (60–80 % binding degree) but not too high in order to allow the exact calculation of the binding constant of potent inhibitors. Usually, 50 nM of **8** and 1.5 μM APAH (PA1409), 0.75 μM APAH (PA0321), or 0.47 μM APAH (PA3774) were premixed and incubated in assay buffer for at least 15 min to form the ligand-enzyme complex. Then, the preformed complex was added to the desired inhibitor concentration. After 30 min of equilibration, the fluorescence decay was measured as described before. The binding constants, K_i, to the respective enzymes were calculated from competition experiments using preformed DBD ligand/enzyme complexes and increasing concentrations of different inhibitors. The following equations are based on the simple competition model (E+L=EL

and E+I=EI) where I denotes the inhibitor and EI its complex with the enzyme of interest. Because of the large access of enzyme over ligand probe, L, it follows that

$$[\mathrm{EL}] \ll [\mathrm{EI}] + [\mathrm{E}] \quad \Rightarrow \quad [\mathrm{E}]_0 \approx [\mathrm{EI}] + [\mathrm{E}] \tag{3}$$

Then, the binding degree B.D. becomes

$$\mathrm{B.D.} = \frac{[\mathrm{EL}]}{[\mathrm{L}]_0} = \frac{1}{[\mathrm{L}]_0}\left(\frac{[\mathrm{L}]_0[\mathrm{E}]}{K_1 + [\mathrm{E}]}\right) \tag{4}$$

with

$$[\mathrm{E}] = -\frac{1}{2}\cdot\left([\mathrm{I}]_0 - [\mathrm{E}]_0 + K_i - \sqrt{([\mathrm{I}]_0 + [\mathrm{E}]_0 + K_i)^2 + 4 \times [\mathrm{I}]_0 \cdot [\mathrm{E}]_0}\right) \tag{5}$$

where K_i is the dissociation constant of an inhibitor binding to enzyme E. When using Eq. 4, one has to keep in mind that K_i values much lower than the concentration of enzyme cannot be deduced reliably. In these cases, only upper limits of K_i can be estimated.

Screening assay validation

For screening applications with the aim of identifying hit compounds rather than calculating binding constants, a large measuring window between the positive and negative control is advantageous, which means about 90 % binding degree of the applied 50 nM DBD ligand. This was achieved, e.g., by the addition of 1.2 μM APAH (PA3774) in a total volume of 60 μl in the before mentioned black 96-well half area microtiter plates. The negative controls contained DMSO in the same concentration than in the reaction mixtures with screening compounds. The positive control contained 20 μM SAHA. The assay format was validated by filling three independent 96-well microtiter plates in each case with 48 positive and 48 negative controls. The same reaction mixtures were measured after incubation times of 2, 30, 90, 210, 720, and 1,860 min to demonstrate the robustness of the assay over time. After 210 min, the microtiter plates were transferred to 4 °C in the dark and 30 min equilibrated to room temperature before the next measurement. One microtiter plate was measured within 12 min. Saving complete datasets of fluorescence decay curves for each compound could generate data storage problems considering millions of datasets in a screening context. However, these data could be greatly reduced by fitting the fluorescence decay curves to a one-exponential function and saving only the corresponding FLT values. The fitting procedure for one microtiter plate with 96 samples took about 20 s. The Z' value was calculated according to Zhang et al. [8] as a measure for the performance of the FLT-based binding assay:

$$Z' = \frac{3\cdot[s(\mathrm{High}) + s(\mathrm{Low})]}{\left|\overline{\mathrm{High}} - \overline{\mathrm{Low}}\right|} \tag{6}$$

with the measurement value of the negative control, High, and the positive control, Low; the overstrike denotes the mean and s the standard deviation of the respective control values. Z' values higher than 0.7 or even 0.8 hallmark excellent assay performance highly suitable for compound screening campaigns.

Dissociation kinetics

Dissociation kinetics of the DBD probe ligand **8** from its complexes with APAHs PA3774, PA0321, and PA1409 were determined by addition of a high access of SAHA to an equilibrated solution of the preformed complex between DBD probe ligand and the respective APAH. Therefore, 200 nM of **8** were mixed with 0.33 μM APAH (PA3774), 1.66 μM APAH (PA1409), or 2.5 μM APAH (PA0321) in assay buffer and equilibrated for 30 min at 22 °C. The equilibrated solution was placed in a spectrofluorimeter (F-7000, Hitachi) and the fluorescence was measured at an excitation wavelength of 456 nm and an emission wavelength of 580 nm. Rapid addition of 100 μM SAHA and mixing resulted in a decay of the measured fluorescence, which was recorded until the mean signal changed less than 2 % over a period of 30 s. The obtained data was fitted to a single-phase exponential decay model yielding the dissociation rate of the APAH/DBD probe ligand complex as reciprocal time constant.

Enzyme activity assay

The IC_{50} values of the described inhibitors were determined using a standard fluorogenic enzyme activity assay [28]. The protein concentration of all three APAHs was 50 nM. Boc-Lys(Ac)-TFA-AMC at a concentration of 20 μM was used as fluorogenic substrate in all APAH enzyme activity assays. The inhibitor concentrations were varied from 0 up to 50 μM. The enzymes and the inhibitor were incubated for 30 min at 30 °C and the reaction was started by adding the fluorogenic substrate along with trypsin at a concentration of 0.5 mg/ml. The experiment was carried out in a PheraStar Fluorescence Spectrometer (BMG Labtech). The data were analyzed with the program Graph Pad Prism and the IC_{50} value was determined

using the following four-parameter logistic function [29]

$$EA = E_0 + \frac{(E_{max} - E_0)}{1 + 10^{[(\log IC_{50} - x)\cdot h]}} \quad (7)$$

with enzyme activity, EA, at a certain inhibitor concentration x; E_{max} and E_0 are the measured enzyme activity at no and complete inhibition; IC_{50} denotes the inhibitor concentration, where half of the enzyme is inhibited; and h is the hill slope.

Results and discussion

Synthesis of DBD ligand probe

The DBD dyes represent a new class of FLT probes having high photostability, exceptionally large stokes shift, and strong dependency of FLT on the polarity of the microenvironment [30, 31]. To exploit these outstanding features in a binding assay, we designed a DBD ligand for APAHs and HDAC homologues in general. The transfer of the free ligand probe from its aqueous environment to the very hydrophobic binding pockets of APAHs and HDACs was anticipated to generate a large FLT change.

The convergent synthesis of the DBD ligand **8** for the APAHs from *P. aeruginosa* is shown in Fig. 1. The ligand consists of an Acyl-DBD dye, a short diaminoethyl-linker and a hydroxamic acid with a hydrophobic alkyl chain. The latter moiety is a known structural motive to recognize and bind histone deacetylases and homologue enzymes particularly related to the Zn^{2+}-dependent HDAC classes I and IIb. Experimental details to the chemical synthesis and analytical data are provided in the Electronic supplementary material.

Binding of DBD ligand probe to APAH enzymes

The application of FLT as readout parameter for ligand-enzyme binding assays has been described in some recent articles. Lebakken et al. [16] and Meyer-Almes et al. [15] have synthesized ligands which were conjugated to AlexaFluor 647 or Atto-700 having relatively short FLTs of less than 2 ns and a difference of only about 0.5 ns when bound to the respective enzyme. More recently, Pritz et al. reported a phosphorylation assay using a peptide substrate containing an acridone fluorophore [14]. The FLT of the substrate increased about 4 ns upon phosphorylation. However, the substrate had to be used in micromolar concentration and the excitation and emission wavelength were unfavorable low at 405 and 450 nm, respectively. The DBD ligand used in this study was more red shifted and exhibited a much larger stokes shift with an excitation maximum at 457 nm an emission maximum at 634 nm in water (spectra see Electronic supplementary material). The extinction coefficient was 3,200 M^{-1} cm^{-1} in water at 457 nm. Moreover, the dramatic dependency of the fluorescence properties of the ligand conjugate on the polarity of its microenvironment was reflected by a pronounced FLT change of 4.9–7.2 ns upon binding to the respective APAH from *P. aeruginosa* (Table 1).

The binding isotherms of the DBD ligand to all three APAHs are shown in Fig. 2. The resulting binding constants range between 0.19 and 1.31 μM (Table 1).

Competitive binding assay for APAH inhibitors

Binding constants of inhibitors, K_i, were obtained from displacement titrations of a preformed complex consisting of DBD ligand and the respective APAH enzyme with increasing concentrations of inhibitors.

Typical displacement curves of selected inhibitors of APAH (PA3774) with graduated potencies are shown in Fig. 3. The curves became steeper when the fitted K_i value approached or undershot the concentration of the employed APAH. However, due to the very high precision of the experimental data all inhibitors with K_i values >0.03 μM could be satisfactorily calculated using Eqs. 4 and 5. Very potent inhibitors with K_i values <0.03 μM were characterized by extremely deep fit curves which could not be distinguished anymore (see Electronic supplementary material Fig. S8). The K_i values of the binding assay were compared with those calculated from IC_{50} values obtained from an enzyme activity assay measuring the deacetylation of lysine and summarized in Table 2 (the complete set of dose response curves is provided in the Electronic supplementary material). In general, K_i values of the competitive binding assay showed good to excellent correlation with the corresponding dissociation constants derived from IC_{50} values of the enzyme activity assay using the formalism of Cheng and Prusoff. This was highlighted by Pearson coefficients of 0.99, 0.84, and 0.97 for the data sets of APAHs PA0321, PA1409, and PA3774, respectively. However, there are still few larger differences between the K_i values of both assay types observed for single compounds, e.g., for MB265 against APAHs PA1407 and PA3774. A possible explanation could be a noncovalent interaction of this compound with either the ligand probe in the binding assay or the fluorogenic substrate in the enzyme activity assay. Such artifacts are known for fluorescence based HTS assays. One of the most prominent examples is resveratrol which was long believed to be a direct activator of SIRT1 until an HPLC analysis of unlabeled and labeled substrate peptides revealed that the observed activation occurred only, if the fluorogenic Fluor de Lys-SIRT1 peptide substrate was employed [32]. Therefore, it is indispensable to confirm hits of fluorescence based HTS assays by more elaborate but time consuming methods.

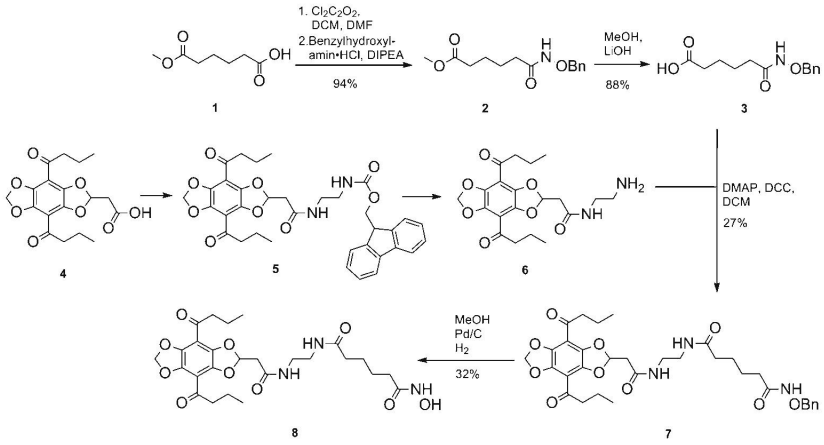

Fig. 1 Synthesis scheme for DBD ligand **8**

But when looking at the complete set of data for all three APAHs, no active compound would have been overlooked in a screening situation using the FLT-based binding assay. Moreover, in both assays, the binding and enzyme activity assay, provided a very similar ranking of the compounds regarding potency against the respective APAH.

Assay validation for screening applications

Screening campaigns aimed at many thousands to several million substances to identify inhibitors or activators of a certain target protein of interest must fulfill particular specifications for the applied assay system. Since such a screening projects usually takes several days up to weeks, the assay has to be extraordinary robust in terms of both, chemical stability of reagents as well as the mostly optical readout. In addition, the used reagents must not adsorb to the connecting tubing and pipetting systems of the robotic hardware. In this study we investigated the suitability of our FLT-based binding assay for screening applications using APAH (PA3774) as exemplary target protein. The validation procedure included elaborated experiments for the determination of the performance and robustness of the binding assay. The large polarity change upon binding of 1.2 μM APAH caused a big FLT difference (>4 ns) between free and bound DBD ligand probe.

Once the assay reagents were mixed, the mean FLT signal of the free DBD ligand of 2.3 ns remained approximately constant with a coefficient of variance (CV) of 2.9 % for more than 30 h at room temperature (Fig. 4). The mean FLT of the ligand-APAH complex dropped slightly from 2 to 30 min incubation time and then remained at 7.1 ns with a CV of 1.9 % from 30 min to 12 h incubation time. The FLT of 7.1 ns represented 90 % complex formation. If hits are defined to have FLT values below a threshold of 6.5 ns, the statistical false positive rate would be less than 0.01 % which means less than 100 false-positive hits per one million screened compounds, a very good value for an HTS assay. The quality of the assay is sufficient to differentiate clearly between inhibitors that displace 50 % from those that displace 30 % of the DBD ligand probe. If the mean of the FLT values for 50 % (5.0 ns) and 30 % (3.9 ns) displacement is chosen as a threshold to distinguish between 50 and 30 % probe

Table 1 Changes in FLT, binding constant, K_d, of DBD ligand to the respective APAH, quantum yield change, $\Delta\Phi$, upon binding and off rates, k_{off}, of the DBD ligand from different APAHs (PA0321, PA1409, and PA3774). The displacement kinetics of DBD ligand from APAHs was measured as described in material and methods at 22 °C

	PA0321	PA1409	PA3774
ΔFLT/ns	4.9±0.1	7.19±0.06	5.29±0.08
K_d/μM	0.3±0.3	1.31±0.05	0.19±0.01
ΔΦ/%	291	666	412
$k_{off}/(10^{-2}\ s^{-1})$	21±2	3.8±0.1	2.3±0.1

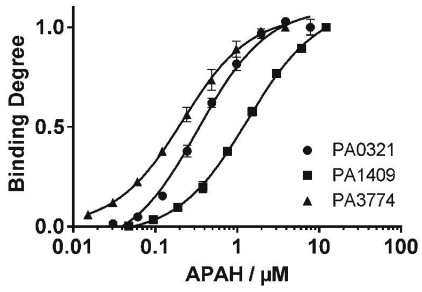

Fig. 2 Binding of 50 nM DBD ligand probe **8** to APAHs PA0321, PA3774 and PA1409. The binding degree is plotted against the respective enzyme concentration. The data were fitted using Eq. 2. The fit curves are represented by the *smooth lines*. The *error bars* represent the standard deviation of three independent measurements. The standard error is in most cases smaller than the size of the symbol of the mean data point

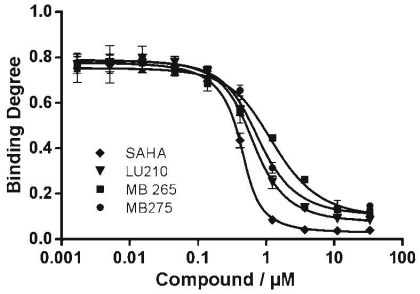

Fig. 3 Competitive binding of denoted inhibitors to APAH (PA3774). A mixture of 50 nM **8** and 0.47 µM APAH was titrated with increasing concentrations of the indicated compound. The data were fitted using Eqs. 4 and 5. The *smooth lines* represent the least square fit model. The determined K_i values are summarized in Table 1. *Error bars* represent the standard deviation of three independent measurements. In many cases the *error bars* are smaller than the symbol of the corresponding data point

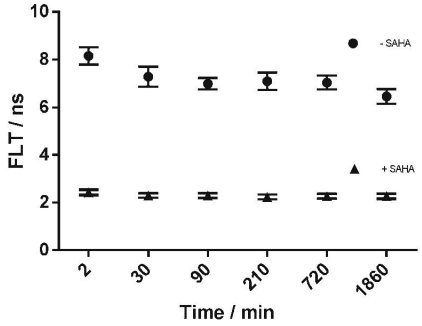

Fig. 4 FLT-values of APAH (PA3774) screening assay containing a preformed complex of 1.2 µM enzyme and 50 nM ligand probe **8** in the absence (−SAHA) and in the presence of 20 µM inhibitor (+SAHA). The data points with error bars represent in each case means and standard deviations of 144 independent experiments from three different microtiter plates at various times after mixing the assay reagents as described in "Material and methods" section

displacing compounds and experimental standard deviations are taken into account, a compound would be assigned correctly with a probability greater than 98 %.

The Z' value remained higher than 0.78 for the observed range of more than 30 h incubation time indicating both, excellent assay performance and robustness (Fig. 5). The results not only proved the excellent robustness of the FLT readout but also the high chemical stability of the APAH used when complexed with the DBD ligand.

One of the major reasons for false-positive hits in a screening campaign is the autofluorescence of test compounds. Therefore, the susceptibility of the FLT-readout was investigated in the presence of the highly fluorescent dye AMC. Usually, the final concentration of compounds in a screening assay is about 10 µM. The FLT-signal was not disturbed up to the tenfold concentration of AMC demonstrating excellent robustness against auto fluorescent compounds (Fig. 6).

Table 2 Binding constants, K_i, for inhibitors of *P. aeruginosa* APAHs (PA0321, PA1409, and PA3774)

		PA1409		PA3774		PA0321	
Chemical Structure	Name	K_i / µM[a]	K_i / µM[b]	K_i / µM[a]	K_i / µM[b]	K_i / µM[a]	K_i / µM[b]
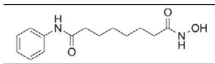	SAHA	< 0.03	0.19 ± 0.02	< 0.03	0.013 ± 0.001	0.059 ± 0.008	0.28 ± 0.02
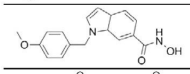	PCI 34051	0.32 ± 0.07	0.74 ± 0.06	0.08 ± 0.02	0.92 ± 0.08	0.18 ± 0.02	0.46 ± 0.02
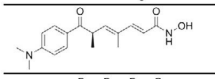	Trichostatin A (TSA)	0.04 ± 0.02	0.26 ± 0.02	0.05 ± 0.01	0.31± 0.02	0.14 ± 0.02	0.36 ± 0.02
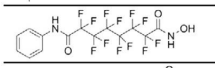	LU210	23 ± 13	10.0 ± 1.7	0.08 ± 0.01	0.01 ± 0.002	0.16 ± 0.02	0.56 ± 0.04
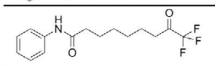	SATFMK	< 0.03	0.12 ± 0.01	< 0.03	0.0033 ± 0.0002	0.019 ± 0.005	0.0034 ± 0.0003
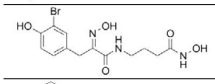	MB275	2.3 ± 0.4	3.9 ± 0.4	0.26 ± 0.04	-	0.62 ± 0.06	2.2 ± 0.1
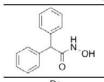	PDF299	0.82 ± 0.01	0.46 ± 0.05	< 0.03	0.025 ± 0.001	0.038 ± 0,006	0.10 ± 0.01
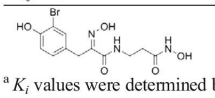	MB265	0.25 ± 0.06	5.8 ± 0.5	0.26 ± 0.04	8.9 ± 0.8	0.17 ± 0.02	0.56 ± 0.03

[a] K_i values were determined by the competitive binding assay as described in section "Material and methods" section

[b] K_i values were calculated from IC_{50} values determined in an enzyme activity assay using the Cheng and Prusoff equation. The K_m values for the deacetylation of the substrate were determined to be 37.6±3.3 µM for PA1409, 9.9±0.7 µM for PA3774 and 19.3±1.1 µM for PA0321. The substrate concentration was in all cases 20 µM

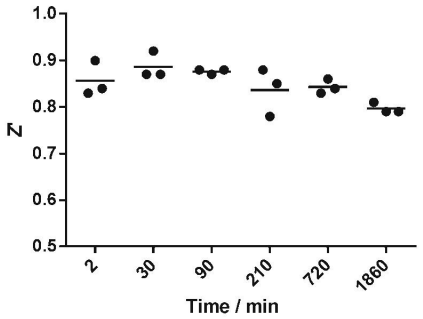

Fig. 5 The performance of the APAH(PA3774) screening assay in terms of *Z′* values is given for three microtiter plates at various times after mixing of the assay reagents. Each data point represents the *Z′* value of one microtiter plate with 48 negative (−SAHA) and 48 positive (+SAHA) controls, respectively. The *horizontal lines* at each point in time denote the mean of the *Z′* values of three independent microtiter plates

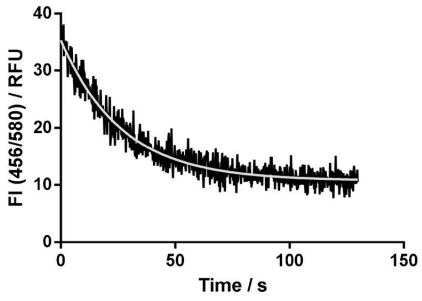

Fig. 7 Displacement kinetics of the DBD ligand from its complex with APAH (PA1409). An excess concentration of 100 μM SAHA was added to a preformed complex consisting of 200 nM **8** and 1.7 μM APAH at 22 °C. The fluorescence intensity, FI, was measured using an excitation wavelength of 456 nm and an emission wavelength of 580 nm. The smooth line in *light gray* represents a one-exponential fitting curve

Dissociation kinetics of DBD ligand

Beyond screening and determination of binding constants, we also investigated the potential of our binding assay to perform kinetic measurements and elucidate the binding mechanism of inhibitors.

The repetition rate of FLT measurements was only about 1 s^{-1}, which is still sufficient for high-throughput screening applications. To achieve a better time resolution for kinetic studies, the change in quantum yield was exploited to follow the displacement kinetics of the DBD ligand from all three APAHs. The change in the transient fluorescence signal indicated the progression of the reaction and could therefore well be separated from constant contributions of, e.g., auto fluorescent or light absorbing compounds. A typical one-exponential displacement kinetics of the DBD ligand from APAH (PA1409) after the addition of high excess of the competitive inhibitor SAHA is shown in Fig. 7. The dissociation rates, the change in quantum yield, and the change in FLT upon binding are summarized in Table 1. These results demonstrate the suitability of the binding assay for the analysis of the binding kinetics of inhibitors to unlabelled target enzyme. Further kinetic studies are ongoing to elucidate the exact binding mechanism of different structural classes of inhibitors to the APAH enzymes.

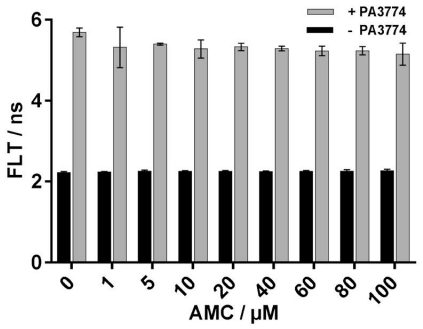

Fig. 6 FLT values of the DBD probe ligand **8** alone and in the presence of 0.4 μM APAH (PA3774) in assay buffer supplemented with indicated concentrations of 7-amino-4-methyl coumarin (AMC). The *error bars* represent means and standard deviations of four independent experiments

Conclusion

A new type of binding assay for enzymes of the histone deacetylase enzyme family was developed and validated for its high-throughput screening capability. The unique features (large stokes shift, high FLT, and extraordinary sensitive to polarity changes) of the recently discovered DBD dyes were exploited to design and synthesize a ligand probe for APAHs from *P. aeruginosa.* Binding of APAHs to the DBD ligand probe generated a large change in FLT of up to 7.2 ns. The readout of the developed binding assay showed extraordinary performance and robustness. Moreover, the binding constants from the FLT-based assay and the reference enzyme activity assay displayed excellent correlation.

Beyond binding assays to APAHs, the combination of DBD dyes and FLT readout appears therefore predestined for the development of more efficient high throughput binding assays to any other protein target. In addition, the associated change in fluorescence intensity can be exploited to investigate fast binding kinetics and mechanisms of inhibitors to their target proteins. This knowledge about, e.g., residence time and induced fit mechanisms is considered to provide invaluable additional information to guide the decisions in the drug development process and to reduce the attrition rate from a lead structure to a drug candidate.

Acknowledgments The work has been supported by a grant of the Deutsche Forschungsgemeinschaft (DFG). The excellent technical support of Michael Schröder is greatfully acknowledged.

References

1. West AC, Johnstone RW (2014) New and emerging HDAC inhibitors for cancer treatment. J Clin Investig 124(1):30–39
2. Andrews KT, Haque A, Jones MK (2011) HDAC inhibitors in parasitic diseases. Immunol Cell Biol 90(1):66–77
3. Eom GH, Kook H (2014) Posttranslational modifications of histone deacetylases: Implications for cardiovascular diseases. Pharmacol Ther. doi:10.1016/j.pharmthera.2014.02.012
4. Stover CK, Pham XQ, Erwin AL, Mizoguchi SD, Warrener P, Hickey MJ, Brinkman FS, Hufnagle WO, Kowalik DJ, Lagrou M, Garber RL, Goltry L, Tolentino E, Westbrock-Wadman S, Yuan Y, Brody LL, Coulter SN, Folger KR, Kas A, Larbig K, Lim R, Smith K, Spencer D, Wong GK, Wu Z, Paulsen IT, Reizer J, Saier MH, Hancock RE, Lory S, Olson MV (2000) Complete genome sequence of *Pseudomonas aeruginosa* PAO1, an opportunistic pathogen. Nature 406(6799):959–964. doi:10.1038/35023079
5. Large PJ (1992) Enzymes and pathways of polyamine breakdown in microorganisms. FEMS Microbiol Rev 8(3–4):249–262
6. Patel CN, Wortham BW, Lines JL, Fetherston JD, Perry RD, Oliveira MA (2006) Polyamines are essential for the formation of plague biofilm. J Bacteriol 188(7):2355–2363
7. Karatan E, Duncan TR, Watnick PI (2005) NspS, a predicted polyamine sensor, mediates activation of vibrio cholerae biofilm formation by norspermidine. J Bacteriol 187(21):7434–7443. doi:10.1128/jb.187.21.7434-7443.2005
8. Zhang JH, Chung TD, Oldenburg KR (1999) A simple statistical parameter for use in evaluation and validation of high throughput screening assays. J Biomol Screen 4(2):67–73
9. Chen B-H, Wang C-C, Lu L-Y, Hung K-S, Yang Y-S (2013) Fluorescence assay for protein post-translational tyrosine sulfation. Anal Bioanal Chem 405(4):1425–1429
10. Geng X, Zhang D, Wang H, Zhao Q (2013) Screening interaction between ochratoxin A and aptamers by fluorescence anisotropy approach. Anal Bioanal Chem 405(8):2443–2449
11. Riester D, Hildmann C, Schwienhorst A, Meyer-Almes FJ (2007) Histone deacetylase inhibitor assay based on fluorescence resonance energy transfer. Anal Biochem 362(1):136–141. doi:10.1016/j.ab.2006.12.019
12. Li Y, Xie W, Fang G (2008) Fluorescence detection techniques for protein kinase assay. Anal Bioanal Chem 390(8):2049–2057
13. Diamandis EP, Christopoulos TK (1990) Europium chelate labels in time-resolved fluorescence immunoassays and DNA hybridization assays. Anal Chem 62(22):1149A–1157A
14. Pritz S, Meder G, Doering K, Drueckes P, Woelcke J, Mayr LM, Hassiepen U (2011) A fluorescence lifetime-based assay for Abelson kinase. J Biomol Screen 16(1):65–72
15. Riester D, Hildmann C, Haus P, Galetovic A, Schober A, Schwienhorst A, Meyer-Almes FJ (2009) Non-isotopic dual parameter competition assay suitable for high-throughput screening of histone deacetylases. Bioorg Med Chem Lett 19(13):3651–3656. doi:10.1016/j.bmcl.2009.04.102
16. Lebakken CS, Kang HC, Vogel KW (2007) A fluorescence lifetime-based binding assay to characterize kinase inhibitors. J Biomol Screen 12(6):828–841
17. Comley J (2003) Assay interference. Drug Discovery:91
18. Maltman BA, Dunsmore CJ, Couturier SC, Tirnaveanu AE, Delbederi Z, McMordie RAS, Naredo G, Ramage R, Cotton G (2010) 9-Aminoacridine peptide derivatives as versatile reporter systems for use in fluorescence lifetime assays. Chem Commun 46(37):6929–6931
19. Chou HT, Kwon DH, Hegazy M, Lu CD (2008) Transcriptome analysis of agmatine and putrescine catabolism in *Pseudomonas aeruginosa* PAO1. J Bacteriol 190(6):1966–1975
20. Riester D, Wegener D, Hildmann C, Schwienhorst A (2004) Members of the histone deacetylase superfamily differ in substrate specificity towards small synthetic substrates. Biochem Biophys Res Commun 324(3):1116–1123. doi:10.1016/j.bbrc.2004.09.155
21. Lombardi PM, Angell HD, Whittington DA, Flynn EF, Rajashankar KR, Christianson DW (2011) Structure of prokaryotic polyamine deacetylase reveals evolutionary functional relationships with eukaryotic histone deacetylases. Biochemistry 50(11):1808–1817. doi:10.1021/bi101859k
22. Wessig P, Wawrzinek R, Möllnitz K, Feldbusch E, Schilde U (2011) A new class of fluorescent dyes based on 1,3-benzodioxole and [1,3]-dioxolo[4.5-f]benzodioxole. Tetrahedron Lett 52(46):6192–6195
23. Henkes LM, Haus P, Jager F, Ludwig J, Meyer-Almes FJ (2012) Synthesis and biochemical analysis of 2,2,3,3,4,4,5,5,6,6,7,7-dodecafluoro-*N*-hydroxy-octanediamides as inhibitors of human histone deacetylases. Bioorg Med Chem 20(2):985–995. doi:10.1016/j.bmc.2011.11.041
24. Boivin J, Kaim LE, Zard SZ (1995) A new and efficient synthesis of trifluoromethyl ketones from carboxylic acids. Part I. Tetrahedron 51(9):2573–2584
25. Shen A, Lupardus PJ, Morell M, Ponder EL, Sadaghiani AM, Garcia KC, Bogyo M (2009) Simplified, enhanced protein purification using an inducible, autoprocessing enzyme tag. PLoS One 4(12):e8119. doi:10.1371/journal.pone.0008119
26. Hochuli E, Bannwarth W, Dobeli H, Gentz R, Stuber D (1988) Genetic approach to facilitate purification of recombinant proteins with a novel metal chelate adsorbent. Nat Biotechnol 6(11):1321–1325
27. Smith PK, Krohn RI, Hermanson GT, Mallia AK, Gartner FH, Provenzano MD, Fujimoto EK, Goeke NM, Olson BJ, Klenk DC (1985) Measurement of protein using bicinchoninic acid. Anal Biochem 150(1):76–85
28. Wegener D, Hildmann C, Riester D, Schober A, Meyer-almes F-J, Deubzer HE, Oehme I, Witt O, Lang S, Jaensch M, Makarov V, Lange C, Busse B, Schwienhorst A (2008) Identification of novel small-molecule histone deacetylase inhibitors by medium-throughput screening using a fluorigenic assay. Biochem J 413(1):143–150. doi:10.1042/bj20080536
29. Volund A (1978) Application of the four-parameter logistic model to bioassay: comparison with slope ratio and parallel line models. Biometrics 34(3):357–365
30. Wawrzinek R, Wessig P, Mollnitz K, Nikolaus J, Schwarzer R, Muller P, Herrmann A (2012) DBD dyes as fluorescent probes for sensing lipophilic environments. Bioorg Med Chem Lett 22(17):5367–5371. doi:10.1016/j.bmcl.2012.07.056
31. Wawrzinek R, Ziomkowska J, Heuveling J, Mertens M, Herrmann A, Schneider E, Wessig P (2013) DBD dyes as fluorescence lifetime probes to study conformational changes in proteins. Chemistry 19(51):17349–17357. doi:10.1002/chem.201302368
32. Beher D, Wu J, Cumine S, Kim KW, Lu SC, Atangan L, Wang M (2009) Resveratrol is not a direct activator of SIRT1 enzyme activity. Chem Biol Drug Des 74(6):619–624. doi:10.1111/j.1747-0285.2009.00901.x

Title:

A fluorescence lifetime-based binding assay for class IIa histone deacetylases.

Authors:

Christian Meyners, Monique Mertens, Pablo Wessig, Franz-Josef Meyer-Almes

Bibliographic Data:

Chemistry – A European Journal
Volume 23, Issue 13, Pages 3107–3116, March 2, 2017. DOI: 10.1002/chem.201605140
First published online: December 6, 2016

Abstract:

Class IIa histone deacetylases (HDACs) show extremely low enzymatic activity and no commonly accepted endogenous substrate is known today. Increasing evidence suggests that these enzymes exert their effect rather through molecular recognition of acetylated proteins and recruiting other proteins like HDAC3 to the desired target location. Accordingly, class IIa HDACs like bromodomains have been suggested to act as “Readers” of acetyl marks, whereas enzymatically active HDACs of class I or IIb are called “Erasers” to highlight their capability to remove acetyl groups from acetylated histones or other proteins. Small-molecule ligands of class IIa histone deacetylases (HDACs) have gained tremendous attention during the last decade and have been suggested as pharmaceutical targets in several indication areas such as cancer, Huntington's disease and muscular atrophy. Up to now, only enzyme activity assays with artificial chemically activated trifluoroacetylated substrates are in use for the identification and characterization of new active compounds against class IIa HDACs. Here, we describe the first binding assay for this class of HDAC enzymes that involves a simple mix-and-measure procedure and an extraordinarily robust fluorescence lifetime readout based on [1,3]dioxolo[4,5-*f*]benzodioxole-based ligand probes. The principle of the assay is generic and can also be transferred to class I HDAC8.

Contributions by C. Meyners:

- Produced the used proteins
- Developed and executed the fluorescence lifetime binding assay
- Performed the ITC measurements
- Analyzed the generated data
- Wrote the manuscript

ChemPubSoc Europe

DOI: 10.1002/chem.201605140

CHEMISTRY
A European Journal
Full Paper

Fluorescent Probes

A Fluorescence-Lifetime-Based Binding Assay for Class IIa Histone Deacetylases

Christian Meyners,[a] Monique Mertens,[b] Pablo Wessig,*[b] and Franz-Josef Meyer-Almes*[a]

Abstract: Class IIa histone deacetylases (HDACs) show extremely low enzymatic activity and no commonly accepted endogenous substrate is known today. Increasing evidence suggests that these enzymes exert their effect rather through molecular recognition of acetylated proteins and recruiting other proteins like HDAC3 to the desired target location. Accordingly, class IIa HDACs like bromodomains have been suggested to act as "Readers" of acetyl marks, whereas enzymatically active HDACs of class I or IIb are called "Erasers" to highlight their capability to remove acetyl groups from acetylated histones or other proteins. Small-molecule ligands of class IIa histone deacetylases (HDACs) have gained tremendous attention during the last decade and have been suggested as pharmaceutical targets in several indication areas such as cancer, Huntington's disease and muscular atrophy. Up to now, only enzyme activity assays with artificial chemically activated trifluoroacetylated substrates are in use for the identification and characterization of new active compounds against class IIa HDACs. Here, we describe the first binding assay for this class of HDAC enzymes that involves a simple mix-and-measure procedure and an extraordinarily robust fluorescence lifetime readout based on [1,3]dioxolo[4,5-*f*]benzodioxole-based ligand probes. The principle of the assay is generic and can also be transferred to class I HDAC8.

Introduction

Members of the histone deacetylase (HDAC) family have emerged as promising protein targets for the treatment of different diseases like cancer, neurodegenerative diseases and parasitic infections.[1–3] The 18 human members of the HDAC family are divided into four classes: class I consists of HDAC1, 2, 3 and 8, class II HDACs are subdivided into class IIa (HDAC4, 5, 7 and 9) and IIb (HDAC6 and 10), class III HDACs consist of the sirtuins, which are not zinc-dependent but require NAD^+ for their catalytic activity, and HDAC11 is the only member of class IV.[4] Class I HDACs are mostly recognised for their ability to control the expression of important genes by the deacetylation of lysine residues of histone proteins.[5] They have therefore emerged as the number one target of all HDAC proteins. Currently, there are four HDAC inhibitors approved by the Food and Drug Administration (FDA) for the treatment of cancer and several more are being tested in clinical trials.[6] Most of these compounds are pan inhibitors, which target mainly class I and class IIb HDACs and cause severe side-effects like fatigue, nausea and thrombocytopenia.[7,8] One approach to overcome these unwanted side-effects is the development of more specific inhibitors. Class IIa HDACs are different from other HDAC isoforms because they show very weak catalytic activity against conventional acetylated substrates and have a large N-terminal domain through which they interact with several transcription factors.[9] Furthermore, they are able to recruit class I HDACs through protein–protein interactions resulting in large corepressor complexes like NcoR and CoREST.[10] There has been an extensive scientific dispute over whether class IIa HDACs possess endogenous catalytic activity. In fact, their catalytic deacetylation activities are about 1000-fold weaker than those of class I HDACs, and there is no commonly accepted specific substrate identified for class IIa enzymes today.[9,11,12] However, if class IIa HDACs are immunoprecipitated, lysine deacetylase activity can be measured, which is most likely due to co-purified class I HDACs.[13–15] The vanishing activity of class IIa HDACs can be dramatically increased by a H967Y mutation, whereas a mutation of the corresponding Y into H in class I HDACs leads to inactivation, thereby confirming that class IIa HDACs are very inefficient deacetylases due to this difference in a pivotal amino acid position.[9] Furthermore, transcriptional repression of MEF2 by HDAC4 was shown to be mediated only by protein–protein interactions and not to depend on deacetylase activity.[9,16] Accordingly, class IIa HDACs have also been suggested as epigenetic readers of acetyl marks with dissociation constants within the range of binding affinities reported for bromodomains (K_d = 10–100 μM).[17–19] These findings have culminated in the currently,

[a] C. Meyners, Prof. Dr. F.-J. Meyer-Almes
Fachbereich Chemie- und Biotechnologie, Hochschule Darmstadt
Haardtring 100, 64295 Darmstadt (Germany)
E-mail: franz-josef.meyer-almes@h-da.de

[b] M. Mertens, Prof. Dr. P. Wessig
Institut für Chemie, Universität Potsdam
Karl-Liebknecht-Str. 24–25, 14476 Potsdam (Germany)
E-mail: wessig@uni-potsdam.de

Supporting information and the ORCID identification number for the author of this article can be found under http://dx.doi.org/10.1002/chem.201605140.

broadly accepted view of a mostly non-catalytic role of class IIa HDACs.[11,17,20–22] Although their function is as yet little understood, huge effort has been directed towards the development of specific HDAC class IIa inhibitors.[20,23] The therapeutic indication area for HDAC class IIa inhibitors ranges from cancer to neurodegenerative diseases like Huntington's chorea.[14,22,24] The ongoing efforts in the development of HDAC inhibitors and the large pharmacological interest clearly indicate an urgent need for devoted assays suitable for high-throughput screening (HTS) campaigns. Most commercially available assay systems for the evaluation of HDAC inhibitors rely on the deacetylation of a substrate and subsequent enzymatic conversion into a quantifiable fluorophore.[25–27] As class IIa HDACs are believed to act mainly as readers that recognise acetylated lysines, chemically activated substrates were developed exploiting a trifluoroacetylated lysine.[28] Direct HDAC binding assays rely on the displacement of usually hydroxamic acid based probes.[29–32] Recently, such an assay was published for HDAC-like prokaryotic enzymes. The authors used the environment sensitivity of [1,3]dioxolo[4,5-*f*]benzodioxole (DBD) dyes to monitor the binding of a hydroxamic acid–DBD conjugate through the large change of its fluorescence lifetime upon binding. Thus, a stable signal was produced that was insensitive to auto-fluorescence in the UV region. The presented assay was further exploited to determine the affinity of a set of HDAC inhibitors by using a competitive binding assay.[33] Unfortunately, these probes are not applicable to class IIa HDACs as hydroxamic acids are known to be mostly weak inhibitors of these enzymes.[34,35] In fact, before now, there was no direct binding assay for HDAC class IIa enzymes, although the molecular recognition of acetylated lysine residues is supposed to be their primary mode of action. In this study, we have developed a binding assay to fill this gap and meet the urgent need for a binding assay applicable to class IIa HDACs.

Results and Discussion

The development of the assay was inspired by a binding assay for class I and IIb HDACs that involves a ligand probe containing a hydroxamate group. In this study, a series of DBD probes with a trifluoromethyl ketone (TFMK) pharmacophoric group instead of a hydroxamic acid were synthesised, because compounds containing a TFMK group have been described as reasonable ligands for class IIa HDACs.[35,36]

For the synthesis of the DBD ligands, a convergent route, shown in Scheme 1, was chosen. The DBD amines **6** and **7** were synthesised by the coupling of the known acyl and ester DBD acids **1** and **2** to *N*-Boc-protected ethylenediamine (**3**) followed by deprotection of the intermediates **4** and **5** catalysed by trifluoroacetic acid (TFA).[37] For the TFMK building blocks, the synthesis of **12a**,**b** started with commercially available glutaric acid diethyl ester (**10a**) and adipic acid monomethyl ester (**10b**). The synthesis of **12c** started with compound **10c**, which was synthesised by dehydration of pimelic acid (**8**) with acetic anhydride as dehydration agent according to the known procedure of Cisneros et al. and solvolysis of the resulting anhydride **9** with methanol.[38] Although the diethyl ester **10a**

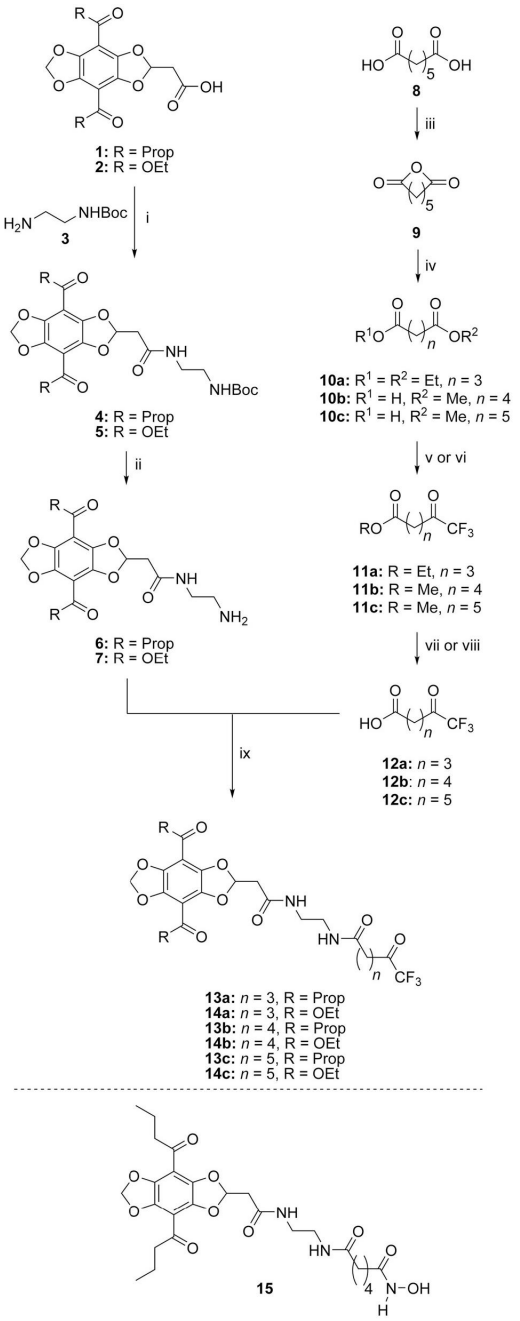

Scheme 1. Synthesis of DBD dyes **13a–c** and **14a–c**. Reagents and conditions: i) 1. $(COCl)_2$, DCM, DMF, 30 min, 0 °C, then RT; 2. DIEA, DCM, **3** (**4**: 87%; **5**: 90%); ii) TFA, DCM (**6**: 94%; **7**: 98%); iii) Ac_2O, reflux; iv) MeOH, reflux (**10c**: over 2 steps, 51%); v) NaOEt, CF_3COOEt, reflux; vi) 1. $(COCl)_2$, DCM, DMF, 30 min, 0 °C, then RT; 2. TFAA, pyridine, 0 °C; vii) 30% H_2SO_4, reflux (**12a**: over 2 steps, 17%); viii) LiOH, THF, H_2O (over 2 steps: **12b**: 41%; **12c**: 35%); ix) TBTU, DIEA, DMF (**13a**: 89%; **13b**: 71%; **13c**: 90%; **14a**: 84%; **14b**: 89%; **14c**: 98%).

was transformed into the corresponding TFMK **12a** according to the procedure of Okano et al., this procedure was not effective for the preparation of TFMKs **12b,c**.[39] Therefore another route was used, which started with the conversion of the carboxylic moieties of **10b,c** to the TFMKs **11b,c** under the conditions described by Boivin et al.[40] Then, the monomethyl ester moieties were saponified with lithium hydroxide to give the TFMKs **12b,c** by a procedure similar to that of Frey et al.[36] Finally, the DBD amines **6,7** were coupled with the TFMKs **12a–c** under standard peptide coupling conditions.

A mixture of two tautomers was observed, especially for compounds **13,14a**. The cyclic forms **13,14a′** predominates over the linear forms in $CDCl_3$ (Scheme 2). Dissolving the samples in MeOH led to a shift of equilibrium to the linear forms **13,14a**. This can be shown by ^{19}F NMR spectroscopy, for which

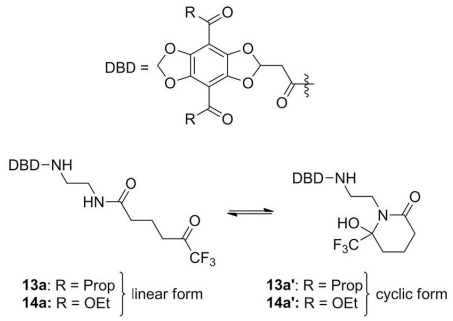

Scheme 2. Dynamic equilibrium between the tautomers of compounds **13,14a**.

the samples were concentrated from methanol and subsequently spectra in $CDCl_3$ were recorded (see Figures S1 and S2 in the Supporting Information). Specifically, for **13a**, a ratio of 1:1 of **13a** and **13a"** could be observed. Recording a second spectrum after a few hours showed a ratio of 10:1 with **13a"** as the predominant form. Similar behaviour was observed for compound **14a**. Thus, we assume a dynamic equilibrium between the different tautomers depending on the solvent.

The obtained ligands were first analysed for their potential to inhibit human HDAC1–8. As expected, the hydroxamic acid DBD probe **15** was inactive towards class IIa HDACs and active towards the other HDAC isoforms (Table 1). In contrast, **13b**, bearing the TFMK moiety, showed inhibitory activity against class IIa HDACs in the micromolar range, with stronger activity towards HDAC3 and HDAC8. Although a reduction of the spacer to three CH_2 units in **13a** resulted in a mostly inactive compound, an increment of one spacer unit to five CH_2 units in **13c** resulted in an increase of the inhibitory activity. This effect was more pronounced for class IIa HDACs, with the activities increased by factors of between 14 and 220 compared with increases of activity by factors of between 2 and 5 for the other HDACs. Similar observations were made for the ester variants of the DBD probes **14a–c**, which showed, in general, IC_{50} values similar to the acyl DBD probes **13a–c**. Only the inhibition of HDAC8 by **14a** was about 15 times stronger than for its acyl counterpart.

Next, the changes in fluorescence lifetimes (FLTs) upon the binding of the DBD ligands to HDAC isoforms 4, 5, 7 and 8 were measured in titration experiments. The unbound acyl probes exhibited FLTs of around 1.6 ns. Upon addition of the respective HDAC isoform, the FLTs of the DBD probes **13b** and **13c** increased in a concentration-dependent manner, whereas the binding of **13a** was not detectable in the investigated concentration range (Figure 1 and Table 2). The largest change in FLT was determined for the binding of **13b** to HDAC4, with a difference of 6.1 ns. In general, the probe **13b** exhibited a larger change in FLT of at least 1.9 ns compared with the longer probe **13c**. The concentration dependency of the change in the FLT of the DBD probes was further exploited to determine the dissociation constants (K_d) for binding. The K_d values are comparable to the IC_{50} values and were found to be between 1.2 and 0.01 μM. The strong increase in affinity towards class IIa HDACs upon increasing the spacer by one CH_2 unit was confirmed by the K_d values. For the binding to HDAC8, both probes **13b** and **13c** behaved similarly, binding with a comparable affinity and exhibiting a similar change in their FLTs.

The ester variants exhibited long FLTs of 25 ns in their unbound state, which would be expected to decrease upon binding. Unfortunately, this was only observable for the binding of **14a** to HDAC8. In this case, the FLT decreased by 13 ns and it was possible to determine a value of K_d of 0.69 μM (Table 2 and Figure S3 in the Supporting Information). The other ester variants showed no difference in their FLTs, neither for the binding to HDAC8 nor for the binding to class IIa HDACs.

Table 1. Inhibition of HDACs by DBD probes.

Probe	IC_{50}[a] [μM]							
	HDAC1	HDAC2	HDAC3	HDAC4	HDAC5	HDAC6	HDAC7	HDAC8
13a	>50	>50	>50	10±1	4.0±1.0	>50	1.9±0.2	4.8±0.3
13b	1.6±0.1	7.6±0.4	0.11±0.01	2.2±0.3	1.4±0.2	3.8±0.2	1.6±0.1	0.091±0.008
13c	0.82±0.03	3.2±0.1	0.042±0.003	0.010±0.002	0.10±0.01	0.79±0.1	0.036±0.006	0.021±0.001
14a	>50	>50	>50	14±1	5.3±0.5	>50	3.6±0.2	0.31±0.02
14b	2.5±0.1	21±1	0.18±0.01	3.9±0.2	2.4±0.1	2.9±0.5	2.5±0.1	0.14±0.01
14c	1.0±0.1	4.3±0.4	0.075±0.002	0.032±0.002	0.21±0.03	1.0±0.1	0.030±0.009	0.058±0.003
15	0.53±0.02	1.0±0.03	2.5±0.5	>50	>50	5.2±0.9	>50	3.2±0.3

[a] IC_{50} values were determined by using a fluorogenic enzyme activity assay as described in the Experimental Section.

Table 2. Changes in FLTs and binding constants (K_d) for the binding of DBD probes to HDAC4, 5, 7 and 8.

Probe	HDAC4		HDAC5		HDAC7		HDAC8	
	K_d [μM]	ΔFLT [ns]	K_d [μM]	ΔFLT [ns]	K_d [μM]	ΔFLT [ns]	K_d [μM]	ΔFLT [ns]
13a	>10	–	>10	–	>10	–	>10	–
13b	1.2±0.2	6.1±0.2	0.40±0.03	1.92±0.05	0.38±0.04	3.9±0.1	0.051±0.006	2.43±0.06
13c	0.010±0.003	0.89±0.02	0.078±0.008	1.28±0.03	0.046±0.008	1.23±0.03	0.024±0.003	1.87±0.05
14a	–	–	–	–	–	–	0.69±0.06	−13.2±0.3

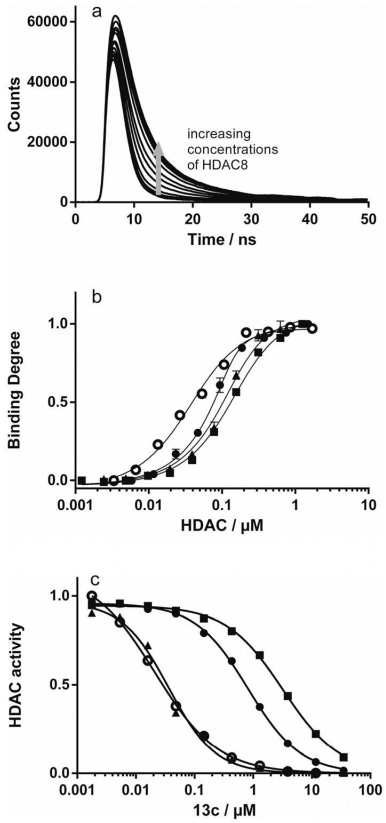

Figure 1. Binding of DBD probe **13c** to HDACs. a) Fluorescence decay curves of 0.025 nM **13c** in the presence of increasing HDAC8 concentrations. The binding of the DBD probe resulted in a concentration-dependent increase in the FLT of the probe, which was exploited to determine the degree of binding, as described in the Experimental Section. b) Degree of binding of **13c** plotted against the concentration of HDAC4 (●), HDAC5 (■), HDAC7 (▲) and HDAC8 (○). The solid lines represent the calculated fits to Equation (3). The determined binding constants are presented in Table 2. c) Inhibition of enzymatic HDAC activity by the DBD probe **13c**. The HDAC activities of HDAC1 (○), HDAC2 (■), HDAC7 (▲) and HDAC8 (●) were determined as described in the Experimental Section. The solid lines represent the calculated fits to Equation (1), which yields the IC_{50} values presented in Table 1.

To determine the specificity of the binding and to simulate the performance of the assay under screening conditions, a number of known HDAC inhibitors were used at typical screening concentrations and incubated with HDAC4 or HDAC8 and 50 nM of the DBD probe **13b**. After an incubation period of 1 hour, the fluorescence decay was measured and the FLT was determined. Compared with the FLT of the HDAC–probe complex, a decrease in the FLT was observable for all HDAC inhibitors (Figure 2). Thus, the weak HDAC4 and HDAC8 inhibitors, namely SAHA and TSA, showed a smaller decrease in the FLT than the stronger competitors SATFMK and PDF306. Furthermore, the specific reference inhibitors PCI34051 and TMP269 were both only active towards their respective target HDAC isoform.

For the strong competitors, the concentration dependency of the displacement of the probe was exploited to determine the respective inhibitor binding constants (K_i). The resulting curves for the binding to HDAC4 and the probe **13b** are quite

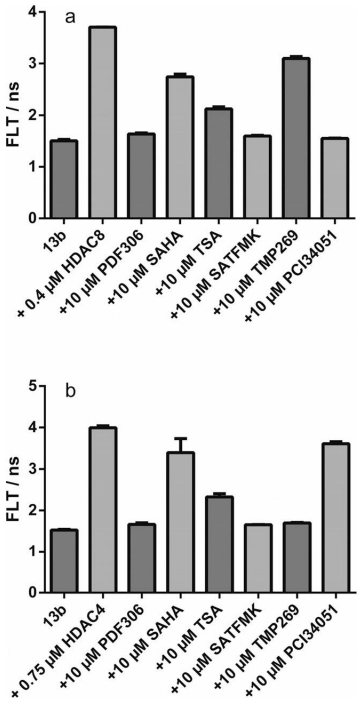

Figure 2. Displacement of DBD **13b** by competitive HDAC inhibitors. The FLT of 0.125 μM of the DBD probe **13b** was measured alone, in the presence of: a) 0.4 μM HDAC8, or b) 0.75 μM HDAC4 and with the addition of 10 μM of the indicated inhibitors.

Table 3. Comparison of inhibitor binding constants (K_i) determined by the FLT binding assay with K_d values determined by ITC and the IC_{50} values of the inhibitors of HDAC4 and HDAC8.

Inhibitor	HDAC4			HDAC8		
	K_i [μM]	K_d [μM]	IC_{50} [μM]	K_i [μM]	K_d [μM]	IC_{50} [μM]M
SATFMK	0.012 ± 0.003	0.047 ± 0.01	0.10 ± 0.01	0.023 ± 0.005	0.08 ± 0.01	0.035 ± 0.002
PDF306	0.23 ± 0.02	0.22 ± 0.04	0.40 ± 0.02	0.12 ± 0.01	0.058 ± 0.01	0.18 ± 0.06
TMP269	0.14 ± 0.01	–	0.26 ± 0.03	–	–	–
PCI34051	–	–	–	0.028 ± 0.006	–	0.024 ± 0.002

steep and produced equal values of K_i of around 0.08 μM for all three inhibitors (see Figure S4 in the Supporting Information). This and the high error in the determined K_i values indicated that these values could not be determined reliably, which presumably originates from the big difference in affinity between the probe and the inhibitors. To overcome these limitations the more affine binding probe **13c** was used. The resulting curves allowed a more exact determination of the K_i values, which are in good agreement with the K_d values determined by ITC and the IC_{50} values determined from an enzyme activity assay (Figure 3, Figure S5 and Table 3). For HDAC8, the binding of the probe **13b** was more affine, which allowed a reliable determination of the K_i values of the tested compounds.

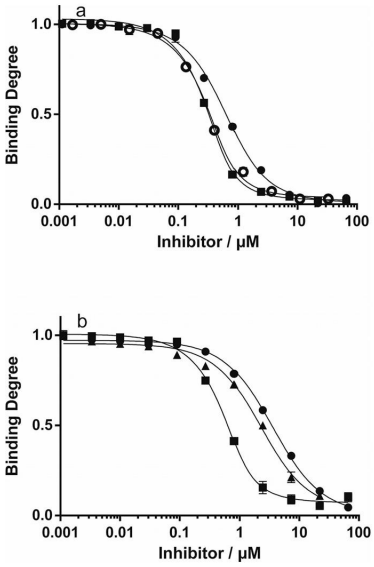

Figure 3. Determination of the binding constants for the binding of unlabelled HDAC inhibitors to: a) HDAC8, and b) HDAC4. A serial dilution of the unlabelled HDAC inhibitors PDF306 (○), SATFMK (■), TMP269 (▲) or PCI34051 (●) was incubated with either 0.45 μM HDAC8 and 0.125 μM of the DBD probe **13b** or 0.8 μM HDAC4 and 0.125 μM of the DBD probe **13c**. After equilibration, the FLTs of the probes were measured and translated into the degree of binding, as described in the Experimental Section. The solid lines represent the calculated fits to Equation (4), which yields the binding constants presented in Table 3.

Conclusions

The presented assay is the first reported direct binding assay for class IIa HDACs. The assay relies on DBD probes that show a large change in FLT of up to 6.1 ns upon binding to the enzymes. The general procedure is extremely simple (mix and measure), without the need for any additional incubation step for the reactions of target and/or detecting enzymes, and exploits the proven robust FLT readout of DBD resulting in a high-performance assay suitable for HTS applications. The assay is capable of identifying strong as well as weak ligands under typical screening conditions, and the binding constants of strong binders could be determined reliably, showing good correlation with the IC_{50} values determined by enzyme activity assays. The inhibitory activities of the DBD probes towards other HDAC isoforms also suggest that they may be used as generic tools in binding assays for class I and IIb HDACs.

Experimental Section

All reagents and solvents were purchased from commercial suppliers and used with further purification only if necessary. SAHA was bought from Cayman chemicals and TSA and PCI-34051 were bought from Selleckchem. HDAC isoforms 1, 2, 3 and 6 were ordered from BPS Bioscience. The compounds SATFMK, PDF306 and **15** were prepared as described elsewhere.[33,41,42] SUMO protease 1 (Ulp 1) was prepared as described by Malakhov et al.[43] Reactions were performed under an inert atmosphere (nitrogen or argon) whenever anhydrous solvents were used and were monitored by TLC using aluminium sheets coated with silica gel (SiO_2-60, F254). Flash chromatography was carried out on silica gel 60 (40–63 μm). NMR spectra were recorded on a Bruker Avance 300 spectrometer. Chemical shifts are reported as δ in parts per million (ppm) relative to the solvent signal (^{1}H NMR: $CDCl_3$: $\delta = 7.26$ ppm, $[D_4]$MeOD: $\delta = 3.31$ ppm; ^{13}C NMR: $CDCl_3$: $\delta = 77.0$ ppm, $[D_4]$MeOD: $\delta = 49.15$ ppm). For ^{19}F NMR spectroscopy, trifluoroacetic acid (TFA) ($\delta = -76.55$ ppm) was used as external standard. NMR chemical shifts were assigned on the basis of correlation spectroscopy (COSY, HSQC). HRMS were recorded on a quadrupole time-of-flight (TOF) mass spectrometer. Melting points were determined on an Elektrothermal 9100 melting-point instrument. IR spectra were recorded on a Perkin-Elmer FTIR Spectrum 2 spectrometer.

Synthesis of DBD probes

Note: Some compounds with a DBD backbone show in the ^{1}H NMR spectra signals of an AB system caused by the methylene group belonging to the DBD. This will be marked as "AB" and the value in Hz is the distance between the inner signals of such

a spin system. The outer signals of higher order are usually too small to be able to perform an analysis.

***tert*-Butyl (2-{2-[4,8-dibutyrylbenzo[1,2-*d*:4,5-*d'*]bis([1,3]dioxol)-2-yl]acetamido}ethyl)carbamate (4)**: Oxalyl chloride (0.2 mL, 2.33 mmol, 8.3 equiv) and 1 drop of anhydrous DMF were added to a cooled solution (0 °C) of the carboxylic acid **1** (102.4 mg, 281.05 μmol) in anhydrous DCM (25 mL). After 4 h the solution was concentrated under reduced pressure. The resulting solid was dissolved in anhydrous DCM (20 mL) and slowly added dropwise to a solution of *N*,*N*-diisopropylethylamine (DIEA; 100 μL, 574.09 μmol, 2.0 equiv) and *tert*-butyl (2-aminoethyl)carbamate (**3**; 50 μL, 324.56 μmol, 1.1 equiv) in anhydrous DCM (20 mL). The solution was stirred overnight for 18 h and then added to a saturated aqueous solution of $NaHCO_3$ (50 mL). The aqueous phase was extracted with DCM (4×50 mL) and washed with aqueous HCl (0.1 N, 50 mL) and then saturated aqueous NaCl (50 mL). The combined organic phases were dried ($MgSO_4$), filtered and concentrated under reduced pressure. The residue was purified by silica gel chromatography (DCM/MeOH, 99:1→92:8) to afford **4** as an orange solid (124.4 mg, 87%). R_f = 0.50 (DCM/MeOH, 25:1); m.p. 164–165 °C; ^{1}H NMR (300 MHz, $CDCl_3$, 27 °C): δ = 6.75 (br s, 1H; NH), 6.62 (t, ^3J = 5.2 Hz, 1H; CH), 6.09 (s, 2H; CH_2), 5.30 (br s, 1H; NH), 3.46–3.34 (m, 2H; CH_2), 3.33–3.19 (m, 2H; CH_2), 2.89 (d, ^3J = 5.0 Hz, 2H; CH_2), 2.87 (t, ^3J = 7.2 Hz, 4H; CH_2), 1.76–1.62 (m, 4H; CH_2), 1.41 (s, 9H; CH_3), 0.96 ppm (t, ^3J = 7.4 Hz, 6H; CH_3); ^{13}C NMR (75 MHz, $CDCl_3$, 27 °C): δ = 196.4 (2C; C=O), 166.8 (1C; C=O), 156.8 (1C; C=O), 141.1 (2C; C_q), 140.4 (2C; C_q), 110.5 (1C; CH), 110.0 (2C; C_q), 102.6 (1C; CH_2), 79.6 (1C; C_q), 45.6 (2C; CH_2), 42.0 (1C; CH_2), 40.8 (1C; CH_2), 40.3 (1C; CH_2), 28.3 (3C; CH_3), 17.1 (2C; CH_2), 13.7 ppm (2C; CH_3); IR (ATR): $\tilde{\nu}$ = 3293, 2966, 1682, 1654, 1436, 1279, 1236, 1175, 1087, 1036 cm^{-1}; HRMS (EI): *m/z* calcd for $[M]^+$: 506.2264; found: 506.2272.

Diethyl 2-[2-({2-[(*tert*-butoxycarbonyl)amino]ethyl}amino)-2-oxoethyl]benzo[1,2-*d*:4,5-*d'*]bis([1,3]dioxole)-4,8-dicarboxylate (5): Compound 5 was synthesised from the carboxylic acid **2** (98.7 mg, 267.99 μmol) by following the procedure described above for the synthesis of compound **4**. The desired product was obtained as a yellow solid (123.3 mg, 90%). R_f = 0.34 (DCM/MeOH, 25:1); m.p. 165–167 °C; ^{1}H NMR (300 MHz, $CDCl_3$, 27 °C): δ = 6.61 (t, ^3J = 5.3 Hz, 1H; CH), 6.10 (AB, J = 0.46 Hz, 2H; CH_2), 5.26 (br s, 1H; NH), 4.38 (q, ^3J = 7.1 Hz, 4H; CH_2), 3.44–3.33 (m, 2H; CH_2), 3.33–3.20 (2H; CH_2), 2.90 (d, ^3J = 5.3 Hz, 2H; CH_2), 1.41 (s, 9H; CH_3), 1.36 ppm (t, ^3J = 7.1 Hz, 6H; CH_3); ^{13}C NMR (75 MHz, $CDCl_3$, 27 °C): δ = 166.8 (1C; C=O), 161.8 (2C; C=O), 156.6 (1C; C=O), 141.9 (2C; C_q), 141.2 (2C; C_q), 110.7 (1C; CH), 103.2 (2C; C_q), 102.9 (1C; CH_2), 79.5 (1C; C_q), 61.7 (2C; CH_2), 42.1 (1C; CH_2), 40.5 (1C; CH_2), 40.3 (1C; CH_2), 28.3 (3C; CH_3), 14.2 ppm (2C; CH_3); IR (ATR): $\tilde{\nu}$ = 3275, 2977, 1710, 1656, 1450, 1294, 1261, 1155, 1080 cm^{-1}; HRMS (EI): *m/z* calcd for $[M]^+$: 510.1850; found: 510.1840.

2-{2-[4,8-Dibutyrylbenzo[1,2-*d*:4,5-*d'*]bis([1,3]dioxol)-2-yl]acetamido}ethan-1-aminium 2,2,2-trifluoroacetate (6): Compound **4** (96.0 mg, 189.52 μmol) was added to a solution of DCM/TFA (3:1, 12 mL). After 30 min, all the volatile compounds were removed and the residue was suspended in toluene. The solvent was removed under reduced pressure and this procedure was repeated once again. Then the crude product was dissolved in hot MeOH, cooled to RT and precipitated with petroleum ether (PE, 40–60 °C). Filtration and drying under reduced pressure yielded the title compound **6** as an orange solid (92.4 mg, 94%). M.p. 149–151 °C; ^{1}H NMR (300 MHz, [D_4]MeOH, 25 °C): δ = 6.67 (t, ^3J = 5.3 Hz, 1H; CH), 6.14 (AB, J = 1.2 Hz, 2H; CH_2), 3.54 (t, ^3J = 5.9 Hz, 2H; CH_2), 3.14 (t, ^3J = 5.9 Hz, 2H; CH_2), 3.00 (d, ^3J = 5.3 Hz, 2H; CH_2), 2.96 (t, ^3J = 7.2 Hz, 4H; CH_2), 1.82–1.60 (m, 4H; CH_2), 1.00 ppm (t, ^3J = 7.4 Hz, 6H; CH_3); ^{13}C NMR (75 MHz, [D_4]MeOH, 25 °C): δ = 199.0 (2C; C=O), 171.6 (1C; C=O), 143.4 (2C; C_q), 142.6 (2C; C_q), 113.1 (1C; CH), 112.0 (2C; C_q), 104.9 (1C; CH_2), 47.4 (2C; CH_2), 43.0 (1C; CH_2), 41.7 (1C; CH_2), 39.0 (1C; CH_2), 19.0 (2C; CH_2), 14.9 ppm (2C; CH_3); IR (ATR): $\tilde{\nu}$ = 3275, 3099, 2964, 1660, 1567, 1439, 1282, 1187, 1119, 1039, 837, 723 cm^{-1}; HRMS (ESI): *m/z* calcd for $[M\text{H}]^+$: 407.1818; found: 407.1811.

2-{2-[4,8-Bis(ethoxycarbonyl)benzo[1,2-*d*:4,5-*d'*]bis([1,3]dioxol)-2-yl]acetamido}ethan-1-aminium 2,2,2-trifluoroacetate (7): Compound **7** was synthesised from 5 (60.2 mg, 117.92 μmol) by following the procedure described above for the synthesis of compound **6**. The desired product was obtained as yellow solid (60.8 mg, 98%). M.p. 176 °C (decomp.); ^{1}H NMR (300 MHz, [D_6]DMSO, 25 °C): δ = 8.33 (t, ^3J = 5.4 Hz, 1H; NH), 7.87 (br s, 3H; NH), 6.62 (t, ^3J = 5.2 Hz, 1H; CH), 6.12 (s, 2H; CH_2), 4.28 (q, ^3J = 7.1 Hz, 4H; CH_2), 3.43–3.28 (2H; CH_2), 2.88 (d, ^3J = 5.3, 2H; CH_2), 2.88–2.83 (2H; CH_2), 1.26 ppm (t, ^3J = 7.1 Hz, 6H; CH_3); ^{13}C NMR (75 MHz, [D_6]DMSO, 25 °C): δ = 168.1 (1C; C=O), 161.8 (2C; C=O), 141.9 (2C; C_q), 141.8 (2C; C_q), 112.1 (1C; CH), 103.6 (2C; C_q), 103.3 (1C; CH_2), 62.0 (2C; CH_2), 41.5 (1C; CH_2), 39.4 (1C; CH_2), 37.2 (1C; CH_2), 15.0 ppm (2C; CH_3); IR (ATR): $\tilde{\nu}$ = 3270, 3091, 2984, 1719, 1661, 1451, 1298, 1268, 1177, 1091, 1022, 955, 723 cm^{-1}; HRMS (ESI): *m/z* calcd for $[M\text{H}]^+$ 410.1325; found: 410.1310.

7-Methoxy-7-oxoheptanoic acid (10c):[38] Compound **9** was synthesised according to the procedure of Cisneros et al. starting from pimelic acid (**8**; 3.02 g, 18.84 mmol). After heating in anhydrous acetic acid (47 mL) at reflux for 5 h all volatile compounds were removed. The resulting white solid was dried under high vacuum and then heated at reflux in anhydrous methanol (10 mL) for 5 h. After removal of the solvent under reduced pressure the residue was purified by distillation (100 °C, 1.2×10^{-2} mbar) to yield **10c** as a colourless oil (1.67 g, 51% over two steps). ^{1}H NMR (300 MHz, $CDCl_3$, 25 °C): δ = 10.82 (s, 1H; OH), 3.63 (s, 3H; CH_3), 2.32 (t, ^3J = 7.5 Hz, 2H; CH_2), 2.29 (t, ^3J = 7.6 Hz, 2H; CH_2), 1.70–1.54 (m, 4H; CH_2), 1.41–125 ppm (m, 2H; CH_2); ^{13}C NMR (75 MHz, $CDCl_3$, 25 °C): δ = 179.8 (1C; C=O), 174.1 (1C; C=O), 51.4 (1C; CH_3), 33.7 (2C; CH_2), 28.4 (1C; CH_2), 24.4 (1C; CH_2), 24.2 ppm (1C; CH_2); IR (ATR): $\tilde{\nu}$ = 2950, 2866, 1733, 1708, 1437, 1198, 1171 cm^{-1}; HRMS (EI): *m/z* calcd for $[M\text{H}]^+$ 175.0965; found: 175.0964.

Methyl 8,8,8-trifluoro-7-oxooctanoate (11c): Compound **11c** was synthesised by a procedure similar to that described by Boivin et al.[40] One drop of anhydrous DMF was added to a stirred solution of pimelic acid monomethyl ester **10c** (1.36 g, 7.81 mmol) in anhydrous DCM (20 mL). After cooling to 0 °C, oxalyl chloride (1.2 mL, 15.62 mmol, 2.0 equiv) was added slowly and the solution was stirred for 18 h at RT. After removing of all the volatile compounds under reduced pressure, the corresponding acid chloride of **10c** was dissolved in anhydrous DCM (50 mL), cooled to 0 °C, treated with trifluoroacetic anhydride (4.4 mL, 31.25 mmol, 4.0 equiv) and pyridine (3.8 mL, 46.87 mmol, 6.0 equiv) and the solution stirred for 30 min at 0 °C. Ice-water (20 mL) was added slowly and the solution was then stirred for a further 60 min. After the addition of distilled water (100 mL) to the solution and separation of the organic phase, the inorganic phase was extracted with DCM (4×50 mL). The combined organic phases were washed with a saturated aqueous solution of NaCl, dried over $MgSO_4$ and concentrated under reduced pressure. The residue was purified by silica gel chromatography (DCM/PE, 1:1) to give **11c** as a pale-yellow oil (1.58 g, 58%), which was contaminated with small amounts of starting material that could not be separated from the product. ^{1}H NMR (300 MHz, $CDCl_3$, 25 °C): δ = 3.65 (s, 3H; CH_3), 2.71 (t, ^3J = 7.2 Hz, 2H; CH_2), 2.31 (t, ^3J = 7.4 Hz, 2H; CH_2), 1.75–1.53 (4H; CH_2), 1.43–1.28 ppm (m, 2H; CH_2); ^{13}C NMR (75 MHz, $CDCl_3$, 25 °C): δ = 191.4 (q, ^2J(C,F) = 34.8 Hz, 1C; C=O), 176.0 (1C; C=O), 115.5 (q,

^{1}J(C,F) = 292.0 Hz, 1C; CF_3); 52.3 (1C; CH_3), 36.0 (1C; CH_2), 33.7 (1C; CH_2), 28.0 (1C; CH_2), 24.4 (1C; CH_2), 21.9 ppm (1C; CH_2); ^{19}F NMR (282 MHz, $CDCl_3$, 25 °C): δ = −80.0 ppm (s, 3F; CF_3); IR (ATR): $\tilde{\nu}$ = 2952, 2869, 1763, 1735, 1438, 1404, 1368, 1291, 1203, 1152, 1023 cm^{-1}.

7,7,7-Trifluoro-6-oxoheptanoic acid (12b):[36] The carboxylic acid **12b** was synthesised by a procedure similar that described by Frey et al.[36] The trifluoromethyl ketone **11b** (1.02 g, 4.81 mmol) was dissolved in THF (20 mL) at RT and treated with an aqueous solution of LiOH (2 M, 24 mL) for 8 h. Then the reaction mixture was washed with MTBE (2×10 mL) and acidified with aqueous HCl (1 N) to pH 2. The inorganic phase was extracted with EtOAc (4×20 mL) and the combined organic phases were dried ($MgSO_4$), filtered and concentrated under reduced pressure. The desired trifluoromethyl ketone **12b** was obtained as a white solid (0.67 g, 70%) and used without further purification. The analytical data are in agreement with those reported previously.

8,8,8-Trifluoro-7-oxooctanoic acid (12c):[36] The trifluoromethyl ketone **12c** was synthesised from the methyl ester **11c** (737.5 mg, 3.26 mmol) by following the procedure described above for compound **12b**. The crude product was purified by silica gel chromatography (DCM/MeOH, 30:1) to afford the trifluoromethyl ketone **12c** as a highly viscous oil (425.1 mg, 61%). The analytical data are in agreement with those reported previously.

***N*-(2-{2-[4,8-Dibutyrylbenzo[1,2-*d*:4,5-*d*′]bis([1,3]dioxol)-2-yl]acetamido}ethyl)-6,6,6-trifluoro-5-oxohexanamide (13a)**: The amine **6** (38.7 mg, 74.36 μmol, 1.0 equiv) was added to a mixture of the carboxylic acid **12a** (20.0 mg, 108.63 μmol, 1.5 equiv), DIEA (26.0 μL, 149.26 μmol, 2.0 equiv) and N,N,N′,N′-tetramethyl-O-(benzotriazol-1-yl)uronium tetrafluoroborate (TBTU; 35.0 mg, 109.00 μmol, 1.5 equiv) in anhydrous DMF (1.5 mL). After 16 h the solvent was removed under reduced pressure and the residue was dissolved in DCM and worked up with aqueous HCl (1 N) and saturated aqueous NaCl. The organic phase was dried ($MgSO_4$), filtered and concentrated under reduced pressure and the crude product purified by silica gel chromatography (DCM/MeOH/TEA, 100:1:0.1). After washing with saturated aqueous NaCl and drying over $MgSO_4$, the trifluoromethyl ketone **13a** was obtained as an orange solid (37.7 mg, 89%). The NMR spectra showed that the title compound exists as a mixture of two tautomers. Which tautomer is predominant depends on the solvent. The present data show a 1:1 mixture (as judged by ^{1}H und ^{19}F NMR). R_f = 0.49 (DCM/MeOH, 10:1); m.p. 124–127 °C; ^{1}H NMR (300 MHz, $CDCl_3$, 27 °C): δ = 6.90 (brt, 0.5H; NH), 6.74 (brt, 0.5H; NH), 6.68–6.49 (1.5H; NH, CH), 6.18–6.05 (2H; CH_2), 4.26–4.12 (m, 0.5H; CH), 3.87–3.73 (m, 0.5H; CH), 3.56–3.24 (3H; CH_2), 3.00–2.78 (6H; CH_2), 2.57–2.35 (1.5H; CH, CH_2), 2.29 (t, ^{3}J = 7.1 Hz, 1H; CH_2), 2.12–1.93 (1.5H; CH, CH_2), 1.91–1.62 (6H; CH_2), 0.97 ppm (t, ^{3}J = 7.4 Hz, 6H; CH_3); ^{13}C NMR (75 MHz, $CDCl_3$, 27 °C): δ = 196.7 (2C; C=O), 196.6 (2C; C=O), 172.7 (1C; C=O), 172.3 (1C; C=O), 168.2 (1C; C=O), 167.0 (1C; C=O), 141.2 (2C; C_q), 140.4 (2C; C_q), 110.6 (2C; C_q), 110.5 (2C; C_q), 110.1 (1C; CH), 102.6 (1C; CH_2), 102.5 (1C; CH_2), 45.7 (2C; CH_2), 42.2 (1C; CH_2), 39.9 (1C; CH_2), 39.8 (1C; CH_2), 35.5 (1C; CH_2), 34.2 (1C; CH_2), 31.6 (1C; CH_2), 18.2 (1C; CH_2), 17.1 (2C; CH_2), 17.0 (2C; CH_2), 13.7 ppm (2C; CH_3); ^{19}F NMR (282 MHz, $CDCl_3$, 25 °C): δ = −77.6 (s, 3F), −79.7 ppm (s, 3F); IR (ATR): $\tilde{\nu}$ = 3283, 2964, 2877, 1685, 1660, 1438, 1283, 1204, 1120, 1093 cm^{-1}; HRMS (EI): *m/z* calcd for $[M]^+$ 572.1982; found: 572.1986.

Diethyl 2-(2-oxo-2-{[2-(6,6,6-trifluoro-5-oxohexanamido)ethyl]amino}ethyl)benzo[1,2-*d*:4,5-*d*′]bis([1,3]dioxole)-4,8-dicarboxylate (14a): Following the procedure described above for the synthesis of **13a**, the trifluoromethyl ketone **14a** was obtained from the carboxylic acid **12a** (18.0 mg, 97.77 μmol, 1.3 equiv), DIEA (26 μL, 149.26 μmol, 2.0 equiv), TBTU (33.59 mg, 104.61 μmol, 1.4 equiv) and the amine **7** (38.7 mg, 73.80 μmol) in anhydrous DMF (1.5 mL) as a yellow solid (35.7 mg, 84%). The NMR spectra revealed that the title compound exists as a mixture of two tautomers. Which tautomer is predominant depends on the solvent. The present data show a 1:1 mixture (as judged by ^{1}H und ^{19}F NMR). R_f = 0.47 (DCM/MeOH, 10:1); m.p. 155–158 °C; ^{1}H NMR (300 MHz, $CDCl_3$, 25 °C): δ = 6.78 (brs, 0.5H; NH), 6.72–6.36 (2H; NH, CH), 6.11 (s, 2H; CH_2), 4.37 (q, ^{3}J = 7.1 Hz, 4H; CH_2), 4.25–4.11 (m, 0.5H; CH), 3.86–3.70 (m, 0.5H; CH), 3.61–3.20 (3H; CH_2), 3.02–2.88 (2H; CH_2), 2.82 (t, ^{3}J = 6.8 Hz, 1H; CH_2), 2.52–2.32 (1.5H; CH, CH_2), 2.27 (t, ^{3}J = 7.0 Hz, 1H; CH_2), 2.10–1.75 (m, 2.5H; CH_2), 1.38 ppm (t, ^{3}J = 7.1 Hz, 6H; CH_3); ^{13}C NMR (75 MHz, $CDCl_3$, 25 °C): δ = 172.6 (1C; C=O), 172.2 (1C; C=O), 168.3 (1C; C=O), 167.3 (1C; C=O), 161.9 (2C; C=O), 141.9 (2C; C_q), 141.2 (2C; C_q), 110.9 (1C; CH), 110.7 (1C; CH), 103.2 (2C; C_q), 102.9 (1C; CH_2), 61.7 (2C; CH_2), 42.2 (1C; CH_2), 41.7 (1C; CH_2), 40.3 (2C; CH_2), 39.6 (2C; CH_2), 35.5 (1C; CH_2), 34.1 (1C; CH_2), 32.3 (1C; CH_2), 31.5 (1C; CH_2), 18.1 (1C; CH_2), 15.4 (1C; CH_2), 14.2 ppm (2C; CH_3); ^{19}F NMR (282 MHz, $CDCl_3$, 25 °C): δ = −77.9 (s, 3F), −79.9 ppm (s, 3F); IR (ATR): $\tilde{\nu}$ = 3405, 2976, 1720, 1654, 1449, 1296, 1176, 1078, 1023 cm^{-1}; HRMS (EI): *m/z* calcd for $[M]^+$ 576.1567; found: 576.1548.

***N*-(2-{2-[4,8-Dibutyrylbenzo[1,2-*d*:4,5-*d*′]bis([1,3]dioxol)-2-yl]acetamido}ethyl)-7,7,7-trifluoro-6-oxoheptanamide (13b)**: Following the procedure described above for the synthesis of **13a**, the trifluoromethyl ketone **13b** was obtained from the carboxylic acid **12b** (20.0 mg, 108.63 μmol, 1.5 equiv), DIEA (26 μL, 149.26 μmol, 2.0 equiv), TBTU (35.0 mg, 109.00 μmol, 1.5 equiv) and the amine **6** (38.7 mg, 74.36 μmol) in anhydrous DMF (1.5 mL). Purification by silica gel chromatography (DCM/MeOH/TEA, 100:1:0.1) gave the title compound as an orange solid (26.8 mg, 71%). R_f = 0.47 (DCM/MeOH, 10:1); m.p. 175 °C (decomp.); ^{1}H NMR (300 MHz, $CDCl_3$, 25 °C): δ = 6.82 (brs, 1H; NH), 6.65 (brs, 1H; NH), 6.59 (t, ^{3}J = 4.8 Hz, 1H; CH), 6.11 (s, 2H; CH_2), 3.54–3.33 (4H; CH_2), 2.97–2.83 (6H; CH_2), 2.73 (brt, 2H; CH_2), 2.26 (brt, 2H; CH_2), 1.88–1.56 (8H; CH_2), 0.97 ppm (t, ^{3}J = 7.3 Hz, 6H; CH_3); ^{13}C NMR (75 MHz, $CDCl_3$, 25 °C): δ = 196.7 (2C; C=O), 173.3 (1C; C=O), 167.2 (1C; C=O), 141.2 (2C; C_q), 140.4 (2C; C_q), 110.6 (2C; C_q), 110.0 (1C; CH), 102.6 (1C; CH_2), 45.7 (2C; CH_2), 42.2 (1C; CH_2), 40.0 (1C; CH_2), 39.9 (1C; CH_2), 36.1 (1C; CH_2), 35.7 (1C; CH_2), 24.5 (1C; CH_2), 21.8 (1C; CH_2), 17.1 (2C; CH_2), 13.7 ppm (2C; CH_3); ^{19}F NMR (282 MHz, $CDCl_3$, 25 °C): δ = −79.8 ppm (s, 3F); IR (ATR): $\tilde{\nu}$ = 3284, 2962, 2936, 2877, 1678, 1642, 1560, 1436, 1281, 1089 cm^{-1}; HRMS (EI): *m/z* calcd for $[M]^+$ 586.2138; found: 586.2128.

Diethyl 2-(2-oxo-2-{[2-(7,7,7-trifluoro-6-oxoheptanamido)ethyl]amino}ethyl)benzo[1,2-*d*:4,5-*d*′]bis([1,3]dioxole)-4,8-dicarboxylate (14b): Following the procedure described above for the synthesis of **13a**, the trifluoromethyl ketone **14b** was obtained from the carboxylic acid **12b** (15.5 mg, 78.23 μmol, 1.1 equiv), DIEA (30 μL, 172.23 μmol, 2.5 equiv), TBTU (25.5 mg, 79.42 μmol, 1.1 equiv) and the amine **7** (36.6 mg, 69.79 μmol, 1.0 equiv) in anhydrous DMF (3.0 mL). Purification by silica gel chromatography (DCM/MeOH/TEA, 10:1:0.0→10:1:0.1) gave the title compound as a yellow solid (36.5 mg, 89%). R_f = 0.45 (DCM/MeOH, 10:1); m.p. 182 °C (decomp.); ^{1}H NMR (300 MHz, $CDCl_3$, 25 °C): δ = 6.72 (brs, 1H; NH), 6.67–6.46 (2H; NH, CH), 6.11 (s, 2H; CH_2), 4.38 (q, ^{3}J = 7.1 Hz, 4H; CH_2), 3.57–3.30 (4H; CH_2), 3.02–2.83 (m, 2H; CH_2), 2.82–2.65 (m, 2H; CH_2), 2.36–2.12 (m, 2H; CH_2), 1.77–1.58 (m, 4H; CH_2), 1.37 ppm (t, ^{3}J = 7.2 Hz, 6H; CH_3); ^{13}C NMR (126 MHz, $CDCl_3$, 25 °C): δ = 161.9 (2C; C=O), 141.9 (2C; C_q), 141.2 (2C; C_q), 110.8 (1C; CH), 103.2 (2C; C_q), 102.9 (1C; CH_2), 61.7 (2C; CH_2), 42.2 (1C; CH_2), 40.0 (1C; CH_2), 39.9 (1C; CH_2), 36.1 (1C; CH_2), 35.7 (1C; CH_2), 24.5 (1C; CH_2), 21.8 (1C; CH_2), 14.2 ppm (2C; CH_3); ^{19}F NMR (282 MHz, $CDCl_3$, 25 °C): δ =

−79.8 ppm (s, 3F); IR (ATR): $\tilde{\nu}$ = 3276, 2943, 1710, 1659, 1557, 1451, 1294, 1262, 1156, 1080, 1025 cm^{-1}; HRMS (EI): *m/z* calcd for $[M]^+$ 590.1723; found: 590.1739.

***N*-(2-{2-[4,8-Dibutyrylbenzo[1,2-*d*:4,5-*d'*]bis([1,3]dioxol)-2-yl]acetamido}ethyl)-8,8,8-trifluoro-7-oxooctanamide (13c)**: Following the procedure described above for the synthesis of **13a**, the trifluoromethyl ketone **13c** was obtained from the carboxylic acid **12c** (18.2 mg, 85.78 μmol, 1.1 equiv), DIEA (35 μL, 200.93 μmol, 2.7 equiv), TBTU (27.3 mg, 85.02 μmol, 1.1 equiv) and the amine **6** (39.2 mg, 75.32 μmol, 1.0 equiv) in anhydrous DMF (4.0 mL). Purification by silica gel chromatography (DCM/MeOH/TEA, 10:1:0.0→10:1:0.1) gave the title compound as an orange solid (40.3 mg, 90%). R_f = 0.53 (DCM/MeOH, 10:1); m.p. 185–186 °C; ^{1}H NMR (300 MHz, $CDCl_3$, 25 °C): δ = 6.72 (brt, 1H; NH), 6.60 (brt, 1H; NH), 6.59 (t, ^3J = 5.3 Hz, 1H; CH), 6.11 (s, 2H; CH_2), 3.47–3.36 (4H; CH_2), 2.93–2.86 (6H; CH_2), 2.71 (t, ^3J = 7.1 Hz, 2H; CH_2), 2.22 (t, ^3J = 7.4 Hz, 2H; CH_2), 1.77–1.58 (8H; CH_2), 1.41–1.24 (m, 2H; CH_2), 0.97 ppm (t, ^3J = 7.4 Hz, 6H; CH_3); ^{13}C NMR (75 MHz, $CDCl_3$, 25 °C): δ = 196.6 (2C; C=O), 173.8 (1C; C=O), 167.0 (1C; C=O), 141.2 (2C; C_q), 140.4 (2C; C_q), 110.6 (1C; CH), 110.1 (2C; C_q), 102.6 (1C; CH_2), 45.7 (2C; CH_2), 42.2 (1C; CH_2), 40.2 (1C; CH_2), 39.9 (1C; CH_2), 36.1 (1C; CH_2), 35.9 (1C; CH_2), 28.2 (1C; CH_2), 25.0 (1C; CH_2), 22.0 (1C; CH_2), 17.1 (2C; CH_2), 13.7 ppm (2C; CH_3); ^{19}F NMR (282 MHz, $CDCl_3$, 25 °C): δ = −79.8 ppm (s, 3F); IR (ATR): $\tilde{\nu}$ = 3275, 2933, 1710, 1658, 1557, 1451, 1293, 1262, 1155, 1079, 1051 cm^{-1}; HRMS (EI): *m/z* calcd for $[M]^+$ 600.2295; found: 600.2304.

Diethyl 2-(2-oxo-2-{[2-(8,8,8-trifluoro-7-oxooctanamido)ethyl]amino}ethyl)benzo[1,2-*d*:4,5-*d'*]bis([1,3]dioxole)-4,8-dicarboxylate (14c): Following the procedure described above for the synthesis of **13a**, the trifluoromethyl ketone **14c** was obtained from the carboxylic acid **12c** (17.9 mg, 84.37 μmol, 1.1 equiv), DIEA (35 μL, 200.93 μmol, 2.7 equiv), TBTU (27.2 mg, 84.71 μmol, 1.1 equiv) and the amine **7** (39.2 mg, 74.75 μmol, 1.0 equiv) in anhydrous DMF (4.0 mL). Purification by silica gel chromatography (DCM/MeOH/TEA, 20:1:0.1) gave the title compound as a yellow solid (44.4 mg, 98%). R_f = 0.48 (DCM/MeOH, 10:1); m.p. 195 °C (decomp.); ^{1}H NMR (300 MHz, $CDCl_3$, 25 °C): δ = 6.75 (brt, 1H; NH), 6.64–6.56 (1H; NH), 6.60 (t, ^3J = 5.3 Hz, 1H; CH), 6.11 (d, AB, J = 1.6 Hz, 2H; CH_2), 4.38 (q, ^3J = 7.1 Hz, 4H; CH_2), 3.49–3.34 (4H; CH_2), 2.91 (d, ^3J = 5.3 Hz, 2H; CH_2), 2.71 (t, ^3J = 7.0 Hz, 2H; CH_2), 2.23 (t, ^3J = 7.4 Hz, 2H; CH_2), 1.73–1.58 (m, 4H; CH_2), 1.41–1.28 (m, 2H; CH_2), 1.37 ppm (t, ^3J = 7.1 Hz, 6H; CH_3); ^{13}C NMR (75 MHz, $CDCl_3$, 25 °C): δ = 167.3 (1C; C=O), 161.8 (2C; C=O), 141.9 (2C; C_q), 141.2 (2C; C_q), 110.8 (1C; CH), 103.2 (2C; C_q), 102.9 (1C; CH_2), 61.7 (2C; CH_2), 42.1 (1C; CH_2), 40.1 (1C; CH_2), 39.8 (1C; CH_2), 36.1 (1C; CH_2), 35.6 (1C; CH_2), 28.2 (1C; CH_2), 25.1 (1C; CH_2), 22.0 (1C; CH_2), 14.2 ppm (2C; CH_3); ^{19}F NMR (282 MHz, $CDCl_3$, 25 °C): δ = −79.5 ppm (s, 3F); IR (ATR): $\tilde{\nu}$ = 3278, 2931, 1710, 1657, 1557, 1450, 1293, 1261, 1155, 1079, 1051 cm^{-1}; HRMS (EI): *m/z* calcd for $[M]^+$ 604.1880; found: 604.1869.

Protein expression and purification of HDACs

The genes encoding the catalytic domains of HDAC4 (amino acids 648–1057), HDAC5 (amino acids 655–1122), HDAC7 (amino acids 518–952) and full-length HDAC8 were codon-optimised and ordered from GenScript. The genes were delivered in a pUC57 plasmid and cloned into a pET14b-SUMO (HDAC8) or a pET14b-SUMO-CPD (HDAC4, 5 and 7) vector. All HDACs were recombinantly expressed in *E. coli* BL21(DE3) as fusion proteins, whereby their N-terminus was fused to a 6×His-SUMO tag.[43] HDAC4, 5 and 7 were additionally fused to a C-terminal cysteine protease domain (CPD), which possess an autocatalytic activity and cuts itself from the HDAC upon induction by phytic acid.[44] Bacterial cultures were grown at 37 °C in LB media to an optical density at 600 nm of 0.6–0.8. Protein expression was induced by the addition of 1 mM isopropyl-β-D-thiogalactopyranoside and the cells were further cultured overnight at 25 °C. Cells were harvested by centrifugation (15 min, 15000*g*, 4 °C) and the pellet was re-suspended in lysis buffer (50 mM HEPES, pH 8.0, 300 mM NaCl). Cells were lysed by sonication and cell fragments were removed by centrifugation (30 min, 25000*g*, 4 °C). The supernatant was analysed by immobilised metal affinity chromatography using a cOmplete His-Tag purification resin (Roche), which was equilibrated with lysis buffer. The resin was washed with 20 volumes of lysis buffer. For the CPD fusion constructs the resin was afterwards incubated for 1 h with 200 μM phytic acid in lysis buffer. The SUMO fusion proteins were eluted by the addition of 100 mM imidazole in lysis buffer. The SUMO tag was cleaved by incubation with 20 μg Ulp 1 at 4 °C, overnight. The proteins were purified further by gel filtration using a Sephadex 200 16/60 column equilibrated with HDAC buffer (50 mM HEPES, pH 8.0, 20 mM NaCl, 10 mM KCl). HDAC-containing fractions were pooled and concentrated. The protein concentration was determined by means of the bicinchoninic acid assay. Protein solutions were supplemented with 10% glycerol, flash frozen with liquid nitrogen and stored at −20 °C.

Enzyme activity assay

The HDAC activity assay was conducted as described elsewhere.[26] In brief, a serial dilution of the DBD probe or inhibitor in assay buffer (25 mM Tris-HCl, pH 8.0, 75 mM KCl, 0.001% Pluronic F-127) was placed in a black 96-well microtiter plate (Greiner) and incubated with 1 nM of the respective HDAC isoform for 30 min at 30 °C. The reaction was then initiated by the addition of either 50 μM Boc-Lys(Ac)-AMC (AMC = 7-amino-4-methylcoumarin) (for HDAC1, 2, 3 and 6) or 20 μM Boc-Lys(trifluoroacetyl)-AMC (for HDAC4, 5, 7 and 8) as substrate. After incubation for 60 min at 30 °C, the reaction was stopped by the addition of 20 μM SAHA or SATFMK and the deacetylated substrate was converted into a fluorescent product by the addition of 0.5 mg mL^{-1} trypsin. The release of AMC was followed in a microplate reader and correlated to enzyme activity. Dose-response curves were generated by using GraphPad Prism and fitted to the following four parameter logistic model [Eq. (1)] to obtain the respective IC_{50} value:[45]

$$EA = E_0 + \frac{(E_{max} - E_0)}{1 + 10^{[(\log IC_{50} - x)h]}} \quad (1)$$

in which EA denotes the enzyme activity at a certain inhibitor concentration *x*, E_{max} and E_0 are the enzyme activities determined at zero and complete inhibition and IC_{50} denotes the inhibitor concentration at which half of the enzyme is inhibited and *h* is the slope of the curve.

Isothermal titration calorimetry

To validate the K_i values determined by the fluorescence lifetime binding assay, the binding of SATFMK and PDF306 to HDAC4 and HDAC8 was investigated by ITC. Thus, 20–40 μM HDAC in HDAC buffer was placed in the sample cell of a PEAQ-ITC instrument (Malvern Instruments Ltd) at 25 °C. The syringe was loaded with 100–200 μM of the inhibitor suspended in HDAC buffer. To minimise the heat of dilution the DMSO and glycerol concentrations were adjusted to be identical in the sample cell and syringe. Nevertheless, the resulting final DMSO concentrations of up to 2% resulted in a reduction of the active binding HDAC concentration, which resulted in an observed stoichiometry of between 0.13 and

0.4. The measurements were carried out at 25 °C and the inhibitor was titrated by injecting 19×2 μL into the sample cell with a spacing of 150–300 s. The amount of heat released following each injection was determined by integrating the area under the curve by using the MicroCal PEAQ-ITC Analysis software. The resulting data points were then fitted to a one-site binding model supplied with the software.

Fluorescence lifetime binding assay

To determine the equilibrium dissociation constants of the binding of the acyl DBD ligands **13a–c** to HDAC4, 5, 7 and 8, a serial dilution of the respective HDAC was placed in the aforementioned microtiter plate and mixed with 25–125 nM of the DBD ligand. After incubation for 30 min at 25 °C, the fluorescence decay was measured by using an LF502 nanoscan instrument from Berthold Detection Systems GmbH (Pforzheim, Germany) behind a 630 nm band-pass filter after pulse excitation at 456 nm. For the binding of the ester DBD ligands **14a–c**, the experiments were conducted under the same conditions, but the band-pass filter was exchanged to 520 nm and the pulse excitation was produced at 405 nm. The binding of the DBD ligands resulted in an increased FLT, which was exploited to determine the degree of binding (BD) according to Equation (2):

$$\mathrm{BD} = \frac{A - A_{\mathrm{min}}}{A_{\mathrm{max}} - A_{\mathrm{min}}} \tag{2}$$

in which A is the FLT in the presence of a certain enzyme concentration of interest, A_{min} is the FLT in the absence of enzyme and A_{max} is the FLT in the presence of saturating enzyme concentrations.

From the determined binding isotherms, the equilibrium dissociation constant (K_d) can be fitted by using Equation (3):

$$\mathrm{BD} = \frac{[\mathrm{EL}]}{[\mathrm{L}]_0} = \frac{1}{2[\mathrm{L}]_0}\left([\mathrm{E}]_0 + [\mathrm{L}]_0 + K_d - \sqrt{([\mathrm{E}]_0 + [\mathrm{L}]_0 + K_d)^2 - 4[\mathrm{L}]_0[\mathrm{E}]_0}\right) \tag{3}$$

in which [EL] is the equilibrium concentration of the complex between the enzyme E and the respective DBD ligand L. Initial concentrations are marked by the subscript 0.

To determine the inhibitor binding constant (K_i) of unlabelled HDAC inhibitors, a serial dilution of the respective inhibitor in assay buffer supplemented with 0.125 μM of the respective DBD probe was carried out in the aforementioned microtiter plate. HDAC8 or HDAC4, at a concentration of 0.45–0.8 μM, was added and the plates were incubated for 1 h at room temperature. Afterwards the FLT of the DBD probe was determined as stated above. The binding reaction was analysed by using a simple competition model (E+L=EL and E+I=EI) in which the inhibitor I binds to the enzyme E to form the enzyme–inhibitor complex EI, which competes with the formation of the complex EL between the DBD probe L and enzyme E [Eq. (4)]:

$$B.D. = \frac{1}{2[E]_0}\left(-\frac{K_I + \frac{K_d}{[L]_0}(K_I + [I]_0 - [E]_0)}{\frac{K_d}{[L]_0}\left(\frac{K_d}{[L]_0} + 1\right)}\right) + \sqrt{\left(\frac{K_I + \frac{K_d}{[L]_0}(K_I + [I]_0 - [E]_0)}{\frac{K_d}{[L]_0}\left(\frac{K_d}{[L]_0} + 1\right)}\right)^2 + \frac{4[E]_0 K_I [L]_0}{K_d\left(\frac{K_d}{[L]_0} + 1\right)}} \tag{4}$$

Acknowledgements

The work was supported by the Deutsche Forschungsgemeinschaft (DFG, Grant ME 3122/2-1).

Keywords: drug discovery · enzymes · fluorescent probes · high-throughput screening · hydrolases

[1] I. Hoshino, H. Matsubara, *Surg. Today* **2010**, *40*, 809–815.
[2] D.-M. Chuang, Y. Leng, Z. Marinova, H.-J. Kim, C.-T. Chiu, *Trends Neurosci.* **2009**, *32*, 591–601.
[3] K. T. Andrews, A. Haque, M. K. Jones, *Immunol. Cell Biol.* **2012**, *90*, 66–77.
[4] X.-J. Yang, E. Seto, *Nat. Rev. Mol. Cell Biol.* **2008**, *9*, 206–218.
[5] I. Gregoretti, Y.-M. Lee, H. V. Goodson, *J. Mol. Biol.* **2004**, *338*, 17–31.
[6] S. Yoon, G. H. Eom, *Chonnam Med. J.* **2016**, *52*, 1–11.
[7] P. A. Marks, R. Breslow, *Nat. Biotechnol.* **2007**, *25*, 84–90.
[8] P. A. Marks, W.-S. Xu, *J. Cell. Biochem.* **2009**, *107*, 600–608.
[9] A. Lahm, C. Paolini, M. Pallaoro, M. Nardi, P. Jones, P. Neddermann, S. Sambucini, M. J. Bottomley, P. lo Surdo, A. Carfí, U. Koch, R. de Francesco, C. Steinkühler, P. Gallinari, *Proc. Natl. Acad. Sci. USA* **2007**, *104*, 17335–17340.
[10] A. Clocchiatti, E. di Giorgio, F. Demarchi, C. Brancolini, *Cell. Signalling* **2013**, *25*, 269–276.
[11] M. Lobera, K. P. Madauss, D. T. Pohlhaus, G. Q. Wright, M. Trocha, D. R. Schmidt, E. Baloglu, R. P. Trump, M. S. Head, G. A. Hofmann, M. Murray-Thompson, B. Schwartz, S. Chakravorty, Z. Wu, P. K. Mander, L. Kruidenier, R. A. Reid, W. Burkhart, B. J. Turunen, J. X. Rong, C. Wagner, M. B. Moyer, C. Wells, X. Hong, J. T. Moore, J. D. Williams, D. Soler, S. Gosh, M. A. Nolan, *Nat. Chem. Biol.* **2013**, *9*, 319–325.
[12] P. Jones, S. Altamura, R. de Francesco, P. Gallinari, A. Lahm, P. Neddermann, M. Rowley, S. Serafini, C. Steinkühler, *Bioorg. Med. Chem. Lett.* **2008**, *18*, 1814–1819.
[13] W. Fischle, F. Dequiedt, M. J. Hendzel, M. G. Guenther, M. A. Lazar, W. Voelter, E. Verdin, *Mol. Cell.* **2002**, *9*, 45–57.
[14] A. Clocchiatti, E. di Giorgio, S. Ingrao, F.-J. Meyer-Almes, C. Tripodo, C. Brancolini, *FASEB J.* **2013**, *27*, 942–954.
[15] E. di Giorgio, A. Clocchiatti, S. Piccinin, A. Sgorbissa, G. Viviani, P. Peruzzo, S. Romeo, S. Rossi, A. P. dei Tos, R. Maestro, C. Brancolini, *Mol. Cell. Biol.* **2013**, *33*, 4473–4491.
[16] D. B. Sparrow, E. A. Miska, E. Langley, S. Reynaud-Deonauth, S. Kotecha, N. Towers, G. Spohr, T. Kouzarides, T. J. Mahun, *EMBO J.* **1999**, *18*, 5085–5098.
[17] C. H. Arrowsmith, C. Bounta, P. V. Fish, K. Lee, M. Schapira, *Nat. Rev. Drug Discovery* **2012**, *11*, 384–400.
[18] J. E. Bradner, N. West, M. L. Grachan, E. F. Greenberg, S. J. Haggarty, T. Warnow, R. Mazitschek, *Nat. Chem. Biol.* **2010**, *6*, 238–243.
[19] S. Mujtaba, L. Zeng, M. M. Zhou, *Oncogene* **2007**, *26*, 5521–5527.
[20] E. di Giorgio, E. Gagliostro, C. Brancolini, *Cell. Mol. Life Sci.* **2015**, *72*, 73–86.
[21] H. L. Fitzsimons, *Neurobiol. Learn Mem.* **2015**, *123*, 149–158.
[22] M. Mielcarek, D. Zielonka, A. Carnemolla, J. T. Marcinkowski, F. Guidez, *Front. Cell. Neurosci.* **2015**, *9*, 42.
[23] C. A. Luckhurst, P. Breccia, A. J. Stott, O. Aziz, H. L. Birch, R. Bürli, S. J. Hughes, R. E. Jarvis, M. Lamers, P. M. Leonard, K. L. Matthews, G. McAllister, S. Pollack, E. Saville-Stones, G. Wishart, D. Yates, C. Dominguez, *ACS Med. Chem. Lett.* **2016**, *7*, 34–39.
[24] M.-C. Choi, T. J. Cohen, T. Barrientos, B. Wang, M. Li, B. J. Simmons, J. S. Yang, G. A. Cox, Y. Zhao, T. P. Yao, *Mol. Cell.* **2012**, *47*, 122–132.
[25] N. A. Wolfson, C. A. Pitcairn, E. D. Sullivan, C. G. Joseph, C. A. Fierke, *Anal. Biochem.* **2014**, *456*, 61–69.
[26] D. Wegener, C. Hildmann, D. Riester, A. Schwienhorst, *Anal. Biochem.* **2003**, *321*, 202–208.
[27] F. Halley, J. Reinshagen, B. Ellinger, M. Wolf, A. L. Niles, N. J. Evans, T. A. Kirkland, J. M. Wagner, M. Jung, P. Gribbon, S. Gul, *J. Biomol. Screening* **2011**, *16*, 1227–1235.
[28] D. Riester, D. Wegener, C. Hildmann, A. Schwienhorst, *Biochem. Biophys. Res. Commun.* **2004**, *324*, 1116–1123.

[29] R. K. Singh, T. Mandal, N. Balasubramanian, G. Cook, D. Srivastava, *Anal. Biochem.* **2011**, *408*, 309 – 315.
[30] D. Riester, C. Hildmann, P- Haus, A. Galetovic, A. Schober, A. Schwienhorst, F.-J. Meyer-Almes, *Bioorg. Med. Chem. Lett.* **2009**, *19*, 3651 – 3656.
[31] C. Meyners, M. G. Baud, M. J. Fuchter, F.-J. Meyer-Almes, *J. Mol. Recognit.* **2014**, *27*, 160 – 172.
[32] L. Neumann, K. von König, D. Ullmann, *Methods Enzymol.* **2011**, *493*, 299 – 320.
[33] C. Meyners, R. Wawrzinek, A. Krämer, S. Hinz, P. Wessig, F.-J. Meyer-Almes, *Anal. Bioanal. Chem.* **2014**, *406*, 4889 – 4897.
[34] C. Micelli, G. Rastelli, *Drug Discovery Today* **2015**, *20*, 718 – 735.
[35] A. S. Madsen, H. M. Kristensen, G. Lanz, C. A. Olsen, *ChemMedChem* **2014**, *9*, 614 – 626.
[36] R. R. Frey, C. K. Wada, R. B. Garland, M. L. Curtin, M. R. Michaelides, J. Li, L. J. Pease, K. B. Glaser, P. A. Marcotte, J. J. Bouska, S. S. Murphy, S. K. Davidsen, *Bioorg. Med. Chem. Lett.* **2002**, *12*, 3443 – 3447.
[37] R. Wawrzinek, J. Ziomkowska, J. Heuveling, M. Mertens, A. Herrmann, E. Schneider, P. Wessig, *Chem. Eur. J.* **2013**, *19*, 17349 – 17357.
[38] J. A. Cisneros, E. Björklund, I. González-Gil, Y. Hu, A. Canales, F. J. Medrano, A. Romero, S. Ortega-Gutiérrez, C. J. Fowler, M. L. López-Rodríguez, *J. Med. Chem.* **2012**, *55*, 824 – 836.
[39] T. Okano, T. Sakaida, S. Eguchi, *J. Org. Chem.* **1996**, *61*, 8826 – 8830.
[40] J. Boivin, L. el Kaim, S. Z. Zard, *Tetrahedron* **1995**, *51*, 2573 – 2584.
[41] T. K. Nielsen, C. Hildmann, D. Riester, D. Wegener, A. Schwienhorst, R. Ficner, *Acta Crystallogr. Sect. F* **2007**, *63*, 270 – 273.
[42] P. Jones, M. J. Bottomley, A. Carfí, O. Cecchetti, F. Ferrigno, P. L. Surdo, J. M. Ontoria, M. Rowley, R. Scarpelli, C. Schultz-Fademrecht, C. Steinkühler, *Bioorg. Med. Chem. Lett.* **2008**, *18*, 3456 – 3461.
[43] M. P. Malakhov, M. R. Mattern, O. A. Malakhova, M. Drinker, S. D. Weeks, T. R. Butt, *J. Struct. Funct. Genomics* **2004**, *5*, 75 – 86.
[44] A. Shen, P. J. Lupardus, M. Morell, E. L. Ponder, A. M. Sadaghiani, K. C. Garcia, M. Bogyo, *PLoS One* **2009**, *4*, e8119.
[45] A. Volund, *Biometrics* **1978**, *34*, 357 – 365.

Manuscript received: November 4, 2016
Accepted Article published: December 6, 2016
Final Article published: January 30, 2017

4.2. Determining the kinetic binding mechanism of histone deacetylase inhibitors

Title:

Kinetic method for the large-scale analysis of the binding mechanism of histone deacetylase inhibitors.

Authors:

Christian Meyners, Matthias G. J. Baud, Matthew J. Fuchter, Franz-Josef Meyer-Almes

Bibliographic Data:

Analytical Biochemistry
Volume 460, Pages 39–46, September 1, 2014. DOI: 10.1016/j.ab.2014.05.014
First published online: June 2, 2014

Abstract:

Performing kinetic studies on protein ligand interactions provides important information on complex formation and dissociation. Beside kinetic parameters such as association rates and residence times, kinetic experiments also reveal insights into reaction mechanisms. Exploiting intrinsic tryptophan fluorescence a parallelized high-throughput Förster resonance energy transfer (FRET)-based reporter displacement assay with very low protein consumption was developed to enable the large-scale kinetic characterization of the binding of ligands to recombinant human histone deacetylases (HDACs) and a bacterial histone deacetylase-like amidohydrolase (HDAH) from *Bordetella/Alcaligenes*. For the binding of trichostatin A (TSA), suberoylanilide hydroxamic acid (SAHA), and two other SAHA derivatives to HDAH, two different modes of action, simple one-step binding and a two-step mechanism comprising initial binding and induced fit, were verified. In contrast to HDAH, all compounds bound to human HDAC1, HDAC6, and HDAC8 through a two-step mechanism. A quantitative view on the inhibitor-HDAC systems revealed two types of interaction, fast binding and slow dissociation. We provide arguments for the thesis that the relationship between quantitative kinetic and mechanistic information and chemical structures of compounds will serve as a valuable tool for drug optimization.

Contributions by C. Meyners:

- Produced the used proteins
- Developed and executed the kinetic binding assay
- Determined the binding mechanisms by global fit analysis
- Participated in writing of the manuscript

Analytical Biochemistry 460 (2014) 39–46

Contents lists available at ScienceDirect

Analytical Biochemistry

journal homepage: www.elsevier.com/locate/yabio

Kinetic method for the large-scale analysis of the binding mechanism of histone deacetylase inhibitors

Christian Meyners [a], Matthias G.J. Baud [b,c], Matthew J. Fuchter [b], Franz-Josef Meyer-Almes [a,*]

[a] University of Applied Sciences Darmstadt, Department of Chemical Engineering and Biotechnology, Schnittspahnstrasse 12, 64287 Darmstadt, Germany
[b] Imperial College London, Department of Chemistry, South Kensington Campus, London SW7 2AZ, UK
[c] University of Cambridge, Department of Chemistry, Lensfield Rd, CB2 1EW, UK

ARTICLE INFO

Article history:
Received 21 February 2014
Received in revised form 19 May 2014
Accepted 21 May 2014
Available online 2 June 2014

Keywords:
Binding mechanism
Kinetics
Histone deacetylases
Inhibitors
Binding assay

ABSTRACT

Performing kinetic studies on protein ligand interactions provides important information on complex formation and dissociation. Beside kinetic parameters such as association rates and residence times, kinetic experiments also reveal insights into reaction mechanisms. Exploiting intrinsic tryptophan fluorescence a parallelized high-throughput Förster resonance energy transfer (FRET)-based reporter displacement assay with very low protein consumption was developed to enable the large-scale kinetic characterization of the binding of ligands to recombinant human histone deacetylases (HDACs) and a bacterial histone deacetylase-like amidohydrolase (HDAH) from *Bordetella/Alcaligenes*. For the binding of trichostatin A (TSA), suberoylanilide hydroxamic acid (SAHA), and two other SAHA derivatives to HDAH, two different modes of action, simple one-step binding and a two-step mechanism comprising initial binding and induced fit, were verified. In contrast to HDAH, all compounds bound to human HDAC1, HDAC6, and HDAC8 through a two-step mechanism. A quantitative view on the inhibitor-HDAC systems revealed two types of interaction, fast binding and slow dissociation. We provide arguments for the thesis that the relationship between quantitative kinetic and mechanistic information and chemical structures of compounds will serve as a valuable tool for drug optimization.

The rational design of selective and highly potent drug candidates is a challenging task of medical and pharmaceutical chemistry. Traditional approaches of rational drug design are often focused only on optimizing the affinity of a compound to a target protein. This approach has been recently highlighted by Stahl et al. as the only reasonable way for structure-based drug design, since other approaches are often highly dependent on the system under investigation [1]. Classically, this gain in affinity is often achieved by adding hydrophobic moieties to the core of a lead structure, which leads to a favorable change in entropy on binding. This procedure generates disadvantages including unfavorable effects on the physiochemical properties of the ligand and a loss of target specificity, since enhanced hydrophobic effects are unspecific in nature [2].

Another approach to increase the affinity of a ligand and even more importantly its selectivity is to optimize lead structures with respect to their thermodynamic signature. Therefore, it is necessary to determine both the entropic and the enthalpic contributions to the binding process. Favorable enthalpic contributions are gained from highly system-specific effects such as hydrogen bonding and van der Waals interactions and should therefore be a major driving force in the binding process. In contrast to binding entropy, optimizing for favorable binding enthalpy is extraordinary difficult [3]. Both approaches, based exclusively on affinity or thermodynamic signature, are based on evaluation of ligand binding under equilibrium conditions in a closed system. In open systems, like the human body, ligand concentrations are fluctuating over the time- and equilibrium-based constants, such as the equilibrium dissociation constant, K_d, and are insufficient to reflect the amount of formed complexes or predict the physiological response. In order to overcome these limitations it is useful to determine the kinetic parameters of the binding reaction and add them to the drug design process [4].

One strategy focusing on optimizing kinetic parameters of ligand binding was introduced with the residence time concept by Copeland et al. in 2006 [5]. In this approach the residence time refers to the half-time of a ligand target complex and indicates how long a ligand stays in the bound state under nonequilibrium conditions. To obtain long-lasting ligand target complexes the residence time must be increased during the drug development processes. Residence times can be determined from ligand displacement

* Corresponding author. Fax: +49 6151 168404.
E-mail address: franz-josef.meyer-almes@h-da.de (F.-J. Meyer-Almes).

http://dx.doi.org/10.1016/j.ab.2014.05.014
0003-2697/

kinetics. Several methods exist for the determination of on- and off-rates of ligand binding. One of the most commonly used methods is surface plasmon resonance (SPR)[1] which involves the attachment of proteins or ligands to a surface and enables the continuous measurement of binding of unlabeled molecules to the immobilized binding partners [6]. The major limitations of this rather expensive and maintenance-intensive method are common problems to conjugate functional proteins to the surface, unspecific surface binding artifacts, and mass transport issues. In principle, enzyme activity dilution assays, e.g., using a Caliper LabChip reader, can also be employed to investigate the dissociation kinetics of ligands from their enzyme target [7]. Since such studies are rather indirect and depend on the turnover number of the enzyme, the method is not suitable for the detailed investigation of fast binding kinetics and more complicated mechanisms. In addition, the interactions between the typically artificial substrate and the test compound could impair the measuring result. Homogeneous solution phase binding assays are a useful alternative to assays employing binding to surfaces. An experimental procedure for the thermodynamic and kinetic characterization of ligand binding was suggested by Neumann et al. [8], based on displacement of a fluorescent probe on binding of a ligand, which causes a change in the measured fluorescence intensity. A recent example to assess structure–kinetics relationships with this method was reported by Schneider et al. [9]. The particular fluorescent probe employed in these studies was not specified however. One major requirement for the setup of a reporter displacement assay is that the designed probe exhibits a faster dissociation rate than the association rate of the ligand. Beside determination of residence times a kinetic characterization can be used to analyze binding mechanisms in more detail. The simplest and most often assumed binding mechanism is a one-step association and dissociation model. In many cases binding reactions are more complex and include target isomerization, conformational selection, multiple binding sites, or modes. Compounds, whose binding mechanism includes target isomerisation, often show prolonged residence times. The determination of the corresponding binding mechanism is believed to bear great potential as an additional criterion to categorize and select compounds for further optimization in a relatively early phase of drug development [4].

In this study a previously reported FRET-based reporter displacement assay, which is suitable for thermodynamic characterization of histone deacetylase inhibitors (HDACi), is adapted to allow for the kinetic characterization of HDACi [10]. HDACi have been developed to target different types of cancer [11]. As first-in-class drugs suberoylanilide hydroxamic acid (SAHA) and romidepsin have been approved by U.S. Food and Drug Administration for the treatment of cutaneous T-cell lymphoma [12]. Particularly SAHA is rather unselective and inhibits most isoforms of Zn^{2+}-dependent histone deacetylases (HDACs). Zn^{2+}-dependent HDACs are divided into class I (HDAC1, 2, 3, and 8), class IIa (HDAC4, 5, 7, and 9), class IIb (HDAC6 and 10), and class IV (HDAC11). Class III consists of 7 isoforms, the sirtuins, which require NAD^+ as a cofactor for their catalytic activity instead of Zn^{2+} [13]. Together with their opponents, the histone acetyl transferases (HATs), HDACs are mostly recognized for their roles in cellular differentiation, proliferation, and apoptosis by altering genetic expression through determining the acetylation status of lysine residues of histones [14]. Beside histones a number of proteins, including cancer-relevant proteins like p53 and other cytosolic proteins such as HSP90 and α-tubulin, have been identified as substrates of HDACs, which exemplifies the involvement of HDACs in the regulation of many cellular processes [15,16]. The role of HDACs in different cancer types has been intensively investigated and reviewed over the last decade [11,17]. Consequently, efforts in the development of HDACi have been increased in order to generate more specific drugs, which are hypothesized to cause fewer side effects such as fatigue, nausea, dehydration, diarrhea, thrombocytopenia, or electrocardiogram changes [12,18].

Beside eukaryotic HDACs a number of bacterial homologues, such as the histone deacetylase-like protein (HDLP) form *Aquifex aeolicus* and the histone deacetylase-like amido-hydrolase (HDAH) from *Bordetella*/*Alcaligenes*, have been described [19,20]. HDAH is structurally closely related to HDACs and shares an identity of 35% with the second catalytical domain of human HDAC6 [21]. Several experimental results, including similar substrate and inhibitor selectivities, prove that HDAH serves as a good model for HDAC6 [22,23]. Beyond the use as model enzymes for human HDACs several bacterial and protozoan parasite deacetylases are currently investigated as protein targets for the treatment of bacterial infections or parasitic diseases [24–27].

The results of this study provide arguments and evidence that kinetic data are important for an understanding of the mode of action between ligands and proteins and for differentiating between compounds having different association rates and residence times on target proteins with occasionally undistinguishable equilibrium binding affinities.

Materials and methods

All chemicals if not stated otherwise were obtained from Sigma/Aldrich (USA), AppliChem (Germany), Roth (Germany), and Merck (Germany). Boc-Lys(Ac)-AMC and Boc-Lys(trifluoracetyl)-AMC were obtained from Bachem (Switzerland). SAHA and TSA were purchased from Cayman Chemical (USA). LU210 and SATFMK were prepared as described elsewhere [28,29]. Dansyl-conjugate probes with varying spacer lengths were synthesized as described previously [10]. HDAC1 and 6 were purchased from BPS Bioscience (USA). His-tagged FB188 HDAH and His-tagged recombinant HDAC8 were prepared as described elsewhere [20,30]. The assay buffer consisted of 250 mM sodium chloride, 15 mM Tris–HCl, 0.001% Pluronic F-167, and 50 mM potassium phosphate at pH 8.0. For experiments with FB188 HDAH the assay buffer was supplemented with 250 μM EDTA. All reactions were performed in black half-area 96-well microplates (Greiner Bio-One, Germany). The obtained data were fitted using Prism 5 (GraphPad Software, USA) or Gepasi 3.3 [31].

Enzyme activity assay

The determination of the inhibitory effect of all SAHA derivatives on the catalytic activity of HDAC1, HDAC6, and HDAC8 was carried out by an enzyme activity assay, which was reported earlier by Wegener et al. [32], In these experiments a serial dilution of the respective compound was incubated with 1 nM of the respective HDAC for 30 min at 25 °C in assay buffer. The catalytic reaction was initiated by the addition of 40 μM Boc-Lys(Ac)-AMC for HDAC1 and 6 or 20 μM Boc-Lys(trifluoracetyl)-AMC for HDAC8. After an incubation for 60 min at 25 °C the reaction was stopped by the addition of 40 μM SAHA and the deacetylated substrate was converted into a fluorescent product by the addition of 0.5 mg/ml trypsin. The release of AMC was correlated to the enzyme activity. From the obtained data points the K_d values of

[1] *Abbreviations used:* AMC, 7-amino-4-methylcoumarin; Dansyl, 5-(dimethylamino)naphthalene-1-sulfonyl; FRET, fluorescence resonance energy transfer; HDAH, histone deacetylase-like amidohydrolase from Bordetella/Alcaligenes; HDAC, histone deacetylase; K_d value, dissociation constant; LU210, 2,2,3,3,4,4,5,5,6,6,7,7-dodecafluorooctanedioic acid hydroxyamide phenyl-amide; SAHA, suberoylanilide hydroxamic acid; SATFMK, suberoylanilide trifluoromethylketone; SPR, surface plasmon resonance; TSA, trichostatin A.

the respective compounds were calculated by using a competitive binding model, which was implemented in Prism 5.

FRET-based reporter displacement assay

To determine the dissociation rate of the dansyl-conjugate probes a solution of 0.4 μM HDAC8, 0.1 μM HDAH, HDAC1 or 0.05 μM HDAC6, and 5 μM of one of the respective dansyl-conjugate probes **1–6** in assay buffer was added to a microtiter plate and tempered to 25 °C. After an incubation time of 30 min, when equilibrium was achieved, the displacement of the dansyl-conjugate probe was initiated by the addition of 500 μM SAHA in assay buffer. The final assay volume was 100 μl. The displacement kinetic was followed in a fluorescence microplate reader (BMG Labtech, PHERAstar FS) using a 280 nm excitation filter and a 530 nm emission filter. The microtiter plate was shaken at 300 rpm for 5 s before measuring. Data points were taken every 3 to 7 s until the mean fluorescence signal changed less than 5% over a time period of 60 s, indicating chemical equilibrium. The obtained data points were fitted to a single phase exponential decay model.

In cases in which the dissociation rate was above the detection limit of 0.1 s^{-1} the dissociation rate was determined by using a stopped-flow machine with a dead time of 1.6 ms (Biologic, SFM-3000). In these experiments 0.4 μM HDAC8, 0.1 μM HDAC1, or 0.05 μM HDAC6 were premixed with 5 μM of the respective dansyl-conjugate probe and incubated for 30 min at 25 °C. The dissociation of the enzyme–dansyl-conjugate complex was initiated by a rapid addition of 500 μM SAHA in assay buffer. The decay in the fluorescence was followed by using an excitation wavelength of 295 nm and a 515 nm cutoff filter. The obtained data points were fitted to a single phase exponential decay model.

The kinetic properties of the binding of unlabeled ligands were investigated further by determining the concentration dependence of the dissociation rate constant of the enzyme–dansyl-conjugate complex. A serial dilution of the corresponding ligand in assay buffer complemented with 5 μM of the dansyl-conjugate probe (to exclude a confounding dissociation effect due to dilution) was placed in a microtiter plate and tempered to 25 °C. The reaction was started by a rapid addition of a pre tempered solution of 0.05 or 0.5 μM HDAH, 0.1 μM HDAC1, 0.4 μM HDAC8 or 0.05 μM HDAC6, and 5 μM of the dansyl-conjugate probe in assay buffer to each well. The final assay volume was 100 μl. The change in fluorescence was observed using the same settings as stated above. The obtained data points were fitted to a single phase exponential decay model or subjected to global fit analysis.

Calculation of the kinetic rate constants

For a one-step binding and dissociation mechanism, the kinetic rate constants and the equilibrium dissociation constants of the binding of unlabeled ligands to HDAH, HDAC1, or HDAC6 were calculated from the pseudo-first-order rate constants, which were obtained from the FRET-based reporter displacement assay. The ligand concentration, $[L]_0$, was at least 5× bigger than the enzyme concentration, [E]. The pseudo-first-order rate constants, k_{obs}, were then plotted against $[L]_0$, and fitted to one of the following binding mechanisms.

The first mechanism is a simple reversible one-step binding mechanism, where the ligand, *L*, binds to an enzyme, *E*, to form a bimolecular complex, *EL*,

$$E + L \underset{k_2}{\overset{k_1}{\rightleftarrows}} EL$$

$$k_{obs} = k_1[L]_0 - k_2, \tag{1}$$

where k_{obs} is the observed pseudo-first-order rate constant, k_1 is the association rate constant, $[L]_0$ is the total ligand concentration, and k_2 is the dissociation rate constant. The equilibrium dissociation constant, K_d, is calculated from the ratio of the rate constants:

$$k_{off} = k_2 \tag{2}$$

$$K_d = \frac{k_2}{K_1}. \tag{3}$$

The second binding mechanism comprises two steps involving an induced fit. In the first step the initial complex, *EL*, is formed by a bimolecular interaction of ligand *L* with the enzyme, *E*. The second step is a unimolecular conformational change to yield a more stable complex, *EL**,

$$E + L \underset{k_2}{\overset{k_1}{\rightleftarrows}} EL \underset{k_2}{\overset{k_1}{\rightleftarrows}} EL^*, \tag{4}$$

where k_1 is the association rate and k_2 the dissociation rate of the initial complex, k_3 and k_4 are the rate constants for the transformation between the intermediate complex, *EL*, and the final complex, *EL**. For the second mechanism the kinetic constants were determined from global fit analysis of raw kinetic time courses. The model for the two-step binding mechanism was therefore implemented in Gepasi 3.3 and all displacement kinetic curves of an experimental series with varying inhibitor concentrations were analyzed simultaneously using a genetic and a multistart Levenberg-Marquardt algorithm [33]. From the fitted rate constants the observed overall dissociation rate, k_{off}, and the overall equilibrium dissociation constant, K_d, were calculated according to [4]

$$k_{off} = \frac{k_2 \times k_4}{k_a + K_2 + k_4} \tag{5}$$

$$K_d = \frac{k_2}{k_1 + k_1 \times \frac{k_3}{k_4}}. \tag{6}$$

The residence time for both mechanisms calculates to

$$residence\ time = \frac{1}{k_{off}} \tag{7}$$

Results and discussion

Dissociation rates of dansyl ligand probes

For the development of a reporter displacement assay suitable for the kinetic characterization of unlabeled ligands, it was necessary to determine the off-rates of the synthesized dansyl-conjugate probes from complexes with HDAH, HDAC1, HDAC6 and HDAC8 (Fig. 1). For a time-resolved measurement of the binding of the dansyl-conjugate probes, the previously reported FRET was exploited by measuring the change in the fluorescence intensity at 530 nm (Fig. 2) [7]. Applying a 100-fold molar excess of SAHA to a preformed complex of the respective dansyl-conjugate and HDAH, HDAC1, or HDAC6 enabled determination of the rate-limiting dissociation rate of the dansyl-conjugates from displacement kinetics. For binding to HDAH the dissociation rate showed a spacer length-dependent relationship with values ranging from $(20 \pm 1) \times 10^{-3}\ s^{-1}$ for **2** down to $(1.47 \pm 0.03) \times 10^{-3}\ s^{-1}$ for **6** (Table 1). A similar ranking was previously observed for the K_d values of the binding of the respective dansyl hydroxamates to HDAH [10]. The displacement of the dansyl-conjugates from a complex with HDAC1, HDAC6, or HDAC8 by SAHA resulted in a time-dependent decrease of the fluorescence intensity at 525 nm. The determined dissociation rates of the binding of **3**–**6** to HDAC1, HDAC6, and HDAC8 are summarized in Table 1. Most dissociation rates

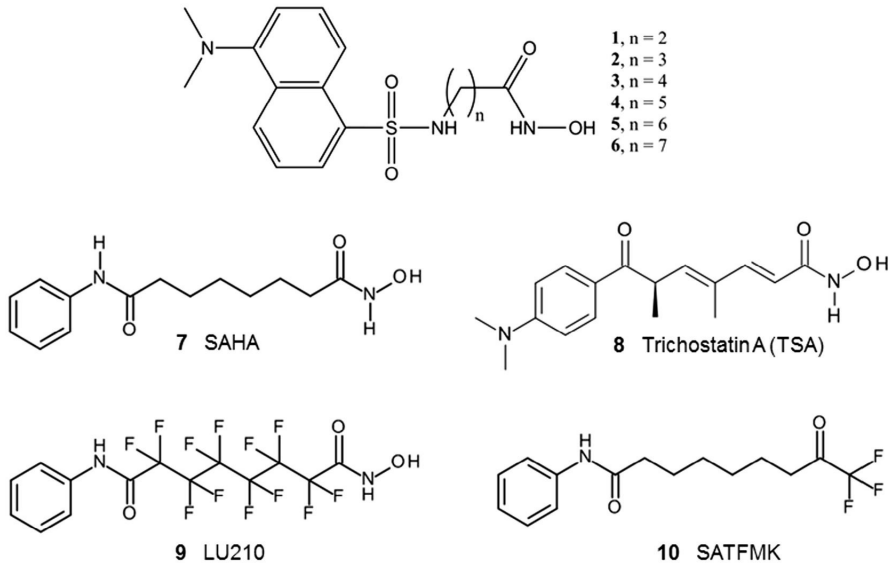

Fig.1. Structures of the dansyl-conjugate probes and HDAC inhibitors used.

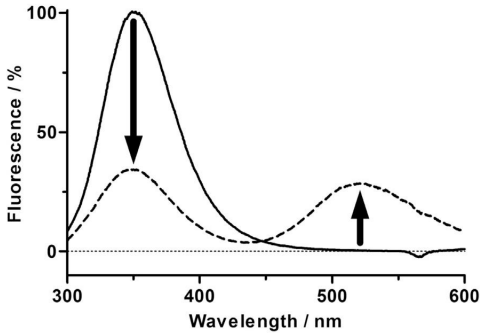

Fig.2. Fluorescence spectra of 100 nM HDAH in assay buffer in the absence (solid line) and in the presence (dashed line) of 12.8 μM of **4** at 25 °C. The samples were excited at 285 nm. The obtained fluorescence intensities were corrected for contributions of the dansyl-conjugate, normalized with respect to the maximal fluorescence, and plotted against the wavelength. The increase of the fluorescence emission at 525 nm and the simultaneous decrease of the fluorescence at 350 nm on binding of **4** to HDAH were indicative for Förster resonance energy transfer. The perturbation around 570 nm is due to suboptimal correction of second-order diffraction at the excitation grating monochromator.

were determined using the standard microtiter plate assay. The rapid dissociation rates above 0.1 s^{-1} were measured using a stopped-flow instrument. The fast dissociating dansyl-conjugates were perfectly suited for investigating the slower binding kinetics of unlabeled ligands.

Kinetics and binding mechanisms of unlabeled ligands to HDAH

The determination of the binding kinetics and mechanism of protein–ligand interactions has been considered to contribute valuable information for the design and optimization of inhibitors. Recently, Swinney, Copeland, and others emphasized that a more quantitative understanding of the kinetics and mechanism of binding interaction is important for the identification of drugs with an advantageous therapeutic index [4,34,35]. In this respect, the concept of prolonged residence time has been discussed as a useful strategy for developing improved lead compounds [4,36,37]. Although several cases were reported, where residence time correlates with *in vivo* efficacy [38–40], the concept cannot be applied to all cases and depends on the physiological context. For example, long-lasting drug action on ion channels could be toxic, and some drugs, e.g., memantine, an inhibitor of NMDA receptor, reduce toxicity by a fast dissociation rate [41]. All these examples underline the impact of a more detailed mechanistic investigation of protein–ligand interactions and inspired us to initiate this study on the binding mechanisms of four structurally similar HDACi to HDAC1 and HDAC6, as representatives of HDAC classes I and II, as well as HDAC8 which stands at the interface between class I and class II HDACs but is still assigned to class I. Displacement experiments with unlabeled ligands and a preformed HDAH–dansyl-conjugate complex resulted in a time- and concentration-dependent decrease of the FRET signal (Figs. 3a, 4, S1 in Supplemental Data). For the kinetic characterization of the binding of the fast ligands TSA and SAHA the HDAH concentration was set to 50 nM to maintain pseudo-first-order conditions at low ligand concentrations. Thereby, the usage of the dansyl-conjugate **2** provided a good compromise between a fast dissociation rate and a good signal amplitude. For experiments with the slow binding ligand LU210 an HDAH concentration of 500 nM was sufficient to obtain a good signal-noise ratio with 5 μM of the dansyl-conjugate **3**. Plotting of the calculated rate constants, k_{obs}, against the concentration of TSA and SAHA revealed in both cases linear dependencies (Fig. 3b). For the binding of SAHA to HDAH an association rate constant, k_1 value, of $(12 \pm 2) \times 10^3$ M^{-1} s^{-1} and a k_2 value of $(4 \pm 1) \times 10^{-3}$ s^{-1} were calculated (Table 2). The binding of TSA to HDAH occurred with similar kinetics with a k_1 value of $(6 \pm 0.9) \times 10^3$ M^{-1} s^{-1} and a k_2 value of $(5.1 \pm 0.5) \times 10^{-3}$ s^{-1}. The corresponding K_d values of 0.9 ± 0.2 μM for TSA and of 0.4 ± 0.1 μM for SAHA agreed with previous determined K_d values [23,42]. The residence times for the binding of SAHA and TSA were calculated according to Eqs. (2) and (6) to be 4 ± 1 and 3.3 ± 0.3 min, respectively. An analysis of the residual plots of the

Table 1
Apparent K_d values calculated from equilibrium titration experiments and dissociation rates of the dansyl-conjugates from ligand–protein complexes with HDAH, HDAC1, HDAC6, and HDAC8 in assay buffer at 25 °C.

Dansyl-conjugate	K_d value/μM				Dissociation rate/(10^{-3} s^{-1})			
	HDAH[a]	HDAC1[b]	HDAC6[b]	HDAC8[b]	HDAH	HDAC1	HDAC6	HDAC8
2	>20	1.3 ± 0.1	2.2 ± 0.2	1.4 ± 0.5	20 ± 1	1050 ± 6	125 ± 2	1688 ± 20
3	5.4 ± 0.7	0.12 ± 0.03	0.29 ± 0.03	1.1 ± 0.2	14.9 ± 0.3	31 ± 4	5.7 ± 0.5	1267 ± 10
4	0.96 ± 0.05	0.09 ± 0.01	0.28 ± 0.03	0.41 ± 0.06	4.73 ± 0.03	27 ± 3	6.5 ± 0.6	952 ± 5
5	0.30 ± 0.02	0.13 ± 0.03	0.16 ± 0.04	0.19 ± 0.02	3.99 ± 0.04	35 ± 6	3.9 ± 0.5	9 ± 1
6	0.059 ± 0.007	0.11 ± 0.01	0.057 ± 0.007	0.14 ± 0.01	1.47 ± 0.03	26 ± 4	5.1 ± 0.6	9.8 ± 0.7

The dissociation rates were determined in displacement experiments, where 500 μM SAHA was added to an equilibrated solution of 100 nM HDAH, 100 nM HDAC1 or 50 nM HDAC6, and 5 μM of the respective dansyl-conjugate.
[a] K_d values were determined previously [10].
[b] K_d values were calculated from previously determined IC_{50} values [10] according to Cheng and Prusoff [52]. The substrate concentration was 40 μM for HDAC1 and HDAC6 and 20 μM for HDAC8. The K_m values were determined previously to be 78 μM for HDAC1, 30 μM for HDAC8, and 99 μM for HDAC6 [28].

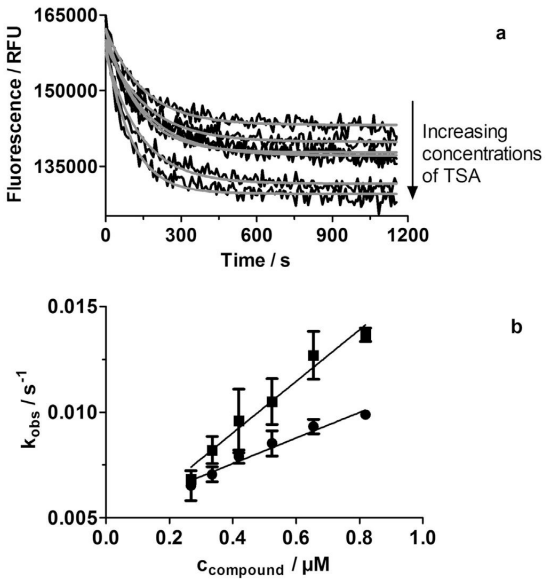

Fig.3. Association kinetics of the binding of TSA to HDAH and observed pseudo-first-order rate constants for the binding of SAHA and TSA to HDAH. (a) The binding kinetics of TSA to HDAH was started by adding an equilibrated solution of 50 nM HDAH and 5 μM of the dansyl-conjugate **2** to different concentrations of the compounds in assay buffer at 25 °C as described under Materials and methods. The fluorescence intensity at 530 nm is plotted against the time. The obtained curves were fitted to a single phase exponential decay model, whose least-square fits are represented by the continuous lines. (b) The observed pseudo-first-order rate constants of the binding of SAHA (squares) and TSA (dots) to HDAH are plotted against the concentration of the respective compound. All data points are means of triplicates and the standard errors are displayed as error bars. The observed pseudo-first-order rate constants were fitted to a one-step binding and dissociation mechanism as described under Materials and methods (Eq. (1)). The calculated kinetic rate constants are summarized in Table 2.

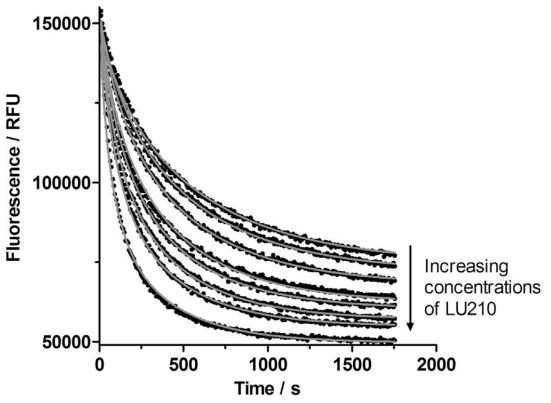

Fig.4. Association kinetics of LU210 to HDAH in assay buffer at 25 °C. The association kinetics were measured using a FRET-based reporter displacement assay as described under Materials and methods with 0.5 μM HDAH and 5 μM of the dansyl-conjugate **3** in assay buffer. Concentrations of LU210 ranged from 8.4 to 50 μM. The obtained fluorescence signal at 530 nm is plotted against the time. The obtained kinetics were fitted globally to a two-step binding mechanism (mechanism 2 under Materials and methods). The least-square fits are represented by the smooth curves. The calculated kinetic rate constants are summarized in Table 2.

displacement kinetics with LU210 showed that a single phase exponential decay model was insufficient to describe the obtained curves and a two phase exponential decay model had to be applied instead (Fig. S2 in Supplemental Data). This indicated at first glance a more complex mechanism than a simple one-step binding and the obtained displacement kinetics were therefore analyzed on the basis of mechanism 2 using a global fit to all kinetic time courses of a set of binding experiments with 8 different LU210 concentrations (Fig. 4). The global fit analysis for a two-step binding and dissociation mechanism (mechanism 2) revealed a good agreement between all experimental time courses and the corresponding fitting curves. The initial complex formation between LU210 and HDAH occurred at rate constants calculated to be $k_1 = (63 \pm 30) \times 10^3\ M^{-1}\ s^{-1}$ and $k_2 = 1.437 \pm 0.7\ s^{-1}$, which resulted in a microscopic K_d value of 228 μM for the initial complex formation. The rate constants for the unimolecular conformational change were calculated to be $k_3 = (7.91 \pm 0.08) \times 10^{-3}\ s^{-1}$ and $k_4 = (0.525 \pm 0.002) \times 10^{-3}\ s^{-1}$, respectively. Taken together the rate constants revealed an apparent K_d value of 1.4 ± 0.2 μM for the overall complex formation. The residence time was calculated to be 31.9 ± 0.1 min. The determined K_d value for the overall complex formation was comparable to an experimental apparent K_d value in an enzyme activity assay, which was previously reported as 0.51 ± 0.02 μM at a slightly higher temperature of 30 °C [28]. This reasonable agreement in the apparent K_d values and the presence of the multiexponential association kinetics of LU210 to HDAH confirmed that the stated two-step binding and dissociation model is not only necessary but also sufficient to explain all kinetic and enzyme activity data. The binding of the electrophilic trifluoromethylketone SATFMK to HDAH showed a kinetics similar to that of LU210. Unlike SAHA and TSA but characteristic for LU210 and SATFMK was the fast initial binding process which hampered the precise determination of the absolute values of the rate

Table 2
Kinetic constants of the binding of SAHA, TSA, and LU210 to HDAH, HDAC1, HDAC6, and HDAC8 at 25 °C.

Enzyme	Compound	$k_1/(10^3\ M^{-1}\ s^{-1})$	$k_2/(10^{-3}\ s^{-1})$	$k_3/(10^{-3}\ s^{-1})$	$k_4/(10^{-3}\ s^{-1})$	K_d/μM	Residence time/min
HDAH	SAHA	12 ± 2	4 ± 1	–	–	0.4 ± 0.1	4 ± 1
	TSA	6.0 ± 0.9	5.1 ± 0.5	–	–	0.9 ± 0.2	3.3 ± 0.3
	LU210	63 ± 30	1437 ± 700	7.91 ± 0.08	0.525 ± 0.002	1.4 ± 0.2	31.9 ± 0.1
	SATFMK	51 ± 57	1500 ± 1600	4.0 ± 0.1	0.41 ± 0.01	2.7 ± 0.4	40.8 ± 0.5
HDAC1	SAHA	826 ± 1	64 ± 1	13.8 ± 0.2	3.16 ± 0.02	0.015 ± 0.004	6.67 ± 0.05[a]
	TSA	139 ± 7	59 ± 16	153 ± 18	2.2 ± 0.3	0.006 ± 0.001	27 ± 7
	LU210	576 ± 131	407 ± 63	8 ± 2	9.1 ± 0.8	0.37 ± 0.07	1.9 ± 0.2[a]
	SATFMK	292 ± 29	315 ± 32	19 ± 1	3.63 ± 0.05	0.17 ± 0.02	4.93 ± 0.08
HDAC6	SAHA	542 ± 12	159 ± 3	13.7 ± 0.2	4.81 ± 0.03	0.076 ± 0.008	3.87 ± 0.02[a]
	TSA	162 ± 1	44.9 ± 0.4	8.8 ± 0.1	0.40 ± 0.01	0.012 ± 0.002	50.3 ± 0.7
	LU210	213 ± 127	251 ± 140	17 ± 2	2.4 ± 0.3	0.14 ± 0.08	7 ± 1
	SATFMK	88 ± 3	93 ± 2	4.7 ± 0.1	0.84 ± 0.01	0.16 ± 0.02	20.9 ± 0.3
HDAC8	SAHA	943 ± 82	202 ± 13	9.4 ± 0.9	21 ± 1	0.15 ± 0.02	0.89 ± 0.04[a]
	TSA	2352 ± 130	194 ± 6	18.2 ± 0.8	22.1 ± 0.4	0.045 ± 0.008	0.90 ± 0.02[a]
	LU210	685 ± 167	344 ± 63	29 ± 6	31 ± 2	0.26 ± 0.06	0.63 ± 0.04[a]
	SATFMK	29.77 ± 0.06	5.49 ± 0.04	11.38 ± 0.08	0.355 ± 0.002	0.0056 ± 0.0003	147 ± 1

[a] Indicated dissociation curves would exhibit a biphasic behavior. The indicated residence time describes the rate-limiting dissociation.

constants k_1 and k_2 of the first step for these compounds. However, the remaining rate constants as well as the ratio k_2/k_1 were accurately calculated using the global fit of the kinetic time courses (Table 2). The observed striking differences of the binding kinetics of very similar inhibitor structures underline the importance of kinetic studies for a detailed understanding of the mode of ligand–protein interactions. While the affinities of the hydroxamate inhibitors and the trifluoromethylketone were within the same order of magnitude, the perfluoration of the spacer of SAHA resulted in a more complex binding mechanism and a dramatically increased residence time from 4 to 31.9 min. The postulated induced fit for binding of LU210 is supposed to reflect the larger steric requirements of the perfluorated alkyl linker chain compared with the alkyl chain of SAHA which requires pronounced structural rearrangement of the rather narrow HDAH binding pocket to accommodate LU210 (protein data bank: 1ZZ1).The replacement of the hydroxamic acid chelating group of SAHA by a trifluoromethylketone moiety also resulted in the change of the reaction mechanism involving a second conformational change to stabilize initially bound SATFMK. Interestingly, both fluorination of the alkyl chain of SAHA and the exchange of the chelating group lead to the more complex two-step binding model with induced fit. The subsequent conformational stabilization of the ligand–HDAH complex seemed to be key for the about 10 times increased residence times of LU210 and SATFMK.

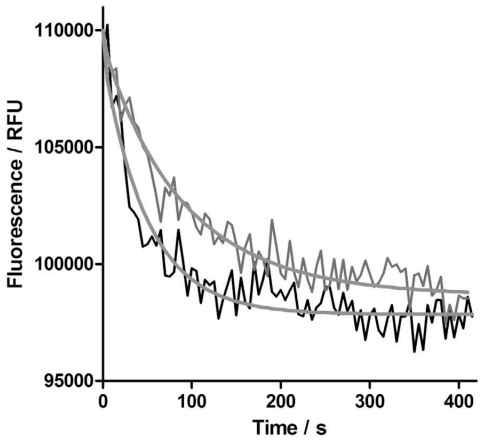

Fig.5. Association kinetics of the binding of 0.42 (gray curve) and 1.3 μM (black curve) TSA to HDAC1 at 25 °C. The association kinetics were determined using a FRET-based reporter displacement assay as described under Materials and methods with 0.1 μM HDAC1 and 5 μM of the dansyl-conjugate **2** in assay buffer. The obtained fluorescence signal at 530 nm is plotted against the time. The raw time courses were subjected to a global fit to a two-step binding mechanism (mechanism 2). The fit curves are represented by smooth lines. The kinetic rate constants for the binding mechanism are summarized in Table 2.

Binding of unlabeled ligands to human HDACs 1, 6, and 8

In contrast to the different observed binding modes to the bacterial HDAC homologue HDAH, all unlabeled HDAC inhibitors displayed the same two-step binding mechanism and stronger binding affinities to recombinant human HDACs. This binding model is in agreement with recent kinetic studies about the binding of SAHA and TSA to HDAC8 [43] as well as the binding of SAHA and an aminobenzamide inhibitor to HDAC1 [44]. In addition, the postulated conformational change of the initial complex in the two-step binding model would be consistent with recent modeling studies of the active site of HDAC8, indicating flexible binding surfaces and induced fit [45]. Our parallelized assay format enabled a broader systematic study of structurally closely related HDAC inhibitors to dissect the kinetic and mechanistic impact of structural changes at the chelating group and the alkyl spacer of the well-known HDAC inhibitor SAHA on the formation of the ligand–enzyme complex. Binding of all unlabeled inhibitors to HDAC1, HDAC6, or HDAC8 resulted in a time- and concentration-dependent decrease of the FRET signal (Figs. 5 and S4–S15 in Supplemental Data). To make the global fitting procedure more robust against compensation effects of the varied parameters, K_d values were calculated from enzyme activity assays and held fixed throughout the fitting procedure. This practice was key for the accurate calculation of the desired rate constants from a global fit of the corresponding data set comprising displacement kinetics employing different concentrations of unlabeled ligand. The determined K_d values for TSA and SAHA were in reasonable agreement with previously published values of different research groups [46–48]. The perfect agreement between the experimental data and the two-step binding model, when using the independently determined K_d value, validated the proposed binding mechanism. The only compound that showed a discrepancy between the K_d value calculated from an enzyme activity assay and the K_d value of the binding assay was LU210. A possible explanation for that compound includes a possible interaction with

the bound dansyl ligand probe, thereby quenching its fluorescence or a second contact area for LU210 on the protein surface where the compound interferes stronger with the binding of the dansyl probe than with the interaction between substrate and enzyme in the activity assay. Nevertheless, if the K_d value was not constrained during the global fitting procedure, the data sets for LU210 could also be well described by the obtained two-step kinetic model with small errors for the rate constants k_3, k_4 of the induced fit and moderate errors for the rate constants k_1 and k_2 of the first association step. Despite some relatively noisy data sets, e.g., the binding of TSA to HDAC1 or HDAC6 (Fig. 5), the unequivocal necessity of the two-step binding model versus the one-stop model was proven using the Akaike information criterion [49], taking into account the goodness of fit and the differing complexity of the compared models. This analysis revealed a clear preference for the two-step model to be the most suited model to describe all experimental data for binding to human recombinant HDACs. When looking at the microscopic rate constants for the initial recognition and the following induced fit step of the two-step protein–ligand binding mechanism, two major types of HDAC inhibitors, fast binding and slowly dissociating compounds, became apparent (Table 2). If the conformational change of the second step contributes significantly to binding (high ratio of k_3/k_4), the residence time is significantly increased, e.g., for the binding partners TSA/HDAC1, TSA/HDAC6, or SATFMK/HDAC8. The longest observed residence time of 147 min was observed for the interaction between SATFMK and HDAC8. In the cases of slow dissociating compounds, the bimolecular association rate constant k_1 was smaller compared with ligands having a shorter residence time. For fast binding compounds, such as LU210 to HDAC1, SAHA to HDAC8, or TSA to HDAC8, the overall binding affinities resulted mainly from the first bimolecular binding step. The ranking of the K_d values, residence times, and the kinetic rate constants for the binding of unlabeled compounds to HDAC1 and HDAC6 was comparable with TSA being the most potent inhibitor with the largest residence time and SAHA as the fastest binder with relatively short residence time. The differences between fast binders and slow dissociating compounds became particularly visible for HDAC8: TSA exhibits the highest observed bimolecular association rate of $k_1 = (2.35 \pm 0.13) \times 10^6\ M^{-1}\ s^{-1}$ and a very short residence time of 0.90 ± 0.02 min. In contrast, the association rate constant of SATFMK is about two orders of magnitude smaller and the residence time more than 2 orders of magnitude larger compared with TSA. When discussing the impact of kinetics on selecting compounds in the early phase of drug discovery, the concept of residence time introduced by Copeland received most attention [36]. It was expected that inhibitors with slow-binding and dissociating characteristics would allow for a less intensive dosing and possibly fewer associated toxicities. This assumption is supported for HDAC inhibitors by cell-based *in vitro* as well as *in vivo* data. Kral et al. clearly demonstrated that the application of the fast binding SAHA to HCT116 cells caused a fast induction of apoptosis and a delayed response in case of the slow binding and dissociating HDAC inhibitor DW2a [44]. After washout, the SAHA-induced effects were rapidly reversed, whereas DW2a was much more persistent. In the same study, xenograft tumor-bearing mice were treated with SAHA and DW2a and both drugs showed similar efficacy, although dosing of DW2a was applied much less frequently. In addition, compared with SAHA, DW2a displayed a prolonged effect on histone deacetylation. These effects have also been observed *in vivo* applying a derivative of DW2a [50]. However, long-lasting drug action might induce on-target toxicity effects on other target proteins as is known for, e.g., ion channels [37] or dopamine D_2 receptors [51], where fast dissociating drugs are more advantageous. Very recently, association kinetics has gained more attention in determining the efficacy of drugs. Fast binding compounds should better compete with endogenous substrates and ligands and generate an earlier onset of the desired pharmacological effect. Therefore, a fast binding drug would be better suited to counteract an emergency. Considering the diverging known relationships between kinetics and biological efficacy, it depends on the physiological context, whether a fast binding compound or a slowly or fast dissociating compounds would be desired for the target protein of interest. We are convinced that the biochemical analysis of binding kinetics and the elucidation of the corresponding binding mechanism provide a valuable additional parameter to select the most promising lead compounds to be taken further in the drug development process. In light of many different mechanisms of action, it is highly desirable, to define a target not only as the macromolecule where a ligand binds, but also in terms of its kinetic mechanism and how the initial binding is coupled to the biological response. Once the relationship between kinetics and efficacy is understood, structure–kinetics relationship analysis will streamline the decision process in drug discovery.

Conclusion

The reported kinetic assay method enables the elucidation of the binding mechanism and provides deep insight into the elementary steps of ligand–protein interactions. The procedure is straightforward, consumes only small amounts of protein, and enables the high-throughput characterization of the binding kinetics of many test compounds in parallel on microtiter plates. The assay provides not only the measurement of residence time as one important kinetic parameter but also a detailed analysis of the binding mechanism of unlabeled inhibitors. Using the example of a bacterial homolog of human histone deacetylases, HDAH, it was demonstrated that four structurally closely related inhibitors with similar apparent binding affinities revealed not only different microscopic rate constants but also different binding mechanisms. The classical approach to the assessment of potential drug candidates merely based on affinity constants would have overlooked these dramatic kinetic and mechanistic differences. All SAHA homologues displayed a two-step binding mechanism to human HDAC1, HDAC6, and HDAC8. A closer look at the rate constants revealed two major types of interactions between inhibitors and HDACs: fast association and slow dissociation. The presented method should also be expandable to homolog enzymes from bacteria, protozoan parasites, fungi, or other organisms. We hypothesize that high density and throughput kinetic assays like the presented displacement assay will serve as a valuable tools to guide the selection of the best compounds for further drug optimization. But to take maximal advantage of a structure–kinetics relationship for many compounds, it is desirable to understand the mechanism of initial binding to the physiological target and its transduction into the desired biological response.

Acknowledgments

This work has been supported by a grant of the Landesoffensive zur Entwicklung Wissenschaftlich-oekonomischer Exzellenz (LOEWE Soft Control) to F.J. Meyer-Almes and by the Association for International Cancer Research (AICR Grant 08-0407) to M.J. Fuchter. The excellent support of Michael Schröder is gratefully acknowledged.

Appendix A. Supplementary data

Supplementary data associated with this article can be found, in the online version, at http://dx.doi.org/10.1016/j.ab.2014.05.014.

References

[1] C. Bissantz, B. Kuhn, M. Stahl, A medicinal chemist's guide to molecular interactions, J. Med. Chem. 53 (2010) 5061–5084.
[2] J.E. Ladbury, G. Klebe, E. Freire, Adding calorimetric data to decision making in lead discovery: a hot tip, Nat. Rev. Drug Discov. 9 (2010) 23–27.
[3] J.B. Chaires, Calorimetry and thermodynamics in drug design, Annu. Rev. Biophys. 37 (2008) 135–151.
[4] P.J. Tummino, R.A. Copeland, Residence time of receptor–ligand complexes and its effect on biological function, Biochemistry 47 (2008) 5481–5492.
[5] R.A. Copeland, D.L. Pompliano, T.D. Meek, Drug-target residence time and its implications for lead optimization, Nat. Rev. Drug Discov. 5 (2006) 730–739.
[6] D.G. Myszka, R.L. Rich, Implementing surface plasmon resonance biosensors in drug discovery, Pharm. Sci. Technol. Today 3 (2000) 310–317.
[7] R.A. Copeland, Evaluation of Enzyme Inhibitors in Drug Discovery: A Guide for Medicinal Chemists and Pharmacologists, Wiley, 2013.
[8] L. Neumann, K. von König, D. Ullmann, HTS reporter displacement assay for fragment screening and fragment evolution toward leads with optimized binding kinetics, binding selectivity, and thermodynamic signature, Methods Enzymol. 493 (2010) 299–320.
[9] E.V. Schneider, J. Bottcher, R. Huber, K. Maskos, L. Neumann, Structure-kinetic relationship study of CDK8/CycC specific compounds, Proc. Natl. Acad. Sci. U.S.A. 110 (2013) 8081–8086.
[10] C. Meyners, M.G. Baud, M.J. Fuchter, F.J. Meyer-Almes, Thermodynamics of ligand binding to histone deacetylase like amidohydrolase from Bordetella/Alcaligenes, J. Mol. Recognit. 27 (2014) 160–172.
[11] I. Hoshino, H. Matsubara, Recent advances in histone deacetylase targeted cancer therapy, Surg. Today 40 (2010) 809–815.
[12] P. Marks, W.S. Xu, Histone deacetylase inhibitors: potential in cancer therapy, J. Cell. Biochem. 107 (2009) 600–608.
[13] X.-J. Yang, E. Seto, The Rpd3/Hda1 family of lysine deacetylases: from bacteria and yeast to mice and men, Nat. Rev. Mol. Cell Biol. 9 (2008) 206–218.
[14] I. Gregoretti, Y.-M. Lee, H.V. Goodson, Molecular evolution of the histone deacetylase family: functional implications of phylogenetic analysis, J. Mol. Biol. 338 (2004) 17–31.
[15] G.I. Aldana-Masangkay, K.M. Sakamoto, The role of HDAC6 in cancer, BioMed Res. Int. 2011 (2010).
[16] J. Luo, F. Su, D. Chen, A. Shiloh, W. Gu, Deacetylation of p53 modulates its effect on cell growth and apoptosis, Nature 408 (2000) 377–381.
[17] W. Weichert, HDAC expression and clinical prognosis in human malignancies, Cancer Lett. 280 (2009) 168–176.
[18] P.A. Marks, R. Breslow, Dimethyl sulfoxide to vorinostat: development of this histone deacetylase inhibitor as an anticancer drug, Nat. Biotechnol. 25 (2007) 84–90.
[19] K. Vanommeslaeghe, C. Van Alsenoy, F. De Proft, J.C. Martins, D. Tourwé, P. Geerlings, Ab initio study of the binding of trichostatin A (TSA) in the active site of histone deacetylase like protein (HDLP), Org. Biomol. Chem. 1 (2003) 2951–2957.
[20] C. Hildmann, M. Ninkovic, R. Dietrich, D. Wegener, D. Riester, T. Zimmermann, O.M. Birch, C. Bernegger, P. Loidl, A. Schwienhorst, A new amidohydrolase from Bordetella or Alcaligenes strain FB188 with similarities to histone deacetylases, J. Bacteriol. 186 (2004) 2328–2339.
[21] T.K. Nielsen, C. Hildmann, A. Dickmanns, A. Schwienhorst, R. Ficner, Crystal structure of a bacterial class 2 histone deacetylase homologue, J. Mol. Biol. 354 (2005) 107–120.
[22] C. Hildmann, D. Wegener, D. Riester, R. Hempel, A. Schober, J. Merana, L. Giurato, S. Guccione, T.K. Nielsen, R. Ficner, Substrate and inhibitor specificity of class 1 and class 2 histone deacetylases, J. Biotechnol. 124 (2006) 258–270.
[23] D. Riester, C. Hildmann, P. Haus, A. Galetovic, A. Schober, A. Schwienhorst, F.J. Meyer-Almes, Non-isotopic dual parameter competition assay suitable for high-throughput screening of histone deacetylases, Bioorg. Med. Chem. Lett. 19 (2009) 3651–3656.
[24] J.E. Jackman, C.A. Fierke, L.N. Tumey, M. Pirrung, T. Uchiyama, S.H. Tahir, O. Hindsgaul, C.R. Raetz, Antibacterial agents that target lipid a biosynthesis in gram-negative bacteria inhibition of diverse UDP-3-O-(R-3-hydroxymyristoyl)-N-acetylglucosamine deacetylases by substrate analogs containing zinc binding motifs, J. Biol. Chem. 275 (2000) 11002–11009.
[25] P.M. Lombardi, K.E. Cole, D.P. Dowling, D.W. Christianson, Structure, mechanism, and inhibition of histone deacetylases and related metalloenzymes, Curr. Opin. Struct. Biol. 21 (2011) 735–743.
[26] K.T. Andrews, T.N. Tran, A. Lucke, P. Kahnberg, G. Le, G. Boyle, D. Gardiner, T. Skinner-Adams, D. Fairlie, Potent antimalarial activity of histone deacetylase inhibitor analogues, Antimicrob. Agents Chemother. 52 (2008) 1454–1461.
[27] N.C. Wheatley, K.T. Andrews, T.L. Tran, A.J. Lucke, R.C. Reid, D.P. Fairlie, Antimalarial histone deacetylase inhibitors containing cinnamate or NSAID components, Bioorg. Med. Chem. Lett. 20 (2010) 7080–7084.
[28] L.M. Henkes, P. Haus, F. Jager, J. Ludwig, F.J. Meyer-Almes, Synthesis and biochemical analysis of 2,2,3,3,4,4,5,5,6,6,7,7-dodecafluoro-N-hydroxy-octanediamides as inhibitors of human histone deacetylases, Bioorg. Med. Chem. 20 (2012) 985–995.
[29] R.R. Frey, C.K. Wada, R.B. Garland, M.L. Curtin, M.R. Michaelides, J.L. Li, L.J. Pease, K.B. Glaser, P.A. Marcotte, J.J. Bouska, S.S. Murphy, S.K. Davidsen, Trifluoromethyl ketones as inhibitors of histone deacetylase, Bioorg. Med. Chem. Lett. 12 (2002) 3443–3447.
[30] D. Riester, D. Wegener, C. Hildmann, A. Schwienhorst, Members of the histone deacetylase superfamily differ in substrate specificity towards small synthetic substrates, Biochem. Biophys. Res. Commun. 324 (2004) 1116–1123.
[31] P. Mendes, GEPASI: a software package for modelling the dynamics, steady states and control of biochemical and other systems, Comput. Appl. Biosci. 9 (1993) 563–571.
[32] D. Wegener, C. Hildmann, D. Riester, A. Schwienhorst, Improved fluorogenic histone deacetylase assay for high-throughput-screening applications, Anal. Biochem. 321 (2003) 202–208.
[33] P. Mendes, D. Kell, Non-linear optimization of biochemical pathways: applications to metabolic engineering and parameter estimation, Bioinformatics 14 (1998) 869–883.
[34] D.C. Swinney, Kinetic binding mechanisms: their contribution to an optimal therapeutic index, Label-Free Technol. Drug Discov. (2011) 283–302.
[35] C.F. Wong, S. Bairy, Drug design for protein kinases and phosphatases: flexible-receptor docking, binding affinity and specificity, and drug-binding kinetics, Curr. Pharm. Des. 19 (2013) 4739–4754.
[36] R.A. Copeland, D.L. Pompliano, T.D. Meek, Drug–target residence time and its implications for lead optimization, Nat. Rev. Drug Discov. 5 (2006) 730–739.
[37] R. Zhang, F. Monsma, The importance of drug-target residence time, Curr. Opin. Drug Discov. Dev. 12 (2009) 488.
[38] Y. Inada, M. Ojima, R. Kanagawa, Y. Misumi, K. Nishikawa, T. Naka, Pharmacologic properties of candesartan cilexetil—possible mechanisms of long-acting antihypertensive action, J. Hum. Hypertens. 13 (Suppl. 1) (1999) S75–S80.
[39] E.R. Wood, A.T. Truesdale, O.B. McDonald, D. Yuan, A. Hassell, S.H. Dickerson, B. Ellis, C. Pennisi, E. Horne, K. Lackey, A unique structure for epidermal growth factor receptor bound to GW572016 (Lapatinib) relationships among protein conformation, inhibitor off-rate, and receptor activity in tumor cells, Cancer Res. 64 (2004) 6652–6659.
[40] G.S. Harris, J.W. Kozarich, Steroid 5alpha-reductase inhibitors in androgen-dependent disorders, Curr. Opin. Chem. Biol. 1 (1997) 254–259.
[41] S.A. Lipton, Paradigm shift in neuroprotection by NMDA receptor blockade: memantine and beyond, Nat. Rev. Drug Discov. 5 (2006) 160–170.
[42] D. Riester, C. Hildmann, A. Schwienhorst, F.J. Meyer-Almes, Histone deacetylase inhibitor assay based on fluorescence resonance energy transfer, Anal. Biochem. 362 (2007) 136–141.
[43] R.K. Singh, N. Lall, T.S. Leedahl, A. McGillivray, T. Mandal, M. Haldar, S. Mallik, G. Cook, D.K. Srivastava, Kinetic and thermodynamic rationale for suberoylanilide hydroxamic acid being a preferential human histone deacetylase 8 inhibitor as compared to the structurally similar ligand, trichostatin A, Biochemistry 52 (2013) 8139–8149.
[44] A.M. Kral, N. Ozerova, J. Close, J. Jung, M. Chenard, J. Fleming, B.B. Haines, P. Harrington, J. Maclean, T.A. Miller, P. Secrist, H. Wang, R.W. Heidebrecht Jr., Divergent kinetics differentiate the mechanism of action of two HDAC inhibitors, Biochemistry 53 (2014) 725–734.
[45] M. Brunsteiner, P.A. Petukhov, Insights from comprehensive multiple receptor docking to HDAC8, J. Mol. Model. 18 (2012) 3927–3939.
[46] R. Furumai, Y. Komatsu, N. Nishino, S. Khochbin, M. Yoshida, S. Horinouchi, Potent histone deacetylase inhibitors built from trichostatin A and cyclic tetrapeptide antibiotics including trapoxin, Proc. Natl. Acad. Sci. U.S.A. 98 (2001) 87–92.
[47] C.B. Botta, W. Cabri, E. Cini, L. De Cesare, C. Fattorusso, G. Giannini, M. Persico, A. Petrella, F. Rondinelli, M. Rodriquez, A. Russo, M. Taddei, Oxime amides as a novel zinc binding group in histone deacetylase inhibitors: synthesis, biological activity, and computational evaluation, J. Med. Chem. 54 (2011) 2165–2182.
[48] C.A. Olsen, M.R. Ghadiri, Discovery of potent and selective histone deacetylase inhibitors via focused combinatorial libraries of cyclic alpha3beta-tetrapeptides, J. Med. Chem. 52 (2009) 7836–7846.
[49] H. Akaike, A new look at the statistical model identification, IEEE Trans. Automatic Control 19 (1974) 716–723.
[50] C.J. Chou, D. Herman, J.M. Gottesfeld, Pimelic diphenylamide 106 is a slow, tight-binding inhibitor of class I histone deacetylases, J. Biol. Chem. 283 (2008) 35402–35409.
[51] S. Kapur, P. Seeman, Does fast dissociation from the dopamine d(2) receptor explain the action of atypical antipsychotics? a new hypothesis, Am. J. Psychiatry 158 (2001) 360–369.
[52] Y.-C. Cheng, W.H. Prusoff, Relationship between the inhibition constant (K1) and the concentration of inhibitor which causes 50 per cent inhibition (I50) of an enzymatic reaction, Biochem. Pharmacol. 22 (1973) 3099–3108.

4.3. Combining kinetic binding mechanisms and thermodynamics to assess the selectivity of histone deacetylase inhibitors

Title:

Impact of binding mechanism on selective inhibition of histone deacetylase isoforms.

Authors:

Christian Meyners, Franz-Josef Meyer-Almes

Bibliographic Data:

Submitted for publication in Chemical Biology and Drug Design

Abstract:

Industrialized drug screening campaigns usually deliver hundreds of compounds that are active on a particular pharmaceutical target. In the light of high failure rates of drug candidates due to unforeseeable off-target toxicity, the early identification of the most promising compounds with high potential for target selectivity is an urgent need to improve the quality of lead compounds and lower attrition rates in the drug development process. The reliable prediction of the selectivity of active substances for a target protein is a challenging task.

A comprehensive study of the binding kinetics, thermodynamics and selectivity of chemically related ligands of histone deacetylase (HDAC) like amidohydrolase from *Pseudomonas aeruginosa* ($HDAH_{pa}$) reveals one general binding mechanism for all analyzed compounds consisting of a preceding conformational selection step followed by an optional subsequent induced fit. Depending on the chemical structure the ligands bind to one or two of at least three protein conformations with different rate constants. Although these kinetic and mechanistic differences hamper the predictability of selectivity for the HDAC inhibitors, we demonstrate that the enthalpy weighted binding constant $K_d^{\Delta H}$ is a useful metric to predict isoform selectivity of inhibitors against HDAC enzymes and relatively robust toward different but related binding mechanisms.

Contributions by C. Meyners:

- Produced the used proteins
- Executed the kinetic binding assay, the ITC experiments and the enzyme activity assays
- Determined the binding mechanisms by global fit analysis
- Developed the enthalpy weighted binding constant
- Wrote the manuscript

Impact of binding mechanism on selective inhibition of histone deacetylase isoforms

Christian Meyners[1], Franz-Josef Meyer-Almes[1,*]

[1] Department of Chemical Engineering and Biotechnology, University of Applied Sciences, Haardtring 100, 64295 Darmstadt, Germany.

Short title: Selective inhibition of histone deacetylases

* Corresponding author:

Franz-Josef Meyer-Almes

Email : franz-josef.meyer-almes@h-da.de

Phone: +49 6151168406

Fax : +49 6151168404

Keywords: Histone deacetylases; protein-ligand interaction; thermodynamics; kinetics; reaction mechanism; selective inhibitors

Abstract: (less than 200 words)

Industrialized drug screening campaigns usually deliver hundreds of compounds that are active on a particular pharmaceutical target. In the light of high failure rates of drug candidates due to unforeseeable off-target toxicity, the early identification of the most promising compounds with high potential for target selectivity is an urgent need to improve the quality of lead compounds and lower attrition rates in the drug development process. The reliable prediction of the selectivity of active substances for a target protein is a challenging task.

A comprehensive study of the binding kinetics, thermodynamics and selectivity of chemically related ligands of histone deacetylase (HDAC) like amidohydrolase from *Pseudomonas aeruginosa* ($HDAH_{pa}$) reveals one general binding mechanism for all analyzed compounds consisting of a preceding conformational selection step followed by an optional subsequent induced fit. Depending on the chemical structure the ligands bind to one or two of at least three protein conformations with different rate constants. Although these kinetic and mechanistic differences hamper the predictability of selectivity for the HDAC inhibitors, we demonstrate that the enthalpy weighted binding constant $K_d^{\Delta H}$ is a useful metric to predict isoform selectivity of inhibitors against HDAC enzymes and relatively robust toward different but related binding mechanisms.

Introduction

The development of selective inhibitors is an important task in modern drug development processes as they are believed to cause lesser unwanted side effects. Usually, several hundred hits are identified in a high throughput screening and those compounds to be taken forward in the drug development process have to be identified as early as possible to use the available resources optimally. The selected compounds should be potent but also have a reduced risk to fail due to poor bioavailability or toxicity. The traditional strategy to optimize lead compounds was solely focused on (in vitro) potency or affinity [1]. The easiest way for the optimization of affinity is often achieved by chemical modification of lead compounds with additional hydrophobic moieties like methyl and ethyl groups. These modifications result in an increased entropic contribution to the binding reaction, through desolvation of the hydrophobic moieties. On the other hand these hydrophobic interactions are believed to be a major factor for unspecific interactions and such compounds turned out to be prone to fail in later phases of drug development [2]. Different metrics based on physico chemical properties such as ligand efficiency (LE) or lipophilic efficiency (LPE) aiming at limiting the size and hydrophobicity of lead compounds were developed to identify the most promising drug like molecules in the drug discovery process and to assist the medicinal chemists in the optimization of the best lead compounds. The most promising metrics, LPE, was shown to be linked with binding enthalpy [3]. Ladbury, Chaires, Freire and their colleagues suggested to optimize binding enthalpy in order to achieve more selective lead compounds [2, 4, 5]. This concept is based on the fact that enthalpic contributions result mainly from polar interactions like specific hydrogen bonding, ion-ion and other electrostatic interactions but also from van-der-waals interactions resulting from distinct optimal geometric fit of the ligand to the binding pocket of the protein [6].

Besides thermodynamic and affinity based optimization the evaluation of kinetic parameters gained increasing attention during the last decade. Approaches like the residence time concept introduced by Copeland [7] appeared promising as there are several examples suggesting a correlation between a long residence time of a compound and increased *in vivo* efficiency [7-11]. Moreover, long overall periods of target occupancy were hypothesized to be one important mean to induce a higher selectivity

in non-equilibrium environments. A more detailed dissection of binding kinetics reveals deep insight information on the underlying binding mechanism. In the topical discussion about the prevalence of one of two postulated general binding schemes an induced fit [12] or conformational selection [13] mechanism a combined thermodynamic and kinetic approach using global fit routines was shown to be able to differentiate efficiently between both binding mechanism [14]. However, the relationship between different binding mechanisms of compounds to the same target protein and selectivity against related isoforms is largely understudied.

In this study, a systematic investigation was carried out using a prokaryotic histone deacetylase-like amidohydrolase from *Pseudomonas aeruginosa* ($HDAH_{pa}$) as a model system to elucidate the influence of binding mechanism and thermodynamic parameters of ligand binding on their selectivity. HDAHs have been used before as model systems for the histone deacetylase family including the closely related pharmacologically most relevant human histone deacetylases (HDACs) and show highest similarity to human HDAC6 [15-19].

Methods and Materials

If not stated otherwise chemicals were bought in the highest available purity from Sigma/Aldrich (USA), Roth (Germany) and Merck (Germany). SAHA was obtained from Cayman Chemical (USA) and PFSAHA was bought from Synchem OHG (Germany). The substrates Boc-Lys(Ac)-AMC and Boc-Lys(trifluoracetyl)-AMC were obtained from Bachem (Switzerland). The dansyl-conjugates **1a-f** and SATFMK were prepared as described previously [19]. $HDAH_{pa}$ was prepared as described elsewhere [18]. Recombinant HDACs 1-8 were brought from BPS bioscience (USA). In general the assay buffer for experiments with $HDAH_{pa}$ consisted of 20 mM Tris-HCl and 50 mM NaCl at pH 8.0. Experiments with recombinant HDACs were carried out in 25 mM Tris-HCl and 75 mM KCl at pH 8.0. For reactions performed in half area 96-well microplates (Greiner bio-one, Germany) the assay buffers were supplemented with 0.001% Pluronic F-127. The obtained data were fitted using prism 5 (GraphPad Software, USA), the PEAQ-ITC analysis software (Microcal, USA) or Copasi 4.12.

Enzyme activity assay. The enzyme activity assay was conducted according to Wegener et al. [20]. To determine the inhibitory effect of compounds on HDACs1-8, 1 nM of the respective HDAC isoform were incubated with a serial dilution of the compounds for 30 minutes at 30 °C. The catalytic reaction was carried out by addition of 50 µM of the substrate Boc-Lys(Ac)-AMC for HDACs 1, 2, 3 and 6 or 20 µM of the substrate Boc-Lys(trifluoracetyl)-AMC for HDACs 4, 5, 7 and 8 followed by an incubation for 60 minutes at 30 °C. The reaction was stopped by adding 40 µM SAHA for HDACs 1, 2, 3 and 6 or 20 µM SATFMK for HDACs 4, 5, 7 and 8. The deacetylated substrate was converted into the fluorescent product AMC by addition of 0.5 mg/ml trypsin whose release was followed in a microplate reader (excitation: 360 nm, emission: 460 nm; PHERAstar FS, BMG LABTECH) and then correlated to enzyme activity. For experiments with $HDAH_{pa}$ the enzyme activity assay was carried out in one step as $HDAH_{pa}$ is insensitive to trypsin. Typically, 1 nM of $HDAH_{pa}$ was incubated at 30 °C for 30 minutes with the respective inhibitor and the reaction was started by the addition of 20 µM Boc-Lys(trifluoracetyl)-AMC supplemented with 0.5 mg/ml trypsin. The enzyme kinetics were followed in a microplate reader (excitation: 360 nm, emission: 460 nm; PHERAstar FS, BMG LABTECH) and the slope was correlated to enzyme activity. All obtained dose-response curves were fitted to a 4-parameter fit model provided by Prism 5 yielding the IC_{50}-value.

FRET binding assay. The FRET binding assay was carried out as described earlier [19]. For the determination of the equilibrium dissociation constant, K_d of the fluorescent dansyl-conjugates **1a-f** varying concentrations of the respective dansyl-conjugate were incubated with 0.2 µM $HDAH_{pa}$ in microplates for 30 minutes at 30 °C. The determination of the K_d-value of the unlabeled ligands PFSAHA and SATFMK was conducted by measuring the dissociation of the enzyme-dansyl-conjugate complex upon addition of PFSAHA or SATFMK. Varying concentrations of PFSAHA or SATFMK were incubated with 1 µM of **1a** and 0.2 µM $HDAH_{pa}$ for 1.5 hours at 30 °C. For all cases the binding of the dansyl-conjugate was determined by measuring the fluorescence using a microplate reader (excitation: 280 nm, emission: 530 nm; PHERAstar FS, BMG LABTECH). The obtained data points were corrected for the fluorescence of the unbound probe, normalized with respect to maximal binding and fitted to a one site binding model or a competitive binding model as described elsewhere [19].

ITC measurements. For the determination of the binding thermodynamics of the compounds to $HDAH_{pa}$ 4 to 15 µM of the protein in buffer were placed in the sample cell of an PEAQ-ITC instrument (Microcal, USA). The compounds were diluted in the same buffer to a final concentration of 50 to 150 µM and placed into the syringe. After tempering the cells to 30 °C the ligand concentration was increased stepwise by injecting 2 to 3 µl until only dilution heat was measured. The obtained data points were corrected for the dilution heat and analyzed for a one site binding model using the PEAQ-ITC analysis software (Microcal, USA). To exclude heat produced by proton exchange with the bulk solution experiments were carried out at pH 8.0 in three different buffers consisting of 50 mM NaCl and 20 mM Tris-HCl or 20 mM triethanolamine (TEA) or 20 mM HEPES. The resulting values for the binding enthalpy ΔH^0_{obs} were plotted against the ionization enthalpy ΔH^0_{ion} of the respective buffer and fitted with a linear regression yielding the intrinsic binding enthalpy ΔH^0_{ins} and stoichiometry of the protonation. The resulting intrinsic binding enthalpies were combined with Gibbs energies, which were obtained from the FRET binding assays to determine the binding entropies.

Kinetic binding studies. The association kinetics of the fast binding dansyl-conjugates were investigated using a stopped-flow machine with three independently movable syringes and a dead time of approximately 1.6 ms. After tempering all solutions to 30 °C increasing concentrations of the dansyl-conjugates were rapidly mixed with 0.2 µM of $HDAH_{pa}$ and the increase in fluorescence was observed using an excitation wavelength of 290 nm and a 515 nm cut-off filter. To determine the binding mechanism the obtained binding curves were subjected to a global fit analysis.

The binding kinetics of the slow binding unlabeled compounds PFSAHA and SATFMK were determined by measuring the time depended dissociation of an enzyme-dansyl-conjugate complex as described earlier. A serial dilution of PFASHA or SATFMK supplemented with 1 µM of **1a** was tempered to 30 °C. The binding reaction was initiated by a rapid addition of a pretempered complex of 0.2 µM $HDAH_{pa}$ and 1 µM **1a**. The decay in fluorescence was followed using a microplate reader with

a 280 nm excitation filter and a 530 nm emission filter. The obtained decay curves were subjected to global fit analysis to determine the binding mechanism.

Determination of binding mechanisms with global fit analysis. The global fit analysis of different binding mechanisms was performed with COPASI 4.12 [21]. Potential binding mechanisms of increasing complexity were implemented in the program and the data obtained from the kinetic experiments and the FRET binding assay were fitted simultaneously to each model using a Levenberg-Marquardt algorithm whereby constraints like experimentally determined off rates were implemented into the binding models. The obtained results were then evaluated on the basis of their sum of squares and the Akaike Information Criterion to obtain the most likely binding model [22].

Results and discussion

Thermodynamics of inhibitors binding to $HDAH_{pa}$. Starting with equilibrium binding data the K_d-values of a set of structural related compounds to $HDAH_{pa}$ were determined using a FRET-binding assay [17]. The binding of the dansyl-conjugates **1a-f** to $HDAH_{pa}$ resulted in a binding dependent FRET from the intrinsic tryptophans to the dansyl moiety of the respective ligand, which was exploited to determine the equilibrium binding dissociation constants in a 96-well microplate. The investigated dansyl conjugates bind to $HDAH_{pa}$ with K_d-values ranging from 0.14 µM for **1b** down to 0.006 µM for **1f**. The dependency of the determined K_d-values on the spacer length of the dansyl conjugates indicates a preference for short or longer spacers as the dansyl conjugates with medium sized spacers bound about 2 to 20 times weaker. Interestingly, ITC experiments revealed, that the dansyl conjugate **1d** with 5 methylene groups in the spacer exhibit with -8.4 $kJ*mol^{-1}$ the least favorable binding enthalpy as well as the lowest $\Delta H^0/\Delta G^0$ ratio of 0.21. Increment as well as reduction of the spacer by one CH_2 group results in much more beneficial binding enthalpies of -31 $kJ*mol^{-1}$ respectively -28 $kJ*mol^{-1}$ as well as higher $\Delta H^0/\Delta G^0$ ratios of 0.66 and 0.67. A further increment of the spacer slightly improves the binding enthalpy but not the $\Delta H^0/\Delta G^0$ ratio. Reduction of the spacer to 3 and 2 CH_2 groups improves the binding enthalpy as well as the $\Delta H^0/\Delta G^0$ ratio, whereby **1a** with the shortest spacer exhibits the most favorable binding enthalpy with -50 $kJ*mol^{-1}$ and the highest $\Delta H^0/\Delta G^0$ ratio of 1.16 of all tested dansyl conjugates (Tab.1, Fig. 1 and Fig. S1-S5).

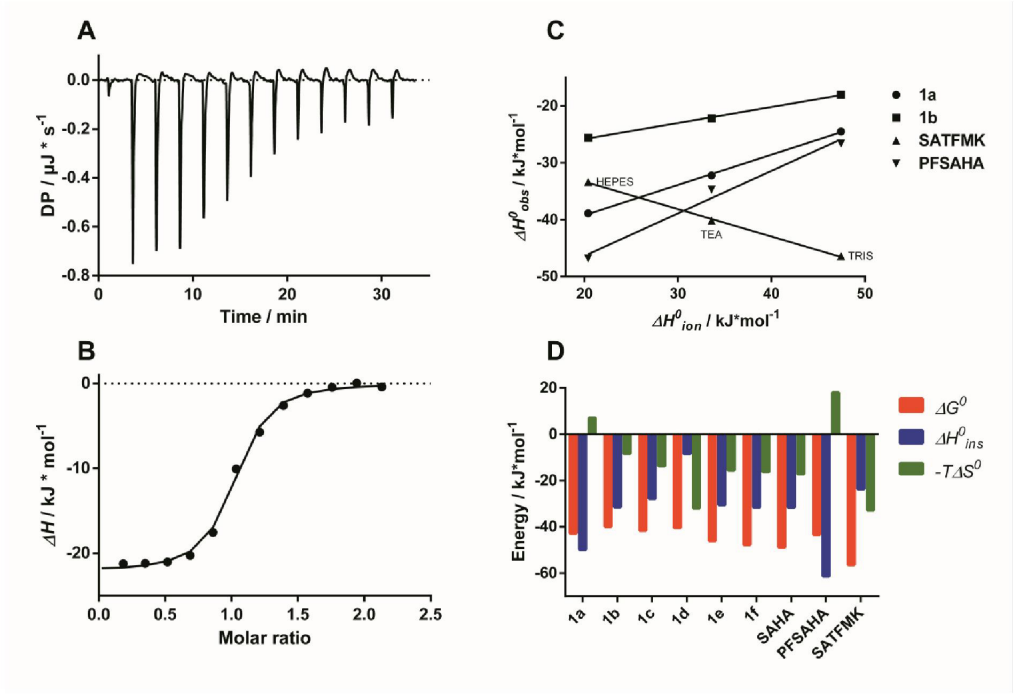

Fig. 1 Thermodynamics of inhibitor binding to HDAH$_{pa}$. Representative ITC data for the binding of **1b** to HDAH$_{pa}$ in 20 mM triethanolamine (TEA) pH 8.0 and 50 mM NaCl at 30 °C from which the observed binding enthalpy ΔH^0_{obs} was determined (**A+B**). Experiments were carried out in three buffer systems (HEPES, TEA and TRIS) with different ionization enthalpies (ΔH^0_{ion}). The determined observed binding enthalpies ΔH^0_{obs} were plotted against the respective ionization enthalpy ΔH^0_{ion} and fitted with linear regression yielding the intrinsic binding enthalpy ΔH^0_{ins} and the stoichiometry of the protonation (**C**). Data points represent the mean of two experiments with less than 5% deviation. Only for binding of **1a**, **1b**, SATFMK and PFSAHA a significant contribution of protonation effects was observable. The intrinsic binding enthalpies were combined with Gibbs energies ΔG^0 to calculate the entropic contribution to binding $-T\Delta S^0$ (**D**).

As for the dansyl conjugates the thermodynamic parameters of the binding of the unlabeled compounds **2-4** were determined by ITC and the K_d-values were determined using a competitive FRET-binding assay [17]. The interaction between the approved drug SAHA (**2**) and HDAH$_{pa}$ is characterized by a binding enthalpy of -32 kJ*mol^{-1} and a K_d-value of 0.0038 µM comparable to binding of 1**f** and ranges between the two derivates PFSAHA (**3**) and SATFMK (**4**), which bound with 0.035 µM and 0.0002 µM, respectively. Interestingly, the 20-fold increase in affinity of SATFMK results solely from higher entropic contributions as the binding enthalpy of -24 kJ*mol^{-1} is less favorable. The perfluorination of the aliphatic spacer of PFSAHA results in decreased affinity, but the binding enthalpy is with -61 kJ*mol^{-1} nearly two times more negative than for SAHA resulting in the highest observed $\Delta H^0/\Delta G^0$-ratio of 1.42 (Fig. S6-S8).

Kinetics and mechanism of compound binding to $HDAH_{pa}$. The determination of the binding kinetics of the dansyl conjugates was straight forward as the binding to $HDAH_{pa}$ resulted in the aforementioned FRET signal. In general, the concentration dependency of the binding reactions was investigated by rapidly mixing different concentrations of dansyl-conjugate with the protein using a stopped-flow machine. For the unlabeled compounds PFSAHA and SATFMK a reporter displacement assay was conducted which was possible as the dissociation of the used dansyl-conjugate was fast compared to the binding of the compounds. Unfortunately, this did not apply for the binding of SAHA to $HDAH_{pa}$ which hampered the determination of the corresponding binding mechanism. For the determination of the most likely kinetic binding mechanism all kinetic traces as well as the equilibrium binding curves of the FRET binding assay were subjected to a global fit analysis [23]. The tested binding models ranged from a simple one step binding mechanism to complex binding models with conformational selection and induced fit steps and the model complexity was successively increased by adding additional isomerization equilibria (Fig. 2 and Fig. S9-S14).

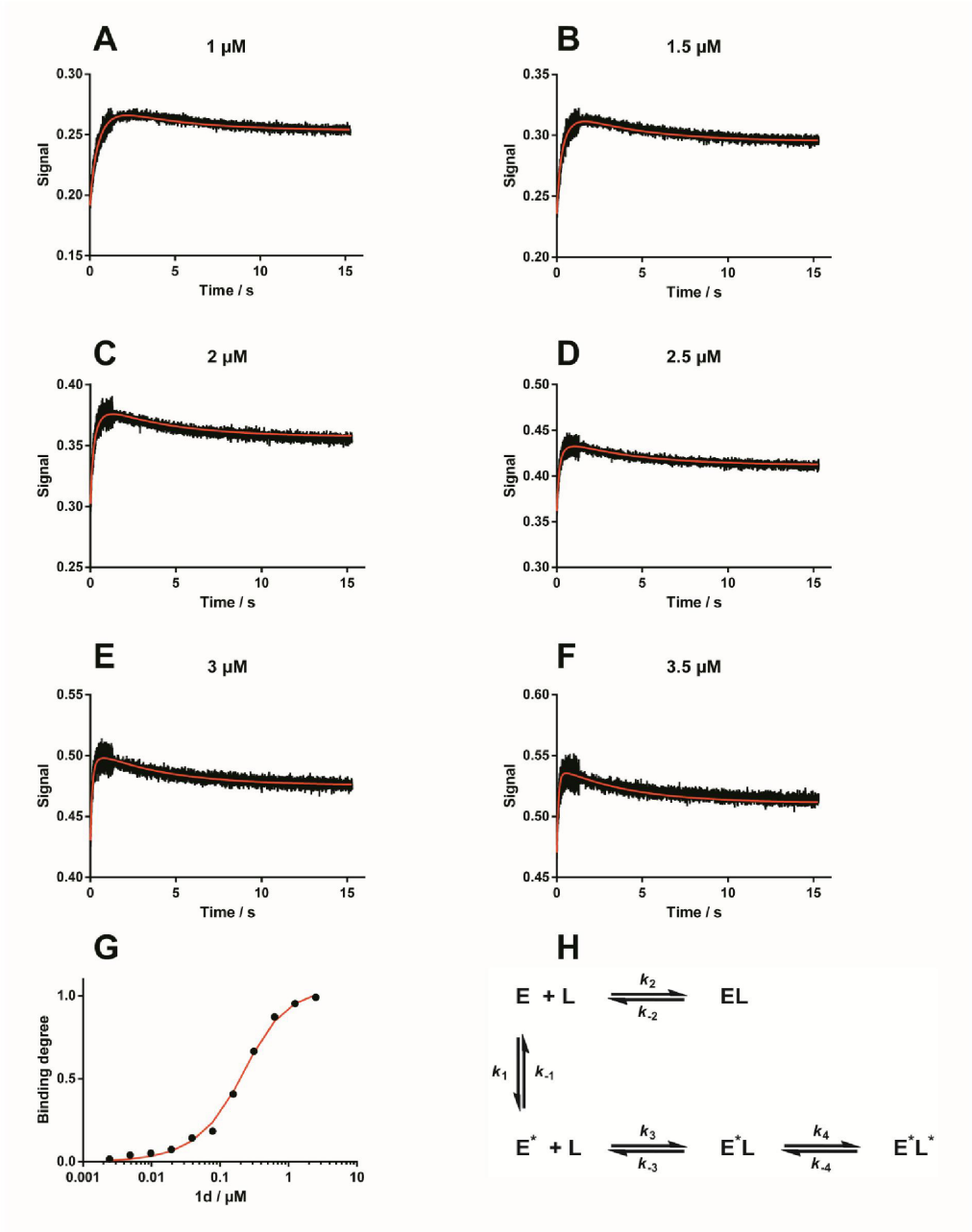

Fig. 2 Global fit analysis of the binding of 1d to HDAH$_{pa}$. Association kinetic traces of varying concentrations of **1d** to HDAH$_{pa}$ (**A-F**) as well as the equilibrium binding curve (**G**) were fitted simultaneously to the indicated binding model (**H**). The association kinetics were measured using a stopped-flow system and the equilibrium binding curve was determined by the FRET binding assay as described in the experimental section. The determined global fit curves are represented by the red lines.

Applying this method to the binding kinetics of ligands to HDAH$_{pa}$ revealed rather complex mechanisms composed of conformational selection as well as induced fit steps. All binding

mechanisms share an upstream equilibrium between various conformational states of $HDAH_{pa}$ with preferential binding of the ligand to one protein conformation. However, there are distinct differences between the group of closely related dansyl-ligands, the perfluorinated PFSAHA and the trifluoromethylketone SATFMK.

The dansyl-conjugates **1a-f** physically bind to two different conformations of $HDAH_{pa}$, which are in chemical equilibrium, via a fast and a slower but more affine step. The complexes resulting from the slower association step of **1a-e** and $HDAH_{pa}$ undergo further isomerization. Of particular note are the identical rate constants of 3.6 and 1.2 s^{-1}, respectively, for the interconversion between both protein conformations within the binding mechanisms of all dansyl-conjugates. This finding suggests that the compounds of the dansyl-series select and bind to the same conformations of $HDAH_{pa}$. The length of the alkyl spacer of the dansyl ligands determines the extent of a subsequent induced fit conformational change of the preferentially formed complex.

In contrast, PFSAHA binds to $HDAH_{pa}$ via a simple conformational selection mechanism (Fig. 3) with a very slow isomerization between a binding inactive and an active conformation of $HDAH_{pa}$. In contrast to the dansyl-ligands, PFSAHA binds exclusively to one protein species and much slower compared with the fast binding steps of dansyl ligands **1a-f**. In addition, the interconversion rates between the conformations of $HDAH_{pa}$ for PFSAHA binding are clearly different from those determined for the dansyl-conjugates suggesting that PFSAHA and the dansyl-conjugates recognize different protein conformations. SATFMK is the only ligand with trifluoromethylketone group to chelate the catalytic zinc ion in the binding pocket of $HDAH_{pa}$. Correspondingly, it is not unexpected that this compound selects another $HDAH_{pa}$ conformation, which is indicated by different interconversion rates between two binding relevant protein species. In the case of SATFMK, the initial complex is able to isomerize into a more stable complex. The initial binding of the sterically less demanding SATFMK is about 7 times faster and 19 times more affine compared with PFSAHA, but slower than the dansyl-ligands. The distinct differences between the binding mechanisms of representatives of diverse compound series are believed to have consequences for oligomerization, protein-protein interactions with other proteins and the transmission of biological signals that require distinct protein conformations. In addition, different and often unknown binding mechanism may

hamper the interpretation of overall thermodynamic parameters like binding enthalpy to make reliable predictions about the potential selectivity of compounds.

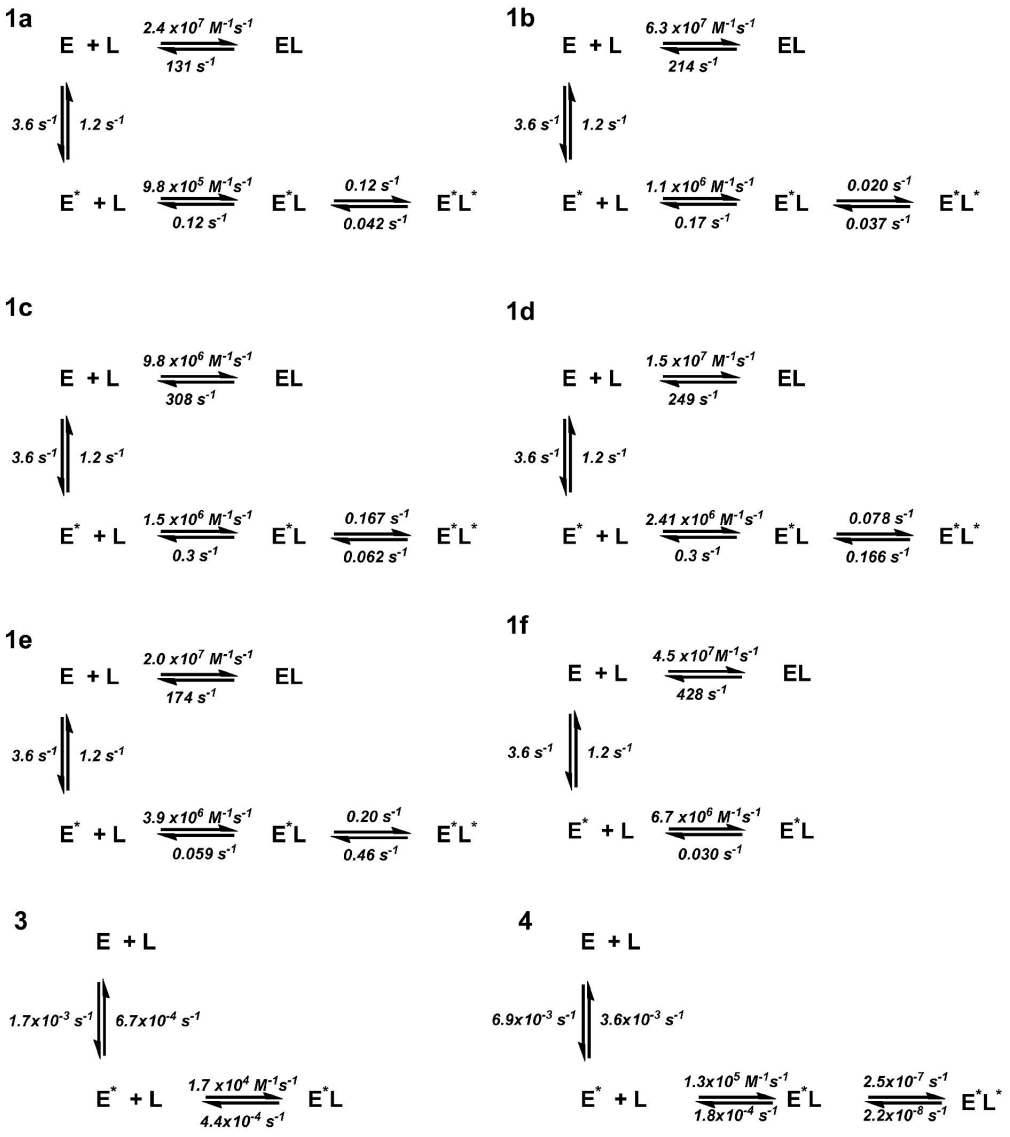

Fig. 3 Determined kinetic binding mechanisms for the binding to $HDAH_{pa}$. The binding mechanisms were determined using a global fit routine, which simultaneously fitted kinetic as well as equilibrium binding data to the indicated model.

Selectivity profiles of $HDAH_{pa}$ inhibitors. In order to investigate the selectivity profile of the $HDAH_{pa}$ inhibitors against human HDACs 1-8 the inhibitory activity of the compounds was

determined by enzyme activity assays. The ratios of the corresponding IC_{50}-values against the IC_{50}-value against $HDAH_{pa}$ served as a measure of selectivity for this enzyme. All compounds are active against $HDAH_{pa}$ with varying IC_{50}-values in the same ranking as the independently determined K_d-values (Tab. 2). As for the affinity itself, the selectivity of the dansyl-conjugates depends on spacer length. The medium sized dansyl-conjugates **1c** and **1d** exhibit a similar selectivity profile and are medium selective against class IIa HDACs and mostly unselective against the other HDAC homologues. Shortening as well as lenghtening of the spacer by one CH_2 unit results in a 5 to 10 times higher selectivity for $HDAH_{pa}$. While a further reduction of the spacer to two CH_2 units yields the highest observed overall selectivity, a further extension of the alkyl spacer results only in a minor improvement of selectivity by a factor of 2. The well-known HDAC inhibitor SAHA exhibits a selectivity profile similar to **1e** and **1f** with good to very good selectivity against class IIa HDACs as well as HDAC8 and poorer selectivity against the other homologues enzymes. Replacement of the hydroxamate zinc binding group in SAHA by the trifluoromethyl group leads to SATFMK resulting in an highly improved selectivity against HDACs 1-3 and 6, but a reduced selectivity against class IIa HDACs and HDAC8. And perfluorination of the alkyl linker of SAHA yielding the sterically more demanding PFSAHA improves selectivity against all proteins, particularly human HDACs 1-3 and 6.

Thermodynamic parameters to assess the selectivity of $HDAH_{pa}$ inhibitors against human HDACs. In order to determine the influence of binding constants and thermodynamics of compound binding to $HDAH_{pa}$ on the selectivity against human HDACs the logarithm of the ratio of the respective IC_{50}-values was plotted either against the logarithm of $\Delta H^0/\Delta G^0$, because a high enthalpic contribution to binding is supposed to correlate with selectivity [2, 19]. Although the two compounds with the highest enthalpic portion are among the most selective ones, a higher enthalpic portion correlates only for HDACs 3, 4, 5 and 8 significantly (p-value < 0.05) with increased selectivity (Fig. 4 and Fig. S15). Interestingly, SATFMK exhibits lower selectivity against these HDAC isoforms. For HDACs 1, 2 and 6 SATFMK appears as sharp outlier from the corresponding data set. SATFMK interacts with $HDAH_{pa}$ through a distinct mechanism involving binding to a different protein conformations plus very slow induced fit. When SATFMK is excluded from the analysis, enthalpic

portion correlates significantly with selectivity against every human HDAC except for HDAC7 (Fig. 4, Fig. S15).

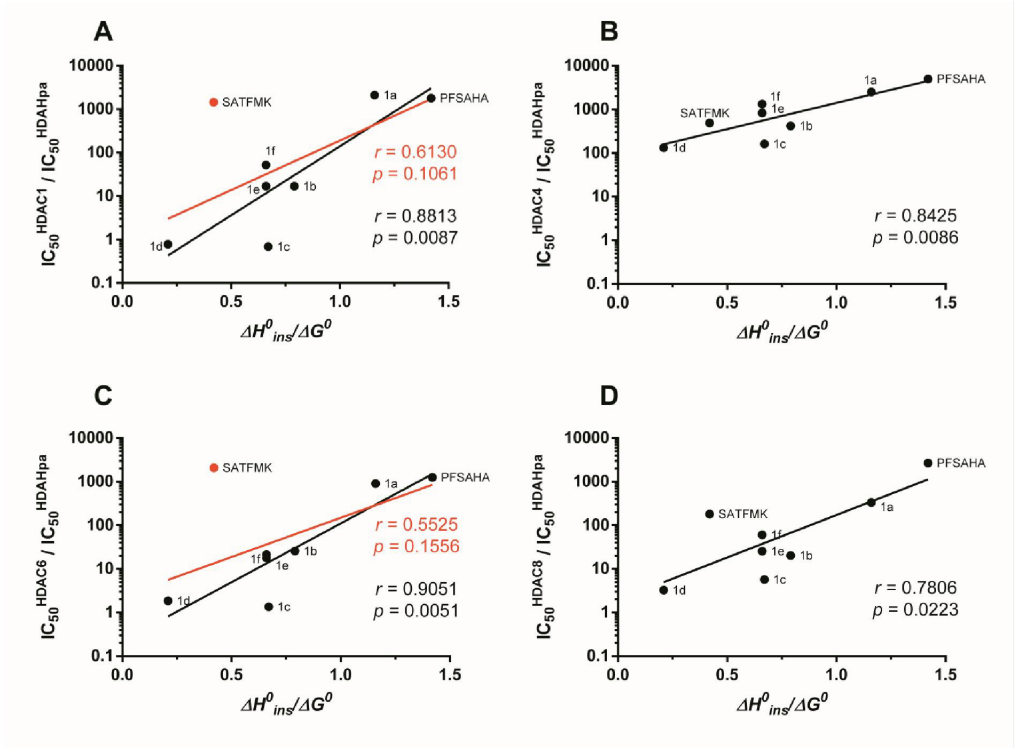

Fig. 4 Influence of thermodynamic parameters on the selectivity of $HDAH_{pa}$ inhibitors against representative human HDACs 1 (class I) (A), 4 (class IIa) (B), 6 (class IIb) (C) and 8 (class I) (D). The ratio of the IC_{50}-values was used as a measure of selectivity and plotted against the ratio $\Delta H^0_{ins}/\Delta G^0$. The Pearson coefficient *r* indicates the correlation between selectivity and the enthalpic contribution to binding. The correlation is significant if the *p*-value is < 0.05. For HDACs 1 and 6 the data was evaluated twice: once with (red) and once without (black) SATFMK that binds to a different conformer of $HDAH_{pa}$.

Although a higher affinity to $HDAH_{pa}$ correlates in no case significantly with increased selectivity, the high affinity binder SATFMK is indeed highly selective against HDACs 1, 2 and 6. Furthermore, the dansyl-conjugates **1c**, **1e** and **1f** show equal $\Delta H^0/\Delta G^0$ ratio of about 0.66 but differ clearly in their selectivity profile. The main difference between these compounds is the affinity for $HDAH_{pa}$ and, interestingly, higher affinity correlates with increased selectivity for these compound, which recognize the same protein conformations. In order to analyze if both, high affinity binding and favorable thermodynamics, are related to the selectivity of the compounds, the K_d and the $\Delta H^0/\Delta G^0$ ratio were combined to yield the enthalpy weighted binding constant $K_d^{\Delta H}$:

$$\log K_d^{\Delta H} = \log K_d \times \left(1 + \frac{\Delta H^0_{ins}}{\Delta G^0}\right) \qquad \text{eq. 1}$$

Plotting the logarithmized ratio of the respective IC_{50}-values against log $K_d^{\Delta H}$ reveal a significant correlation between the selectivity index (IC_{50}-ratio) and $K_d^{\Delta H}$ for all compounds and against all human HDAC isoforms. The best correlation is obtained for HDAC8 with a *p*-value of 0.0003 and a Pearson coefficient *r* of -0.9484. For the other HDACs isoforms the *p*-values ranges between 0.0009 and 0.0416 and the Pearson coefficients *r* between -0.7256 and -0.9266 (Fig. 5 and Fig. S16).

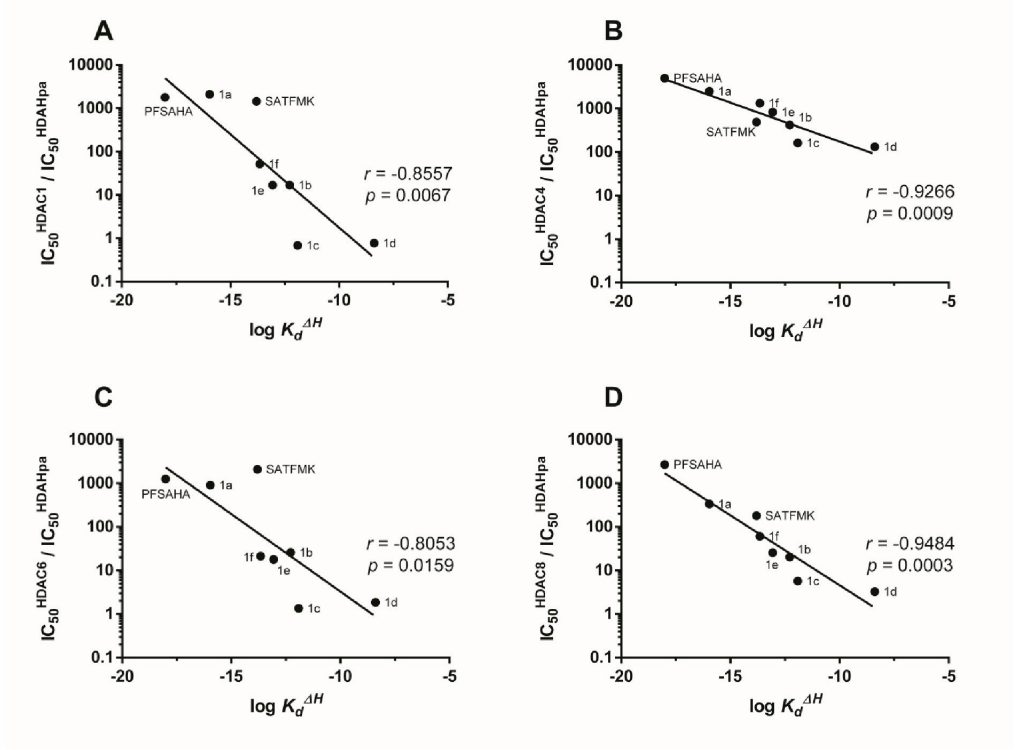

Fig. 5 Relationship between the enthalpy weighted binding constant $K_d^{\Delta H}$ and the selectivity of $HDAH_{pa}$ inhibitors against representative human HDACs 1 (class I) (A), 4 (class IIa) (B), 6 (class IIb) (C) and 8 (class I) (D). The enthalpy weighted binding constant $K_d^{\Delta H}$ was calculated from the affinity (K_d) and the ratio $\Delta H^0_{ins}/\Delta G^0$ by the following equation: $\log(K_d^{\Delta H}) = \log(K_d) * (1+ \Delta H^0_{ins}/\Delta G^0)$. The resulting values were plotted versus the ratio of the IC_{50}-values as a measurement for selectivity. The Pearson coefficient *r* indicates the correlation between both parameters and is significant if the *p*-value is below 0.05.

For HDACs 1, 2, 3 and 6 especially SATFMK s still differs slightly more from the correlation curve and shows higher selectivity than expected. As stated above an analysis of the determined rate constants suggests that PFSAHA and SATFMK bind to unique $HDAH_{pa}$ conformations while the

dansyl-conjugates recognize different conformations. Interestingly, PFSAHA and SATFMK exhibit at least 1000-fold lower IC_{50}-values for $HDAH_{pa}$ compared to HDACs 1, 2 and 6, but only PFSAHA is able to maintain this high selectivity against all HDAC isoforms. Taken together these findings suggest that the selectivity profiles of PFSAHA and SATFMK might be defined by their conformational selection mechanism.

Conclusion

HDAC inhibitors with hydroxamate and trifluoromethylketone functional groups to chelate the catalytic zinc ion at the bottom of the binding pocket interact with $HDAH_{pa}$ via a general mechanism including a preceding equilibrium of at least three, probably more, major conformational protein states. Depending on the chemical structure the ligands select and bind to one or two of at least three conformations followed by an optional induced fit step. Although suggested as suitable guide for identifying the most promising potentially selective active substances in a series of lead candidates, the enthalpy contribution to the interaction between $HDAH_{pa}$ and various ligands correlates only weakly with selectivity against human HDAC isoforms. This is attributed to differences in binding kinetics and mechanisms. However, combining the binding enthalpy with the corresponding equilibrium dissociation constant we propose $K_d^{\Delta H}$ as a useful metric to predict the isoform selectivity of inhibitors against HDAC enzymes. $K_d^{\Delta H}$ is an enthalpy weighted binding constant which is largely robust in light of related variants of the general binding mechanism to $HDAH_{pa}$, although greater mechanistic differences like binding to different protein conformers may still cause significant deviations from the predicted selectivity. It remains to be further investigated whether the proposed selectivity metric, $K_d^{\Delta H}$, can be expanded to other protein-ligand systems.

Acknowledgements

This study was supported by the DFG (grant GZ: ME 3122/2-1).

Conflict of Interest

The authors declare no conflict of interests in this work.

References:

[1] C. Bissantz, B. Kuhn, M. Stahl, A medicinal chemist's guide to molecular interactions, J. Med. Chem., 53 (2010) 5061-5084.

[2] J.E. Ladbury, G. Klebe, E. Freire, Adding calorimetric data to decision making in lead discovery: a hot tip, Nature Reviews Drug Discovery, 9 (2010) 23-27.

[3] M.D. Shultz, The thermodynamic basis for the use of lipophilic efficiency (LipE) in enthalpic optimizations, Bioorg. Med. Chem. Lett., 23 (2013) 5992-6000.

[4] E. Freire, Do enthalpy and entropy distinguish first in class from best in class?, Drug Discov. Today, 13 (2008) 869-874.

[5] J.B. Chaires, Calorimetry and thermodynamics in drug design, Annu. Rev. Biophys., 37 (2008) 135-151.

[6] Y. Kawasaki, E.E. Chufan, V. Lafont, K. Hidaka, Y. Kiso, L. Mario Amzel, E. Freire, How much binding affinity can be gained by filling a cavity?, Chemical Biology & Drug Design, 75 (2010) 143-151.

[7] R.A. Copeland, D.L. Pompliano, T.D. Meek, Drug–target residence time and its implications for lead optimization, Nature reviews Drug discovery, 5 (2006) 730-739.

[8] D.C. Swinney, Kinetic Binding Mechanisms: Their Contribution to an Optimal Therapeutic Index, Label-Free Technologies for Drug Discovery, (2011) 283-302.

[9] N. Yin, J. Pei, L. Lai, A comprehensive analysis of the influence of drug binding kinetics on drug action at molecular and systems levels, Molecular BioSystems, 9 (2013) 1381-1389.

[10] P.J. Tummino, R.A. Copeland, Residence Time of Receptor- Ligand Complexes and Its Effect on Biological Function, Biochemistry, 47 (2008) 5481-5492.

[11] H. Lu, P.J. Tonge, Drug-target residence time: critical information for lead optimization, Curr. Opin. Chem. Biol., 14 (2010) 467-474.

[12] D. Koshland Jr, Application of a theory of enzyme specificity to protein synthesis, Proceedings of the National Academy of Sciences of the United States of America, 44 (1958) 98.

[13] B. Ma, S. Kumar, C.-J. Tsai, R. Nussinov, Folding funnels and binding mechanisms, Protein Engineering, 12 (1999) 713-720.

[14] F.J. Meyer-Almes, Discrimination between conformational selection and induced fit protein-ligand binding using Integrated Global Fit analysis, Eur. Biophys. J., (2015).

[15] C. Hildmann, M. Ninkovic, R. Dietrich, D. Wegener, D. Riester, T. Zimmermann, O.M. Birch, C. Bernegger, P. Loidl, A. Schwienhorst, A new amidohydrolase from Bordetella or Alcaligenes strain FB188 with similarities to histone deacetylases, J. Bacteriol., 186 (2004) 2328-2339.

[16] J. Sykora, F.J. Meyer-Almes, Mechanism of binding of the inhibitor (E)-3-(furan-2-yl)-N-hydroxyacrylamide to a histone deacetylase-like amidohydrolase, Biochemistry, 49 (2010) 1418-1424.

[17] C. Meyners, M.G. Baud, M.J. Fuchter, F.J. Meyer-Almes, Kinetic method for the large-scale analysis of the binding mechanism of histone deacetylase inhibitors, Anal. Biochem., 460 (2014) 39-46.

[18] C. Meyners, R. Wawrzinek, A. Kramer, S. Hinz, P. Wessig, F.J. Meyer-Almes, A fluorescence lifetime-based binding assay for acetylpolyamine amidohydrolases from Pseudomonas aeruginosa using a [1,3]dioxolo[4,5-f][1,3]benzodioxole (DBD) ligand probe, Anal. Bioanal. Chem., 406 (2014) 4889-4897.

[19] C. Meyners, M.G. Baud, M.J. Fuchter, F.J. Meyer-Almes, Thermodynamics of ligand binding to histone deacetylase like amidohydrolase from Bordetella/Alcaligenes, J Mol Recognit, 27 (2014) 160-172.

[20] D. Wegener, C. Hildmann, D. Riester, A. Schwienhorst, Improved fluorogenic histone deacetylase assay for high-throughput-screening applications, Anal. Biochem., 321 (2003) 202-208.

[21] S. Hoops, S. Sahle, R. Gauges, C. Lee, J. Pahle, N. Simus, M. Singhal, L. Xu, P. Mendes, U. Kummer, COPASI--a COmplex PAthway SImulator, Bioinformatics, 22 (2006) 3067-3074.

[22] H. Akaike, A New Look at the Statistical Model Identification, IEEE Transactions on Automatic Control, 19 (1974) 716-723.

[23] F.-J. Meyer-Almes, Kinetic binding assays for the analysis of protein–ligand interactions, Drug Discovery Today: Technologies, 17 (2015) 1-8.

Tables

Tab. 1 Thermodynamic parameters of inhibitor binding to $HDAH_{pa}$ at 30 °C. The binding enthalpy ΔH^0_{ins} was determined by ITC from 4-6 experiments in 2-3 different buffer systems by extrapolation to 0 contribution of buffer ionization. The K_d-values were determined by ITC and the FRET binding assay from 3-6 independent experiments and are reported as mean±SEM. The entropic contribution to binding was calculated from binding enthalpy ΔH^0_{ins} and the more accurate K_d-values determined by the FRET binding assay.

ID	Structure	K_d[a] µM	K_d[b] µM	ΔH^0_{ins} kJ*mol^{-1}	$-T\Delta S^0$ kJ*mol^{-1}	$\Delta G^0/\Delta H^0_{ins}$
1a	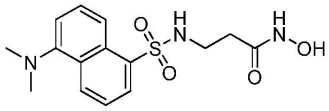	0.042 ±0.005	0.06 ±0.02	-50±2	7±2	1.16
1b	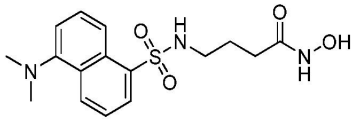	0.14 ±0.01	0.15 ±0.03	-31±1	-8±1	0.79
1c	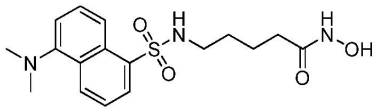	0.07 ±0.01	0.12 ±0.02	-28±1	-14±1	0.67
1d	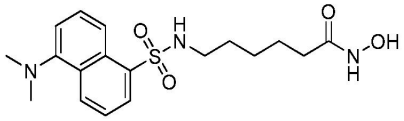	0.12 ±0.02	0.13 ±0.04	-8.4±0.3	-32±1	0.21
1e	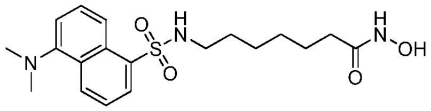	0.012 ±0.002	0.022 ±0.007	-31±1	-15±1	0.66
1f	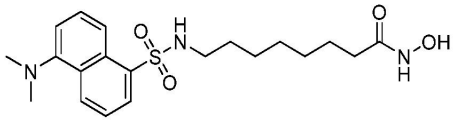	0.006 ±0.001	0.006 ±0.004	-31±1	-16±1	0.66
2	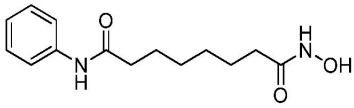	0.0038 ±0.0007	0.008 ±0.006	-32±1	-17±1	0.57
3	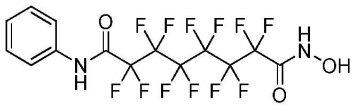	0.035 ±0.001	0.054 ±0.016	-61±2	18±2	1.42
4	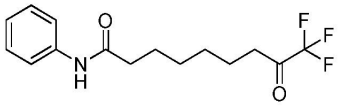	0.00019 ±0.00004	0.004 ±0.003	-23±1	-33±1	0.42

a K_d-values determined by the FRET binding assay; b K_d-values determined by ITC

Tab. 2 Selectivity profiles of $HDAH_{pa}$ inhibitors. The IC_{50}-values in µM were determined from dose response curves with 10 data points at 30 °C using a fluorogenic enzyme activity assay as described in the experimental section.

ID	HDAC1	HDAC2	HDAC3	HDAC4	HDAC5	HDAC6	HDAC7	HDAC8	$HDAH_{pa}$
1a	42 ±13	31 ±3	>50	>50	36 ±2	18 ±6	16 ±1	6.6 ±0.9	0.02 0±0.001
1b	2.0 ±0.1	4.0 ±0.6	1.0 ±0.3	>50	>50	3.1 ±0.2	>50	2.4 ±0.8	0.12 ±0.01
1c	0.21 ±0.06	0.65 ±0.7	0.11 ±0.0	>50	22 ±2	0.41 ±0.04	17 ±4	1.8 ±0.3	0.31 ±0.02
1d	0.16 ±0.04	0.43 ±0.04	0.15 ±0.02	28 ±2	15 ±1	0.38 ±0.05	14±1	0.68 ±0.09	0.21 ±0.04
1e	0.21 ±0.04	0.23 ±0.02	0.11 ±0.02	10 ±1	7.4 ±0.4	0.22 ±0.04	12 ±2	0.32 ±0.03	0.012 ±0.004
1f	0.20 ±0.03	0.27 ±0.03	0.10 ±0.02	5.0 ±0.2	4.6 ±0.3	0.080 ±0.009	8.4 ±0.7	0.23 ±0.03	0.0038 ±0.0007
2	0.062 ±0.004	0.17 ±0.01	0.054 ±0.003	27 ±3	24 ±3	0.090 ±0.007	12 ±1	5.3 ±0.8	0.010 ±0.004
3	18 ±3	>50	>50	>50	26 ±5	12 ±2	15 ±2	27 ±5	0.010 ±0.006
4	0.29 ±0.03	0.97 ±0.04	0.051 ±0.001	0.098 ±0.007	0.059 ±0.008	0.42 ±0.02	0.063 ±0.007	0.036 ±0.002	<0.001

Title:

Perflourinated hydroxamic acids are potent and selective inhibitors of HDAC-like enzymes from *Pseudomonas aeruginosa*.

Authors:

Christian Meyners, Benjamin Wolff, Alexander Kleinschek, Andreas Krämer, Franz-Josef Meyer-Almes

Bibliographic Data:

Bioorganic and Medicinal Chemistry Letters
Volume 27, Issue 7, Pages 1508–1512, April 1, 2017. DOI: 10.1016/j.bmcl.2017.02.050
First published online: February 21, 2017

Abstract:

A series of perfluorinated SAHA (PFSAHA) was prepared and profiled against a panel of human and bacterial members of the Histone deacetylase (HDAC) family. Some of the active substances show nanomolar inhibitory activity and several hundred fold selectivity for the HDAC like enzyme PA3774 from *P. aeruginosa*. The extraordinary selectivity against human HDACs results from the distinct oligomeric state of PA3774 which consists of two head-to-head dimers. The binding pocket is defined by the surface of both opposite monomers confining the access of ligands to the active site. In addition, the aromatic cap group of PFSAHA undergoes an edge-to-face aromatic interaction with phenylalanine from the opposite monomer.

Contributions by C. Meyners:

- Produced some of the used proteins
- Executed the enzyme activity assays

Bioorganic & Medicinal Chemistry Letters 27 (2017) 1508–1512

Contents lists available at ScienceDirect

Bioorganic & Medicinal Chemistry Letters

journal homepage: www.elsevier.com/locate/bmcl

Perfluorinated hydroxamic acids are potent and selective inhibitors of HDAC-like enzymes from *Pseudomonas aeruginosa*

Christian Meyners, Benjamin Wolff, Alexander Kleinschek, Andreas Krämer, Franz-Josef Meyer-Almes *

Department of Chemical Engineering and Biotechnology, University of Applied Sciences, Haardtring 100, 64295 Darmstadt, Germany

ARTICLE INFO

Article history:
Received 23 January 2017
Revised 17 February 2017
Accepted 18 February 2017
Available online 21 February 2017

Keywords:
HDAC inhibitors
Pseudomonas aeruginosa
Perfluorinated hydroxamic acids
Selectivity

ABSTRACT

A series of perfluorinated SAHA (PFSAHA) was prepared and profiled against a panel of human and bacterial members of the Histone deacetylase (HDAC) family. Some of the active substances show nanomolar inhibitory activity and several hundred fold selectivity for the HDAC like enzyme PA3774 from *P. aeruginosa*. The extraordinary selectivity against human HDACs results from the distinct oligomeric state of PA3774 which consists of two head-to-head dimers. The binding pocket is defined by the surface of both opposite monomers confining the access of ligands to the active site. In addition, the aromatic cap group of PFSAHA undergoes an edge-to-face aromatic interaction with phenylalanine from the opposite monomer.

Human zinc-dependent histone deacetylases (HDACs) are established cancer targets with four inhibitors (vorinostat, romidepsin, belinostat and panabinostat) being approved by the FDA for the treatment of cutaneous T-cell lymphoma or multiple myeloma (Fig. 1).[1–4] HDACs have also suggested as targets in other indication areas, such as neurodegenerative, heart or inflammatory diseases.[5–9] HDAC like amidohydrolases are also found in protozoa or bacteria. Several agents against malaria and Schistosomiasis have been developed with a strong focus on selectivity against human HDACs in order to avoid side effects.[10–12] While the development of anti-parasitic HDAC inhibitors has been pushed for almost a decade, the potential of HDAC inhibition as antibacterial strategy has only recently been explored. In the light of ongoing increases of antibiotic resistance in bacteria, there is an urgent need for effective alternatives in antibacterial therapeutics.[13] Interestingly, *P. aeruginosa*, one of the most threatening hospital pathogen, contains three HDAC like enzymes (PA3774, PA0321 and PA1409), of which two are capable to deacetylate acetylated polyamines, and one of them being an acetyl-lysine deacetylase with hitherto unknown substrate.[14] Although the function of these enzymes is not fully understood, we could show an inhibitory effect on the proliferation of *P. aeruginosa* upon inhibition of the HDAC-like amidohydrolases PA0321 and PA1409 under glucose starvation.[14] We also described, for the first time, novel photoswitchable inhibitors of the bacterial HDAC homologs as potential agents in photopharmacological antimicrobial chemotherapy.[15] In earlier work we synthesized analogs of PFSAHA as weak inhibitors of human HDACs with some preference for class II HDACs.[16]

Notably, these compounds showed also activity against a bacterial HDAC homolog from *Bordetella/Alcaligenes* which was tested as reference enzyme.[16] The selectivity of the perfluorinated hydroxamic acids for this bacterial enzyme with respect to human HDACs (up to 50-fold for **1**) was even greater than among human HDAC classes (<3-fold for **1**). This observation led us to the hypothesis that these compounds could also inhibit homologous HDACs from *P. aeruginosa*.

In this study, we synthesized a series of new perfluorinated hydroxamic acids and explored the structure-activity and structure-selectivity relationship of this class of inhibitors against a panel of bacterial and human HDAC homologs. The new molecules described here were essentially prepared following the previously published synthetic route.[16] In short, dodecafluorooctanedioic acid was transformed to its dichloride and further reacted with 1.5 mol equivalent benzylalcohol to yield the corresponding mono ester. The final compounds were obtained after reaction with different aniline analogs and subsequent transformation into hydroxamic acids by hydroxylamine. Details of organic synthesis and chemical analysis are provided in the Supplemental Data.

The biochemical activity data are summarized in Table 1 and demonstrate the remarkable selectivity of the perfluorinated compounds for the HDAC like enzymes from *P. aeruginosa*. Compound **1** for example is at least 500-fold more active against PA3774 than for any human HDAC isoform (HDAC1: 1300-fold; HDAC4, 2300-fold; HDAC5: 590-fold; HDAC6: 500-fold; HDAC7: 500-fold and HDAC8: 770-fold).[19] With the exception of **12** and **27**, all PFSAHA

* Corresponding author.
E-mail address: franz-josef.meyer-almes@h-da.de (F.-J. Meyer-Almes).

http://dx.doi.org/10.1016/j.bmcl.2017.02.050
0960-894X/

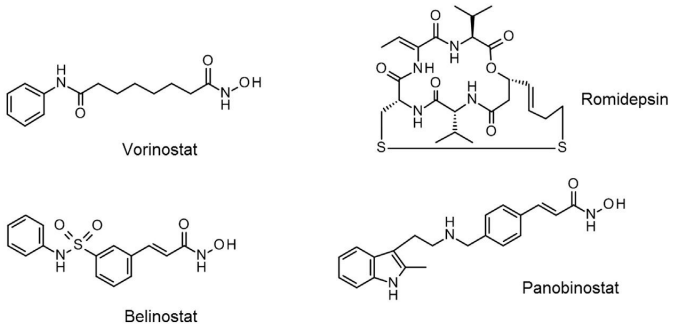

Fig. 1. HDAC inhibitors approved by the FDA for the treatment of different types of cancer.

Table 1
Selectivity profile of perfluorated hydroxamic acids against bacterial and human members of the HDAC protein family.

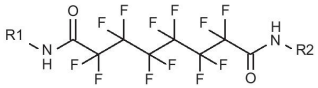

#	R1	R2	K_I (μM)							
			PA0321	PA1409	PA3774	HDAH	HDAC1	HDAC6	HDAC7	HDAC8
1		—OH	0.7 ± 0.2	2.6 ± 0.1	0.022 ± 0.001	0.54 ± 0.02[a]	29 ± 5[a]	11 ± 2[a]	11 ± 1[a]	17 ± 1[a]
2		—OH	2.3 ± 0.1	6.2 ± 0.4	0.19 ± 0.02	0.27 ± 0.02[a]	14 ± 1[a]	>50[a]	>50[a]	34 ± 5[a]
3		—OH	0.27 ± 0.03	11 ± 1	0.092 ± 0.004	0.45 ± 0.08	>50	>50	>50	>50
4		—OH	84 ± 0.1	>50	0.16 ± 0.01	0.62 ± 0.08	>50	>50	>50	>50
5		—OH	2.1 ± 0.1	5.7 ± 0.4	0.17 ± 0.01	0.086 ± 0.008	12 ± 3[a]	23 ± 5[a]	19 ± 6[a]	35 ± 3[a]
6		—OH	0.073 ± 0.006	11 ± 1	0.046 ± 0.004	0.17 ± 0.02	>50	>50	>50	>50
7		—OH	0.8 ± 0.1	>50	0.16 ± 0.01	0.24 ± 0.08	>50	>50	>50	>50
8		—OH	0.49 ± 0.05	>50	0.46 ± 0.04	0.33 ± 0.08	>50	>50	>50	>50
9		—OH	1.1 ± 0.1	4.1 ± 0.4	0.046 ± 0.004	0.39 ± 0.03[a]	14 ± 9[a]	4.2 ± 1[a]	4.1 ± 0.4[a]	36 ± 5[a]
10		—OH	2.8 ± 0.4	7.1 ± 0.4	0.32 ± 0.04	0.23 ± 0.01[a]	18 ± 1[a]	>50[a]	32 ± 4[a]	35 ± 4[a]
11	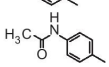	—OH	3.6 ± 0.2	7.6 ± 0.4	0.32 ± 0.04	1.3 ± 0.2[a]	18 ± 3[a]	9.2 ± 2[a]	13 ± 5[a]	36 ± 5[a]
12		—OH	0.37 ± 0.02	>50	1.2 ± 0.1	0.18 ± 0.03	>50	>50	>50	>50
13		—OH	>50	>50	2.7 ± 0.2	>50	>50	>50	>50	>50
14		—OH	1.6 ± 0.1	5.8 ± 0.4	0.10 ± 0.01	0.11 ± 0.01	7.0 ± 0.8	20 ± 10	2.5 ± 0.4	8.4 ± 0.6
15		—OH	2.1 ± 0.1	6.7 ± 0.4	0.24 ± 0.02	0.19 ± 0.02[a]	16 ± 4[a]	1.3 ± 0.2[a]	3.0 ± 0.4[a]	13 ± 1[a]

(*continued on next page*)

Table 1 (*continued*)

#	R1	R2	K_I (μM)							
			PA0321	PA1409	PA3774	HDAH	HDAC1	HDAC6	HDAC7	HDAC8
16		—OH	7 ± 1	21 ± 3	0.35 ± 0.04	0.37 ± 0.03[a]	29 ± 3[a]	32 ± 8[a]	20 ± 4[a]	19 ± 6[a]
17		—OH	1.2 ± 0.2	3.8 ± 0.2	0.53 ± 0.1	0.16 ± 0.02[a]	12 ± 1[a]	6.8 ± 1.8[a]	11 ± 1[a]	49 ± 12[a]
18		—OH	1.5 ± 0.2	3.1 ± 0.4	0.046 ± 0.007	3.8 ± 1.1[a]	31 ± 13[a]	49 ± 36[a]	14 ± 1[a]	>50[a]
19		—OH	1.5 ± 0.1	4.4 ± 0.4	0.10 ± 0.01	0.45 ± 0.05[a]	30 ± 6[a]	15 ± 5[a]	14 ± 1[a]	>50[a]
20		—OH	12 ± 2	17 ± 3	1.1 ± 0.2	0.86 ± 0.05[a]	49 ± 6[a]	9.2 ± 0.9[a]	14 ± 3[a]	5.3 ± 0.5[a]
21		—OH	24 ± 7	>50	2.0 ± 0.2	9.1 ± 0.8[a]	>50[a]	>50[a]	38 ± 8[a]	>50[a]
22		—OH	9 ± 3	11 ± 1	1.1 ± 0.2	0.74 ± 0.06[a]	14 ± 1[a]	5.9 ± 0.8[a]	13 ± 2[a]	1.4 ± 0.3[a]
23		—OH	6 ± 1	11 ± 1	0.25 ± 0.03	0.29 ± 0.04[a]	18 ± 2[a]	10 ± 2[a]	11 ± 1[a]	5.3 ± 0.8[a]
24		—OH	4.1 ± 0.5	16 ± 3	0.23 ± 0.02	0.6 ± 0.2[a]	22 ± 6[a]	17 ± 45[a]	>50[a]	47 ± 11[a]
25	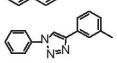	—OH	>50	>50	2.6 ± 0.2	7.0 ± 1[a]	>50[a]	8.2 ± 2[a]	30 ± 7[a]	>50[a]
26		—OH	22 ± 5	15 ± 1	3.1 ± 0.3	4.5 ± 0.5[a]	>50[a]	47 ± 9[a]	12 ± 2[a]	>50[a]
27		—OH	8.5 ±	>50	12 ± 1	2.2 ± 0.2[a]	2.6 ± 0.2[a]	5.4 ± 1.3[a]	1.4 ± 0.2[a]	1.5 ± 0.3[a]
28			>50	>50	10 ± 1	27 ± 3[a]	>50[a]	>50[a]	>50[a]	>50[a]
SAHA			0.32 ± 0.02	0.12 ± 0.01	0.014 ± 0.001	0.30 ± 0.02[a]	0.04 ± 0.01[a]	0.3 ± 0.07[a]	36 ± 16[a]	2.9 ± 0.2[a]

HDAH is the HDAC-like amidohydrolase from *Bordetella/Alcaligenes*. All K_I values were determined using a fluorogenic enzyme activity assay.17 For HDAC1/6 Boc-Lys(Ac)-AMC and for HDAC4/5/7/8 Boc-Lys(trifluoroacetyl)-AMC were used as substrates. After an incubation time of 30 min the deacetylated substrate was converted into a fluorescent dye upon addition of trypsin. K_I values were calculated from IC_{50} values according to Cheng and Prusoff.18 IC_{50} values were calculated from dose response curve containing 10 different ligand concentrations. The K_I values for HDAC4 and HDAC5 were >50 μM for all compounds except for **1** (HDAC5: 13 ± 2 μM) and SAHA (HDAC4: 14 ± 2 μM, HDAC5: 12 ± 2 μM).

[a] Data from Ref. 16.

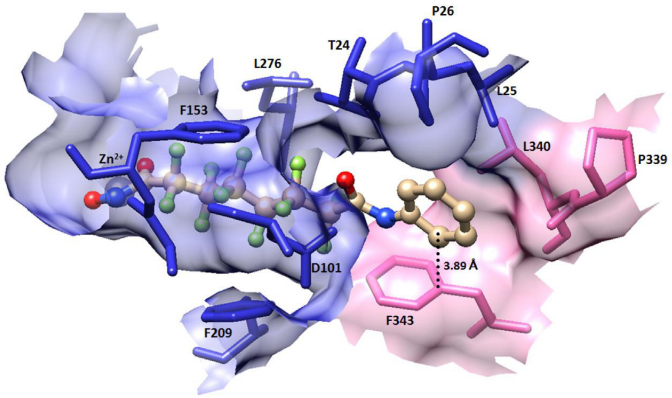

Fig. 2. Binding pose of **1** within the active site of PA3774 (PDB: 5G11). The ligand chelates the catalytic zinc ion at the bottom of the binding pocket in a bidentate fashion and is mainly surrounded by hydrophobic amino acid residues. The binding pocket is formed by two protein monomers (colored in blue and pink) resulting in a particularly hydrophobic upper rim (L25, P26, P339, L340, F343). A characteristic feature is the edge-to-face aromatic interaction between the cap group of **1** and F343 of the opposite monomer.

analogs inhibit PA3774 stronger than PA0321 and PA1409. Obviously, the binding pocket of PA3774 is better suited to accommodate the perfluorinated alkyl chain than any other human HDAC or HDAC like enzyme from *P. aeruginosa*. At the time of this study no structural data of the HDAC homologs from *P. aeruginosa* was available. Therefore, we performed a systematic variation of substituents at the phenyl ring of **1** starting with methyl- and chlorine-scanning (compounds **2**–**7**) to dissect the influence of the cap group on potency and selectivity. Methyl- as well as chlorine-substitution leads to a dramatic drop of potency against PA3774 that was not so pronounced for the other enzymes of *P. aeruginosa*. Substitution at meta-positions leads to the highest activity against PA3774 in both, methyl and chlorine, scans indicating favorable hydrophobic interactions which is confirmed by a comparable activity of a derivative with phenyl group in meta-orientation (**19**). In case of PA0321 the meta-substituted analogs with methyl and chlorine were even more potent than the chemical starting point **1**. The potency of PFSAHA analogs increases from F- to Cl- and I-substitution in para-position (**8** < **5** < **9**). In addition, a phenyl group at this position (**18**) leads to similar activity than iodine pointing towards hydrophobic interactions which were not so obvious from the methyl- and chlorine-scans. This finding is in agreement with unfavorable effects of polar groups (**10**, **11**, **12**, **13**) in para-position.

During the phase of preparation of this report the crystal structure of a complex between the Y313F mutant of PA3774 and **1** (PDB: 5G11) was determined by our group revealing molecular details of this interaction.[19] Although the phenylalanine adopts an "outward" conformation in the mutant protein and the tyrosine in the unliganded wildtype PA3774 (PDB: 5G0Y) and its complex with SATFMK (PDB: 5G10) shows an "inward" conformation, all other amino acids of the binding pocket perfectly superimpose on one another. In addition, both PA3774 complexes, with PFSAHA and SATFMK, show the same characteristic trigonal bipyramidal zinc complexation. We demonstrated that the PA3774 forms a tetramer which is more correctly classified as a dimer of two head-to-head dimers. Furthermore, the head-to-head dimer interface confines the entrance area of the binding pocket suggesting a significant impact on the molecular recognition of ligands.[19] The complex structure of PA3774 and **1** not only confirms the bidentate chelation of the catalytic zinc ion at the bottom of the active site binding pocket as observed in numerous crystal structures of homologous HDAC enzymes (e.g. HDAC4 (PDB: 4LXZ) or HDAC8 (PDB: 2V5X), but also a striking edge-to-face aromatic interaction between the cap group of **1** and F343 of the opposite monomer (Fig. 2; PDB: 5G11). Moreover, the upper rim of the binding pocket is particularly hydrophobic due to amino acids L25, P26, P339, L340 and F343 from both monomers. This region has considerable potential for forming hydrophobic interactions with unpolar substituents in para-position of the phenyl ring in PFSAHA analogs. However, none of the PFSAHA analogs with small group substitutions at the aromatic ring shows higher activity than **1** on PA3774 suggesting that potential hydrophobic interactions with substituents in para- and meta-position of the cap group are counteracted by steric hindrance within the binding pocket of the enzyme. This is supported by the observation that bulkier cap groups like naphthalene, anthracene, phenanthrene or benzpyrene also decrease the activity against PA3774. Interestingly, the unfavorable effects of polar groups in para-position of the cap group are more pronounced than the adverse steric effects of the large benzpyrene group. The sterically demanding phenyl-triazol substituents in para- and meta-position (**25**, **26**) are, probably on account of steric hindrance, also detrimental to potency. If the phenyl ring in **1** is replaced by a thiazole ring, the activity against PA3774 is particularly strongly affected suggesting a vital role of the phenyl group in the molecular recognition of PA3774 with was verified as edge-to-face aromatic interaction in the crystal structure of a PA3774/**1** complex (Fig. 2; PDB: 5G11).

These qualitative insights into the modulation of biological activity by variations at the cap group of PFSAHA were expanded by a quantitative structure-activity relationship (QSAR) model on the basis of IC_{50} values for all perfluorinated compounds listed in Table 1 to summarize the relationship between chemical structure and biological activity against the target protein PA3774 using 15 2D physico-chemical descriptors. The model shows good correlation between experimental and predicted $\log_{10}(IC_{50})$ values with a coefficient of determination of 0.85 (Fig. 3).

A direct comparison of SAHA and its perfluorinated analog **1** reveals similar inhibitory activity against PA3774, but dramatically decreased activity of **1** against human HDAC1 and HDAC6 and to a lesser extent the other tested human HDAC isoforms (Table 1). The high selectivity of **1** for PA3774 is supposed to be induced by the only difference between SAHA and **1** with regard to the fluorination of the alkyl spacer. Apart from the L1-loop that is much longer in PA3774 than in human HDACs the crystal structures of the binding site pocket between the entrance and the catalytic zinc ion are highly conserved and superimposing in PA3774 and human HDACs. Moreover, the fundamental importance of flexible loops lining the binding pocket of HDACs, particularly HDAC8, for the molecular recognition of substrates and inhibitors has been recognized by several groups.[20–23] Therefore, we hypothesize that the bulkier nature of **1** along with different flexibilities of the target enzymes may have a considerable effect on selectivity in ligand recognition.

In summary, we prepared and profiled a variety of PFSAHA derivatives on a panel of bacterial and human HDAC enzymes. Compound **1** is a potent inhibitor of PA3774 from *P. aeruginosa* in the nano-molar range and simultaneously extraordinarily selective against human HDACs. Two major structural features were identified which are responsible for both, potency and selectivity, of the PFSAHA analogs against PA3774. Firstly, the perfluorinated alkyl-chain of the active substances fits better into the binding pocket of PA3774 than in human HDACs and, secondly, the active site binding pocket of PA3774 is formed by the surfaces of two interacting monomers in head-to-head dimers and the phenyl ring of **1** undergoes edge-to-face pi-stacking with a phenylalanine of the opposite monomer. The structure-activity relationship for PA3774 suggests that potentially favorable hydrophobic interactions of meta- or para-substituents at the phenyl ring of PFSAHA analogs with the upper hydrophobic rim of the dimeric binding pocket are overcompensated by adverse steric effects.

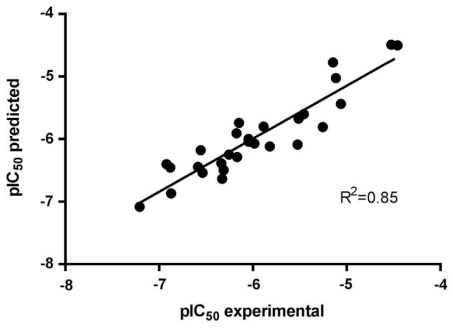

Fig. 3. Correlation of experimental and predicted pIC_{50} values against HDAC like PA3774 from *P. aeruginosa*. Each data point represents one perfluorinated hydroxamic acid analog listed in Table 1. The predicted pIC_{50} values were calculated using a QSAR model based on 15 physico-chemical descriptors.

Acknowledgements

This work was supported by the DFG (grant GZ: ME 3122/2-1).

A. Supplementary material

Detailed synthesis procedures, analytical data, description of biochemical assays and QSAR model. Supplementary data associated with this article can be found, in the online version, at http://dx.doi.org/10.1016/j.bmcl.2017.02.050.

References

1. Marks PA, Breslow R. Dimethyl sulfoxide to vorinostat: development of this histone deacetylase inhibitor as an anticancer drug. *Nat Biotechnol*. 2007;25(1):84–90.
2. Reddy SA. Romidepsin for the treatment of relapsed/refractory cutaneous T-cell lymphoma (mycosis fungoides/Sezary syndrome): use in a community setting. *Crit Rev Oncol Hematol*. 2016;106:99–107.
3. Rashidi A, Cashen AF. Belinostat for the treatment of relapsed or refractory peripheral T-cell lymphoma. *Future Oncol (London, England)*. 2015;11(11):1659–1664.
4. Laubach JP, Moreau P, San-Miguel JF, Richardson PG. Panobinostat for the treatment of multiple myeloma. *Clin Cancer Res*. 2015;21(21):4767–4773.
5. Mielcarek M, Zielonka D, Carnemolla A, Marcinkowski JT, Guidez F. HDAC4 as a potential therapeutic target in neurodegenerative diseases: a summary of recent achievements. *Front Cell Neurosci*. 2015;9:42.
6. Abend A, Kehat I. Histone deacetylases as therapeutic targets – from cancer to cardiac disease. *Pharmacol Ther*. 2015;147:55–62.
7. Fan Z, Yang J, Yang J, Yang C, Ping Z. HDAC inhibition: a novel therapeutic approach for atherosclerosis. *Int J Cardiol*. 2016;202:722–723.
8. Felice C, Lewis A, Armuzzi A, Lindsay JO, Silver A. Review article: selective histone deacetylase isoforms as potential therapeutic targets in inflammatory bowel diseases. *Aliment Pharmacol Ther*. 2015;41(1):26–38.
9. Das Gupta K, Shakespear MR, Iyer A, Fairlie DP, Sweet MJ. Histone deacetylases in monocyte/macrophage development, activation and metabolism: refining HDAC targets for inflammatory and infectious diseases. *Clin Transl Immunol*. 2016;5(1):e62.
10. Andrews KT, Tran TN, Lucke A, et al. Potent antimalarial activity of histone deacetylase inhibitor analogues. *Antimicrob Agents Chemother*. 2008;52(4):1454–1461.
11. Giannini G, Battistuzzi G, Vignola D. Hydroxamic acid based histone deacetylase inhibitors with confirmed activity against the malaria parasite. *Bioorg Med Chem Lett*. 2015;25(3):459–461.
12. Heimburg T, Chakrabarti A, Lancelot J, et al. Structure-based design and synthesis of novel inhibitors targeting HDAC8 from *Schistosoma mansoni* for the treatment of schistosomiasis. *J Med Chem*. 2016.
13. Shlaes DM, Sahm D, Opiela C, Spellberg B. The FDA reboot of antibiotic development. *Antimicrob Agents Chemother*. 2013;57(10):4605–4607.
14. Kramer A, Herzer J, Overhage J, Meyer-Almes FJ. Substrate specificity and function of acetylpolyamine amidohydrolases from *Pseudomonas aeruginosa*. *BMC Biochem*. 2016;17(1):4.
15. Weston CE, Kraemer A, Colin F, et al. Towards photopharmacological antimicrobial chemotherapy using photoswitchable amidohydrolase inhibitors. *ACS Infect Dis*. 2016.
16. Henkes LM, Haus P, Jager F, Ludwig J, Meyer-Almes FJ. Synthesis and biochemical analysis of 2,2,3,3,4,4,5,5,6,6,7,7-dodecafluoro-N-hydroxy-octanediamides as inhibitors of human histone deacetylases. *Bioorg Med Chem*. 2012;20(2):985–995.
17. Wegener D, Hildmann C, Riester D, Schwienhorst A. Improved fluorogenic histone deacetylase assay for high-throughput-screening applications. *Anal Biochem*. 2003;321(2):202–208.
18. Cheng Y-C, Prusoff WH. Relationship between the inhibition constant (K1) and the concentration of inhibitor which causes 50 per cent inhibition (I50) of an enzymatic reaction. *Biochem Pharmacol*. 1973;22(23):3099–3108.
19. Kraemer A, Wagner T, Yildiz Ö, Meyer-Almes FJ. Crystal structure of a histone deacetylase homolog from *Pseudomonas aeruginosa*. *Biochemistry*. 2016. http://dx.doi.org/10.1021/acs.biochem.1026b00613.
20. Deschamps N, Simões-Pires CA, Carrupt P-A, Nurisso A. How the flexibility of human histone deacetylases influences ligand binding: an overview. *Drug Discov Today*. 2015;20(6):736–742.
21. Decroos C, Clausen DJ, Haines BE, Wiest O, Williams RM, Christianson DW. Variable active site loop conformations accommodate the binding of macrocyclic largazole analogues to HDAC8. *Biochemistry*. 2015;54(12):2126–2135.
22. Somoza JR, Skene RJ, Katz BA, et al. Structural snapshots of human HDAC8 provide insights into the class I histone deacetylases. *Structure*. 2004;12(7):1325–1334.
23. Dowling DP, Gantt SL, Gattis SG, Fierke CA, Christianson DW. Structural studies of human histone deacetylase 8 and its site-specific variants complexed with substrate and inhibitors. *Biochemistry*. 2008;47(51):13554–13563.

4.4. Parameters influencing the thermodynamics of the binding of histone deacetylase inhibitors

Title:

The thermodynamic signature of ligand binding to histone deacetylase-like amidohydrolases is most sensitive to the flexibility in the L2-loop lining the active site pocket.

Authors:

Christian Meyners, Andreas Krämer, Özkan Yildiz, Franz-Josef Meyer-Almes

Bibliographic Data:

Biochimica et Biophysica Acta (BBA) - General Subjects

2017, DOI: http://dx.doi.org/10.1016/j.bbagen.2017.04.001

First published online: April 4, 2017

Abstract:

Background

The analysis of the thermodynamic driving forces of ligand-protein binding has been suggested to be a key component for the selection and optimization of active compounds into drug candidates. The binding enthalpy as deduced from isothermal titration calorimetry (ITC) is usually interpreted assuming single-step binding of a ligand to one conformation of the target protein. Although successful in many cases, these assumptions are oversimplified approximations of the reality with flexible proteins and complicated binding mechanism in many if not most cases. The relationship between protein flexibility and thermodynamic signature of ligand binding is largely understudied.

Methods

Directed mutagenesis, X-ray crystallography, enzyme kinetics and ITC methods were combined to dissect the influence of loop flexibility on the thermodynamics and mechanism of ligand binding to histone deacetylase (HDAC)-like amidohydrolases.

Results

The general ligand-protein binding mechanism comprises an energetically demanding gate opening step followed by physical binding. Increased flexibility of the L2-loop in HDAC-like amidohydrolases facilitates access of ligands to the binding pocket resulting in predominantly enthalpy-driven complex formation.

Conclusions

The study provides evidence for the great importance of flexibility adjacent to the active site channel for the mechanism and observed thermodynamic driving forces of molecular recognition in HDAC like enzymes.

General significance

The flexibility or malleability in regions adjacent to binding pockets should be given more attention when designing better drug candidates. The presented case study also suggests that the observed binding enthalpy of protein-ligand systems should be interpreted with caution, since more complicated binding mechanisms may obscure the significance regarding potential drug likeness.

Contributions by C. Meyners:

- Produced the used proteins
- Performed the site-directed mutagenesis
- Executed the ITC experiments and the enzyme activity assays
- Participated in writing the manuscript

ARTICLE IN PRESS

BBA - General Subjects xxx (xxxx) xxx–xxx

Contents lists available at ScienceDirect

BBA - General Subjects

journal homepage: www.elsevier.com/locate/bbagen

The thermodynamic signature of ligand binding to histone deacetylase-like amidohydrolases is most sensitive to the flexibility in the L2-loop lining the active site pocket

Christian Meyners[a], Andreas Krämer[a], Özkan Yildiz[b], Franz-Josef Meyer-Almes[a,*]

[a] Department of Chemical Engineering and Biotechnology, University of Applied Sciences Darmstadt, Haardtring 100, 64295 Darmstadt, Germany
[b] Department of Structural Biology, Max-Planck-Institute of Biophysics, 60438 Frankfurt, Germany

ARTICLE INFO

Keywords:
Thermodynamic signatures
Protein-ligand binding
Histone deacetylases
Binding mechanism
Conformational flexibility

ABSTRACT

Background: The analysis of the thermodynamic driving forces of ligand-protein binding has been suggested to be a key component for the selection and optimization of active compounds into drug candidates. The binding enthalpy as deduced from isothermal titration calorimetry (ITC) is usually interpreted assuming single-step binding of a ligand to one conformation of the target protein. Although successful in many cases, these assumptions are oversimplified approximations of the reality with flexible proteins and complicated binding mechanism in many if not most cases. The relationship between protein flexibility and thermodynamic signature of ligand binding is largely understudied.

Methods: Directed mutagenesis, X-ray crystallography, enzyme kinetics and ITC methods were combined to dissect the influence of loop flexibility on the thermodynamics and mechanism of ligand binding to histone deacetylase (HDAC)-like amidohydrolases.

Results: The general ligand-protein binding mechanism comprises an energetically demanding gate opening step followed by physical binding. Increased flexibility of the L2-loop in HDAC-like amidohydrolases facilitates access of ligands to the binding pocket resulting in predominantly enthalpy-driven complex formation.

Conclusions: The study provides evidence for the great importance of flexibility adjacent to the active site channel for the mechanism and observed thermodynamic driving forces of molecular recognition in HDAC like enzymes.

General significance: The flexibility or malleability in regions adjacent to binding pockets should be given more attention when designing better drug candidates. The presented case study also suggests that the observed binding enthalpy of protein-ligand systems should be interpreted with caution, since more complicated binding mechanisms may obscure the significance regarding potential drug likeness.

1. Introduction

The understanding of the mode and mechanism of ligand binding to proteins is of primary importance for the development of active substances with superior affinity and selectivity to a particular target of interest. Molecular recognition comprises enthalpic effects like the formation or break of hydrogen bonds, salt bridges or other contacts involving polar or nonpolar functional groups as well as entropic contributions like the hydrophobic effect or a change in the flexibility of the molecular system. In reality, there is often an overlap of different contributions which impedes the comprehension of the binding process.

Histone deacetylases (HDACs) have emerged as promising targets for chemotherapeutic intervention in age-related diseases like cancer, neurodegenerative and immune disorders [1–3]. The HDAC enzyme family is subdivided into class I (HDAC1-3 and 8), class IIa (HDAC4,5 and 9), class IIb (HDAC6 and 10), class III (sirtuins SIRT1-7) and class IV (HDAC11). The zinc dependent HDACs of class I, IIa/b and IV operate with a different mechanism than the sirtuins in class III which require NAD^+ for catalysis. Until now, four small molecule ligands of zinc dependent HDACs have been approved as a new therapeutic option for the treatment of different types of cancer (Scheme 1A). Actually, there are increasing efforts to develop next generation HDAC inhibitors particularly with improved selectivity and less unwanted side effects [3]. In the light of the highly conserved binding pocket of HDACs, the development of selective active substances remains a challenging task. Since proteins are dynamic molecules, the flexibility of protein domains

* Corresponding author.
E-mail address: franz-josef.meyer-almes@h-da.de (F.-J. Meyer-Almes).

http://dx.doi.org/10.1016/j.bbagen.2017.04.001
Received 21 November 2016; Received in revised form 8 March 2017; Accepted 2 April 2017

Please cite this article as: Meyners, C., BBA - General Subjects (2017), http://dx.doi.org/10.1016/j.bbagen.2017.04.001

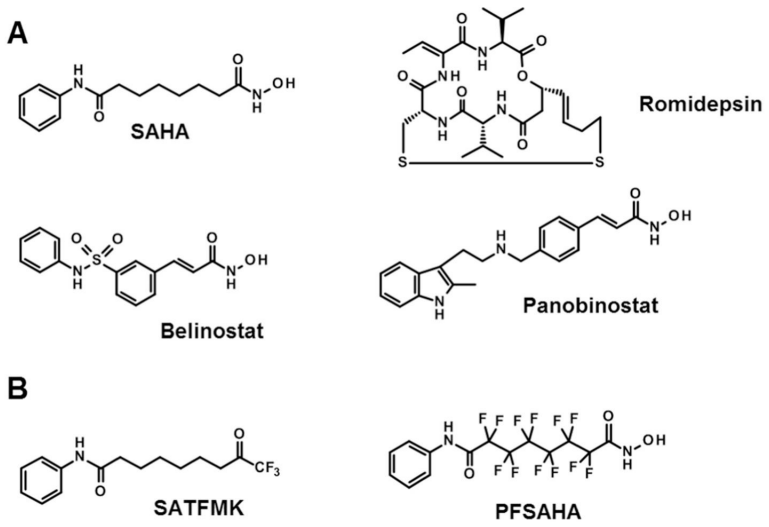

Scheme 1. HDAC inhibitors. A) Approved cancer drugs, B) SAHA analog compounds used in this study.

and particularly loop structures close to the active site binding pocket has earned some attention regarding their impact on ligand binding. HDAC8 is the structurally best characterized human member of Zn^{2+}-dependent HDAC enzymes [4–8]. A characteristic feature among class I HDACs is the striking malleability of the HDAC8 surface and the ability of HDAC8 to accommodate structurally divergent inhibitors in mainly three conformations from wide-open to closed [4,9]. The structural interconversion between these states is essentially accomplished by significant conformational changes of the L1-loop. A recent study showed that sterically demanding macrocyclic Largazole analogues induced alternative conformational changes in both, the L1 and L2-loop. In addition, molecular dynamics simulations and crystal structures of HDAC8-ligand complexes prove the interaction of L1 and L2-loops through K33 (L1-loop) and D101 (L2-loop) [9,10]. The L1 and L2-loop are the most variable regions within HDACs of class I. Different ligand binding between HDAC1 and HDAC8 is for the most part attributed to the L1-loop in HDAC1 which is four amino acids longer than in HDAC8 and appears more rigid compared with HDAC8 as suggested by molecular dynamics simulation studies [11]. Therefore, the enhanced malleability and the different types of interplay between L1 and L2-loop are suggested to be key factors for the accommodation of structurally diverse ligands and have great impact on the selective recognition of substrates and inhibitors.

However, the relationship between hotspots of malleability and the thermodynamics of ligand binding to HDACs has not been investigated before. As a suitable model system of class II HDACs to study the switchover from a rather rigid to a flexible L2-loop lining the active site pocket, two bacterial HDAC like amidohydrolases with high identity of 44 % over the full length of 354 amino acids and more importantly a very high structural similarity with an rmsd (Cα) of 0.853Å were exploited. Among human HDACs HDAC6 is the closest homolog of the histone deacetylase like amidohydrolase from *Bordetella/Alcaligenes* ($HDAH_{bo}$) [12] and *Pseudomonas aeruginosa* ($HDAH_{pa}$) [13] with genome locus tag PA3774 [14]. $HDAH_{bo}$ or $HDAH_{pa}$ share 35% identical residues with the second catalytic domain (CD2) of HDAC6 over 354 residues (Fig. S1). Both, $HDAH_{bo}$ and $HDAH_{pa}$, are inhibited by the pan-inhibitor N-hydroxy-N′-phenyloctanediamide (SAHA) and two closely related analogs 9,9,9-trifluoro-8-oxo-N-phenylnonanamide (SATFMK) [12] and 2,2,3,3,4,4,5,5,6,6,7,7-dodecafluoro-N-hydroxy-N′-phenyloctanediamide (PFSAHA) [15] albeit with different affinities (Scheme 1B). The relationship between the flexibility of the L2-loop in the HDAC like amidohydrolases and the thermodynamic signature of ligand binding was studied combining site-directed mutagenesis, crystal structure analysis and isothermal microcalorimetry.

2. Materials and methods

2.1. Enzyme activity assays

The activity of $HDAH_{bo}$, $HDAH_{bo}$ variants and $HDAH_{pa}$ was determined by a colorimetric assay as described by Wegener et al. [16] in black half area 96-well microplates (Greiner bio-one, Germany). A serial dilution of the substrate Boc-Lys(trifluoracetyl)-AMC in assay buffer (25 mM Tris-HCl pH 8.0, 50 mM NaCl and 0.001% pluronic F-68) was tempered to 30 °C. The reaction was initiated by the addition of 100 nM $HDAH_{bo}$, $HDAH_{bo}$ variant or 10 nM $HDAH_{pa}$ and 0.5 mg/ml trypsin. The release of AMC was followed in a fluorescence microplate reader (PHERAstar FS, BMG LABTECH) and the slope was used to calculate the enzyme activity. The obtained data was fitted to the implemented Michaelis-Menten model of prism 5 (GraphPad Software, USA).

2.2. Isothermal titration calorimetry

In order to determine the K_d-values and the thermodynamic parameters ΔH^0 and ΔS^0 of the binding of PFSAHA and SATFMK to $HDAH_{bo}$, $HDAH_{bo}$ variants and $HDAH_{pa}$ ITC experiments were carried out. Therefore, 5 to 20 µM of the respective protein in buffer were placed in the sample cell of an ITC200 (Microcal, USA) instrument and the syringe of the instrument was filled with 50 to 200 µM of the ligand. After equilibrating the cells to 30 °C the ligand concentration was increased stepwise by 1.5 to 3 µl injections until only dilution heat was measured. The obtained data points were corrected for the dilution heat and fitted to a one site binding model using Origin 7 (OriginLab Corporation, USA). In order to exclude heat produced from protonation effects experiments were carried out at pH 8.0 in three different buffers consisting of 50 mM NaCl and 25 mM Tris-HCl or 25 mM triethanolamine (TEA) or 25 mM HEPES. The resulting values for the binding enthalpy ΔH^0_{obs} were plotted against the ionization enthalpy ΔH^0_{ion} of the respective buffer and fitted with a linear regression yielding the intrinsic binding enthalpy ΔH^0_{ins} and the stoichiometry of the protonation.

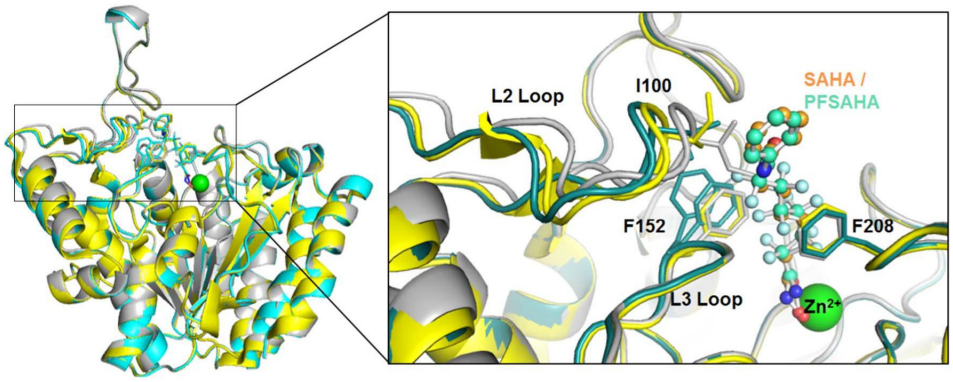

Fig. 1. Superimposition of crystal structures of ligand-free $HDAH_{bo}$ (PDB ID: 5G1B; gray) and $HDAH_{bo}$ in complex with SAHA (PDB ID: 1ZZ1; yellow) and PFSAHA (PDB ID: 5G1A; cyan). In the inset, the binding pocket is represented at larger scale with L2-loop (92-104) including gatekeeper I100 and part of L3-loop (148-154) including F152 lining one face of the binding pocket filled with SAHA (orange) and PFSAHA (cyan). The complex with PFSAHA shows two different occurring conformations of F152.

2.3. Crystallization and data collection

Crystals of native and mutated $HDAH_{bo}$ were grown by hanging drop vapor diffusion against 500 µl reservoir. For $HDAH_{bo}$ T101A the protein was co-crystallized with the inhibitor by adding a 10 fold molar excess to the protein solution. In all cases, the reservoir solution contained 0.1 M malate-imadazole buffer (pH 5.25) and 3–6% PEG400. The reservoir solution and protein (10 mg/ml) were mixed in a 1:1 ratio to a final volume of 4 µl. Crystals grew in three to ten days at 20 °C. The obtained crystals of $HDAH_{bo}$ were soaked with the inhibitor added in 10 fold molar excess directly to the drop and incubated for at least 24 h. Cryoprotection was achieved by washing the crystals in 0.1 M malate-imadazole buffer with a pH of 5.25 and 30% PEG400. The cryoprotected crystals were flash-frozen in liquid nitrogen. Diffraction data were collected at 100 K on beamline PXII at the Swiss Light Source (SLS, Villigen, Switzerland).

2.4. Structure determination and refinement

Diffraction data were indexed and integrated using iMOSFLM [17] and scaled with AIMLESS [18]. The structure was determined by molecular replacement with MOLREP [19] using the $HDAH_{bo}$ structure (PDB ID: 5G1C) as a model [20]. Model building was carried out in COOT [21] and REFMAC5 [22] was used for refinement. All used programs belong to the CCP4 suite [23]. Water molecules were added automatically with COOT and afterwards checked manually for reasonably hydrogen bonding.

3. Results and discussion

Previous studies with HDAC8 revealed a striking malleability of the protein surface. Interconversions between different conformations of L1 and L2-loops as well as interactions between both loops were suggested to correlate with the accommodation of sterically demanding ligands as well as enzyme activity [4,9,10]. The structure of the closest human HDAC homolog, HDAC6, has been determined recently [24,25]. The geometry of the catalytic site is highly conserved among $HDAH_{bo}$, $HDAH_{pa}$, and both catalytic domains of HDAC6 and HDAC8 (Fig. S2). Accordingly, all loops flanking the catalytic site show high sequence similarity with the exception of the highly variable L1- and L2-loops. In contrast to HDAC8, the L1- and L2-loops in the crystal structure of the CD2 domain in HDAC6 were found to be relatively rigid [24].

These striking differences in variability and loop-flexibility of L1- and L2-loops among HDAC homologs inspired this investigation to dissect the relationship between loop flexibility and thermodynamic signature of ligand binding to bacterial homologs of the human HDACs. The chosen enzymes, $HDAH_{bo}$ and $HDAH_{pa}$, show high sequential and structural homology and both form a tetramer composed of two "head-to-head" dimers [12,26]. By a single amino acid exchange in the L2-loop (T101A), the flexibility of $HDAH_{bo}$ was dramatically increased while preserving the overall structural similarity (Fig. 4C). This rational induction of substantial flexibility in the L2-loop allowed for an unconfounded analysis of the accompanying effects on the driving forces of ligand binding by combining site directed mutagenesis, crystal structure analysis and isothermal titration microcalorimetry.

3.1. Sterically demanding inhibitors widen the binding pocket of $HDAH_{bo}$ on one side

To investigate the impact of structurally closely related inhibitors with different steric demands within the binding pocket, we determined the high-resolution crystal structures of wild type $HDAH_{bo}$ in the apo form and in complex with the inhibitor PFSAHA. In addition, we crystallized and determined the structure of the $HDAH_{bo}$ variant T101A in complex with the inhibitor SATFMK (PDB ID: 5G17). For comparison, the crystal structure of the complex with SAHA and SATFMK were taken from the protein data bank (PDB ID: 1ZZ1, 2GH6) [12].

The crystal structures of native enzyme and ligand bound complexes superimpose well (Fig. 1). Significant deviations can only be observed in the L2-loop adjacent to the binding pocket and the connected H5 α-helix. In the native structure of $HDAH_{bo}$ I100 at the rim of the binding pocket adopts an inward conformation resulting in a closed channel entrance (Fig. 1). In the presence of SAHA and PFSAHA the L2-loop is turned to the side and the Cα-atom of I100 is moved by 1.8 Å and 2.8 Å, respectively, resulting in an open binding pocket. As expected, the thicker perfluorinated alkyl linker of PFSAHA causes a larger shift of the L2-loop than the thinner alkyl linker of SAHA. At the same time, F152 in the L3-loop is significantly displaced outwards in the presence of PFSAHA whereas the complex with SAHA shows no notable movement of this pocket lining residue with respect to the unbound enzyme. The flexibility of the F152 residue is demonstrated by two populated conformations in the complex between $HDAH_{bo}$ and PFSAHA. The particular mobility of F152 in $HDAH_{bo}$ is also observed for the corresponding amino acids in crystal structures of human HDACs. The extraordinary displacement of the corresponding F152 is also seen in HDAC8. This structurally by far best investigated HDAC, reveals three major states, wide-open (PDB ID: 1VKG), sub-open (PDB ID: 1T64) and closed (PDB ID: 1T69), in complex with structurally divergent inhibitors (See Table 1).

Table 1
Data collection and refinement statistics.

Dataset	$HDAH_{bo}$ PFSAHA	$HDAH_{bo}$ nativ	$HDAH_{bo}$ T101A SATFMK
PDB code	5G1A	5G1B	5G17
Data processing			
Space group	$P4_22_12$	$P4_22_12$	$P4_22_12$
a, b, c (Å)	101.4, 101.4, 175.9	100.7, 100.7, 175.1	101.3, 101.3, 175.2
α, β, γ (deg)	90.0, 90.0, 90.0	90.0, 90.0, 90.0	90.0, 90.0, 90.0
I/sd(I)[a]	11.8 (2.3)	8.4 (2.3)	11.5 (2.7)
Wavelength (Å)	1.00002	0.99988	1.03894
Resolution range (Å)	87.96–1.42	87.56–1.70	87.68–1.51
Overall observations	1138350	789531	1691308
Unique reflections	168945	99299	142442
Completeness (%)[a]	97.4 (95.4)	100.0 (100.0)	100.0 (100.0)
Multiplicity[a]	6.7 (7.1)	8.0 (8.2)	11.9 (12.2)
R_{pim}[b]	0.035 (0.373)	0.052 (0.336)	0.038 (0.317)
Refinement			
R_{cryst}[c]	0.1435	0.1517	0.1297
R_{free}[d]	0.1701	0.1915	0.1579
Total atoms[e]	6728	6595	6505
Protein residues[e]	740	743	737
Ligand molecules[e]	2	2	2
Metal ions[e]	6	6	6
Water[e]	933	915	915
PEG molecules[e]	10	8	
Rmsd from ideal			
Bond lengths (Å)	0.0082	0.0100	0.0132
Bond angles (deg)	1.520	1.508	1.509
Ramachandran plot (%)			
Most favoured	96.89	96.70	96.42
Allowed	2.55	2.47	2.89
Outliers	0.57	0.82	0.69

[a] Number in parentheses refer to the outer shell.
[b] Given the high multiplicity for the outer shells of these data sets, R_{pim} is a more appropriate measure of the data quality than R_{merge}.
[c] $R_{cryst} = \Sigma||F_o| - |F_c|| / \Sigma |F_o|$, where F_o and F_c are the structure factor amplitudes from the data and the model, respectively. Intensity calculated from replicate.
[d] R_{free} is R_{cryst} with 5% of test set structure factors data.
[e] Per asymmetric unit.

3.2. Similar binding poses of ligands within $HDAH_{bo}$ and $HDAH_{pa}$

In general, the structurally closely related ligands SAHA, PFSAHA and SATFMK bind to $HDAH_{bo}$ and $HDAH_{pa}$ in a very similar fashion (Figs. 2B and 3). However, when comparing matched ligand-enzyme complexes for $HDAH_{bo}$ and $HDAH_{pa}$ distinct differences are observed for the dihedral angles of the linker and the phenyl cap group (Fig. 3). The (perfluoro-) alkyl chains of SAHA and PFSAHA adopt an energetically more unfavorable bent conformation when complexed with $HDAH_{bo}$ compared with PFSAHA bound to $HDAH_{pa}$ with a relaxed straight linker (Fig. 3B,C,D) [26]. Interestingly, the bent binding poses of SAHA and its perfluorinated analog PFSAHA to $HDAH_{bo}$ are in perfect agreement (Fig. 3D) and in contrast to the straight conformations of PFSAHA and SATFMK in complex with $HDAH_{pa}$ indicating subtle but distinct differences between both binding pockets (Fig. 3A,B). The energetically unfavorable conformation of the perfluorinated linker in PFSAHA leads to a 2-fold increase of the K_d-value from 130 nM with the relaxed linker in the $HDAH_{pa}$ complex versus 270 nM with the distorted linker in the $HDAH_{bo}$ complexes, respectively. Interestingly, there is a structural water molecule in $HDAH_{bo}$ complexes with SAHA and PFSAHA bridging the carboxyl group of D98, the backbone nitrogen of G151 and the amide nitrogen of SAHA and PFSAHA in the binding pose with unfavorable diehedral angles (Fig. 3E). In $HDAH_{pa}$ the sequence and structure in this particular L2-loop region is different from $HDAH_{bo}$ (Fig. S2) not allowing for a comparable arrangement of a structural water molecule connecting protein and ligand. The space filling amino acids Q100 and D101 in $HDAH_{pa}$ potentially hinder the approach of the anilide head group and the L2-loop. Both, $HDAH_{pa}$ and $HDAH_{bo}$, form tetramers which are organized as dimers of "head-to-head" dimers (Fig. 2A). The bridging water molecule and a slightly different arrangement at the "head-to-head" dimer interface may contribute to the stabilization of ligands into the observed binding poses in HDAH.

3.3. The elongated L1-loop in $HDAH_{bo}$ and $HDAH_{pa}$ is stabilized by tetramerization

The HDAC like amidohydrolases $HDAH_{bo}$ and $HDAH_{pa}$ are not only sequentially highly similar (44% identity) (Figs. S1 and S2), but show also excellent structural agreement, particularly in the interior of the enzymes (Fig. 2). The characteristic L1-loop in $HDAH_{bo}$ and $HDAH_{pa}$, which is 23 amino acids longer than in human HDAC8 and 20 residues longer than in CD2 of HDAC6, mediates tetramer formation resulting in a very similar quaternary structure (Fig. 2A) [26]. The localization of the exceeding L1-loop at the tetramerization interface causes its unusually high level of rigidity. The related acetylpolyamine amidohydrolase (APAH) from *M. ramosa* forms a dimer but through an 18-amino acid insert in the L2-loop which is characteristic for APAHs [27]. The APAH-dimers form a "L"-shaped active site tunnel involving the dimerization interface which determines the selectivity for acetylated polyamines as substrates. Consequently, the quaternary structure has been suggested as essential factor defining the specific molecular recognition of substrates and certainly also inhibitors of bacterial members of the HDAC family through confining the access of substrate to the active site and probably also enabling additional favorable contacts between ligands and the multimeric enzyme [26].

Protein-protein interactions are also observed with human HDACs that are often involved in multi-protein complexes required to recruit the HDACs to a particular target or regulate its function. Interestingly, recent co-immuno precipitation experiments suggest that human HDACs 1 and 2 are also able to form homo- or heterodimers within HDAC corepressor multi-protein complexes [28]. In addition, the activity of these HDACs was shown to depend on dimer formation.

Another striking example for the regulation of HDAC activity through heteromeric protein-protein interaction is the inositol tetraphosphate mediated interaction between HDAC3 and the deacetylase-activation-domain DAD from the SMRT corepressor [29]. Further studies are necessary to obtain a greater understanding of how homo- and heteromeric protein-protein interactions with HDAC enzymes stabilize particular conformations or modulate the flexibility of regions adjacent to the active site pocket thereby determining the mode and specificity of interactions with ligands and substrates. While the L1-loop in $HDAH_{bo}$ and $HDAH_{pa}$ is tightly packed to the opposing protein subunits, the L1-loop in HDAC8 can move outward to form the wide-open state (PDB ID: 1VKG) or toward the active site pocket thereby creating the closed state (PDB ID: 1T69) and occluding the second pocket in the complex with TSA (PDB ID: 1T64). K33 in the L1-loop of HDAC8 can either interact with the F152 side chain lining the binding pocket occluding the second pocket or turn away from K33 to create the open state conformer. Another difference in the functionality of the L1-loop is the dynamic interaction between the L1- and L2-loop of HDAC8 which was suggested to influence the activity of the enzyme using molecular dynamics simulations [10]. This interaction is not possible in HDAC6 (CD1 or CD2), $HDAH_{bo}$ or $HDAH_{pa}$, because there is no lysine residue at a corresponding position in the L1-loop and the counterpart with the triple aspartate pattern (D87-D89) in the L2-loop of HDAC8 is missing. Moreover, the L1-loop of the bacterial enzymes is largely extended at the position of K33 in HDAC8 and folds in a completely different shape without contacts to the L2-loop. The L1-loop of CD2 in HDAC6 is 5 residues longer than the corresponding loop in HDAC8. The decreasing length of the L1-loop from $HDAH_{bo}$/$HDAH_{pa}$ to HDAC6 to HDAC8 lowers the rim of the active site pocket thereby modulating the access of substrates and inhibitors. In the special case of $HDAH_{bo}$ and

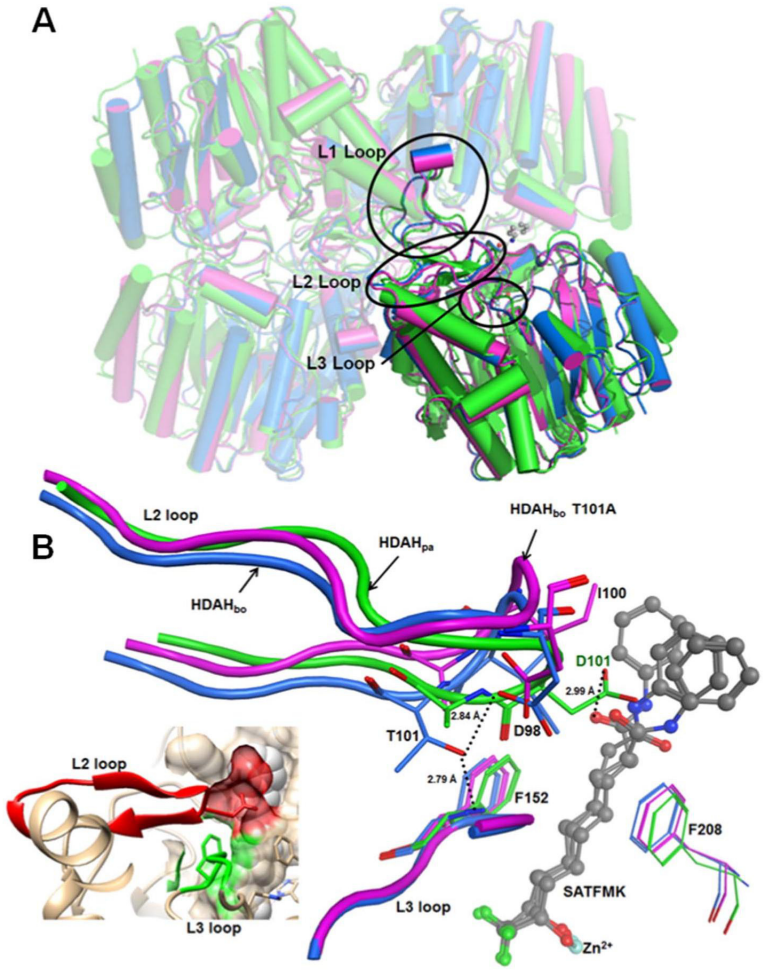

Fig. 2. Crystal structures of HDAH$_{bo}$ (blue, PDB ID: 2GH6), HDAH$_{bo}$ T101A (magenta, PDB ID: 5G17) and HDAH$_{pa}$ (green, PDB ID: 5G10) bound to SATFMK. Black numbers denote amino acids in HDAH$_{bo}$, the green number relates to the corresponding amino acid in HDAH$_{pa}$. A) Similar overal arrangement of the decisive "head-to-head" dimers (two of them form a tetramer organized as a dimer of "head-to-head" dimers). B) L2 and L3-loops lining one face of the binding pocket. The crucial T101 in HDAH$_{bo}$ stabilizes and locates the L2-loop through a simultaneous H-bond network to D98 and F152 in the L3-loop. Gatekeeper I100 in the HDAH$_{bo}$ mutants is substituted by D101 in HDAH$_{pa}$. The inset in the lower left corner demonstrates that one side of the binding pocket is completely lined by the L2 (red) and L3-loop (green).

HDAH$_{pa}$, the molecular recognition of ligands is also determined by the tetrameric quaternary structure [26]. The presented distinct differences in length and sequence of the L1-loops of bacterial and eukaryotic members of the HDAC family determine completely different structural features ranging from mediation of tetramerization in HDAH$_{bo}$ and HDAH$_{pa}$ to surface malleability through dynamic interactions with the L2-loop and F152 in HDAC8. Since the versatile L1-loop is located in the vicinity of the active site pocket, it is supposed to exert substantial influence on the interaction with ligands.

3.4. The L2-loop in HDAH$_{bo}$ is stabilized through a hydrogen bond network and connected to the L3-loop

Although the active site pocket is highly conserved between HDAH$_{bo}$ and HDAH$_{pa}$, there are some important differences particularly on the side lined by the L2 and L3-loop (Fig. 2). Whilst the deeper buried L3-loop and the other loops lining the binding channel in HDAH$_{bo}$ and HDAH$_{pa}$ superimpose to a high degree, the corresponding L2-loops show significant differences. The L2-loop of HDAH$_{pa}$ is two amino acid shorter (Fig. S2) than the corresponding loop in HDAH$_{bo}$ and the analysis of the crystal structures reveals that T101 in the L2-loop of HDAH$_{bo}$ is the center of a hydrogen bond network that connects the L2 and L3-loop and stabilizes the L2-loop by forming hydrogen bonds to one carboxyl oxygen of D98 (L2-loop) and the backbone nitrogens of G151 and F152 (both L3-loop), respectively, through its hydroxyl oxygen (Fig. 2B). An additional hydrogen bond between D98 and G151 reinforces the connection between the L2 and L3-loop. In HDAH$_{pa}$, the pivotal T101 is substituted by alanine (Figs. 2B and S2). To evaluate the hypothesis about the central role of T101 in stabilizing the L2-loop of HDAH$_{bo}$, a T101A variant was generated and also crystallized in complex with SATFMK (Fig. 4AB). Since we compare the crystal structures of HDAH$_{bo}$ and HDAH$_{bo}$ T101A in complex with the same molecule, SATFMK, ligand effects on the local flexibility largely cancel out. The normalized B-factors of the main chain Cα-atoms for free HDAH$_{bo}$ and HDAH$_{bo}$ in complex with PFSAHA or SATFMK are very similar for each residue, but slightly increased for the

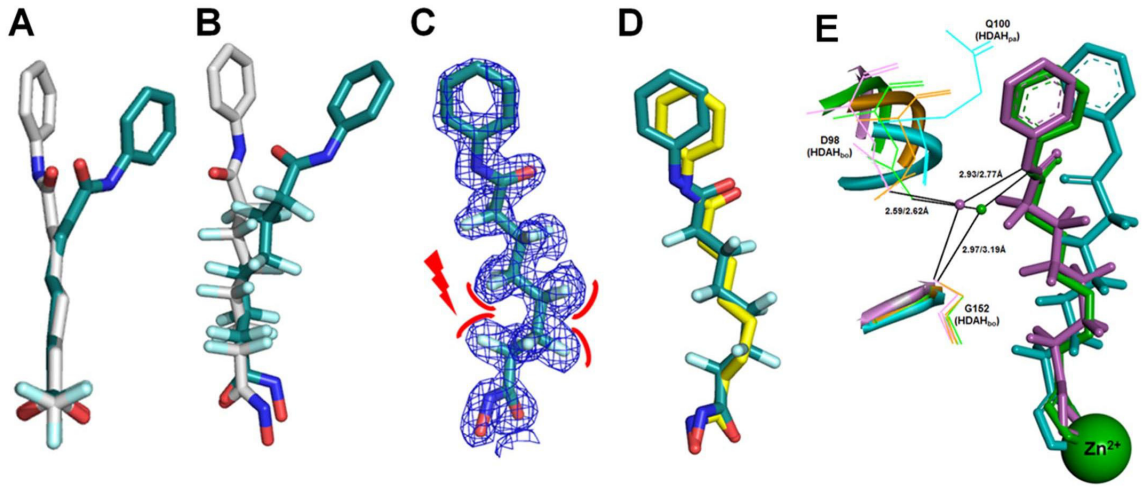

Fig. 3. Ligand poses of SATFMK, SAHA and PFSAHA in crystal structures of complexes with $HDAH_{bo}$ and $HDAH_{pa}$. A) SATFMK bound to $HDAH_{bo}$ (cyan, PDB ID: 2GH6), and $HDAH_{pa}$ (light gray, PDB ID: 5G10) B) PFSAHA bound to $HDAH_{bo}$ (cyan, PDB ID: 5G1A), and $HDAH_{pa}$ Y313F (light gray, PDB ID: 5G11) C) Electron density map ($2F_o$-F_c contoured at 1 σ) of PFSAHA bound to $HDAH_{bo}$ with unfavorable distortion of perfluorinated alkyl backbone. D) Overlay of superimposed SAHA (yellow, PDB ID: 1ZZ1) and PFSAHA (cyan, PDB ID: 5G1A) complexed with $HDAH_{bo}$ showing very good agreement. E) A bridging water molecule connects the ligands SAHA (green, PDB ID: 1ZZ1 chain A) and PFSAHA (magenta, PDB ID: 5G1A) with D98 and G151 in $HDAH_{bo}$.

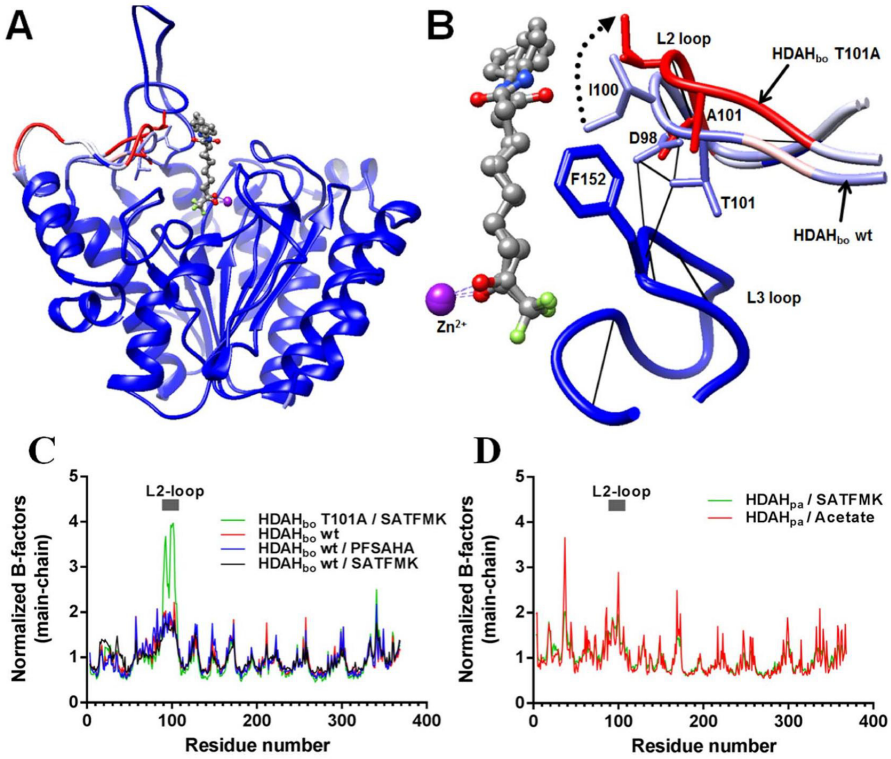

Fig. 4. Comparison of crystal structures and normalized B-factors. A) Superimposed structures of $HDAH_{bo}$ wt (PDB ID: 2GH6) and $HDAH_{bo}$ T101A (PDB ID: 5G17) each complexed with SATFMK (ball and stick models with elementary coloring). The ribbons are colored according to averaged B-factor of the corresponding amino acid to indicate flexible regions (flexible: red, rigid: dark blue); the catalytic zinc ion is shown as a purple sphere. B) Enlarged view of the L2- and L3 loop of $HDAH_{bo}$ wt and $HDAH_{bo}$ T101A. Intramolecular hydrogen bonds are represented by black lines. In $HDAH_{bo}$ wt the central amino acid T101 forms a hydrogen bond network with D98, G151 and F152 connecting and stabilizing the L2- and L3-loop. These hydrogen bonds do not longer exist in the T101A mutant resulting in a shift and increased flexibility of the L2-loop.C) Normalized B-factors of the main chain Cα-atoms of free $HDAH_{bo}$ wt, $HDAH_{bo}$ wt in complex with indicated inhibitors and the complex between $HDAH_{bo}$ T101A and SATFMK as well as D) normalized B-factors of $HDAH_{pa}$ complexed with SATFMK or acetate. The L2-loop (aa 90-106) is marked by a grey bar.

L2-loop (residues 96-102) with respect to the average B-factor of the entire protein sequence (Fig. 4C). The flexibility of the L2-loop in $HDAH_{bo}$ T101A in terms of normalized B-factors is significantly increased (3-fold with regard of the entire protein) as compared with the wildtype enzyme or complexes between $HDAH_{bo}$ wt and SATFMK or PFSAHA (Fig. 4C). The central threonine of the L2-loop stabilizing hydrogen bond network in $HDAH_{bo}$ is not present in $HDAH_{pa}$, but a single hydrogen bond between the carbonyl oxygen of D101 and the amide nitrogen of F152 provides some degree of stabilization to the L2-loop of $HDAH_{pa}$. The L2-loop of human HDAC8 is also known as a region of enhanced flexibility. In crystal structures of unbound HDAC8 the L2-loop is disordered but becomes structured through stabilizing interactions with bound ligands [4,7]. In contrast, unbound $HDAH_{bo}$ exhibits a L2-loop which is similarly flexible than in its complexes with SATFMK or PFSAHA (Fig. 4C). There is also no significant difference in the flexibility of the L2-loop in $HDAH_{pa}$ when complexed with the small ligand acetate or the larger SATFMK or PFSAHA (Fig. 4D). The L2-loop in the second catalytic domain (CD2) of HDAC6 is considerable rigid [24] which may result at least partly from an α-helical secondary substructure which differs from the β-sheet in the L2-loop of $HDAH_{bo}$ and $HDAH_{pa}$. Thus, the L2-loops in HDAC8, HDAC6, and $HDAH_{bo}$/$HDAH_{pa}$ together with the above discussed L1-loops consist not only of the most variable sequences in loops flanking the active site, but also differ considerably in shape and flexibility. Interestingly, a simple substitution of the pivotal T101 in $HDAH_{bo}$ by alanine renders the L2-loop highly flexible confirming the central role of T101 in a hydrogen network stabilizing this loop. The L2-loop lines the active site channel of HDAC enzymes. Therefore, the dynamics and malleability of this loop is supposed to be highly important for binding of substrates and inhibitors. The crystal structures of $HDAH_{bo}$ and $HDAH_{bo}$ T101A in complex with the same inhibitor SATFMK exhibit different flexibilities of the L2-loop and are the basis for the following molecular interpretation of the thermodynamics of ligand binding to HDAC-like enzymes and to get a deeper insight in the mechanism of binding.

3.5. Enzyme kinetics of HDAC-like amidohydrolases

The influence of mutations in the L2-loop region on the enzyme kinetics of $HDAH_{pa}$ and the $HDAH_{bo}$ variants was investigated using a continuous fluorogenic enzyme activity assay. $HDAH_{pa}$ showed an almost 9-fold higher catalytic efficiency in terms of k_{cat}/K_m than $HDAH_{bo}$ (Table 2, Fig. S3). This may be attributed to D101 in $HDAH_{pa}$, which corresponds to D101 in HDAC8 and most other human HDACs that is essential for substrate recognition; substitution of D101 by alanine in HDAC8 renders the enzyme inactive [8]. However, $HDAH_{bo}$ with a corresponding isoleucine residue at this position is still active although about one order of magnitude smaller. Since I100 partly occludes the active site pocket in free HDAH and is pushed to the side by ligands that bind to $HDAH_{bo}$, the side chain of I100 is able to control access to the active site and believed to function as a gatekeeper. Substitution of I100 by alanine negatively influenced the molecular recognition of substrate as indicated by an about 3-fold increase in K_m

Table 2
Michaelis-Menten parameters of enzyme kinetics of indicated enzymes using the enzyme activity assay described in the methods section.

Enzyme	K_m /μM	V_{max} /pmole/(s*nmole)	k_{cat} /s^{-1}	k_{cat}/K_m/(M^{-1} s^{-1})
$HDAH_{bo}$	10 ± 1	10 ± 1	0.010 ± 0.001	1000 ± 140
$HDAH_{bo}$ I100A	28 ± 6	13 ± 2	0.013 ± 0.002	460 ± 120
$HDAH_{bo}$ T101A	4.1 ± 0.6	4.7 ± 0.2	0.0047 ± 0.0002	1150 ± 170
$HDAH_{pa}$	11 ± 1	93 ± 1	0.093 ± 0.001	8450 ± 770

reducing the catalytic efficiency by a factor of about 2. In contrast, the catalytical efficiency of the $HDAH_{bo}$ T101A variant remains unchanged with respect to $HDAH_{bo}$ while both, K_m and V_{max}, are reduced to half of the original value. Thus, the HDAH mutants remain functional and show roughly the same enzyme activity than the HDAH wildtype, but are about one order of magnitude less efficient enzymes than HDAHpa.

3.6. The thermodynamic signatures of ligand binding strongly depends on the flexibility of the L2-loop

The dissection of the thermodynamic driving forces of drug binding to a particular target has been proposed to guide the selection and optimization of the most promising drug candidates. The basic idea is that favorable enthalpy contributions indicate the formation of well oriented hydrogen bonds and van-der-Waals contacts representing specific interactions, whereas favorable entropic contributions stand for an unspecific hydrophobic effect or a decrease of order in the entire system. Therefore, compounds with sufficient potency and the highest possible $\Delta H^0/\Delta G^0$ ratio are supposed to bear the greatest potential for safe drugs with reduced side effects and the lowest risk to fail during the drug development process [30,31]. Typically, the binding of a number of diverse new chemical entities to one particular target protein of interest is analyzed for that purpose. The previous analysis of protein-ligand complex structures in this study suggested prominent roles for I100 as gatekeeper which limits access to the active site pocket in $HDAH_{bo}$ and for T101 as pivotal amino acid in the stabilization of the L2-loop. The influence of these amino acids and the corresponding flexibility of the L2-loop on the thermodynamic signature of ligand binding was analyzed combining our crystal structures with site directed mutagenesis and ITC measurements. The experiments include binding of two ligands, SATFMK and PFSAHA, to $HDAH_{bo}$, its variants $HDAH_{bo}$ I100A and $HDAH_{bo}$ T101A as well as $HDAH_{pa}$. Notably, the binding poses of SATFMK within the highly conserved binding pockets of $HDAH_{bo}$ and $HDAH_{bo}$ T101A are very similar (Fig. 2B) and the main contacts are even identical (Fig. 2B). The formation of both complexes is characterized by similar affinities and thermodynamic signatures with predominantly favorable binding enthalpy. The affinity of SATFMK to $HDAH_{bo}$ I100A is comparable with the other $HDAH_{bo}$ variants, but SATFMK binding to $HDAH_{bo}$ I100A shows significant enthalpy-entropy compensation. The closest distance between a pair of carbons from the side chain of I100 and the alkyl linker of SATFMK in complex with $HDAH_{bo}$ is 3.5 Å (PDB ID: 2GH6) indicating hydrophobic interactions. Without direct prove it appears reasonable that replacement of the extended I100 by the shorter alanine may lead to weaker hydrophobic interactions between SATFMK and $HDAH_{bo}$ I100A but increased residual flexibility of both, protein and ligand, resulting in a balanced thermodynamic profile with about equal enthalpic and entropic contributions to binding. The bulkier PFSAHA requires much more structural rearrangement around the binding pocket than SATFMK and induces a more pronounced effect on the thermodynamic signature upon binding to the different variants of $HDAH_{bo}$. Like for SATFMK, the affinity of PFSAHA to $HDAH_{bo}$, $HDAH_{bo}$ I100A and $HDAH_{bo}$ T101A is very similar. However, the thermodynamic signatures of PFSAHA binding to these protein variants that differ in only one amino acid change significantly from balanced enthalpy-/entropy- driven ($HDAH_{bo}$) to solely enthalpy-driven ($HDAH_{bo}$ I100A and $HDAH_{bo}$ T101A). It is conceivable that the mechanism of binding involves more than one simple recognition step and that the gatekeeper I100 must turn outwards in a preceding step to allow free access to the binding pocket. The movement of I100 upon ligand binding was shown to be connected to a shift of the complete L2-loop which is supposed to have consequences for the enthalpy as well as the entropy of the system. In the crystal structure of the PFSAHA complex with $HDAH_{bo}$ the L2-loop is strongly shifted by about 2.5 Å (Cα of I100) to accommodate the bulky perfluorinated alkyl linker of PFSAHA, whereas SATFMK causes a significantly smaller shift of about 0.38 Å (PDB ID: 2GH6, chain A). In

Table 3
Thermodynamic parameters of SATFMK and PFSAHA binding to indicated protein variants at 30 °C. The binding enthalpy ΔH^0_{ins} was determined by ITC from 4 to 6 experiments in 2–3 different buffer systems by extrapolation to 0 contribution of buffer ionization. The K_d-values and the binding entropy $-T\Delta S^0$ were determined by ITC from 4 to 6 independent experiments and are reported as mean ± SEM.

Protein	SATFMK			PFSAHA		
	K_d /μM	ΔH^0_{ins} /kJ*mol^{-1}	$-T\Delta S^0$ /kJ*mol^{-1}	K_d /μM	ΔH^0_{ins} /kJ*mol^{-1}	$-T\Delta S^0$ /kJ*mol^{-1}
$HDAH_{bo}$	0.23 ± 0.03	−32 ± 2	−6 ± 2	0.27 ± 0.07	−17 ± 1	−22 ± 1
$HDAH_{bo}$ I100A	0.17 ± 0.04	−20 ± 1	−19 ± 1	0.18 ± 0.05	−44 ± 2	4 ± 2
$HDAH_{bo}$ T101A	0.20 ± 0.05	−40 ± 4	0.9 ± 4	0.25 ± 0.05	−57 ± 3	19 ± 3
$HDAH_{pa}$	0.004 ± 0.003	−24 ± 1	−25 ± 2	0.13 ± 0.03	−61 ± 2	21 ± 2

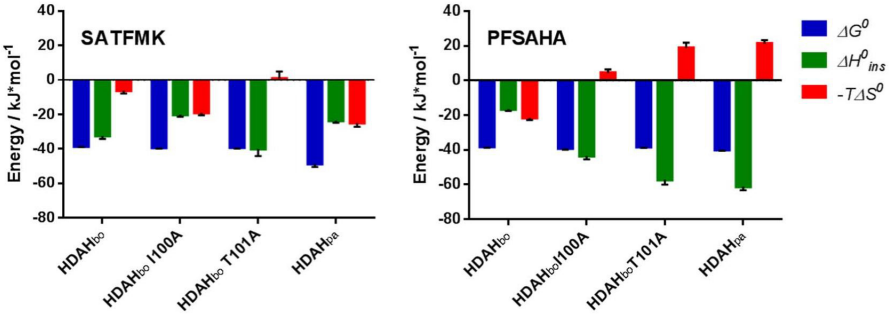

Fig. 5. Thermodynamic signatures of SATFMK and PFSAHA binding to indicated enzymes at 30 °C. Thermodynamic parameters were determined by ITC and calculated from 4 to 6 independent measurements.

addition, F152 is also clearly moved to the side by PFSAHA (PDB ID: 5G1A; Fig. 1) but not by SATFMK (PDB ID: 2GH6). The movement of the L2-loop in unbound $HDAH_{bo}$ upon binding to PFSAHA is supposed to have a negative impact on the hydrogen bond network around the pivotal T101 which stabilizes the L2 loop and connects it to the L3 loop resulting in unfavorable enthalpy (Fig. 2B). The presumed unfavorable positive change in the enthalpy of the preceding gate opening step, which involves movement of I100 and the L2-loop, may compensate for a negative intrinsic enthalpy of the subsequent binding step. When I100 is substituted by alanine, the movement of the L2-loop is less of a requirement to accommodate the bulky PFSAHA yielding a more negative overall binding enthalpy. A possible unfavorable enthalpy effect due to the I100A substitution as observed for SATFMK is supposed to be overcompensated by stronger hydrophobic interactions with the perfluorinated linker of PFSAHA which become also obvious in the PFSAHA/$HDAH_{bo}$ T101A complex. As shown above, substitution of T101 by alanine induces an exceptionally increased flexibility in the L2-loop (Fig. 4C). Although with I100 unchanged in $HDAH_{bo}$ T101A, the access to the binding pocket is even more facilitated than in $HDAH_{bo}$ I100A because of the enhanced overall flexibility of the L2-loop. This is reflected by the thermodynamic signature of PFSAHA binding with very high enthalpy contribution and unfavorable binding entropy. The enthalpy-entropy compensation in the PFSAHA/$HDAH_{bo}$ T101A complex is attributed to enhanced hydrophobic interactions that produce a loss in residual ligand and protein flexibility. The thermodynamic profiles of ligand binding to $HDAH_{pa}$ are difficult to compare with binding to $HDAH_{bo}$ variants, because there are not only multiple sequence differences in the loops surrounding the binding pocket (Fig. S2) but also clearly divergent binding poses for both, SATFMK and PFSAHA (Fig. 3). The slimmer SATFMK binds with the highest observed affinity to $HDAH_{pa}$ showing comparable favorable enthalpy and entropy changes (Table 3, Fig. 5). In contrast, the bulkier PFSAHA binds to $HDAH_{pa}$ solely enthalpy-driven with unfavorable entropy (Table 3, Fig. 5). Similar to $HDAH_{bo}$ T101A, PFSAHA binding to $HDAH_{pa}$ appears to be characterized by dominant hydrophobic interactions that increase complex stability with negative impact on residual compound and protein flexibility.

4. Conclusions

The combination of site directed mutagenesis, crystal structure analysis and isothermal titration microcalorimetry revealed a clear relationship between the flexibility in the L2-loop of HDAC-like amidohydrolases and the mode of ligand recognition as indicated by the thermodynamic signature of ligand binding. The whole picture of data suggests a general binding mechanism for $HDAH_{bo}$ which consists of at least two steps: An outward move of the L2-loop and gatekeeper I100 to open the binding pocket and the subsequent actual binding step in the active site tunnel. If the flexibility of the L2-loop is dramatically increased by destroying the stabilizing hydrogen bond network around the pivotal T101, the general two-step binding mechanism is changed to an apparent one-step mechanism with facilitated direct ligand binding as indicated by the thermodynamic signature of complex formation.

This case study provides evidence for the great importance of flexibility adjacent to the active site channel and shows how specific tuning of L2-loop flexibility changes the mechanism and thermodynamic signature of molecular recognition. The binding enthalpy of protein-ligand systems should be interpreted with caution, since more complicated binding mechanisms may obscure the significance regarding the involved molecular interactions. Particularly, the relevance of the flexibility or malleability in regions adjacent to binding pockets, i.e. the L2-loop in human HDACs and HDAC like amidohydrolases, for ligand binding should be given more attention when designing new drug candidates.

Conflict of interest

The authors declare no competing financial interest.

Transparency document

The http://dx.doi.org/10.1016/j.bbagen.2017.04.001 associated with this article can be found, in the online version.

Acknowledgement

This work was supported by the DFG (grant GZ: ME 3122/2-1). We would also like to thank Michael Schröder for his very helpful assistance. We want to thank the beamline scientists on the PXII - X10SA at the Swiss Light Source for their excellent support during data collection. We also thank Katharina van Pee for the technical support during the crystallization experiments.

Appendix A. Supplementary data

Structure based multiple sequence alignment of used enzymes; Michaelis-Menten kinetics of HDAH_bo, HDAH_pa and variants; crystal structures of HDAH_bo unbound and in complex with different ligands; ITC data in different buffers http://dx.doi.org/10.1016/j.bbagen.2017.04.001.

References

[1] K.J. Falkenberg, R.W. Johnstone, Histone deacetylases and their inhibitors in cancer, neurological diseases and immune disorders, Nat. Rev. Drug Discov. 13 (2014) 673–691.
[2] A. Didonna, P. Opal, The promise and perils of HDAC inhibitors in neurodegeneration, Ann. Clin. Transl. Neurol. 2 (2015) 79–101.
[3] L. Zhang, Y. Han, Q. Jiang, C. Wang, X. Chen, X. Li, F. Xu, Y. Jiang, Q. Wang, W. Xu, Trend of histone deacetylase inhibitors in cancer therapy: isoform selectivity or multitargeted strategy, Med. Res. Rev. 35 (2015) 63–84.
[4] J.R. Somoza, R.J. Skene, B.A. Katz, C. Mol, J.D. Ho, A.J. Jennings, C. Luong, A. Arvai, J.J. Buggy, E. Chi, J. Tang, B.C. Sang, E. Verner, R. Wynands, E.M. Leahy, D.R. Dougan, G. Snell, M. Navre, M.W. Knuth, R.V. Swanson, D.E. McRee, L.W. Tari, Structural snapshots of human HDAC8 provide insights into the class I histone deacetylases, Structure 12 (2004) 1325–1334.
[5] A. Vannini, C. Volpari, G. Filocamo, E.C. Casavola, M. Brunetti, D. Renzoni, P. Chakravarty, C. Paolini, R. De Francesco, P. Gallinari, C. Steinkuhler, S. Di Marco, Crystal structure of a eukaryotic zinc-dependent histone deacetylase, human HDAC8, complexed with a hydroxamic acid inhibitor, Proc. Natl. Acad. Sci. U. S. A. 101 (2004) 15064–15069.
[6] S.M.F. Gantt, C. Decroos, M.S. Lee, L.E. Gullett, C.M. Bowman, D.W. Christianson, C.A. Fierke, General base-general acid catalysis in human histone deacetylase 8, Biochemistry 55 (2016) 820–832.
[7] D.P. Dowling, S.L. Gantt, S.G. Gattis, C.A. Fierke, D.W. Christianson, Structural studies of human histone deacetylase 8 and its site-specific variants complexed with substrate and inhibitors†,‡, Biochemistry 47 (2008) 13554–13563.
[8] A. Vannini, C. Volpari, P. Gallinari, P. Jones, M. Mattu, A. Carfi, R. De Francesco, C. Steinkuhler, S. Di Marco, Substrate binding to histone deacetylases as shown by the crystal structure of the HDAC8-substrate complex, EMBO Rep. 8 (2007) 879–884.
[9] C. Decroos, D.J. Clausen, B.E. Haines, O. Wiest, R.M. Williams, D.W. Christianson, Variable active site loop conformations accommodate the binding of macrocyclic largazole analogues to HDAC8, Biochemistry 54 (2015) 2126–2135.
[10] M.B. Kunze, D.W. Wright, N.D. Werbeck, J. Kirkpatrick, P.V. Coveney, D.F. Hansen, Loop interactions and dynamics tune the enzymatic activity of the human histone deacetylase 8, J. Am. Chem. Soc. 135 (2013) 17862–17868.
[11] S.V. Weerasinghe, G. Estiu, O. Wiest, M.K.H. Pflum, Residues in the 11 Å channel of histone deacetylase 1 promote catalytic activity: implications for designing isoform-selective histone deacetylase inhibitors†, J. Med. Chem. 51 (2008) 5542–5551.
[12] T.K. Nielsen, C. Hildmann, A. Dickmanns, A. Schwienhorst, R. Ficner, Crystal structure of a bacterial class 2 histone deacetylase homologue, J. Mol. Biol. 354 (2005) 107–120.
[13] A. Kramer, J. Herzer, J. Overhage, F.J. Meyer-Almes, Substrate specificity and function of acetylpolyamine amidohydrolases from *Pseudomonas aeruginosa*, BMC Biochem. 17 (2016) 4.
[14] G.L. Winsor, E.J. Griffiths, R. Lo, B.K. Dhillon, J.A. Shay, F.S. Brinkman, Enhanced annotations and features for comparing thousands of Pseudomonas genomes in the Pseudomonas genome database, Nucleic Acids Res. 44 (2016) D646–D653.
[15] L.M. Henkes, P. Haus, F. Jager, J. Ludwig, F.J. Meyer-Almes, Synthesis and biochemical analysis of 2,2,3,3,4,4,5,5,6,6,7,7-dodecafluoro-N-hydroxy-octanediamides as inhibitors of human histone deacetylases, Bioorg. Med. Chem. 20 (2012) 985–995.
[16] D. Wegener, C. Hildmann, D. Riester, A. Schwienhorst, Improved fluorogenic histone deacetylase assay for high-throughput-screening applications, Anal. Biochem. 321 (2003) 202–208.
[17] H.R. Powell, O. Johnson, A.G.W. Leslie, Autoindexing diffraction images with iMosflm, Acta Crystallogr. Sect. D 69 (2013) 1195–1203.
[18] P.R. Evans, G.N. Murshudov, How good are my data and what is the resolution? Acta Crystallogr. Sect. D 69 (2013) 1204–1214.
[19] A. Vagin, A. Teplyakov, Molecular replacement with MOLREP, Acta Crystallogr. D Biol. Crystallogr. 66 (2010) 22–25.
[20] C.E. Weston, A. Kraemer, F. Colin, Ö. Yildiz, M.G. Baud, F.-J. Meyer-Almes, M.J. Fuchter, Towards photopharmacological antimicrobial chemotherapy using photoswitchable amidohydrolase inhibitors, ACS Infect. Dis. 3 (2017) 152–161.
[21] P. Emsley, B. Lohkamp, W.G. Scott, K. Cowtan, Features and development of Coot, Acta Crystallogr. D Biol. Crystallogr. 66 (2010) 486–501.
[22] G.N. Murshudov, P. Skubak, A.A. Lebedev, N.S. Pannu, R.A. Steiner, R.A. Nicholls, M.D. Winn, F. Long, A.A. Vagin, REFMAC5 for the refinement of macromolecular crystal structures, Acta Crystallogr. D Biol. Crystallogr. 67 (2011) 355–367.
[23] E. Potterton, P. Briggs, M. Turkenburg, E. Dodson, A graphical user interface to the CCP4 program suite, Acta Crystallogr. Sect. D 59 (2003) 1131–1137.
[24] Y. Hai, D.W. Christianson, Histone deacetylase 6 structure and molecular basis of catalysis and inhibition, Nat. Chem. Biol. 12 (2016) 741–747.
[25] Y. Miyake, J.J. Keusch, L. Wang, M. Saito, D. Hess, X. Wang, B.J. Melancon, P. Helquist, H. Gut, P. Matthias, Structural insights into HDAC6 tubulin deacetylation and its selective inhibition, Nat. Chem. Biol. 12 (2016) 748–754.
[26] A. Kraemer, T. Wagner, Ö. Yildiz, F.J. Meyer-Almes, Crystal structure of a histone deacetylase homolog from Pseudomonas aeruginosa, Biochemistry (2016), http://dx.doi.org/10.1021/acs.biochem.1026b00613.
[27] P.M. Lombardi, H.D. Angell, D.A. Whittington, E.F. Flynn, K.R. Rajashankar, D.W. Christianson, Structure of prokaryotic polyamine deacetylase reveals evolutionary functional relationships with eukaryotic histone deacetylases, Biochemistry 50 (2011) 1808–1817.
[28] D.H. Khan, S. He, J. Yu, S. Winter, W. Cao, C. Seiser, J.R. Davie, Protein kinase CK2 regulates the dimerization of histone deacetylase 1 (HDAC1) and HDAC2 during mitosis, J. Biol. Chem. 288 (2013) 16518–16528.
[29] P.J. Watson, L. Fairall, G.M. Santos, J.W.R. Schwabe, Structure of HDAC3 bound to co-repressor and inositol tetraphosphate, Nature 481 (2012) 335–340.
[30] J.E. Ladbury, G. Klebe, E. Freire, Adding calorimetric data to decision making in lead discovery: a hot tip, Nat. Rev. Drug Discov. 9 (2010) 23–27.
[31] A.J. Ruben, Y. Kiso, E. Freire, Overcoming roadblocks in lead optimization: a thermodynamic perspective, Chem. Biol. Drug Des. 67 (2006) 2–4.

5. Supplemental Information

This chapter provides the published supplemental information of the articles from section 4.

5.1

A fluorescence lifetime-based binding assay for acetylpolyamine amidohydrolases from Pseudomonas aeruginosa using a [1,3]dioxolo[4,5-f]benzodioxole (DBD) ligand probe. Meyners C, Wawrzinek R, Krämer A, Hinz S, Wessig P, Meyer-Almes F-J. *Anal. Bioanal. Chem.* (2014) 406: 4889–4897

Available online at
https://static-content.springer.com/esm/art%3A10.1007%2Fs00216-014-7886-5/MediaObjects/216_2014_7886_MOESM1_ESM.pdf

5.2

A fluorescence lifetime-based binding assay for class IIa histone deacetylases. Meyners C, Mertens M, Wessig P, Meyer-Almes F-J. *Chem. Eur. J.* (2017) 23: 3107–3116

Available online at
http://onlinelibrary.wiley.com/store/10.1002/chem.201605140/asset/supinfo/chem201605140-sup-0001-misc_information.pdf?v=1&s=f5e2bcf283e848c8bc6aa59e54f1e596c270a482

5.3

Kinetic method for the large-scale analysis of the binding mechanism of histone deacetylase inhibitors. Meyners C, Baud MGJ, Fuchter MJ, Meyer-Almes F-J. *Anal. Biochem.* (2014) 460: 39–46

Available online at
http://www.sciencedirect.com/science/MiamiMultiMediaURL/1-s2.0-S0003269714002255/1-s2.0-S0003269714002255-mmc1.docx/272363/html/S0003269714002255/4a4d10c607d91264d0ba4c3ed7a17d1c/mmc1.docx

5.4

Impact of binding mechanism on selective inhibition of histone deacetylase isoforms. Meyners C, Meyer-Almes F-J. Submitted for publication in *Chemical Biology and Drug Design*

5.5

Perflourinated hydroxamic acids are potent and selective inhibitors of HDAC-like enzymes from *Pseudomonas aeruginosa*. Meyners C, Wolff B, Kleinschek A, Krämer A, Meyer-Almes F-J. *Bioorg. Med. Chem. Lett.* (2017) 27: 1508–1512

Available online at
http://www.sciencedirect.com/science/MiamiMultiMediaURL/1-s2.0-S0960894X17301828/1-s2.0-S0960894X17301828-mmc1.docx/271398/html/S0960894X17301828/cd041e413e28026992fdcdd78d3d4962/mmc1.docx

5.6

The thermodynamic signature of ligand binding to histone deacetylase-like amidohydrolases is most sensitive to the flexibility in the L2-loop lining the active site pocket. Meyners C, Krämer A, Yildiz Ö, Meyer-Almes F-J. *BBA - General subjects* (2017)
DOI: http://dx.doi.org/10.1016/j.bbagen.2017.04.001

Available online at
http://www.sciencedirect.com/science/MiamiMultiMediaURL/1-s2.0-S0304416517301265/1-s2.0-S0304416517301265-mmc2.docx/271022/html/S0304416517301265/706c7b066c10c5655479a0ecaed2eed8/mmc2.docx

5.1. Supplemental information for: A fluorescence lifetime-based binding assay for acetylpolyamine amidohydrolases from *Pseudomonas aeruginosa* using a [1,3]dioxolo[4,5-f]benzodioxole (DBD) ligand probe

Analytical and Bioanalytical Chemistry

Electronic Supplementary Material

A fluorescence lifetime-based binding assay for acetylpolyamine amidohydrolases from *Pseudomonas aeruginosa* using a [1,3]dioxolo[4,5-*f*][1,3]benzodioxole (DBD) ligand probe

C. Meyners, R. Wawrzinek, A. Krämer, S. Hinz, P. Wessig, F.-J. Meyer-Almes

1. Chemical analytics

TLC was performed on TLC aluminiumsheetsSilica Gel 60 F254 (Merck). Column chromatography was performed on silica gel 40–63 mesh, (Merck). 1HNMR-spectra were measured on a BrukerAvance (300.13 MHz) and the 19FNMR-spectra were measured on a BrukerDRX-400 (376.33 MHz) in CDCl3 or DMSO-d6 and referenced to TMS. 19FNMR-spectra were referenced to hexafluorobenzene as external standard. Mass spectra were measured on a FinniganLCQDECA (Thermoquest) using APCI (negative mode).

2. Purification by HPLC

To purify compounds **8** the following reverse phase high performance liquid chromatography (RP-HPLC) setup was used: JASCO LC-Net II/ACD; JASCO PU-987 (pump); JASCO UV-2075 PLUS (UV-VIS-detector); JASCOCHF122SC (fraction collector), ChromPass and FraColl (software, JASCO), KNAUERErosilBioselectC18 (250x16 mm, 10 µm, 300 Å). Mobile phase: Acetonitrile/H2O + trifluoroacetic acid (0.05%), gradient 20% to 90 % (acetonitrile) over 90 minutes.

3. Synthetic procedures and analytical data

Notice: The bridgeCH_2-NMR-signals of BD-/DBD backbone containing compounds show ether singlets or signals of an AB-system. The latter is marked as "AB" and the given value (in Hz) is the distance between the inner signals of such a spin system due to the fact that the outer signals of higher order are usually too small to be identified properly.

(4,8-Dibutyrylbenzo[1,2-d:4,5-d']bis[1,3]dioxole-2-yl)acetic acid (**4**) was prepared according to literature.[1]

(9*H*-Fluoren-9-yl)methyl(2-(2-(4,8-dibutyrylbenzo[1,2-*d*:4,5-*d'*]bis([1,3]dioxole)-2-yl)acetamido)ethyl)carbamate (5):

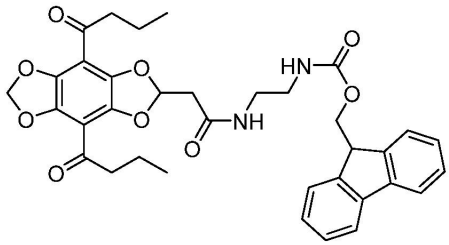

To a stirred solution of **4** (586 mg, 1.61 mmol) in dry DMF (30 mL) 4-methylmorpholine (1.71 mL, 10.62 mmol) was added. After cooling (0°C) *O*-HATU (1.31 mg, 3.46 mmol) and Fmoc-EDA•HCl (872 mg, 2.73 mmol) were added, the solution stirred for 30 minutes at 0°C then 2 h at room temperature. The solvent was evaporated under reduced pressure, and then the residue was dissolved in dichloromethane and washed with NaOH solution (1 %). The aqueous layer was extracted with dichloromethane and the combined organic layers dried over anhydrous $MgSO_4$ and concentrated under reduced pressure. The residue was purified over a short silica gel chromatography column (dichloromethane/methanol 100:1) to afford **5** (802 mg, 1.28 mmol, 79%) as a solid.

^{1}H-NMR (δ/ppm, $CDCl_3$, 300MHz): 0.95 (t, ^3J=7.40, 6H, -CH3); 1.69 (qd, ^3J =7.32,14.59, 4H, -CH_2); 2.84-2.89 (4H, -CH_2); 3.29-3.49 (4H, -CH_2); 4.19 (t, ^3J =6.66, 1H, -CH);4.40 (d, 2H, ^3J =6.66, -CH_2); 6.11 (s, 2H, -CH_2); 6.58 (t, ^3J =5.18, 1H, -CH); 7.30-7.78 (8H, -CH)

DC: DCM/MeOH 100:4 R_f = 0.22

***N*-(2-Aminoethyl)-2-(4,8-dibutyrylbenzo[1,2-*d*:4,5-*d'*]bis([1,3]dioxole)-2-yl)acetamide (6):**

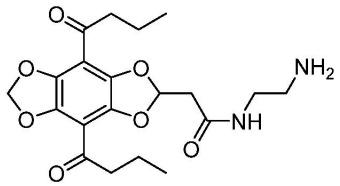

A solution of **5** (802 mg, 1.28 mmol) and dry piperidine (40 mL, 20% in dry DMF) was stirred at ro m temperature for 1 h. The solvent was evaporated under reduced pressure. The residue was dissolved in dichloromethane (100 mL) and washed with 0.1 N HCl (100 mL). To the separated aqueous layer dichloromethane (100 mL) and a saturated solution of $NaHCO_3$ (100 mL) were carefully added. The organic layer was then dried over anhydrous $MgSO_4$ and concentrated under reduced pressure to obtain **6** which was immediately used without further characterization.

DC: DCM/MeOH 100:4 R_f = 0.09

Methyl 6-((benzyloxy)amino)-6-oxohexanoate(2):

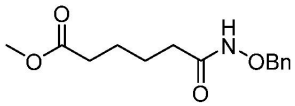

To a stirring cooled (0°C) solution of mono-methyl adipate (**1**) (925 µL, 6.24 mmol) in dry dichloromethane 1.61 mL oxalyl chloride (18.73 mmol) and one drop of DMF were added. After 4 hours the solvent was evaporated under reduced pressure. The residue was then dissolved in 10 mL dry dichloromethane and 1 g *O*-benzylhydroxylamine•HCl (6.27 mmol) and 3.2 mL *N*,*N*-diisopropylethylamine (both dissolved in 25 mL dry dichloromethane) were added and the solution stirred for another 12 hours. The solution was quenched with HCL (50 mL, 0.5 N) and the organic layer then washed with saturated solutions of NaCl and $NaHCO_3$ and dried over anhydrous $MgSO_4$ and concentrated under reduced pressure. The residue was purified over a silica gel chromatography column (dichloromethane/methanol 20:1) to obtain **2** (1.56 g, 5.88 mmol, 94%) as a colourless oil.

^{1}H-NMR (δ/ppm, $CDCl_3$, 300MHz): 1.55-1.65 (4H; -CH_2); 1.90-2.11 (2H, -CH_2); 2.25-2.30 (2H, -CH_2); 3.63 (3H, -CH_3); 4.87 (s, 2H, -CH_2); 7.30-7.40 (5H, -CH)

^{13}C-NMR (δ/ppm, $CDCl_3$, 75MHz): 24.2 (2C); 2.6 (1C); 51.5 (1C); 78.1 (1C); 128.5 (2C), 129.1 (3C); 135.4 (1C); 170.4 (1C); 173.8 (1C)

DC: DCM/MeOH 10:1 R_f = 0.71

MS: (ESI) m/z= 266.1375 $[M+H]^+$, calc.: 266.1392

IR: 3201, 2952, 1736, 1657, 1498, 1455, 1437, 1365, 1209, 1027, 752, 699 cm^{-1}

6-((Benzyloxy)amino)-6-oxohexanoic acid (3):

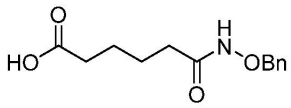

To a stirred solution of **2** (1.5 g, 5.65 mmol) in methanol (50 mL) 13 mL of a aqueous solution of LiOH (2M) were added and refluxed for 1 hour. After cooling down HCl (1 N, 25 mL) and H_2O (50 mL) were added and extracted with ethyl acetate (150 mL). The combined organic layers were dried over anhydrous $MgSO_4$ and concentrated under reduced pressure to obtain **3** (1.24 g, 495 mmol, 88%) as a white solid.

^{1}H-NMR (δ/ppm, $CDCl_3$, 300MHz): 1.50-1.66 (4H, -CH_2); 2.00-2.35 (4H, -CH_2); 4.75-4.90 (2H, -CH_2); 7.26-7.40 (5H, -CH); 10.34 (1H, -OH)

^{13}C-NMR (δ/ppm, $CDCl_3$, 75MHz): 24.0 (1C); 24.6 (1C); 32.5 (1C); 33.5 (1C); 78.1 (1C); 128.6 (2C), 129.2 (3C); 135.0 (1C); 170.8 (1C); 178.2 (1C)

Fp: 77 °C

DC: DCM/MeOH 10:1 R_f = 0.36

MS: (ESI) m/z= 252.1221 [M+], calc.: 252.1236

IR: 3234, 2951, 1691, 1659, 1506, 1432, 1417, 1278, 1198, 1090, 1055, 1023, 968, 908, 733, 694 cm^{-1}

***N*1-(Benzyloxy)-*N*6-(2-(2-(4,8-dibutyrylbenzo[1,2-*d*:4,5-*d'*]bis([1,3]dioxole)-2-yl)acetamido)ethyl)adipamide (7):**

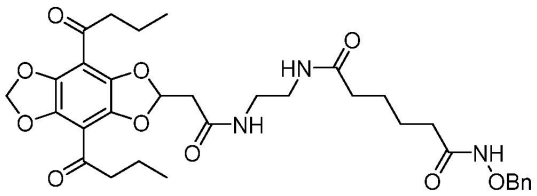

To a cooled stirred solution (0°C) of **3** (518 mg, 1.27 mmol), **6** (480 mg, 1.91 mmol) and DMAP (15 mg, 0.127 mmol) in dry dichloromethane DCC (395 mg, 1.91 mmol) was added. After 24 hours the solution was cooled (-10°C), filtered over CELITE and the solvent evaporated under reduced pressure. The residue was purified over a silica gel chromatography column (dichloromethane/methanol) to afford **7** (220 mg, 3.44 mmol, 27% over two steps starting from **5**) as a yellow oil.

^{1}H-NMR (δ/ppm, $CDCl_3$, 300MHz): 0.97 (t, ^3J=7.40, 6H, -CH_3); 1.60-1.75 (8H, -CH_2); 2.06-2.18 (2H, -CH_2) 2.29-2.36 (2H, -CH_2); 2.87-2.97 6H, -CH_2); 3.40-3.47 (4H, -CH_2); 4.80-4.90 (2H, -CH_2); 6.10 (AB, 4.99 Hz, 2H, -CH_2) ; 6.60 (t, ^3J =4.99, 1H, -CH); 7.32-7.41 (5H, -CH)

DC: DCM/MeOH 10:1 R_f = 0.34

MS: (EI) m/z= 639.2776 [M+], calc.: 639.2765

IR: 3296, 2963, 2931, 1683, 1651, 1550, 1434, 1286, 1085, 953 cm^{-1}

***N*1-(2-(2-(4,8-Dibutyrylbenzo[1,2-*d*:4,5-*d'*]bis([1,3]dioxole)-2-yl)acetamido)ethyl)-*N*6-hydroxyadipamide (8):**

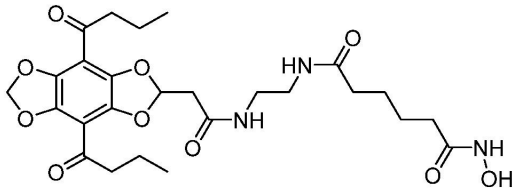

To a stirred solution of **7** (200 mg, 0.313 mmol) in dry methanol (200 mL) 10% palladium on activated charcoal (10 wt %) were added and stirred under an H_2 atmosphere for 3 hours at room temperature. The solution was then filtered over CELITE and the solvent evaporated under reduced pressure. The residue was purified over by RP-HPLC (*see above for details*) to obtain **8** (55 mg, 0.1 mmol, 32%) as a yellow solid.

^{1}H-NMR (δ/ppm, DMSO-d_6, 500MHz): 0.89 (t, ^3J=7.41, 6H, -CH_3); 1.40-1.62 (8H, -CH_2); 1.90-1.95 (1H, -OH); 1.98-2.10 (4H, -CH_2); 2.80-2.87 (6H, -CH_2); 3.05-3-15 (4H, -CH_2); 6.11 (AB, 3.19 Hz, 2H, -CH_2); 6.65 (t, ^3J =5.34, 1H, -CH); 7.24 (1H, -NH); 7.84

(1H, -NH); 8.18 (1H, -NH)

^{13}C-NMR (δ/ppm, DMSO-d_6, 75MHz): 13.4 (2C); 16.6 (2C); 24.8 (2C); 34.8 (1C); 35.1 (1C); 38.0 (2C); 40.6 (1C); 44.2 (2C); 102.4 (2C); 109.4 (1C); 111.0 (1C); 139.9 (2C); 140.3 (2C); 166.3 (1C); 172.0 (1C); 174.0 (1C); 195.3 (2C)

Fp: 155 °C

DC: DCM/MeOH 10:1 R_f = 0.05

MS: (ESI) m/z= 550.2383 $[M+H]^+$, calc.: 550.2401

IR: 3291, 2958, 2931, 1654, 1550, 1434, 1281, 1090, 1058 cm^{-1}

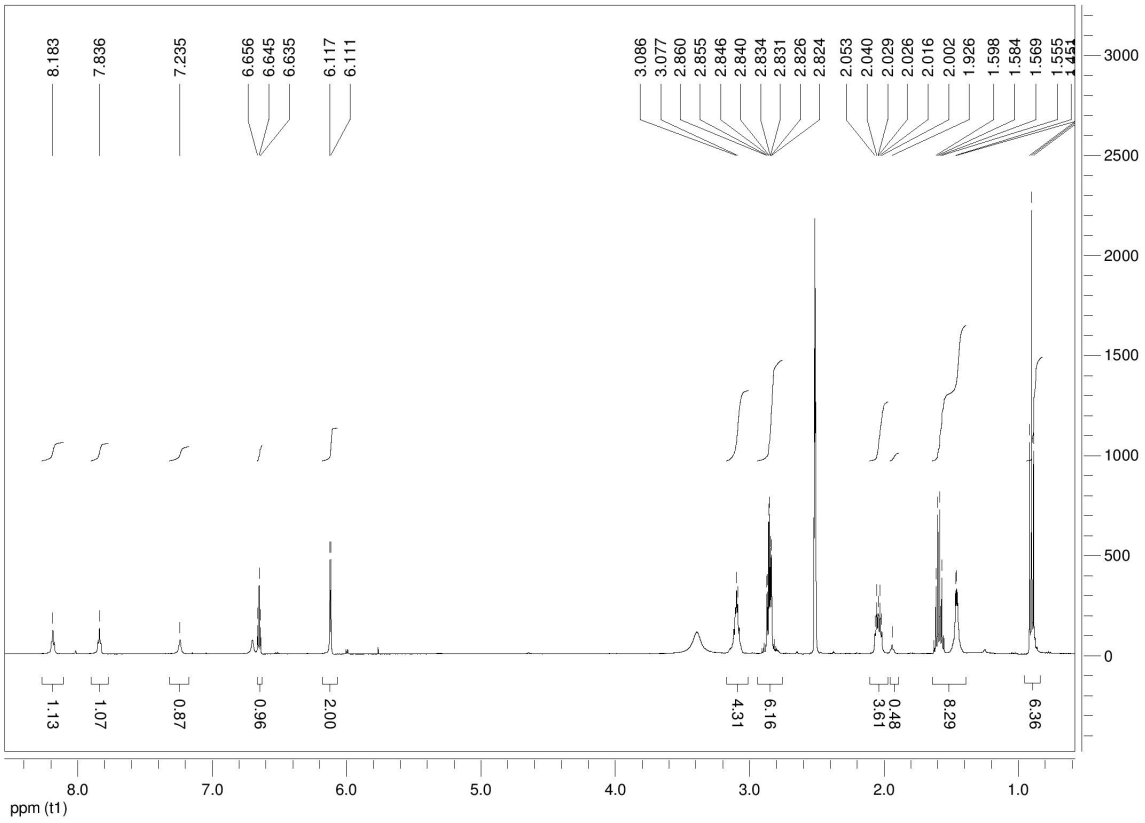
8.183
7.836
7.235
6.656
6.645
6.635
6.117
6.111
3.086
3.077
2.860
2.855
2.846
2.840
2.834
2.831
2.826
2.824
2.053
2.040
2.029
2.026
2.016
2.002
1.926
1.598
1.584
1.569
1.555
1.451
1.13
1.07
0.87
0.96
2.00
4.31
6.16
1.91
0.48
8.29
6.36
ppm (t1)

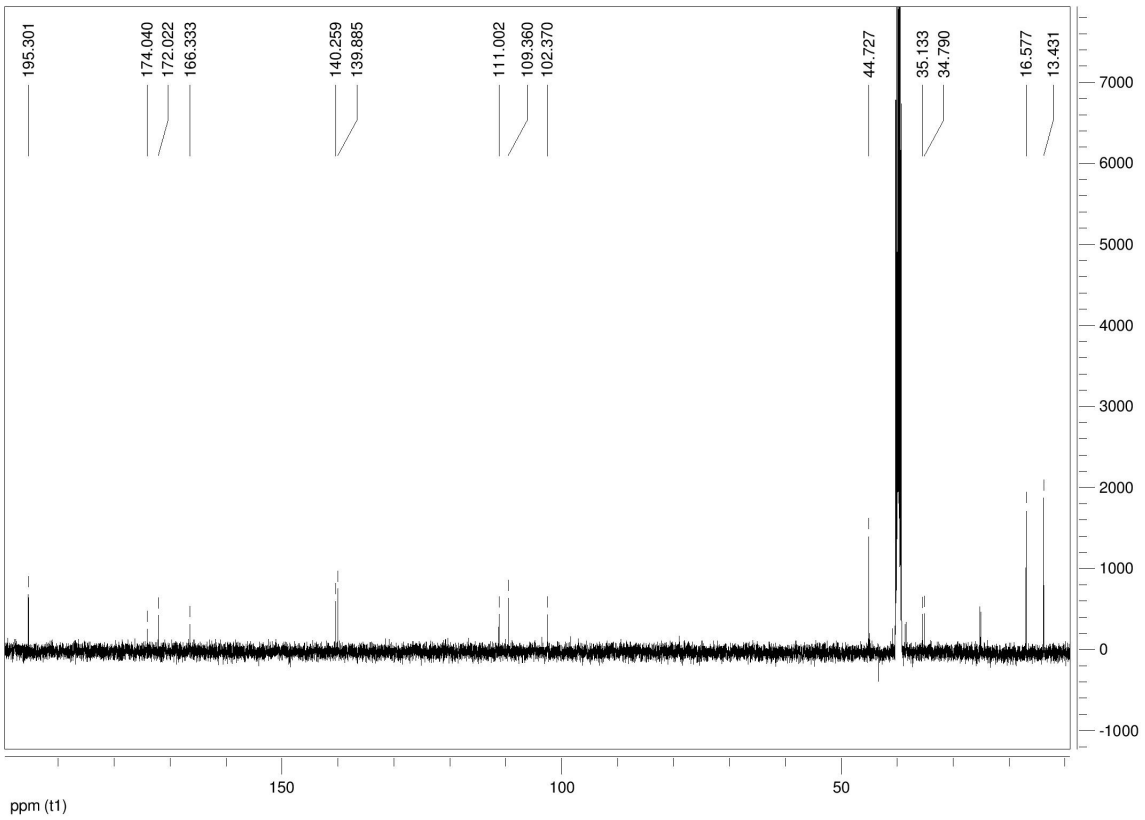
195.301
174.040
172.022
166.333
140.259
139.885
111.002
109.360
102.370
44.727
35.133
34.790
16.577
13.431
ppm (t1)

REFERENCES

[1]Wawrzinek, R.; Ziomkowska, J.; Heuveling, J.; Mertens, M.; Herrmann, A.; Scheider, E. & Wessig, P.,*Chem. Eur. J.,***2013**, *19*, 17349-17357.

4. Sequences and vector construct of APAHs

PA0321

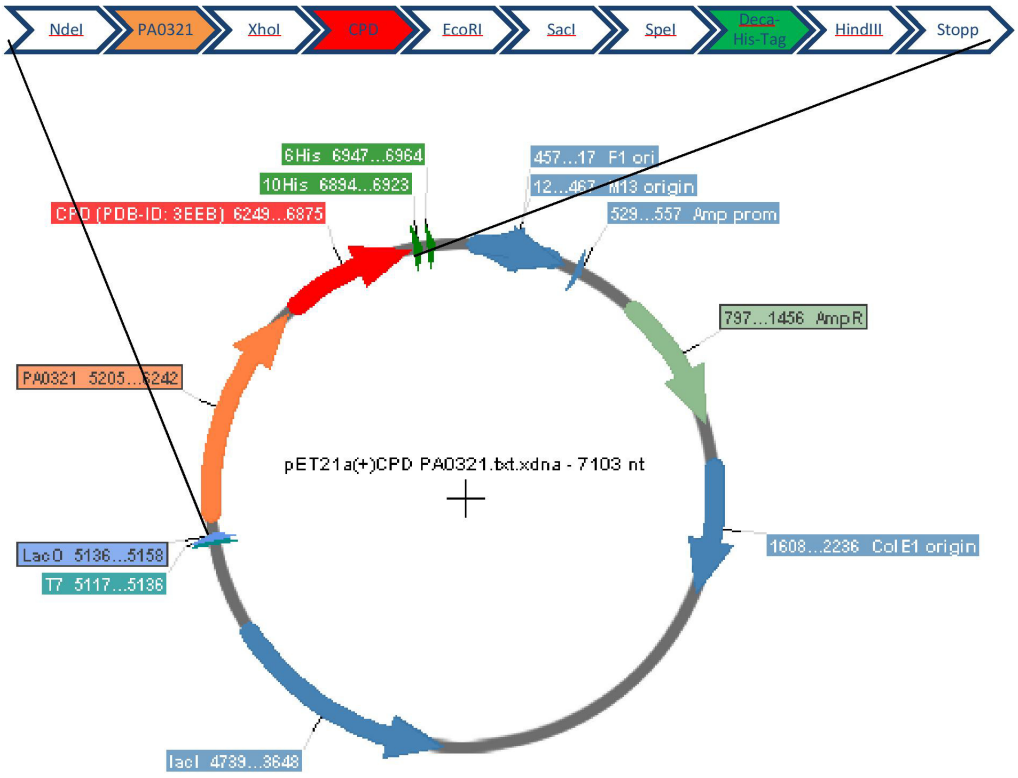

Fig. S1. The modified pET21a(+) vector construct. The close up shows the target protein PA0321 and the CPD along with the specific cutting sites and tag

sequence *pa0321*(codon optimized from strain PA01):

ATGCTGACCATTTACTCTGATGACCATCGTCTGCACCACGGTCGCCATGAACTGATCGGCGGCCAATTTACCCCGTGCTT
TGAAAAACCGTCACGTGCCGATATGGTTCTGGACCGCGTGAAAGCTGTTGGCCTGGGTGAAGTCCGTGCACCGCGCGATT
TTGGCCTGGAACCGATTCGTCGCGTGCATTCAGAAGGTTTTGTTCGTTTCCTGCAGAACGCTTGGCAAGATTGGCTGGCA
ACCGGCCGCTCGCACGACATGCTGCCGATTGCATGGCCGACCCGTCGCCTGCGTCAGACGGAACCGGATAATATCGACGG
CCGCCTGGGTTATTACTCCTTCGATGCAGGTGCACCGATTACCGCAGGCACGTGGCAGGCAATCACCAGCTCTGCTAACG
TGGCGCTGAGTGGCCAATCCGAACTGGCCAATGGTGCACGTAGCGTGTTTAGCCTGTGCCGTCCGCCGGGTCATCACGCA
GCAGCAGATTATATGGGCGGTTACTGCTTTTTCAACAATGCTGCGATTGCAGCACAGGCCTTCCTGGACCGTGGTGCTGG
TCGTGTTGCGATCCTGGATGTCGACTATCATCACGGCAACGGTACCCAAGATATCTTTTATGATCGTGCCGACGTGCTGT
TCACGAGCATCCATGGCGATCCGCGCTTTGAATATCCGTACTTCCTGGGTTATGCGGACGAAAAAGGCAATGGTGTTGGC
ACCGGTTATAACTTTAATTACCCGCTGGCTGCAGGCAGCGATTGGGCTACGTGGTCTCAGGCGCTGCAAGCCGCAATTCG
TCAGATCCAAGCCTATGCTGCGGATGCACTGATTGTCTCTCTGGGCGTGGATACCTTTAAAGAAGACCCGATCAGTCAGT
TCCGTCTGGATTCCCCGGACTATCTGCGCATGGGTGAAGCCATCGGCAAACTGGGTCTGGCAACGCTGTTTGTCATGGAA
GGCGGTTACGCGGTGGAAGAAATCGGTATCAATGCGGTTAATGTGCTGCAAGGCTTTGAAGGCGTCCATCGCCTCGAGgc
cttg

PA1409

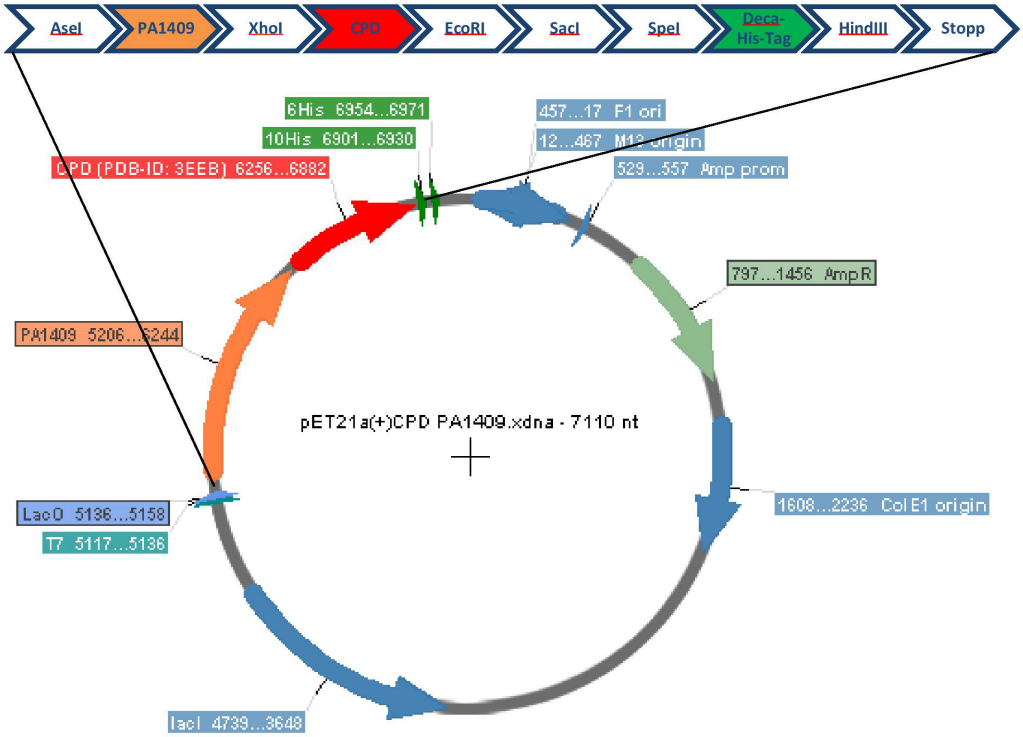

Fig S2: The modified pET21a(+) vector construct. The close up shows the target protein PA1409 and the CPD along with the specific cutting sites and tag

sequence *pa1409* (from strain PA01):

```
ATGCTGAGCGTCTACAGCGACGATCATCGTCTGCACTTCGGCCAGTCGGAACTGGTCGACGGCAAGCTGCAACCCTGTTT
CGAAATGCCCAGCCGGGCCGACACCGTGCTGGCCCGGGTGAAGTCGCAGAACCTTGGCGAGGTGATCGCGCCGAAGGATT
TCGGCCGCGAGCCGCTGCTGCGCCTCCACGACGCCGCCTACCTGGACTTCCTCCAGGGCGCCTGGGCCCGCTGGACCGCC
GAAGGCCACAGCGGCGACCTGGTGTCCACCACCTTCCCCGGCCGCCGCCTGCGCCGCGACGGGCCGATCCCCACGGCGCT
GATGGGCGAGCTGGGCTACTACAGCTTCGACACCGAGGCGCCGATCACCGCCGGCACCTGGCAGGCCATCTACAGCTCCG
CCCAGGTCGCGCTGACCGCCCAGGAGCATATGCGCCAGGGCGCCCGCAGCGCCTTCGCCCTCTGCCGTCCGCCGGGCCAT
CACGCCGGTGGCGACTTCATGGGCGGCTACTGCTTCCTCAACAATGCCGCCATCGCCACCCAGGCGTTCCTCGACCAGGG
TGCCCGGCGCGTGGCGATCCTCGATGTCGACTATCACCATGGCAACGGCACCCAGGACATTTTCTACCGCCGCGACGATG
TGCTGTTCGCCTCGATCCATGGCGATCCGCGGGTCGAATACCCGTACTTCCTCGGCTACGCAGACGAGCGCGGCGAAGGC
GCCGGCGAGGGCTGCAACCACAACTATCCGCTGGCCCATGGCAGCGGCTGGGACCTCTGGTCGGCGGCGCTCGACGACGC
CTGCGTGCGGATCGCCGGCTACGCCCCGGATGCCCTGGTGATTTCCCTTGGCGTGGACACCTACAAGGAAGACCCGATCT
CCCAGTTCAGGCTGGATTCGCCGGACTACCTGCGGATGGGCGAGCGCATCGCCCGGCTGGGCCTGCCGACCCTGTTCATC
ATGGAAGGCGGCTATGCGGTGGAAGCCATCGGCATCAACGCGGTCAACGTGCTGCAGGGCTACGAAGGCGCGGCCCGCCT
CGAGGCCTTG
```

PA3774

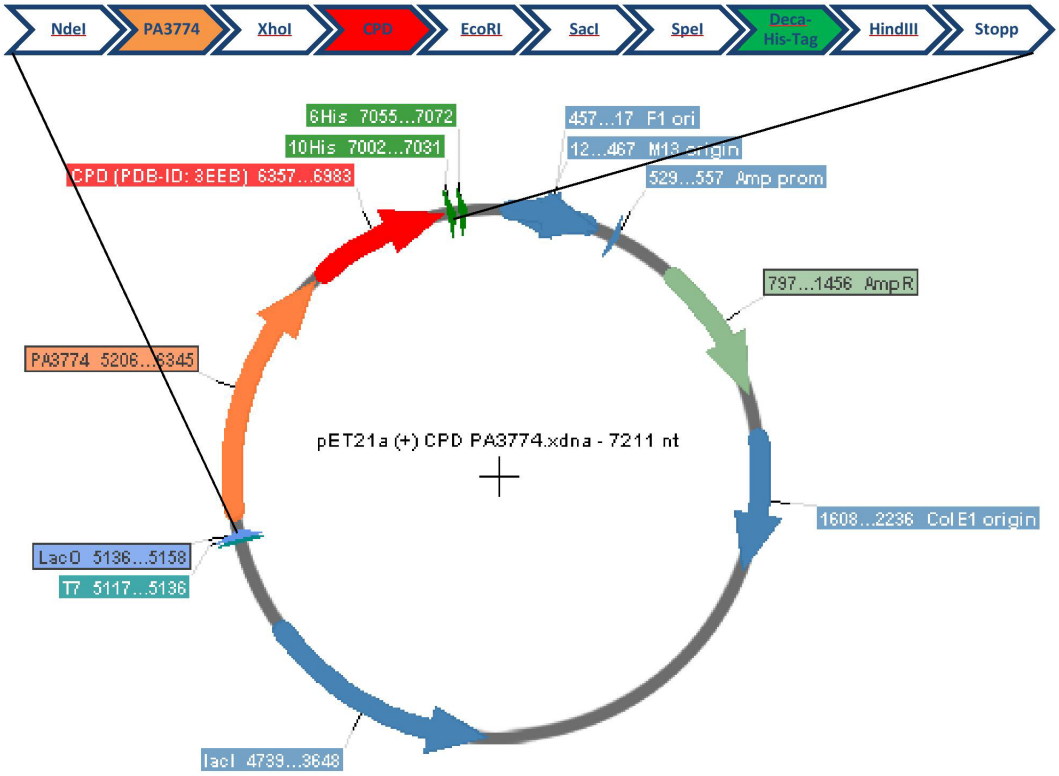

Fig S3: The modified pET21a(+) vector construct. The close up shows the target protein PA3774 and the CPD along with the specific cutting sites and tag

sequence *pa3774* (strain PA01):

ATGACCCGACGTACCGCTTTCTTCTTCGACGAACTCTGCCTCTGGCACGCCGCCGGCCCGCACGCGCTGACCCTGCCGGT
CGGCGGCTGGGTGCAACCGCCTGCCGCCGCCGGACACGCCGAATCACCGGAAACCAAGCGCCGGCTGAAAAGCCTGCTCG
ACGTGTCCGGCCTGACCGCCCGCCTGCAACTGCGCAGCGCACCGCCGGCGAGCGACGAGGACCTGCTGCGCGTGCATCCG
GCGCACTATCTGGAACGCTTCAAGGCATTGAGCGACGCCGGCGGCGGCAGCCTCGGCCAGGACGCGCCGATCGGCCCGGG
CAGCTACGAGATCGCCCGGCTCTCCGCCGGCCTGGCCATCGCCGCGCTGGACGCGGTGCTCGCCGGCGAGGCGGACAACG
CCTACTCGCTGTCGCGGCCGCCAGGTCATCACTGCCTGCCGGACCAGGCGATGGGCTTCTGTTTCTTCGCCAACATCGCC
GTGGCCATCGAGGCGGCCAAGGCGCGCCACGGCGTCGAGCGGGTCGCGGTGCTGGACTGGGACGTGCACCACGGCAACGG
CACCCAGGCGATCTACTACCGGCGCGACGACGTGTTGAGCATTTCCCTGCACCAGGACGGCTGCTTCCCGCCTGGCTACA
GCGGCGCCGAAGACATCGGCGAGGATCGCGGTCGTGGCTTCAACCTCAACGTGCCGCTGCTTCCCGGCGGCGGTCACGAC
GCCTACATGCAGGCCATGCAACGCATCGTGTTGCCGGCGCTGGAGCGCTTCCGCCCGCAATTGATCGTGGTCGCCAGTGG
CTTCGACGCCAACGCGGTGGACCCGCTGGCACGCATGCAACTGCACAGCGACAGCTTCCGGGCGATGACCGCGATGGTCC
GCGACGCGGCCGAGCGGCATGCCGGCGGACGCCTGGTGGTGGTCCACGAAGGCGGCTACTCGGAAGCCTACGTGCCGTTC
TGCGGCTTGGCTGTGATCGAAGAACTCAGCGGCGTGCGCAGCGCGGTGCGCGACCCGCTGCGCGACTTCATCGAGTTGCA
GCAGCCCAACGCGGCGTTCCGCGACTTCCAGCGCCAGCGCCTCGAAGAGCTGGCCGCACAGTTCGGCCTGTGCCCGGCGC
AGCCGCTTCAAGCGGCCAGGCTCGAGGCCTTG

5. Absorption- and Emission-Spectrum of DBD-ligand

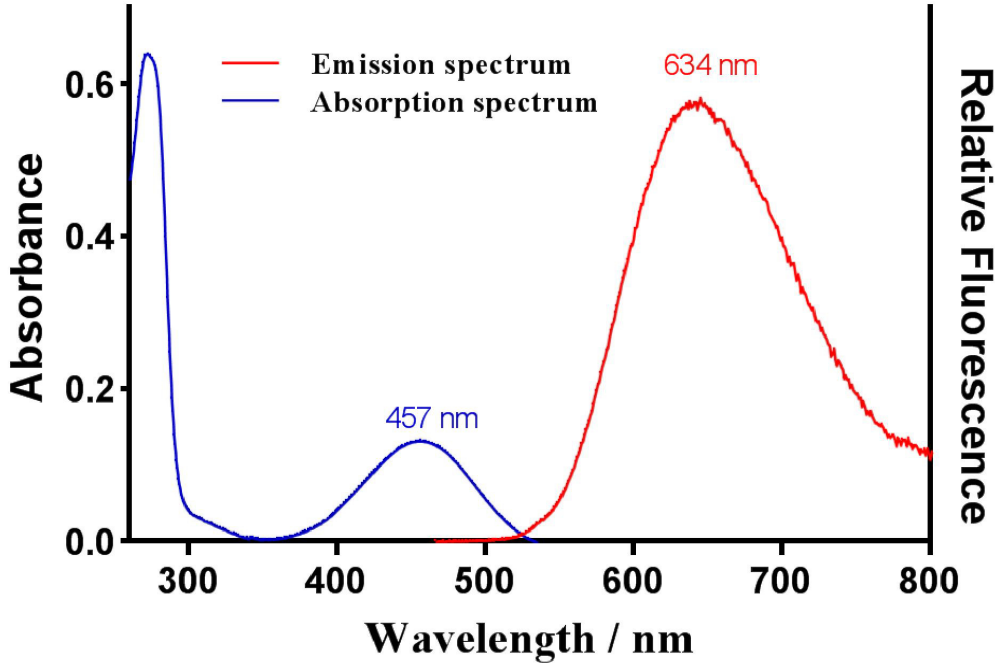

Fig. S4 Absorption and Fluorescence emission spectra of 37 µM DBD-ligand **8** in water. The fluorescence emission spectrum was measured at a fixed excitation wavelength of 457 nm

6. Fluorescence decay curves of free and bound DBD-ligand

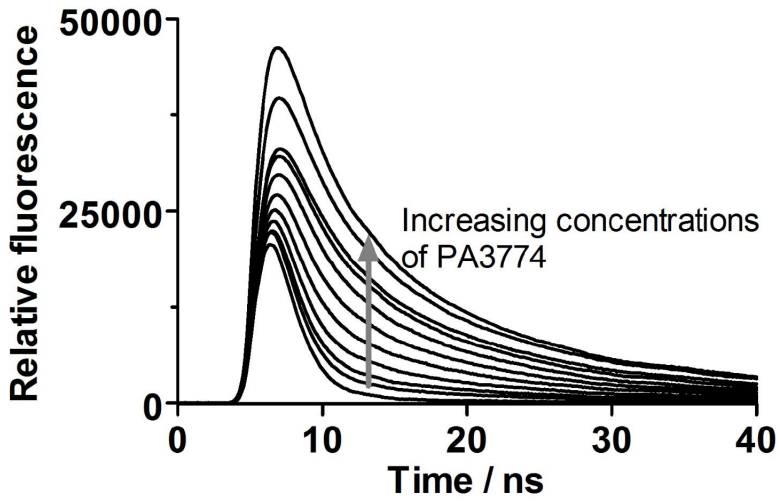

Fig. S5: Binding of 0.05 nM DBD ligand probe **8** to APAH (PA3774). The fluorescence decay curves of ligand probe in the absence and in the presence of increasing concentrations (0.015-3.9 μM) of APAH are shown

7. Dissociation kinetics of DBD-ligand from different APAHs and HDAH

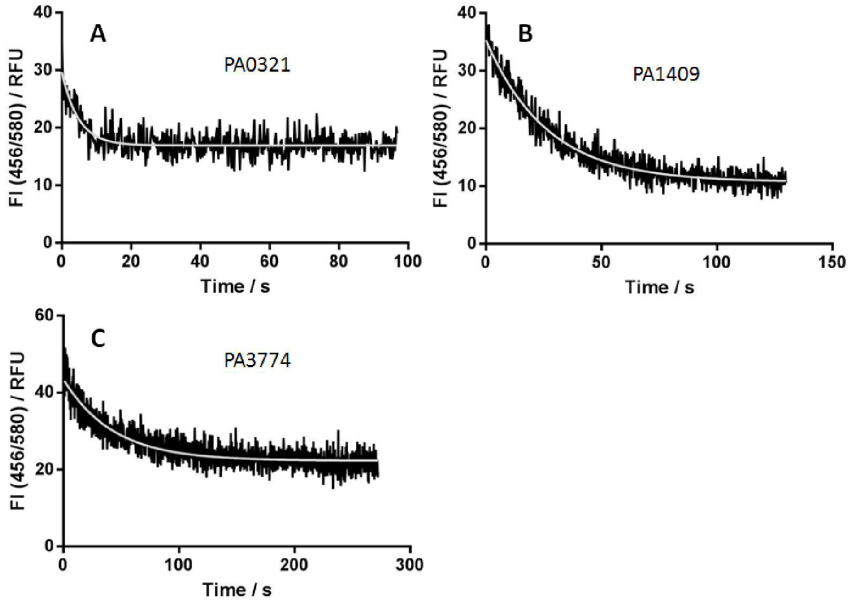

Fig.S6: Dissociation kinetics of DBD-ligand from A) APAH(PA0321), B) APAH(PA1409) and C) APAH(PA3774) at 22^0C. The fluorescence intensity at 456 nm excitation and 580 nm emission is plotted against the time. The obtained curves were fitted to a single phase exponential decay model, whose least-square fits are represented by the continuous lines. Experimental conditions are described in section Material and Methods

8. Dose-response curves of APAH-Inhibitors using the enzyme activity assay

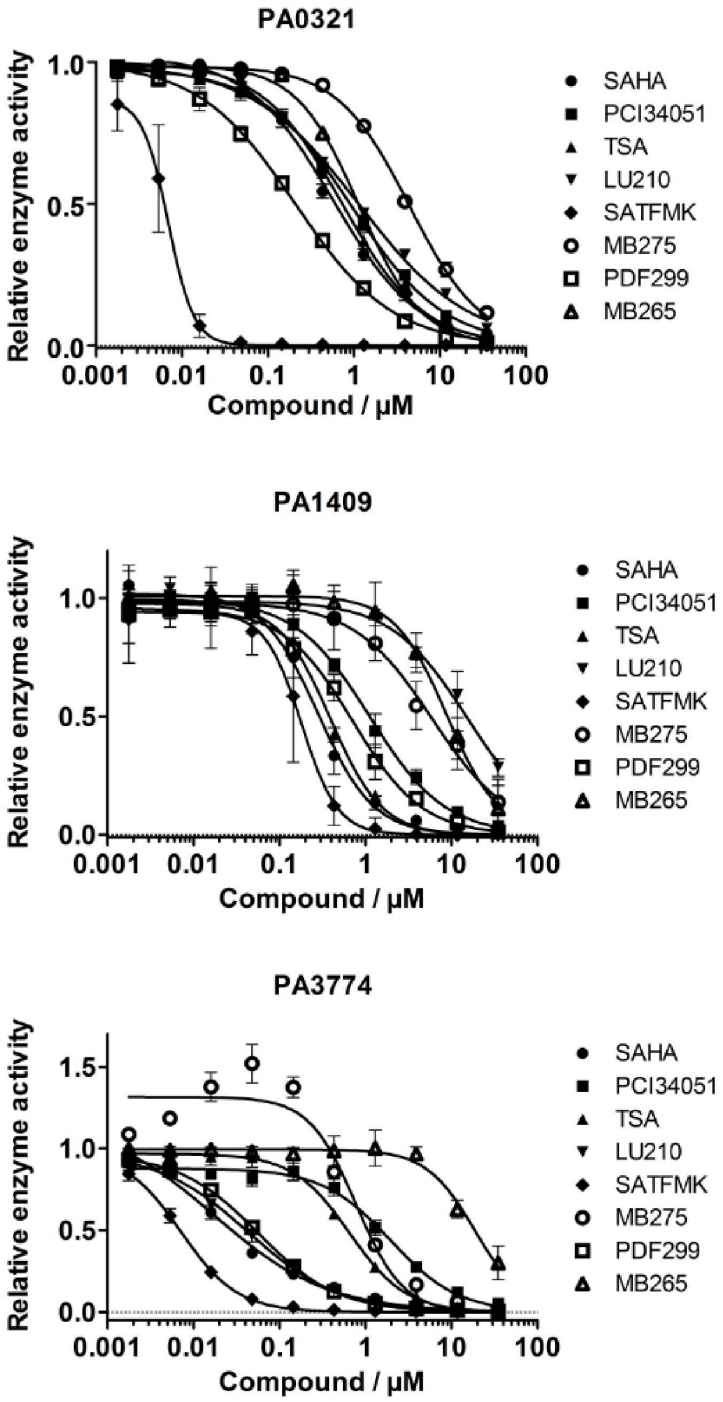

Fig. S7: Dose-response curves of APAH-Inhibitors using the enzyme activity assay described in section material and methods. The relative enzyme activity is plotted versus the concentration of the indicated compound

10. **Dose-response curves of APAH-Inhibitors using the competitive DBD-probe binding assay**
11.

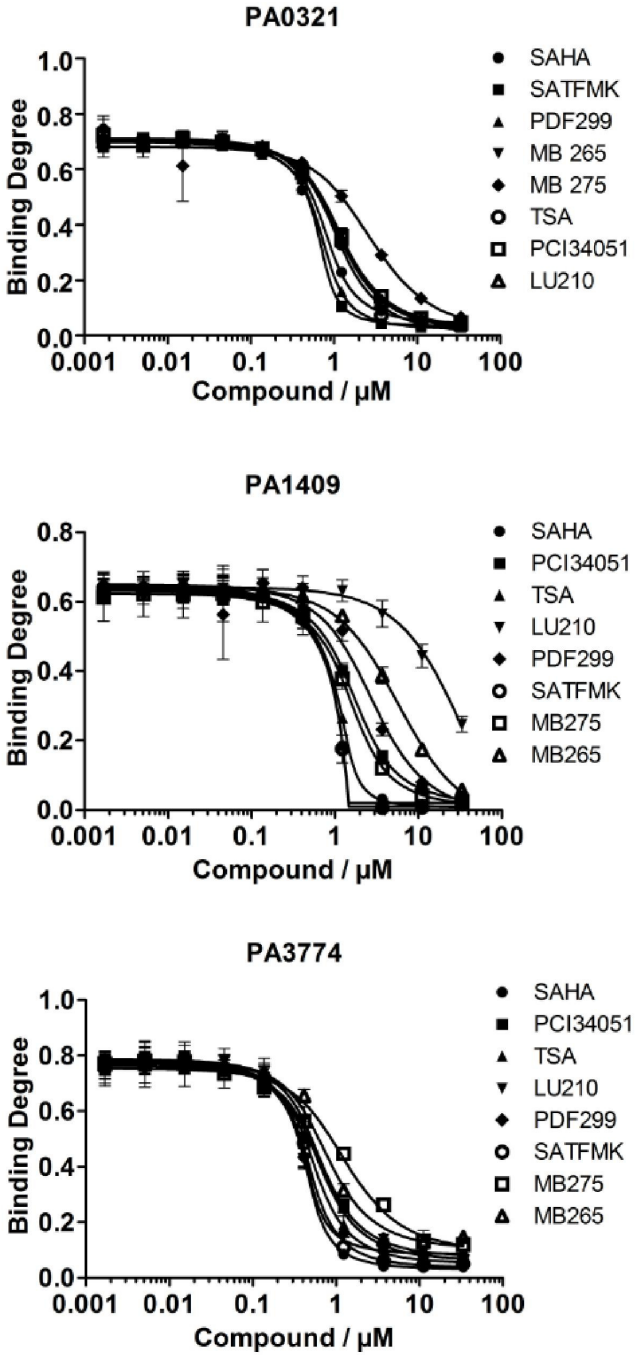

Fig. S8: Dose-response curves of APAH-Inhibitors using the DBD-ligand binding assay described in section material and methods. The calculated binding degree is plotted versus the concentration of the indicated compound.

5.2. Supplemental information for: A fluorescence lifetime-based binding assay for class IIa histone deacetylases

CHEMISTRY
A European Journal

Supporting Information

A Fluorescence-Lifetime-Based Binding Assay for Class IIa Histone Deacetylases

Christian Meyners,[a] Monique Mertens,[b] Pablo Wessig,*[b] and Franz-Josef Meyer-Almes*[a]

chem_201605140_sm_miscellaneous_information.pdf

1. Supplemental figures

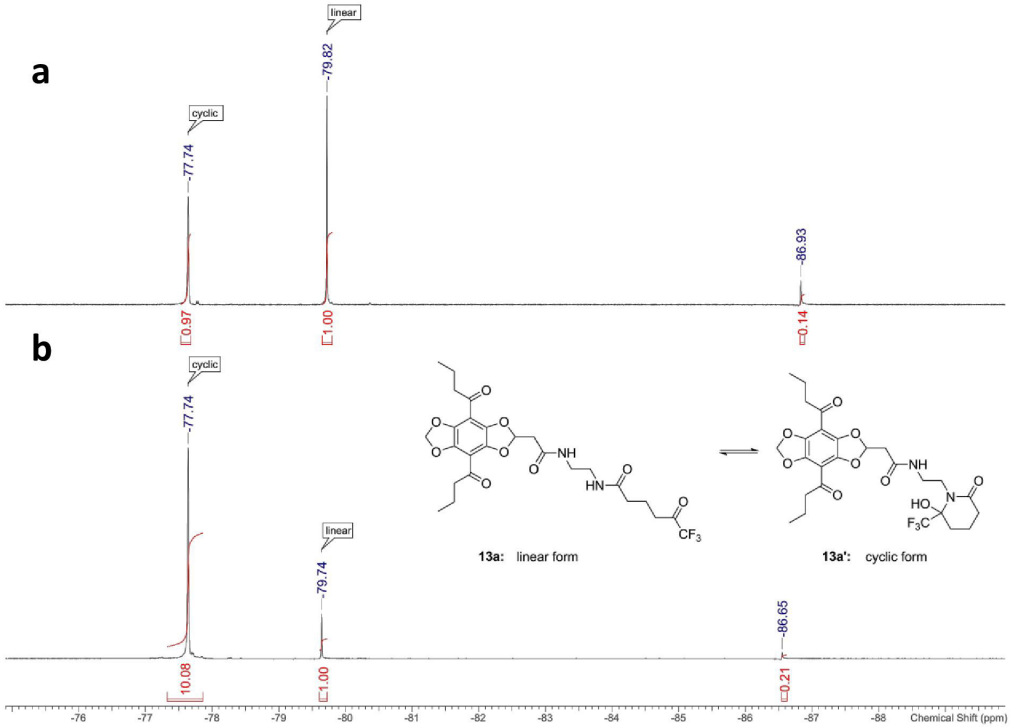

Figure S1 Solvent dependent equilibrium of two tautomers of compound 13a shown by ^{19}F-NMR spectroscopy. The spectrum a showing a 1:1 ratio was recorded in $CDCl_3$ immediately after compound **13a** was concentrated from methanol. The second spectrum b showing a 10:1 ratio where the cyclic form is predominant was recorded after a few hours. Thus we assumed a solvent dependent equilibrium between a linear and a cyclic form of compound **13a**.

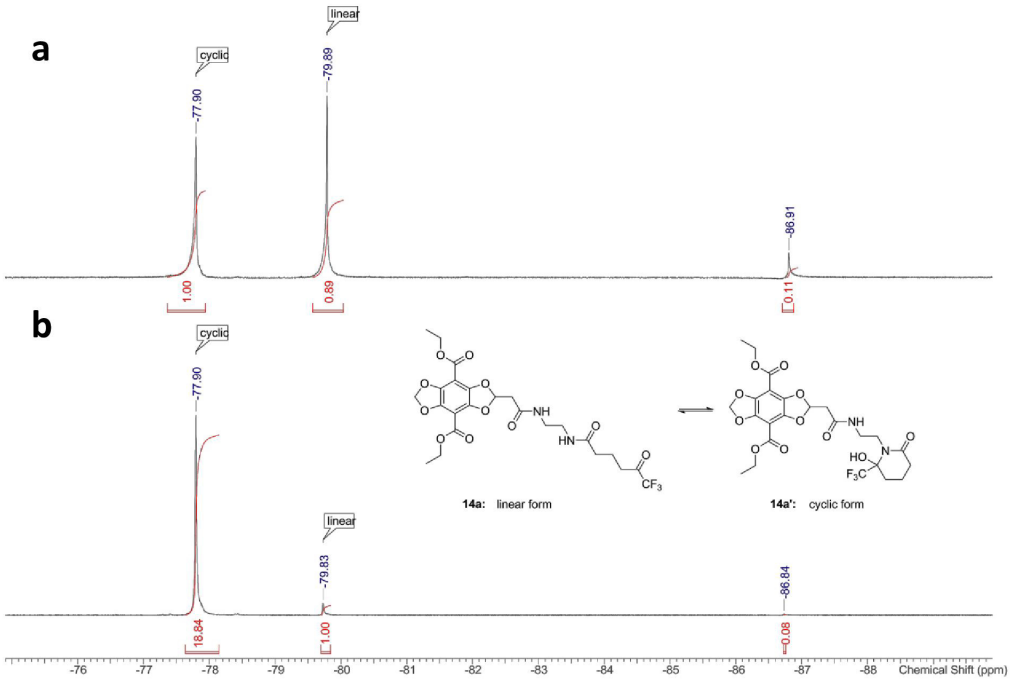

Figure S2 Solvent dependent equilibrium of two tautomers of compound 14a shown by ^{19}F-NMR spectroscopy. The spectrum a showing a 1:1 ratio was recorded in $CDCl_3$ immediately after compound **14a** was concentrated from methanol. The second spectrum b showing a 19:1 ratio where the cyclic form is predominant was recorded after a few hours. Thus we assumed a solvent dependent equilibrium between a linear and a cyclic form of compound **14a**.

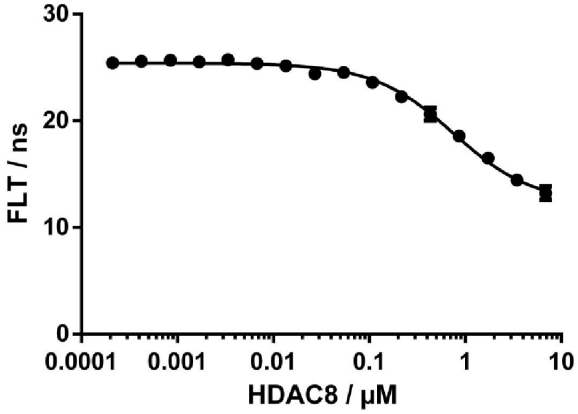

Figure S3 Binding of 14a to HDAC8. After equilibration of a serial dilution of HDAC8 supplemented with 0.125 nM **14a** the FLT was measured behind a 520 nm bandpass filter after pulse excitation at 405 nm. The continuous line represents the calculated fit, which yields the binding constant.

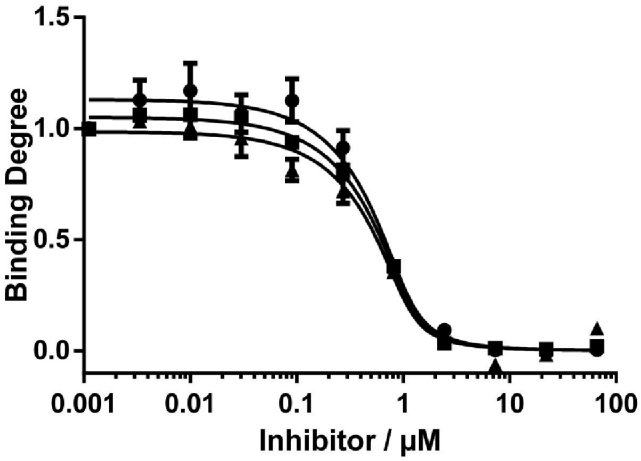

Figure S4 Determination of binding constants of the binding of unlabeled HDAC inhibitors to HDAC4. A serial dilution of the unlabeled HDAC inhibitors PDF306 (dots), SATFMK (squares) or TMP269 (triangles) was incubated with 1µM HDAC4 and 0.05 µM of the DBD probe **13b**. After equilibration the FLT of the probes was measured and translated into binding degree. The continuous line represents the calculated fit, which yields to the binding constants of 0.08±0.05 µM for PDF306, 0.08±0.02 µM for SATFMK and 0.07±0.04 µM for TMP269.

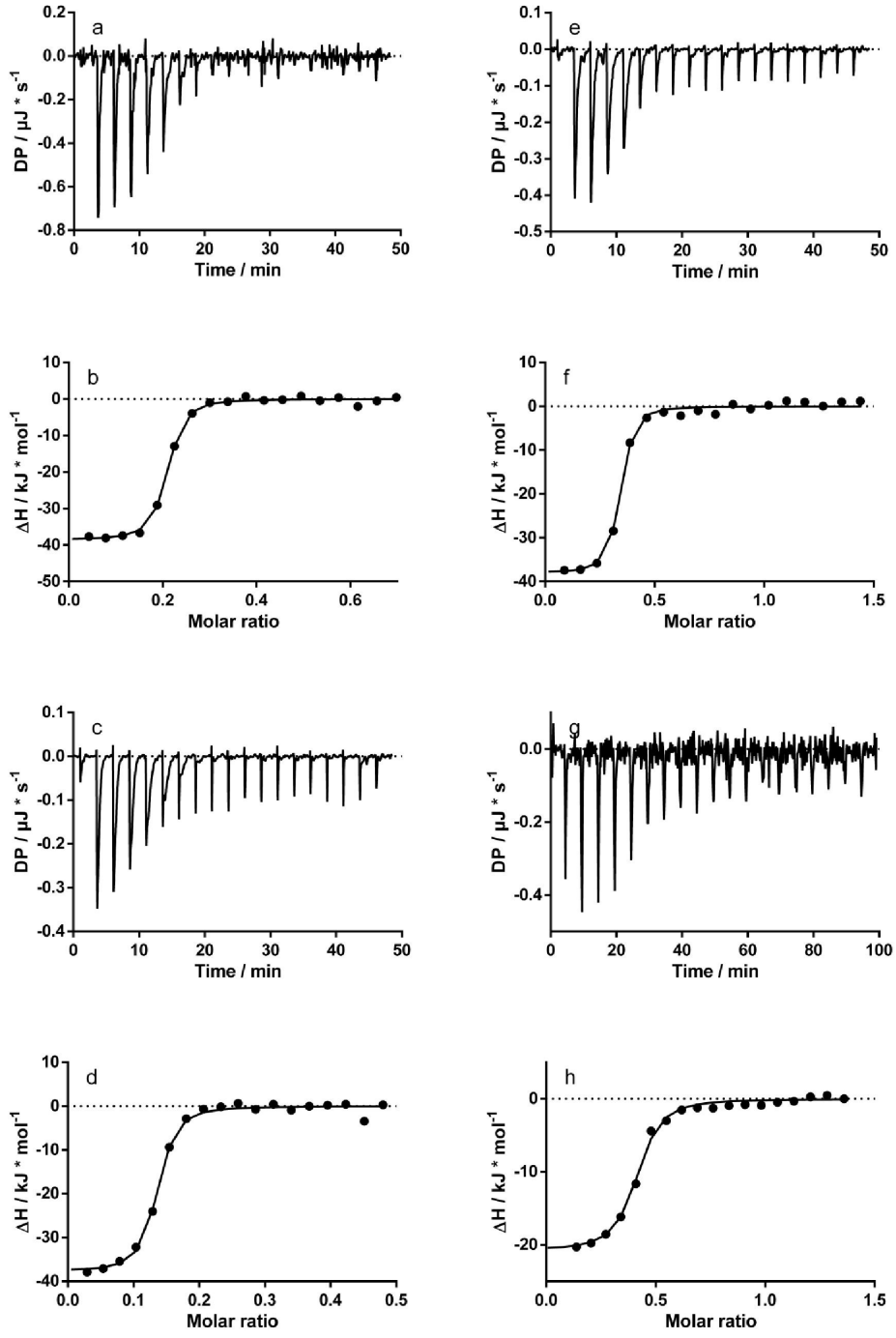

Figure S5 ITC profiles for the binding of SATFMK (a, b, e, f) and PDF306 (c, d, g, h) to HDAC8 (a-d) and HDAC4 (e-H). The plots (b, d, f and h) show the integrated heat signal of the raw data (a, c, e and g) as a function of the molar ratio of enzyme to ligand. The continuous line represents the calculated fit to a one site binding model.

2. NMR spectra of 13a-c and 14a-c

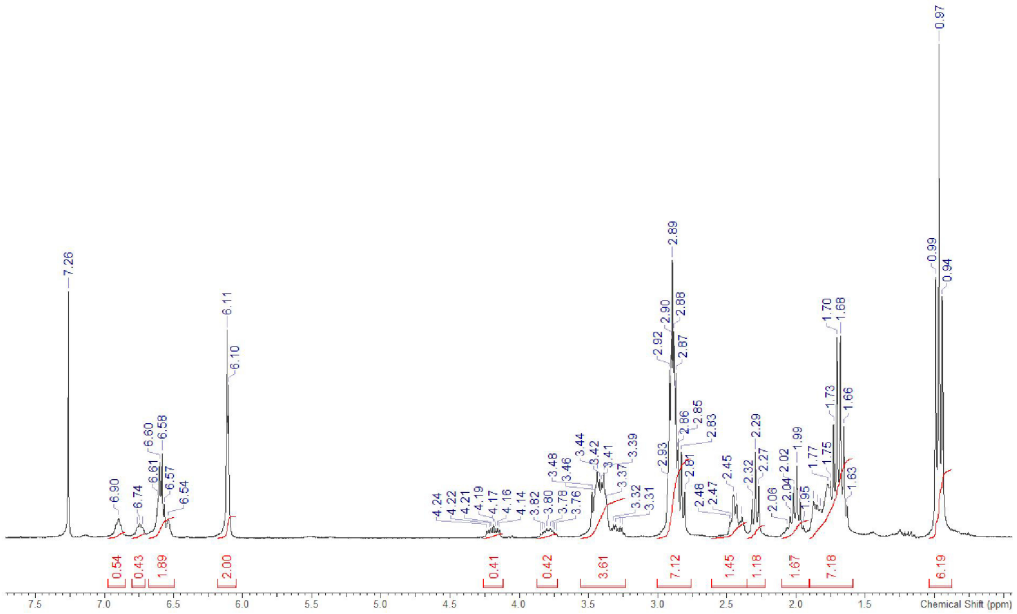

Figure S6 ^{1}H-NMR of 13a

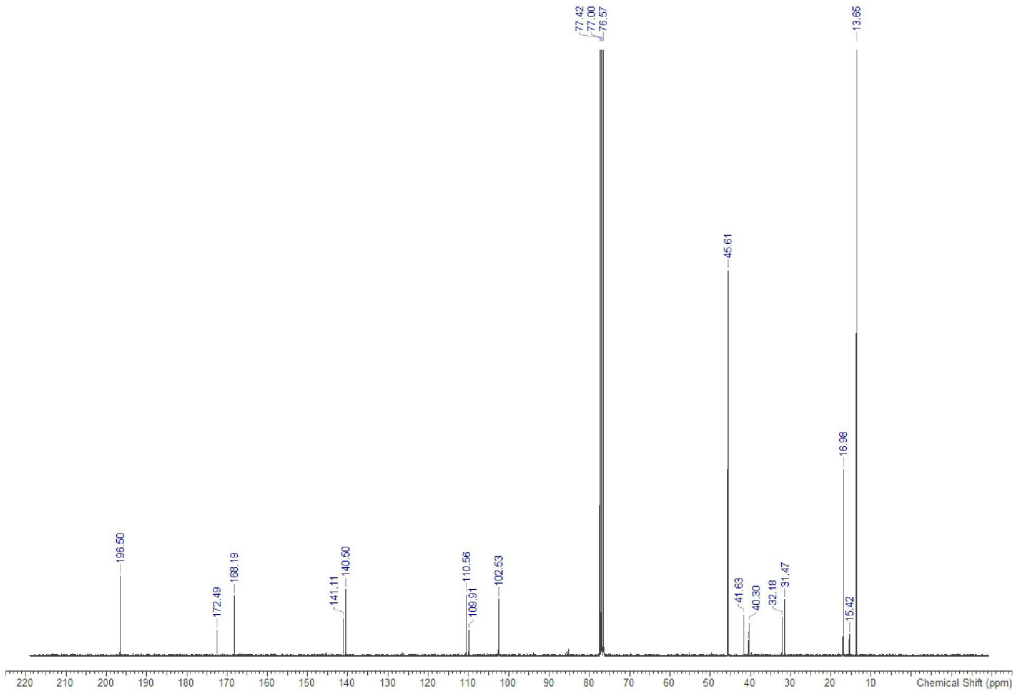

Figure S7 ^{13}C-NMR of 13a

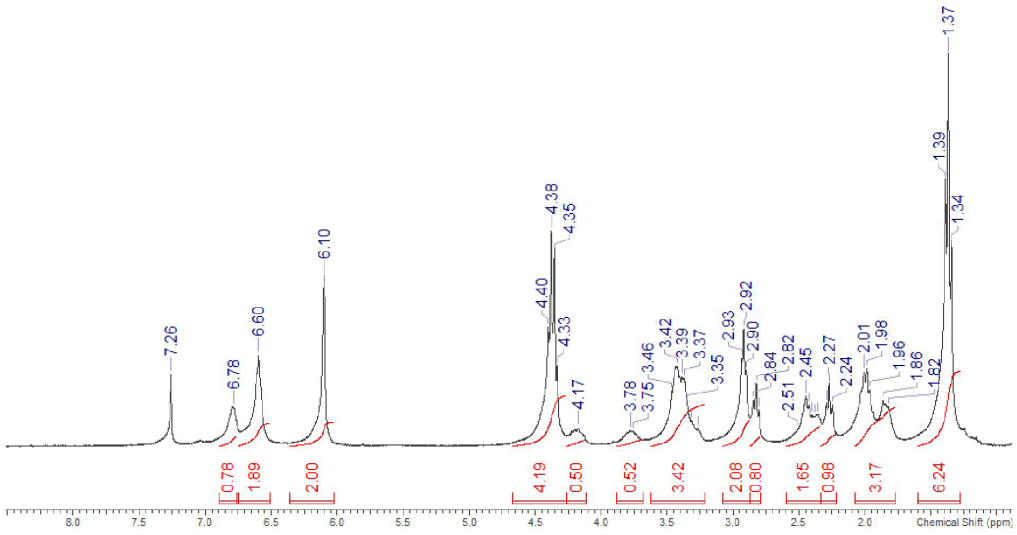

Figure S8 ^{1}H-NMR of 14a

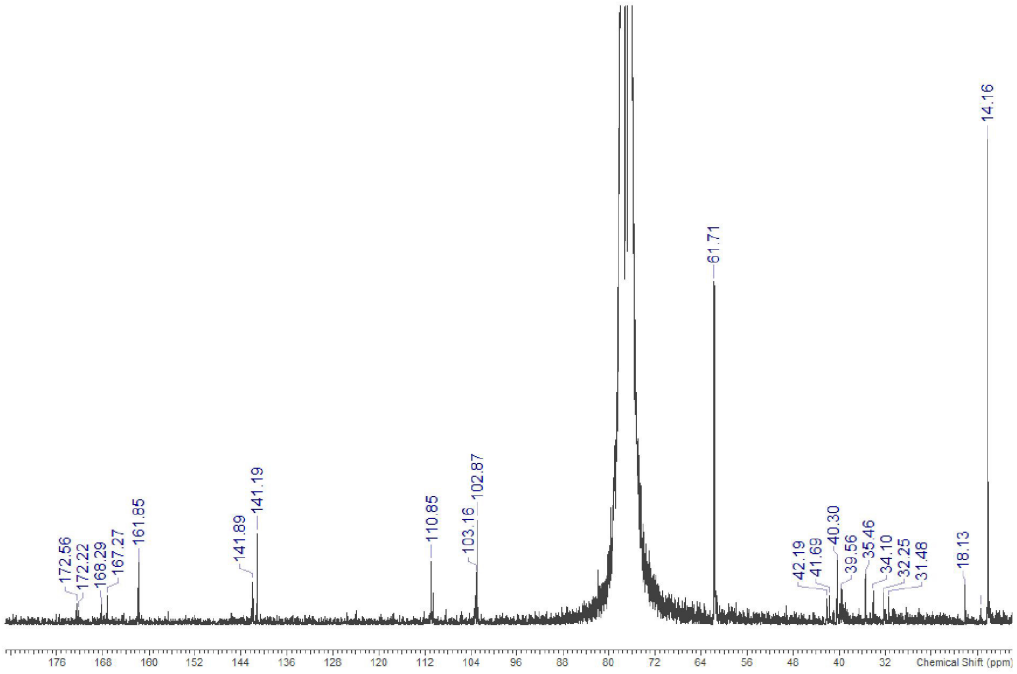

Figure S9 ^{13}C-NMR of 14a

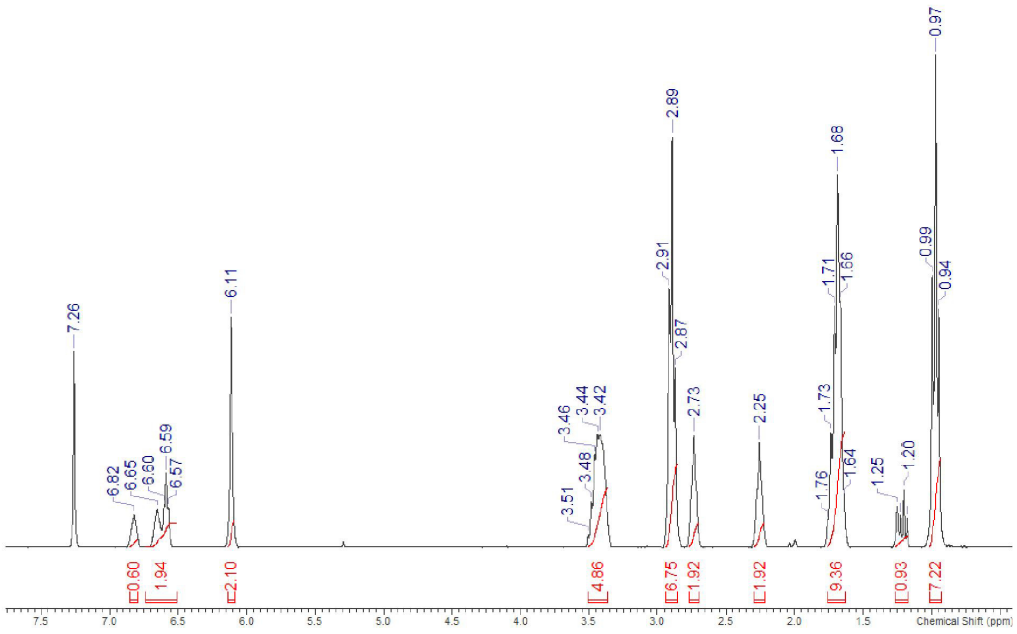

Figure S10 ^{1}H-NMR of 13b

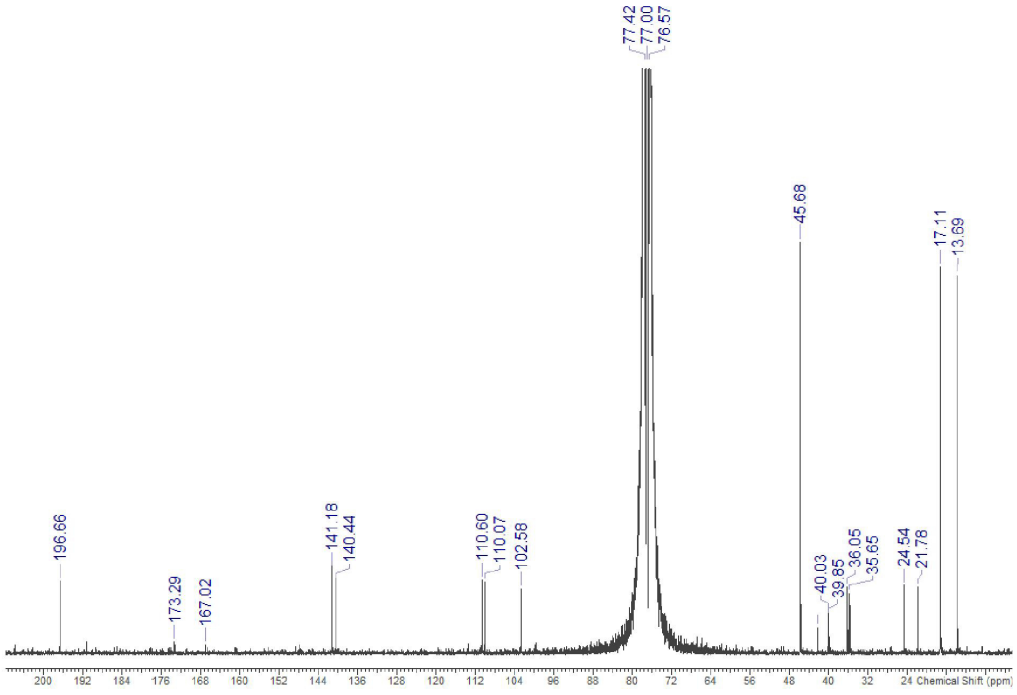

Figure S11 ^{13}C-NMR of 13b

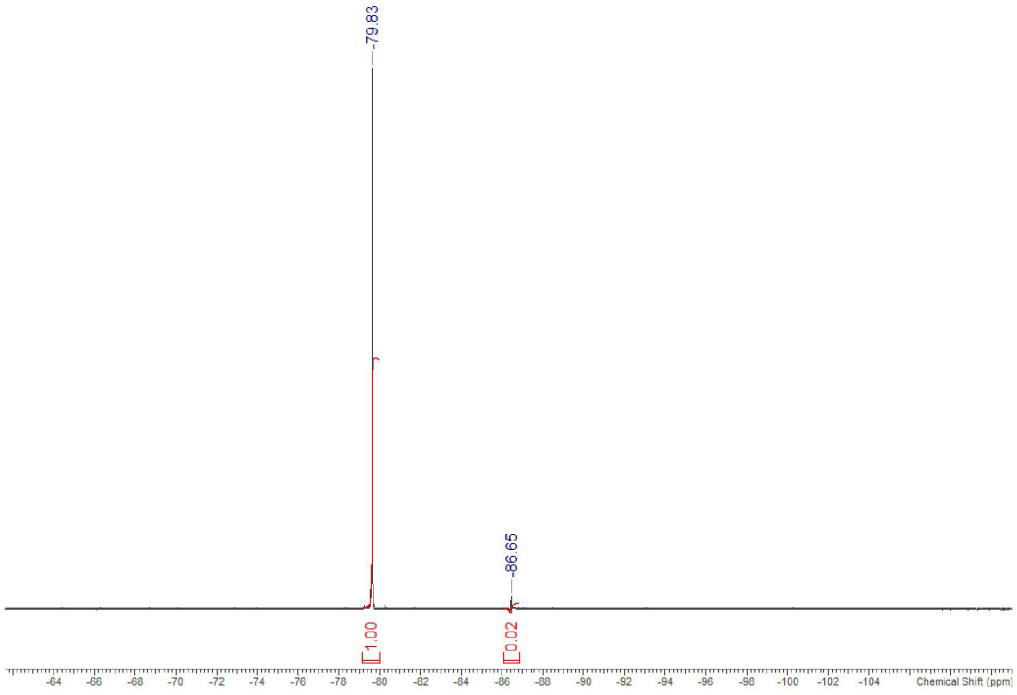

Figure S12 ^{19}F-NMR of 13b

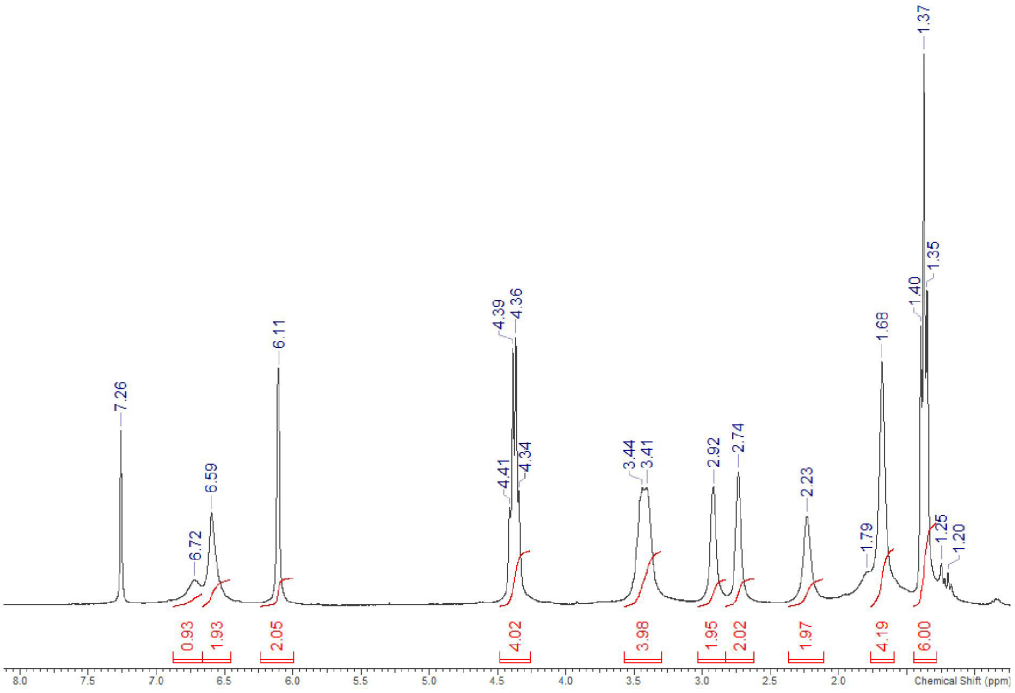

Figure S13 ^{1}H-NMR of 14b

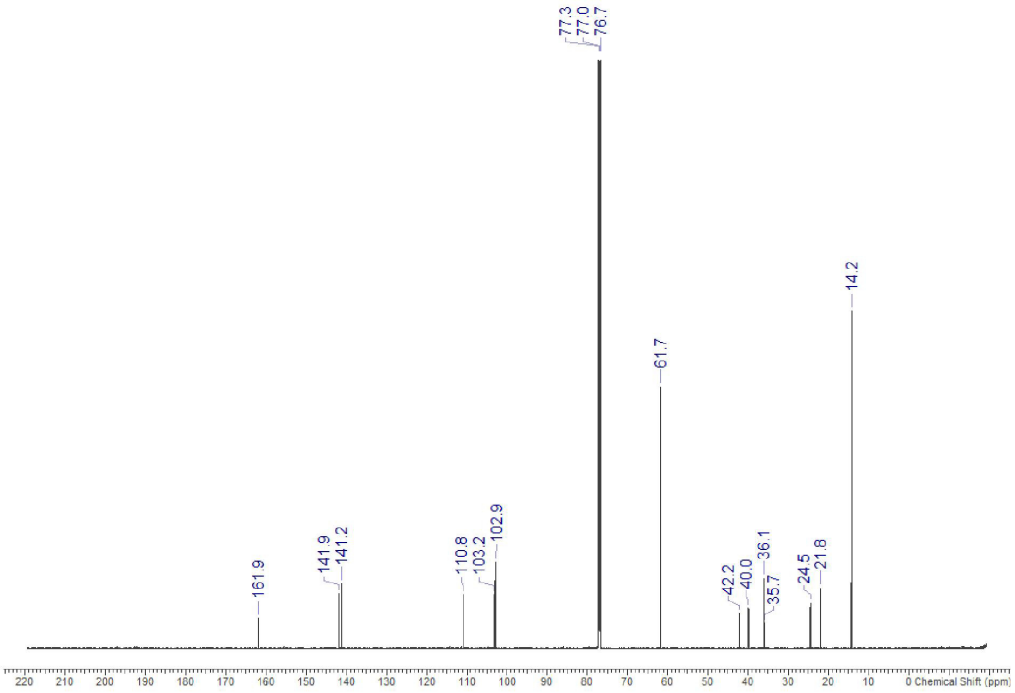

Figure S14 ^{13}C-NMR of 14b

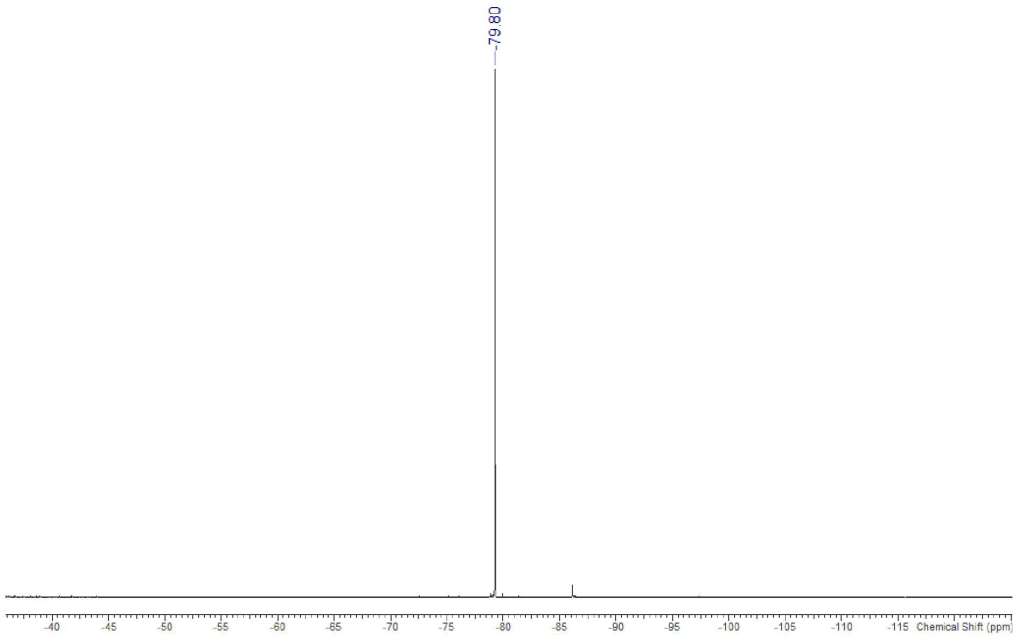

Figure S15 ^{19}F-NMR of 14b

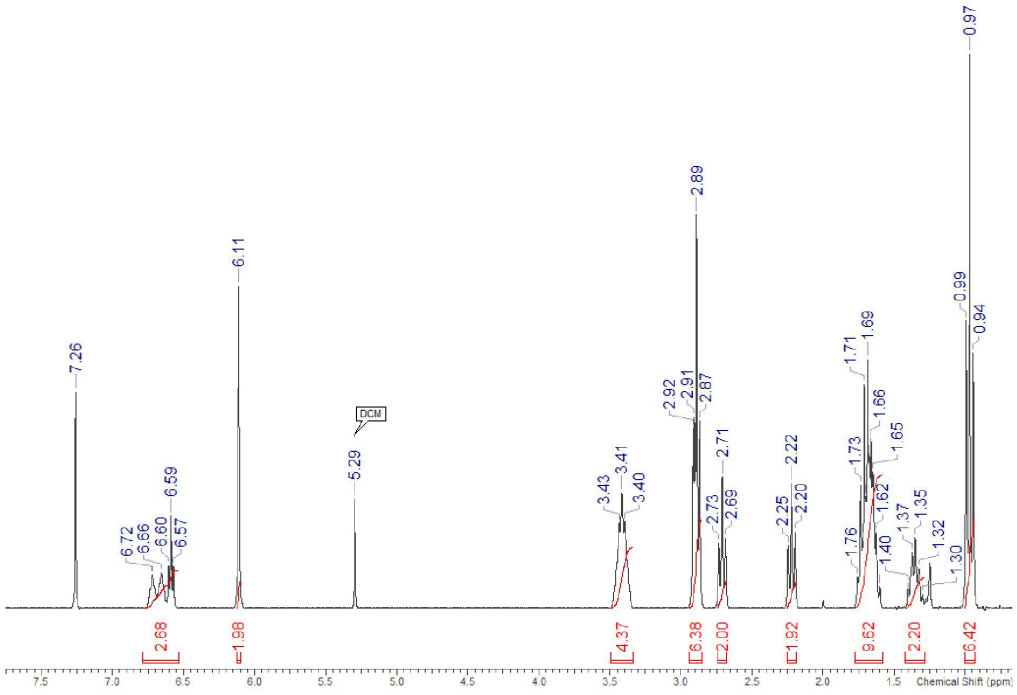

Figure S16 ^{1}H-NMR of 13c

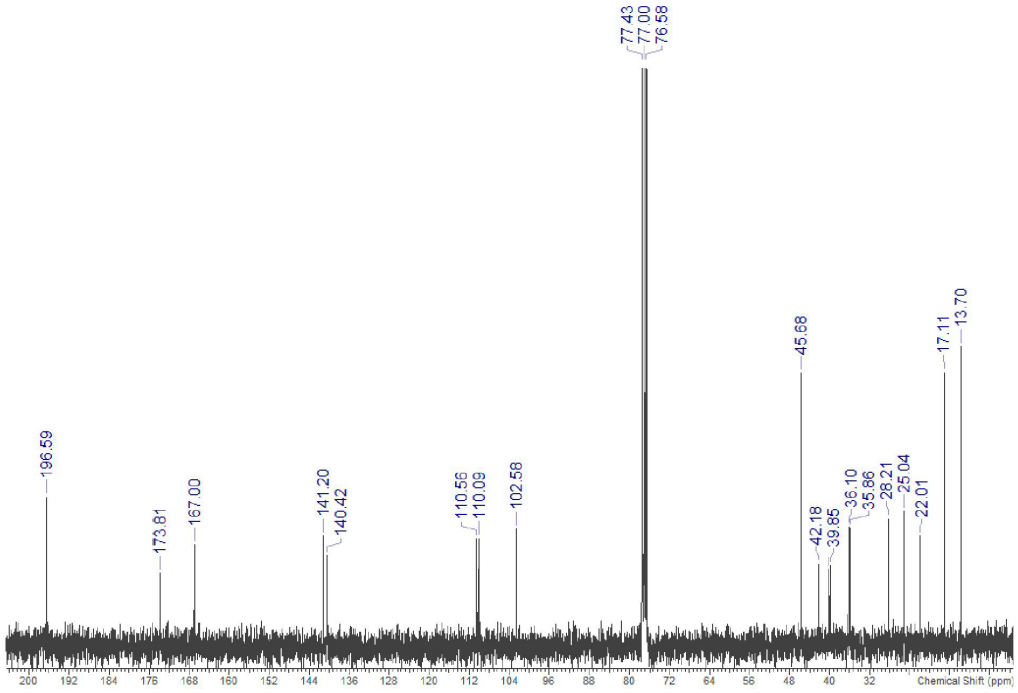

Figure S17 ^{13}C-NMR of 13c

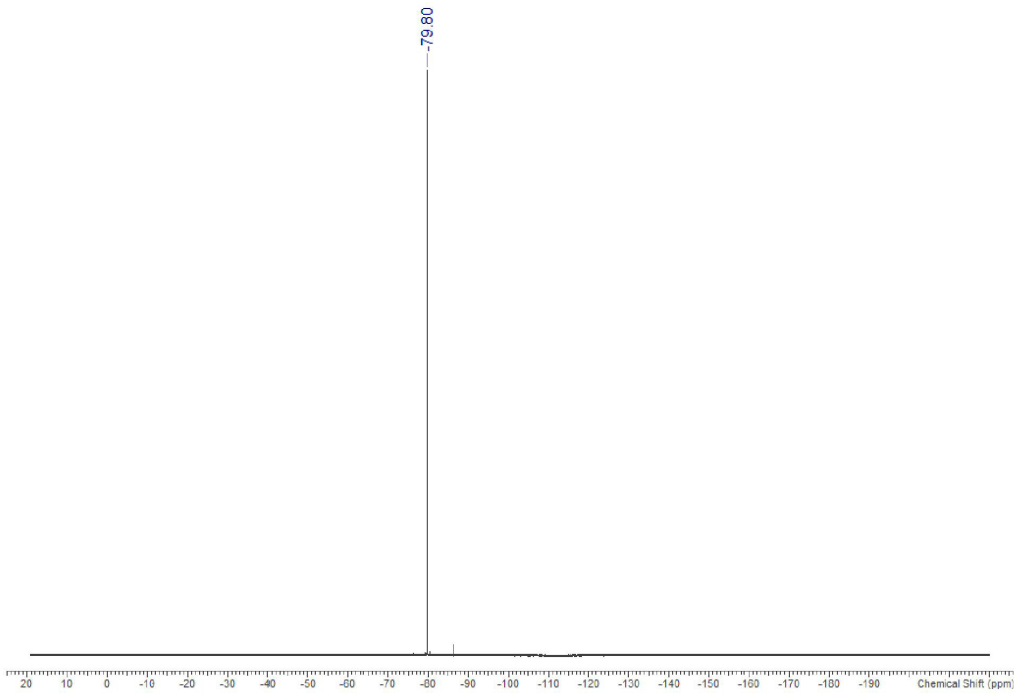

Figure S18 ^{19}F-NMR of 13c

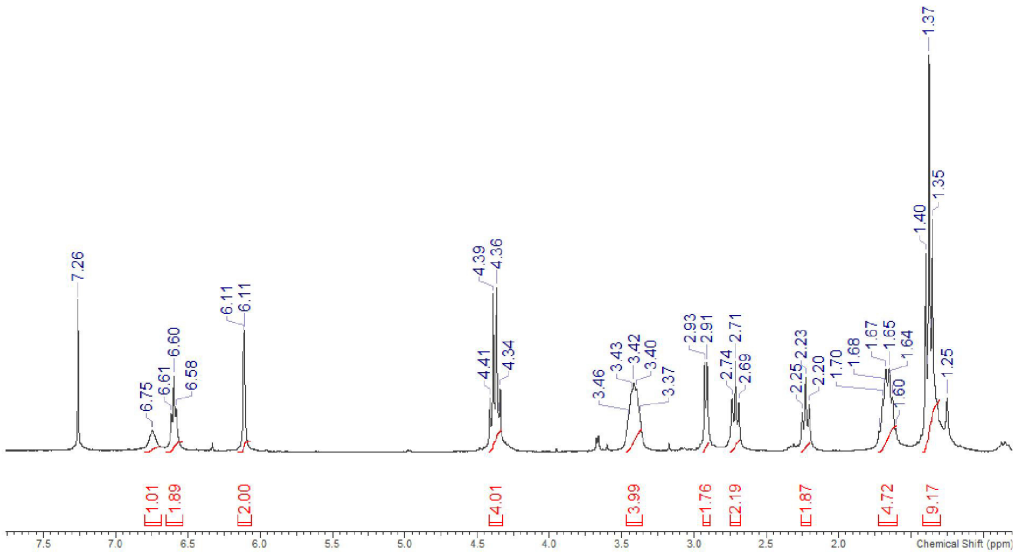

Figure S19 ^{1}H-NMR of 14c

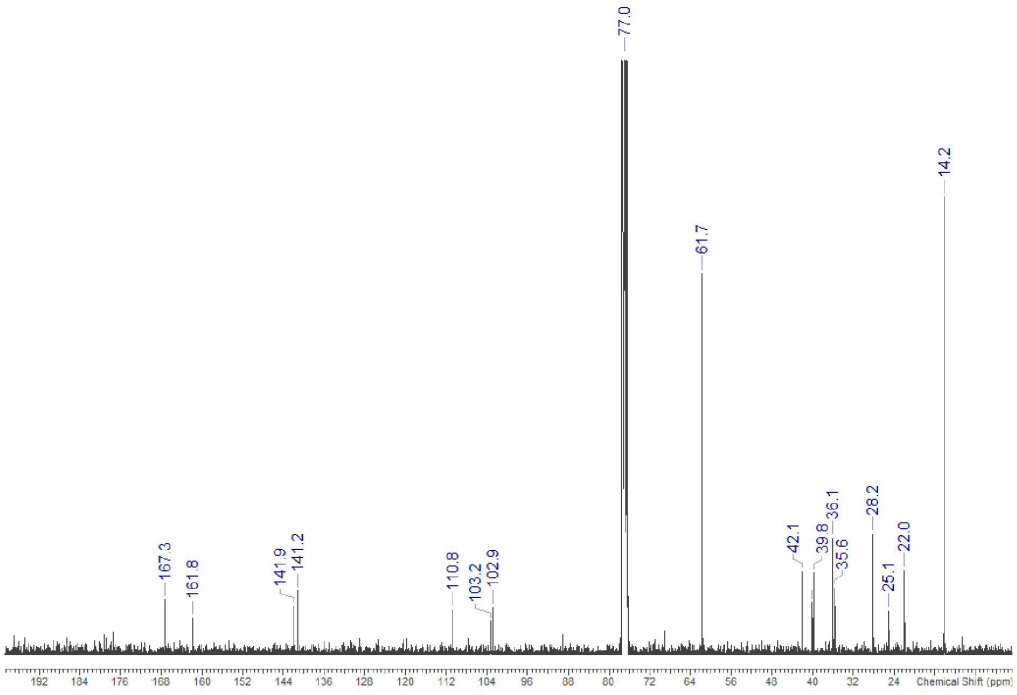

Figure S20 ^{13}C-NMR of 14c

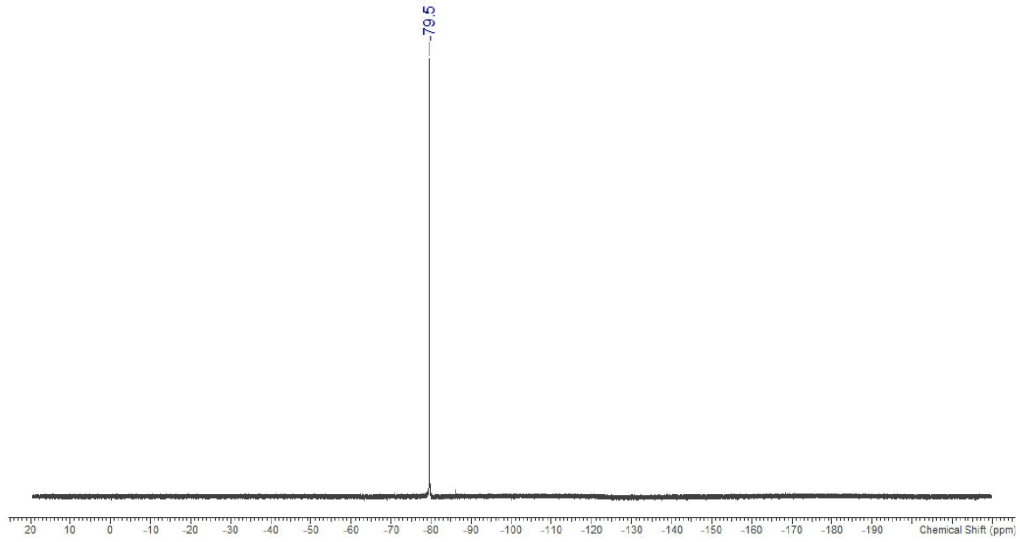

Figure S21 ^{19}F-NMR of 14c

5.3. Supplemental information for: Kinetic method for the large-scale analysis of the binding mechanism of histone deacetylase inhibitors

Supplement

Kinetic method for the analysis of the binding mechanism of histone deacetylase inhibitors

Christian Meyners[1], Matthias G. J. Baud[2, †] , Matthew J. Fuchter[2] and Franz-Josef Meyer-Almes[1, *]

1 University of Applied Sciences Darmstadt, Department of Chemical Engineering and Biotechnology, 64287 Darmstadt, Germany.

2 Imperial College London, Department of Chemistry, London SW7 2AZ, United Kingdom.

ǂ Present adress: University of Cambridge, Department of Chemistry, Lensfield Rd, CB2 1EW, United Kingdom.

* Correspondence: (E-mail): franz-josef.meyer-almes@h-da.de; (tel): +49-6151168406; (fax): +49-6151168404

1. Binding kinetics of SAHA to HDAH

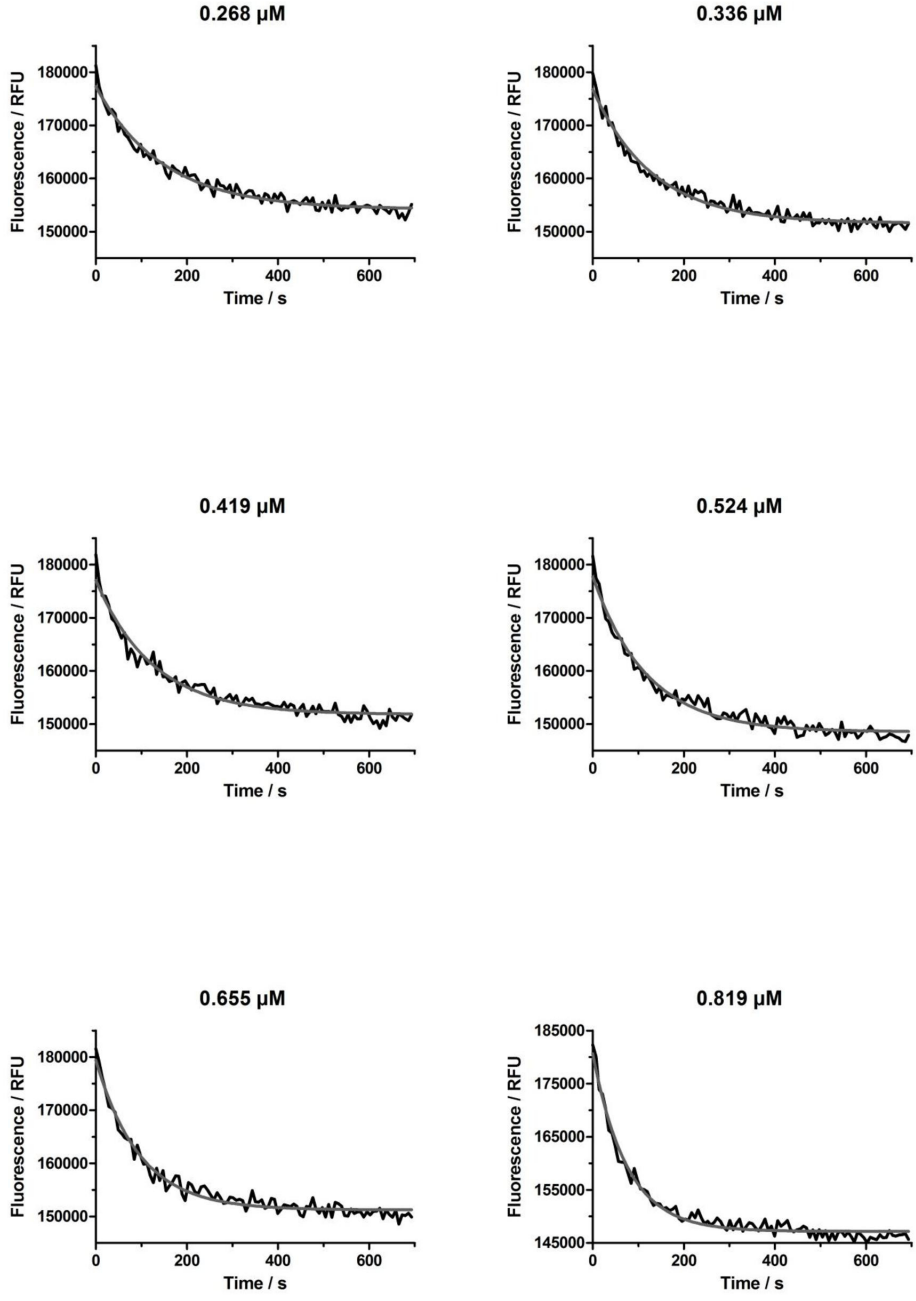

Fig. S1 Association kinetics of SAHA binding to HDAH. The investigation of the association of the indicated concentrations of SAHA to HDAH in assay buffer at 25 °C occurred by adding an equilibrated solution of 50 nM HDAH and 5 µM of the dansyl-conjugate **5b** to equilibrated solutions of SAHA. The fluorescence intensity at 530 nm is plotted against the time. The obtained curves were fitted to a single phase exponential decay model, whose least-square fits are represented by the continuous lines.

2. Binding kinetics of LU210 to HDAH

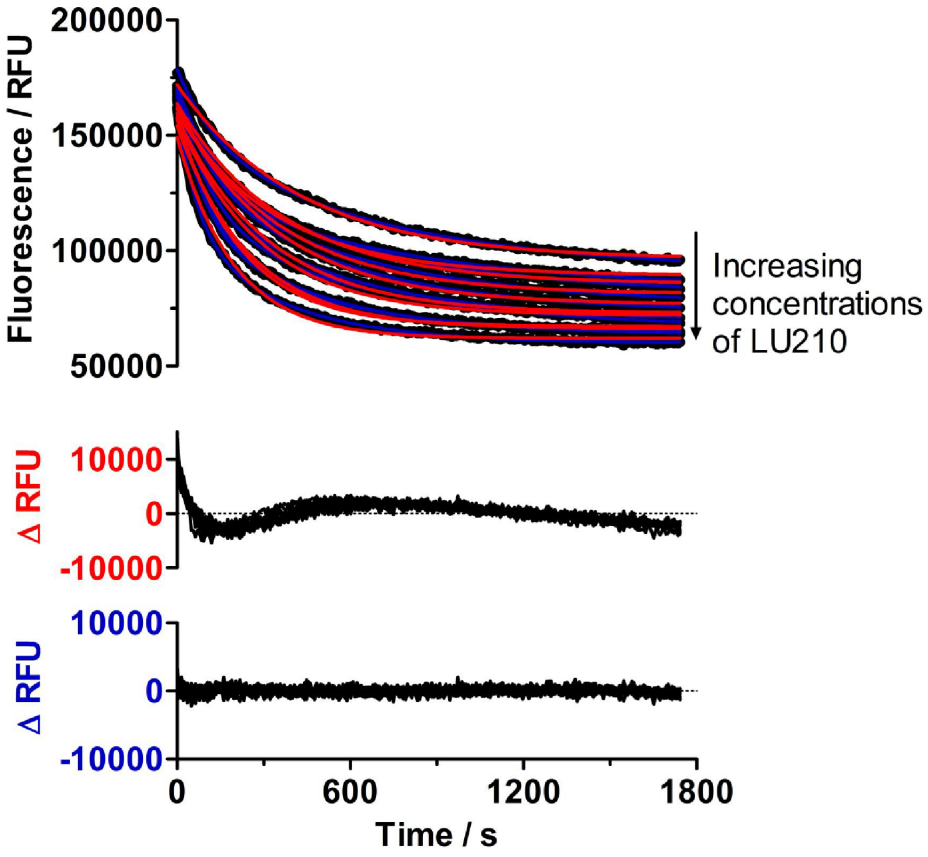

Fig. S2 Association kinetics of LU210 binding to HDAH at 25 °C. The association kinetics were measured using a FRET based reporter displacement assay with 0.5 µM HDAH and 5 µM of the dansyl-conjugate 5c in assay buffer. Concentrations of LU210 ranged from 8.4 to 50 µM. The obtained fluorescence signal at 530 nm is plotted against the time. The obtained kinetics were fitted to a single (red) and a two (blue) phase exponential decay model. An overlay of all residuals for the single (upper residual plot) and the two (lower residual plot) phase model is shown below. The systematic derivation of the single phase model indicates that the two phase model is more sufficient to describe the data.

3. Binding kinetics of SATFMK to HDAH

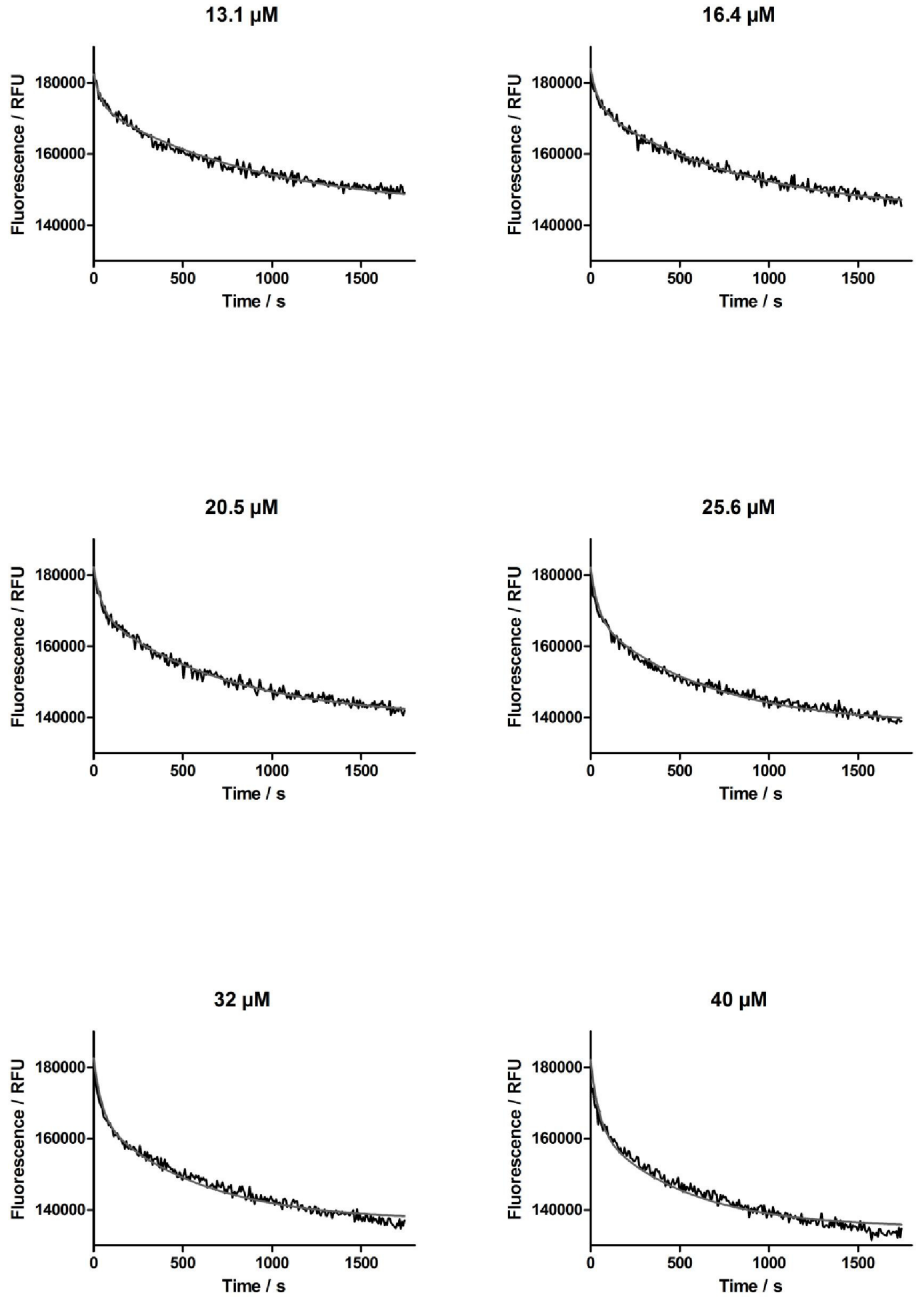

Fig. S3 Association kinetics of SATFMK binding to HDAH. The investigation of the association of the indicated concentrations of SATFMK to HDAH in assay buffer at 25 °C occurred by adding an equilibrated solution of 500 nM HDAH and 5 µM of the dansyl-conjugate **5c** to equilibrated solutions of SATFMK. The fluorescence intensity at 530 nm is plotted against the time. The raw time courses were subjected to a global fit to a two-step binding mechanism. The fit curves are represented by smooth lines.

4. Binding kinetics of TSA to HDAC1

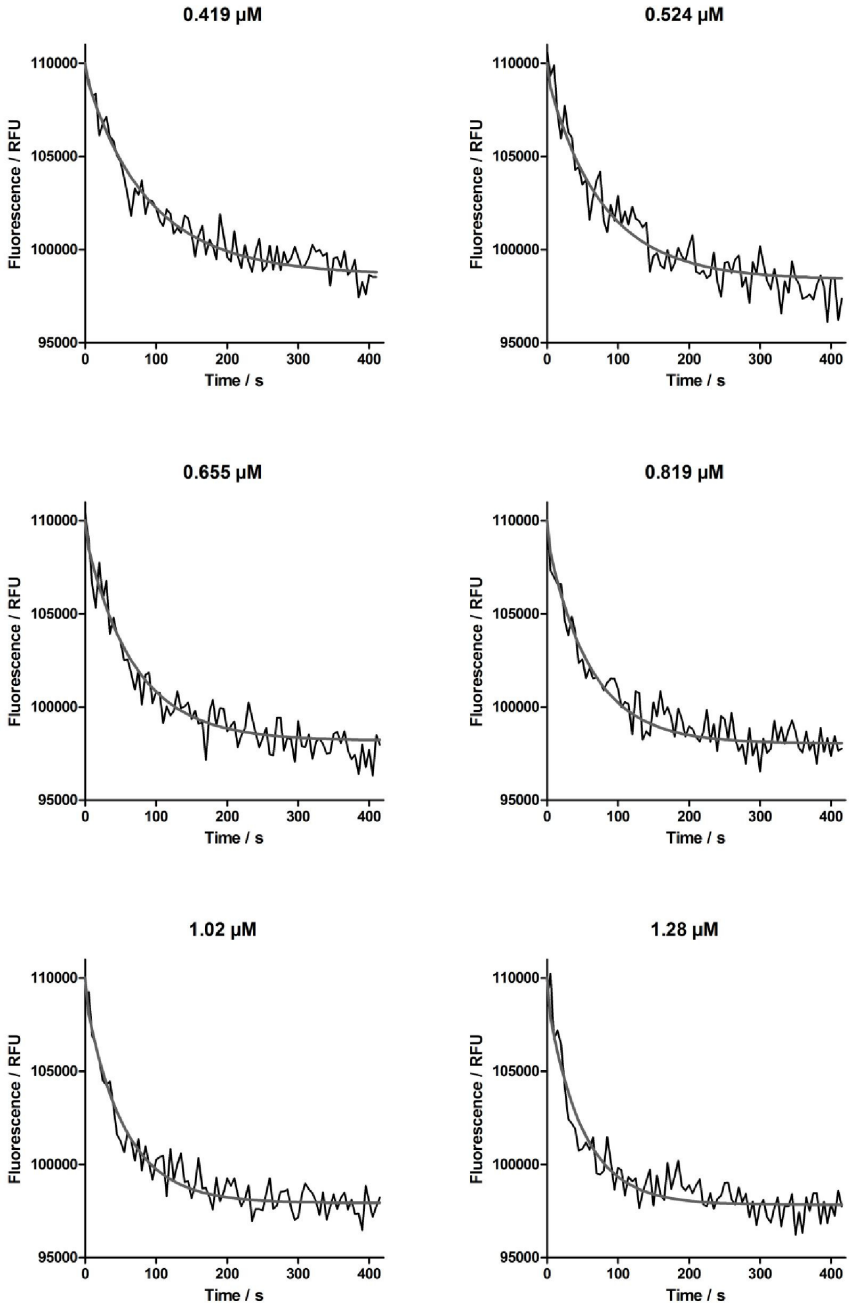

Fig. S4 Association kinetics of TSA binding to HDAC1 at 25 °C. The association kinetics were determined using a FRET based reporter displacement assay with 0.1 µM HDAC1 and 5 µM of the dansyl-conjugate **5b** in assay buffer. Concentrations of TSA were as indicated. The obtained fluorescence signal at 530 nm is plotted against the time. The raw time courses were subjected to a global fit to a two-step binding mechanism. The fit curves are represented by smooth lines.

5. Binding kinetics of SAHA to HDAC1

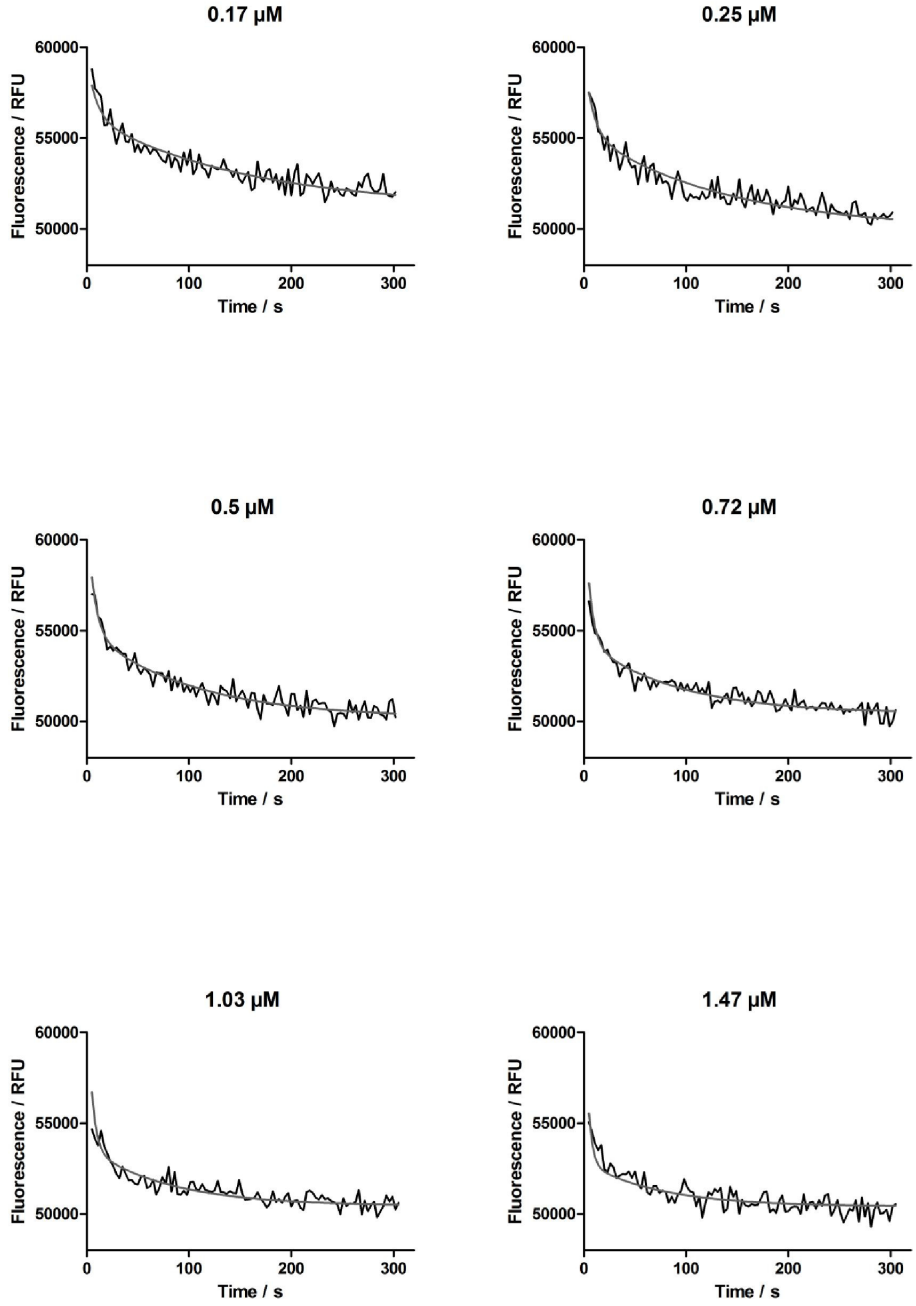

Fig. S5 Association kinetics of SAHA binding to HDAC1 at 25 °C. The association kinetics were determined using a FRET based reporter displacement assay with 0.1 µM HDAC1 and 5 µM of the dansyl-conjugate **5b** in assay buffer. Concentrations of SAHA were as indicated. The obtained fluorescence signal at 530 nm is plotted against the time. The raw time courses were subjected to a global fit to a two-step binding mechanism. The fit curves are represented by smooth lines.

6. Binding kinetics of LU210 to HDAC1

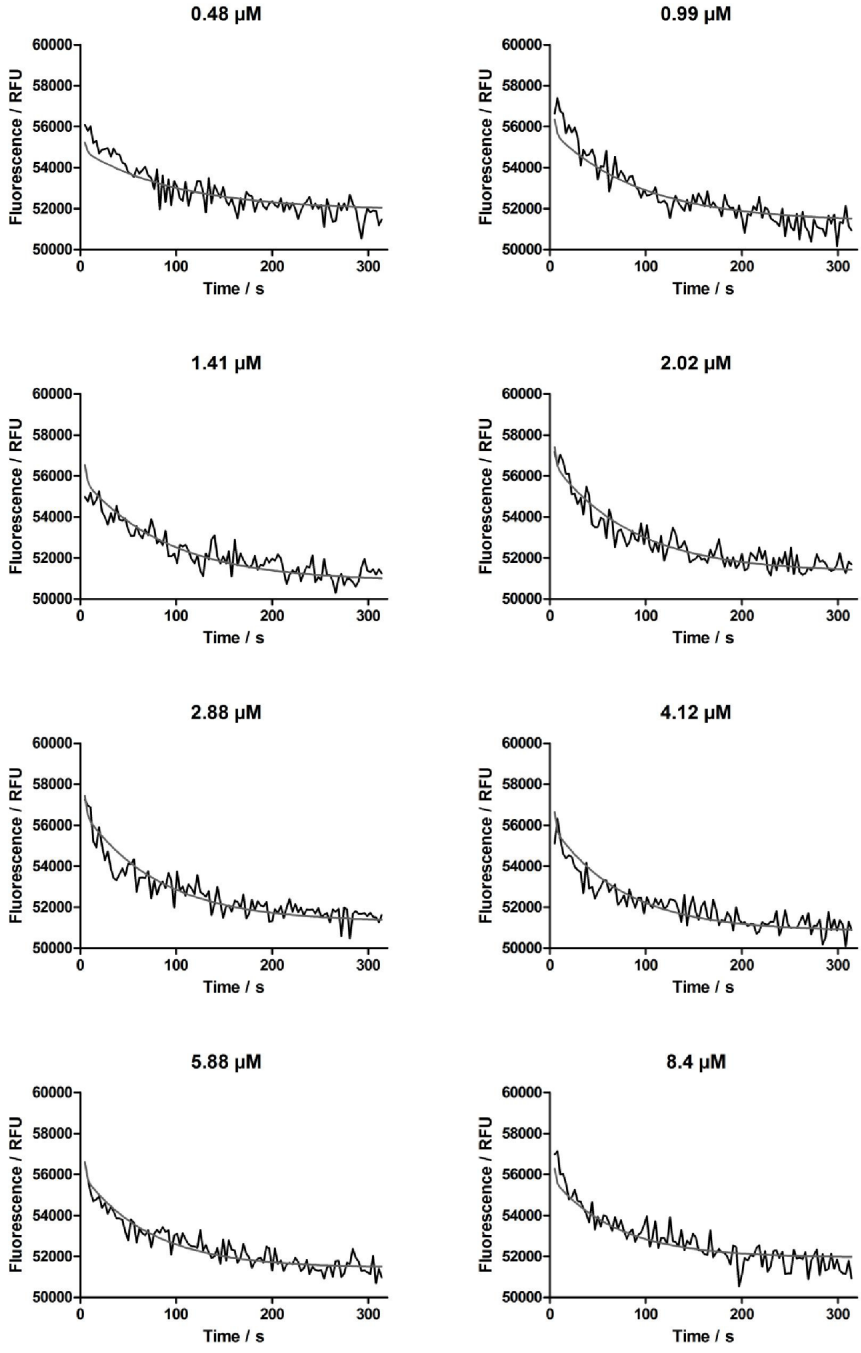

Fig. S6 Association kinetics of LU210 binding to HDAC1 at 25 °C. The association kinetics were determined using a FRET based reporter displacement assay with 0.1 µM HDAC1 and 5 µM of the dansyl-conjugate **5b** in assay buffer. Concentrations of LU210 were as indicated. The obtained fluorescence signal at 530 nm is plotted against the time. The raw time courses were subjected to a global fit to a two-step binding mechanism. The fit curves are represented by smooth lines.

7. Binding kinetics of SATFMK to HDAC1

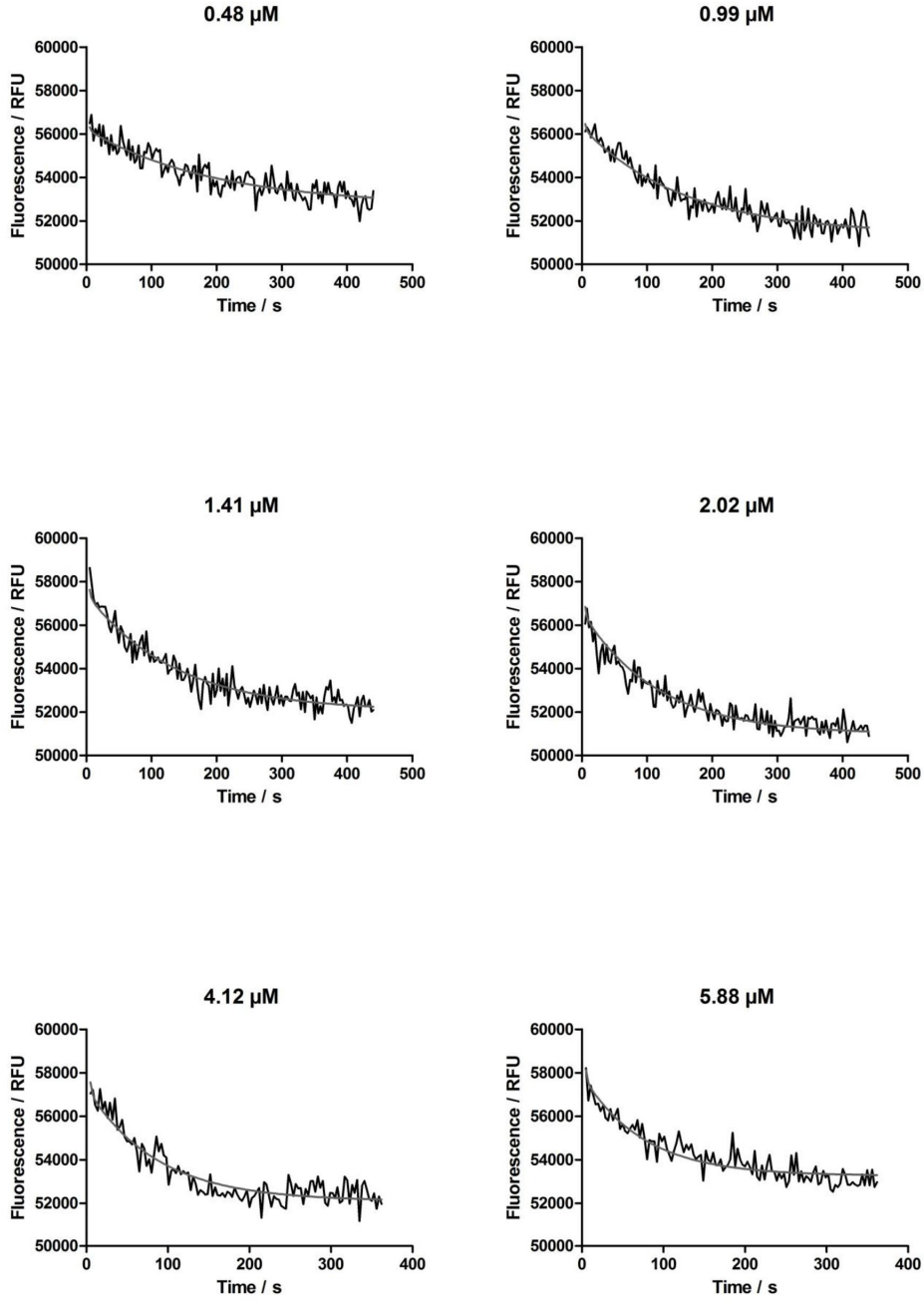

Fig. S7 Association kinetics of SATFMK binding to HDAC1 at 25 °C. The association kinetics were determined using a FRET based reporter displacement assay with 0.1 µM HDAC1 and 5 µM of the dansyl-conjugate **5b** in assay buffer. Concentrations of SATFMK were as indicated. The obtained fluorescence signal at 530 nm is plotted against the time. The raw time courses were subjected to a global fit to a two-step binding mechanism. The fit curves are represented by smooth lines.

9. Binding kinetics of SAHA to HDAC6

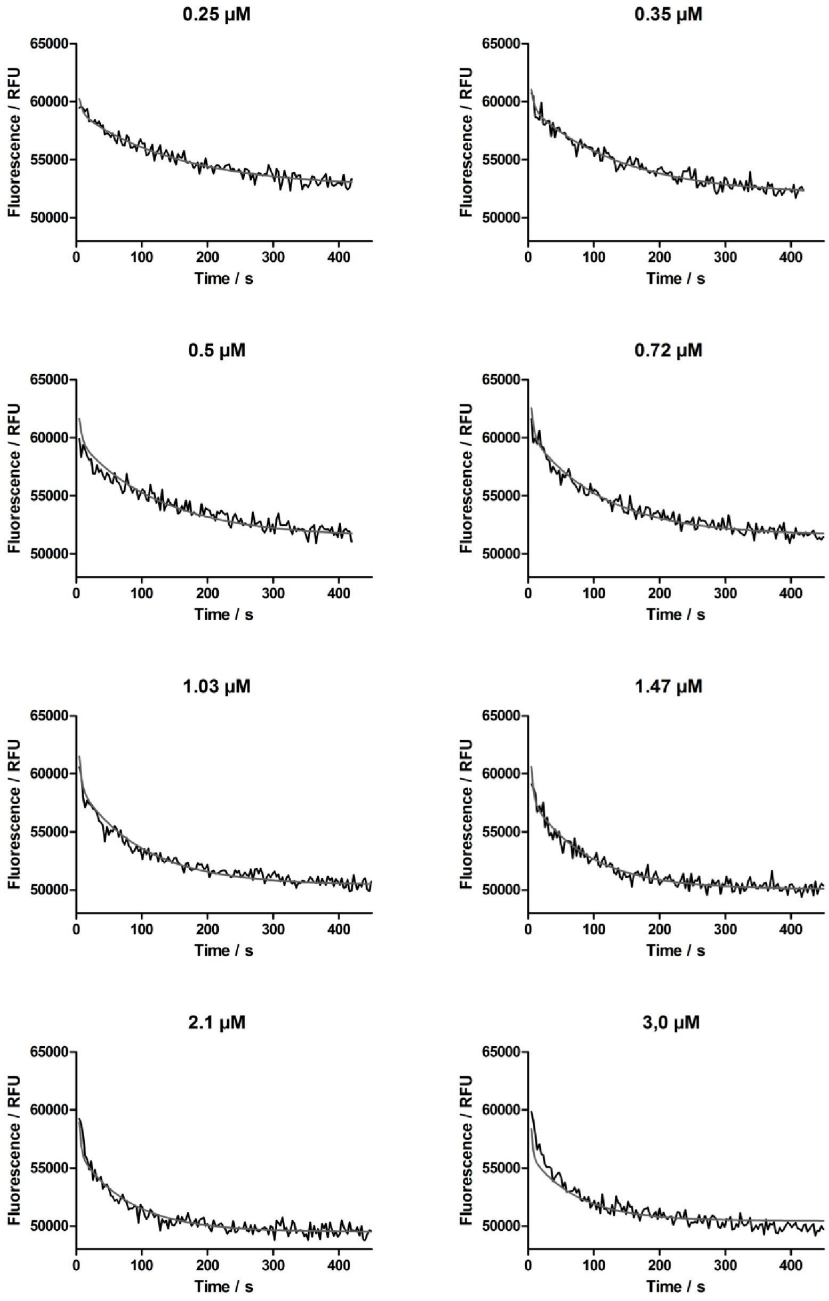

Fig. S9 Association kinetics of SAHA binding to HDAC6 at 25 °C. The association kinetics were determined using a FRET based reporter displacement assay with 0.05 µM HDAC6 and 5 µM of the dansyl-conjugate **5b** in assay buffer. Concentrations of SAHA were as indicated. The obtained fluorescence signal at 530 nm is plotted against the time. The raw time courses were subjected to a global fit to a two-step binding mechanism. The fit curves are represented by smooth lines.

10. Binding kinetics of LU210 to HDAC6

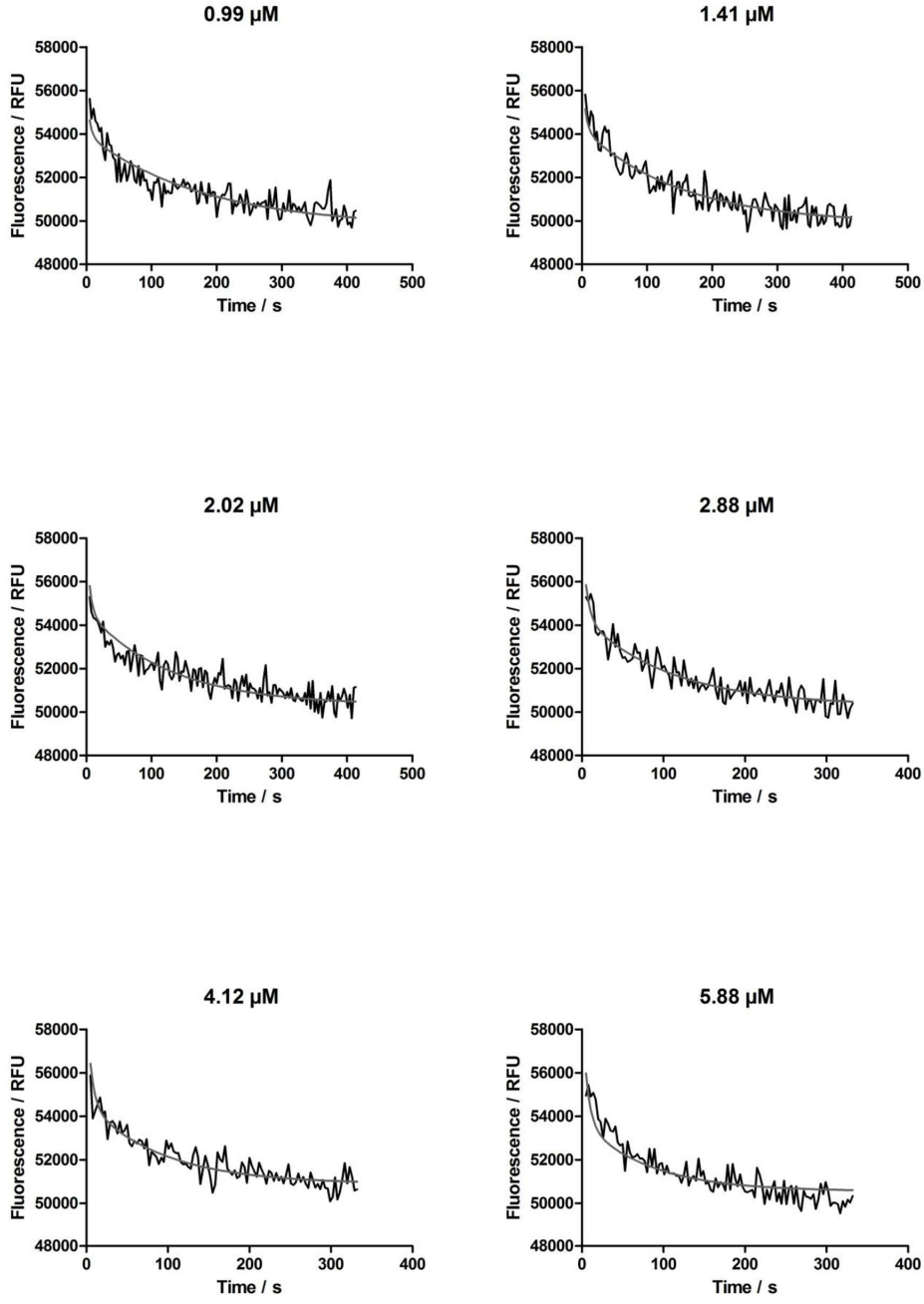

Fig. S10 Association kinetics of LU210 binding to HDAC6 at 25 °C. The association kinetics were determined using a FRET based reporter displacement assay with 0.05 µM HDAC6 and 5 µM of the dansyl-conjugate **5b** in assay buffer. Concentrations of LU210 were as indicated. The obtained fluorescence signal at 530 nm is plotted against the time. The raw time courses were subjected to a global fit to a two-step binding mechanism. The fit curves are represented by smooth lines.

11. Binding kinetics of SATFMK to HDAC6

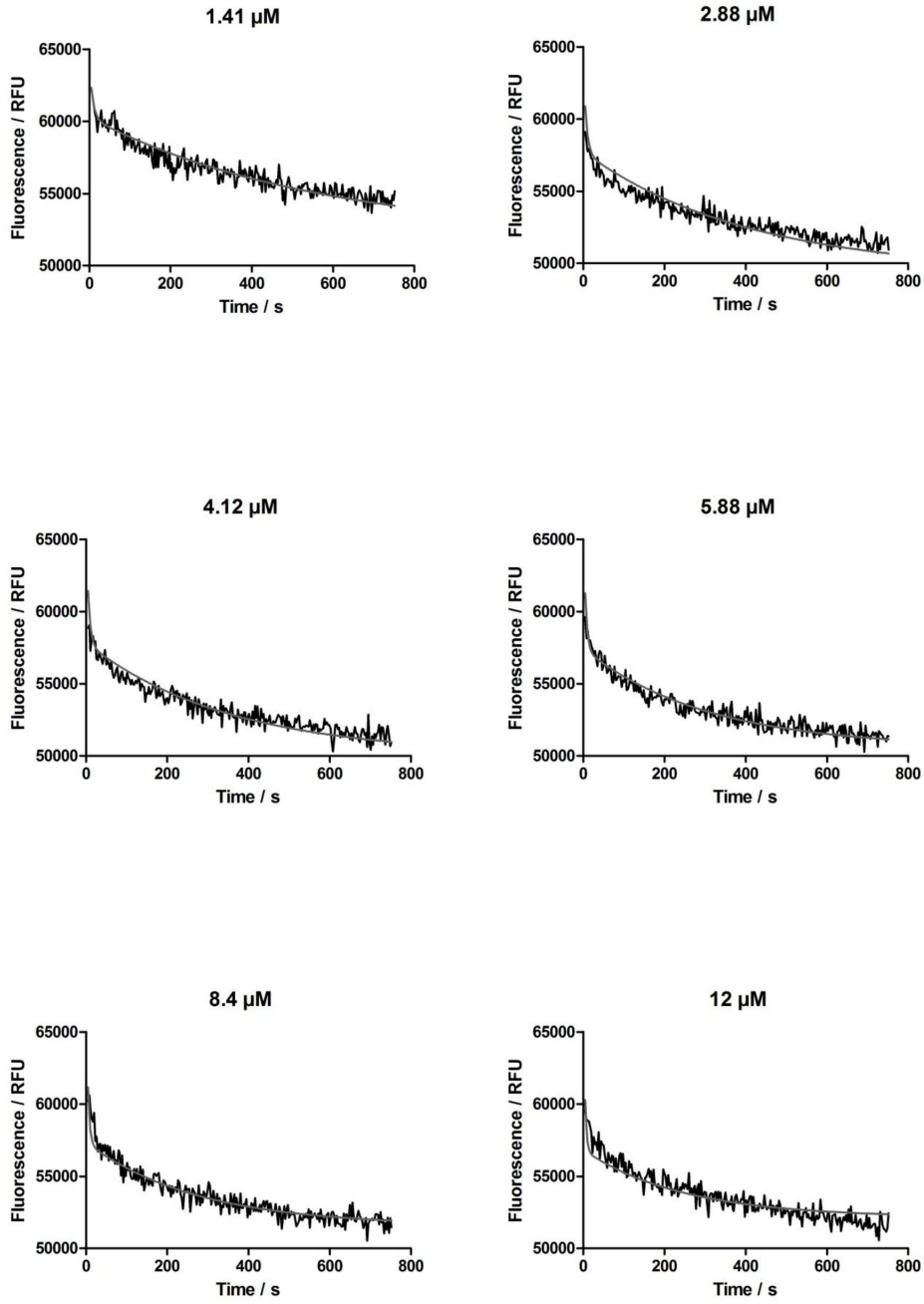

Fig. S11 Association kinetics of SATFMK binding to HDAC6 at 25 °C. The association kinetics were determined using a FRET based reporter displacement assay with 0.05 µM HDAC6 and 5 µM of the dansyl-conjugate **5b** in assay buffer. Concentrations of SATFMK were as indicated. The obtained fluorescence signal at 530 nm is plotted against the time. The raw time courses were subjected to a global fit to a two-step binding mechanism. The fit curves are represented by smooth lines.

12. Binding kinetics of TSA to HDAC8

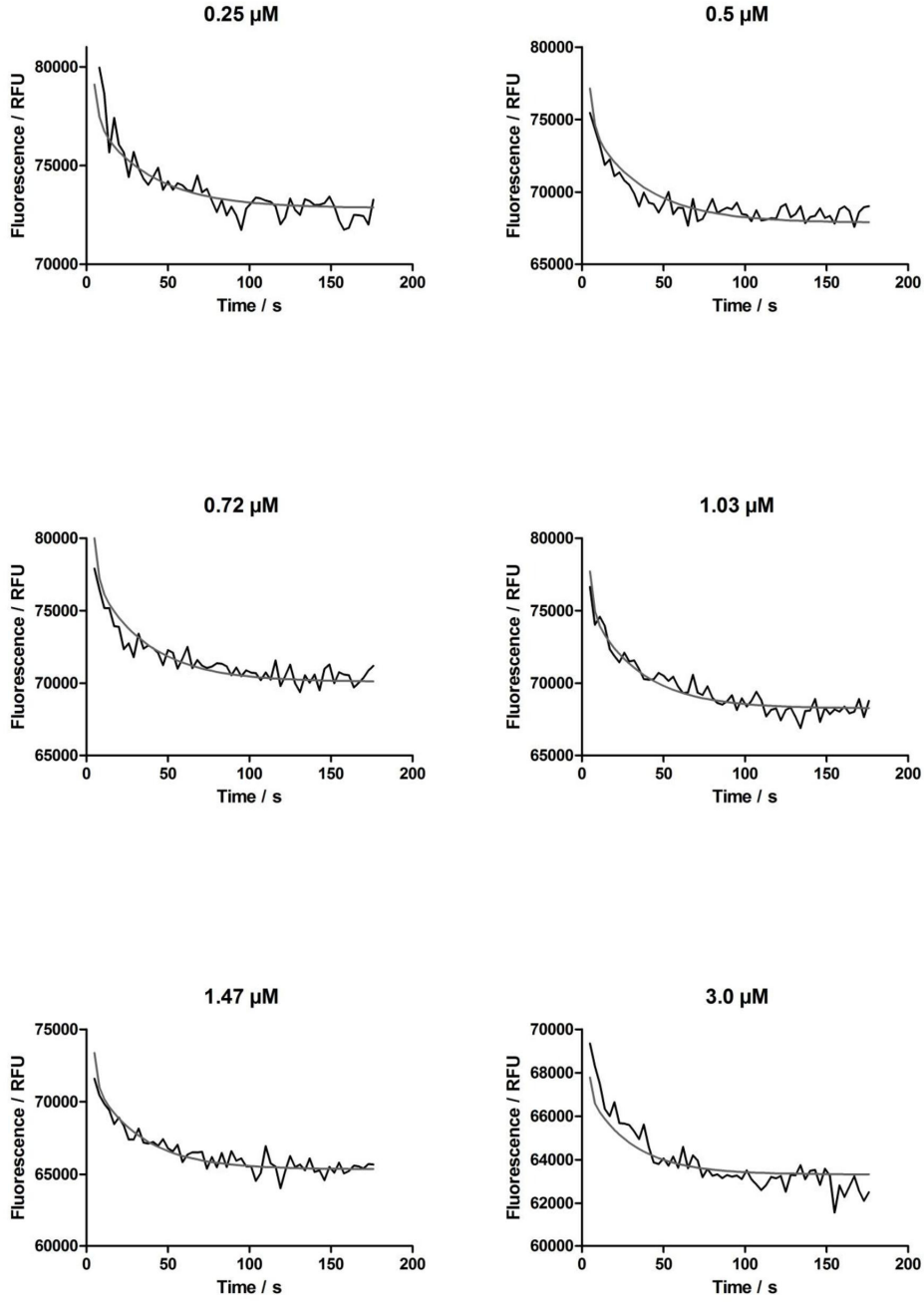

Fig. S12 Association kinetics of TSA binding to HDAC8 at 25 °C. The association kinetics were determined using a FRET based reporter displacement assay with 0.4 µM HDAC8 and 5 µM of the dansyl-conjugate **5b** in assay buffer. Concentrations of TSA were as indicated. The obtained fluorescence signal at 530 nm is plotted against the time. The raw time courses were subjected to a global fit to a two-step binding mechanism. The fit curves are represented by smooth lines.

13. Binding kinetics of SAHA to HDAC8

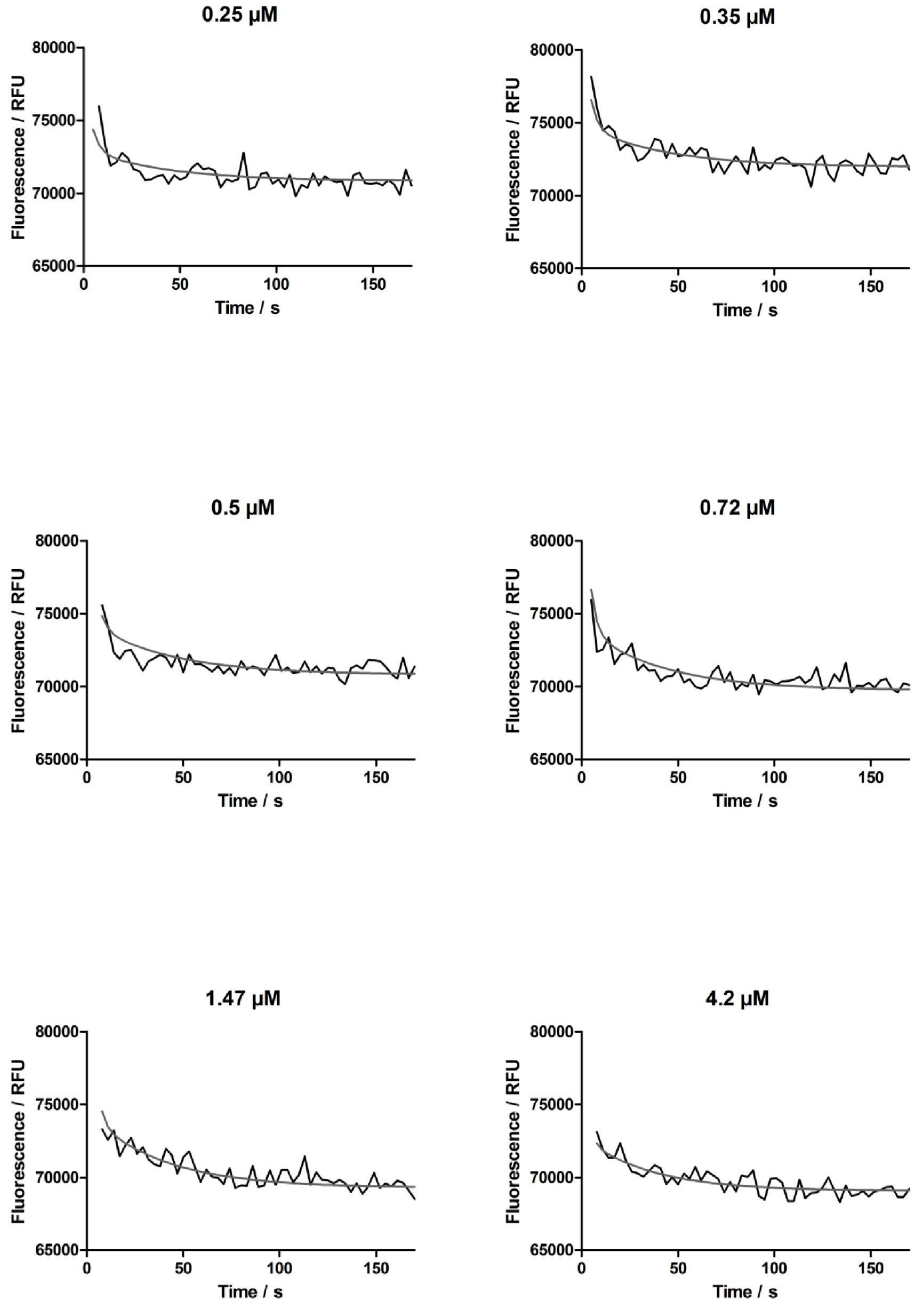

Fig. S13 Association kinetics of SAHA binding to HDAC8 at 25 °C. The association kinetics were determined using a FRET based reporter displacement assay with 0.4 µM HDAC8 and 5 µM of the dansyl-conjugate **5b** in assay buffer. Concentrations of SAHA were as indicated. The obtained fluorescence signal at 530 nm is plotted against the time. The raw time courses were subjected to a global fit to a two-step binding mechanism. The fit curves are represented by smooth lines.

14. Binding kinetics of LU210 to HDAC8

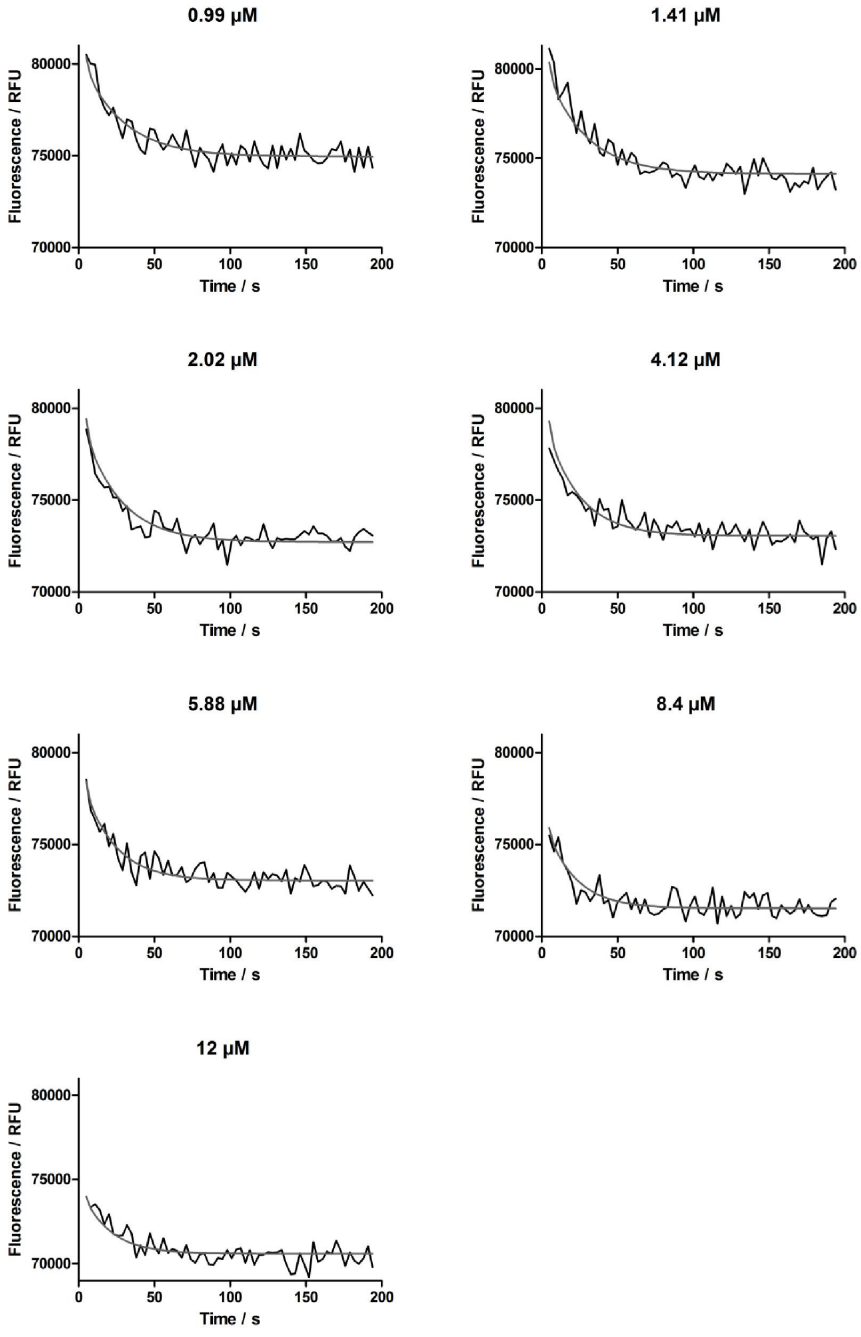

Fig. S14 Association kinetics of LU210 binding to HDAC8 at 25 °C. The association kinetics were determined using a FRET based reporter displacement assay with 0.4 µM HDAC8 and 5 µM of the dansyl-conjugate **5b** in assay buffer. Concentrations of LU210 were as indicated. The obtained fluorescence signal at 530 nm is plotted against the time. The raw time courses were subjected to a global fit to a two-step binding mechanism. The fit curves are represented by smooth lines.

15. Binding kinetics of SATFMK to HDAC8

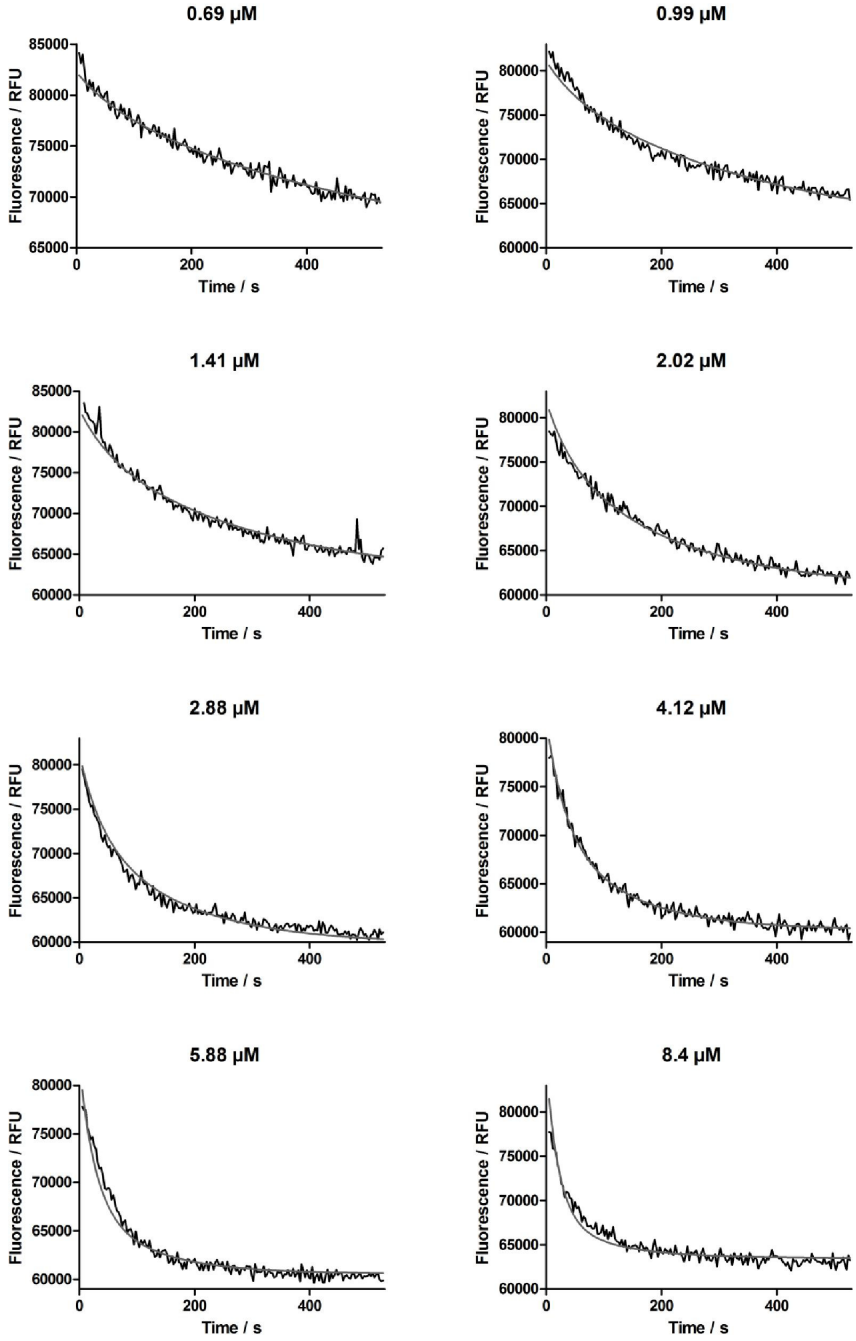

Fig. S15 Association kinetics of SATFMK binding to HDAC8 at 25 °C. The association kinetics were determined using a FRET based reporter displacement assay with 0.4 µM HDAC8 and 5 µM of the dansyl-conjugate **5b** in assay buffer. Concentrations of SATFMK were as indicated. The obtained fluorescence signal at 530 nm is plotted against the time. The raw time courses were subjected to a global fit to a two-step binding mechanism. The fit curves are represented by smooth lines.

5.4. Supplemental information for: Impact of binding mechanism on selective inhibition of histone deacetylase isoforms

Impact of binding mechanism on selective inhibition of histone deacetylase isoforms

Christian Meyners[1], Franz-Josef Meyer-Almes[1,*]

[1] Department of Chemical Engineering and Biotechnology, University of Applied Sciences, Haardtring 100, 64295 Darmstadt, Germany.

Short title: Selectivity of Histone deacetylase inhibitors

* Corresponding author:

Franz-Josef Meyer-Almes

Email : franz-josef.meyer-almes@h-da.de

Phone: +49 6151168406

Fax : +49 6151168404

Keywords: Histone deacetylases; protein-ligand interaction; thermodynamics; kinetics; reaction mechanism; selective inhibitors

Content

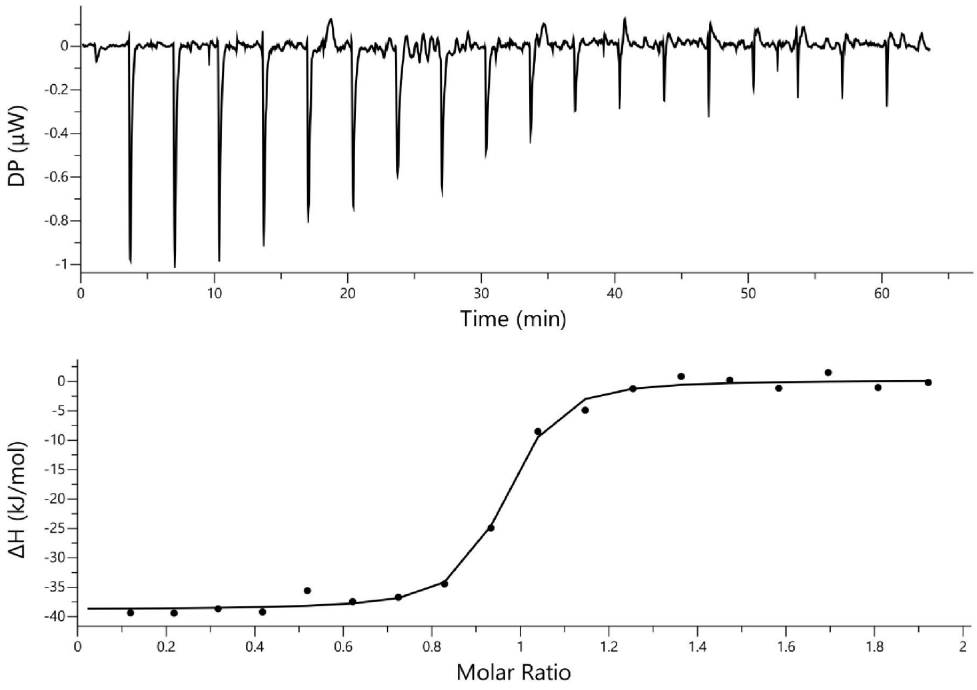

Fig. S1 Representative ITC data for the binding of 1a to $HDAH_{pa}$ in HEPES buffer pH 8.0 at 30 °C.

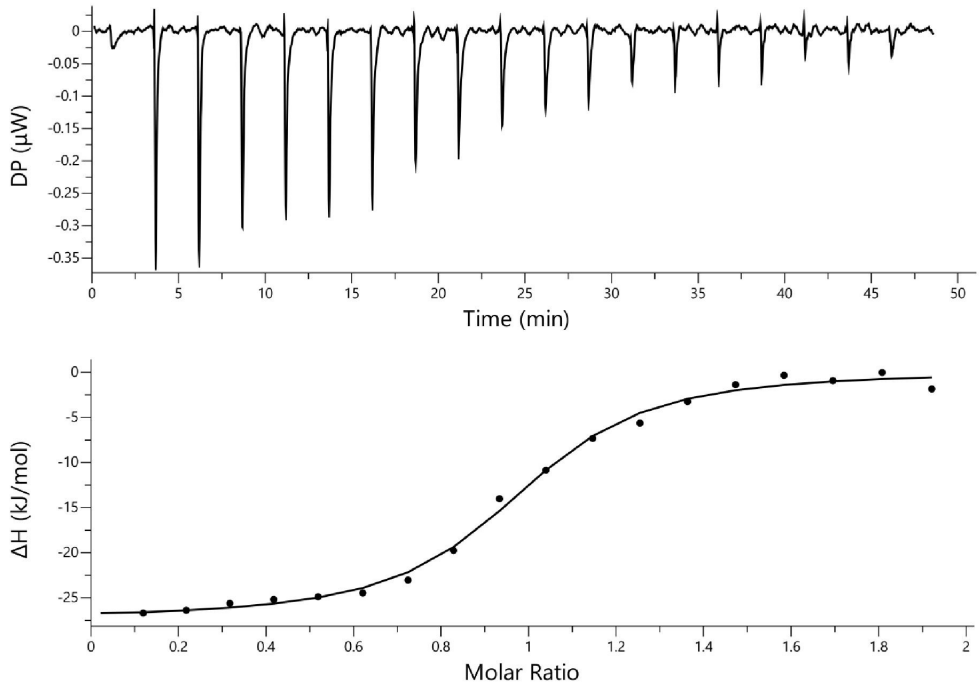

Fig. S2 Representative ITC data for the binding of 1c to $HDAH_{pa}$ in HEPES buffer pH 8.0 at 30 °C.

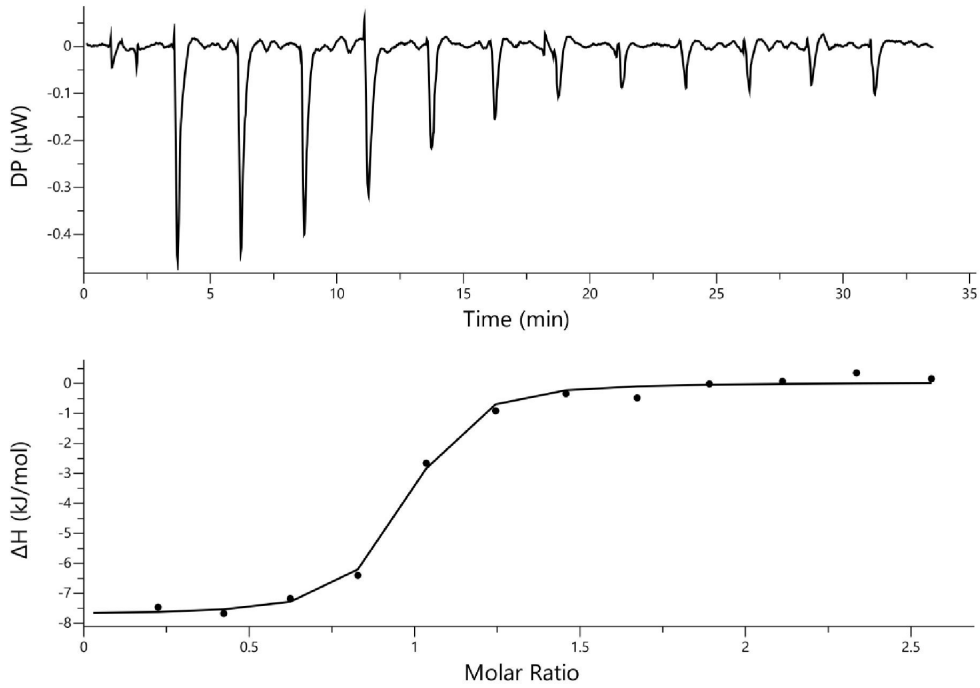

Fig. S3 Representative ITC data for the binding of 1d to $HDAH_{pa}$ in HEPES buffer pH 8.0 at 30 °C.

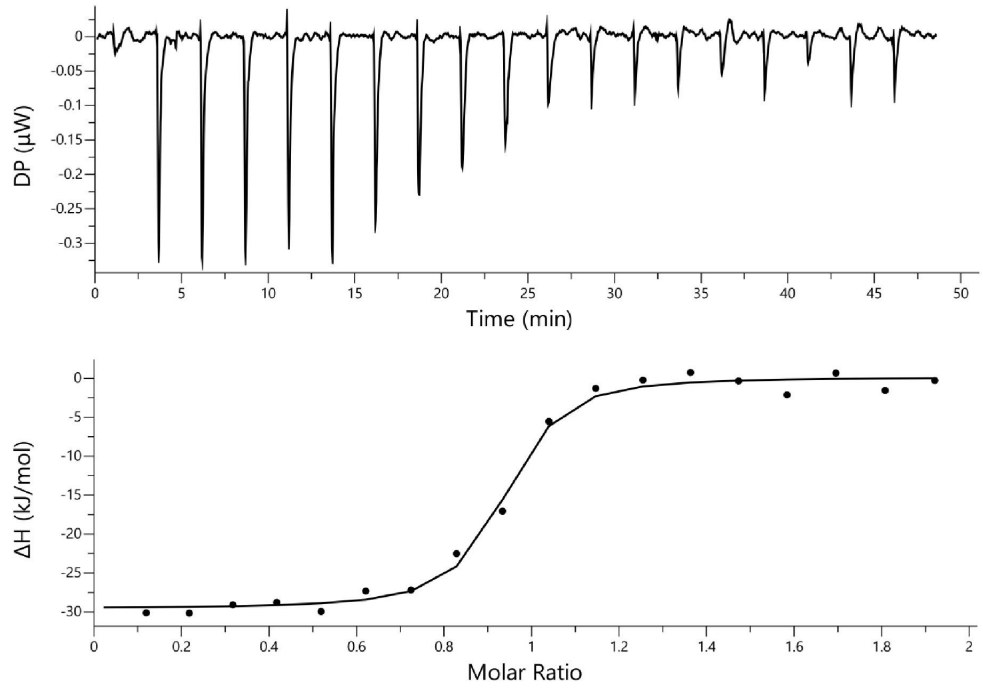

Fig. S4 Representative ITC data for the binding of 1e to $HDAH_{pa}$ in HEPES buffer pH 8.0 at 30 °C.

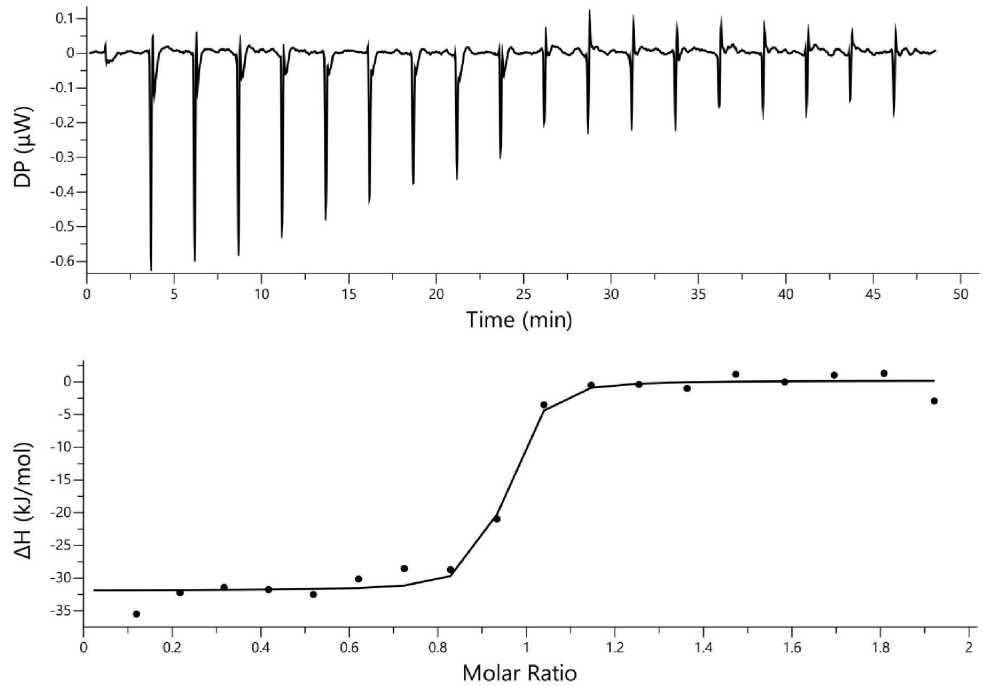

Fig. S5 Representative ITC data for the binding of 1f to $HDAH_{pa}$ in HEPES buffer pH 8.0 at 30 °C.

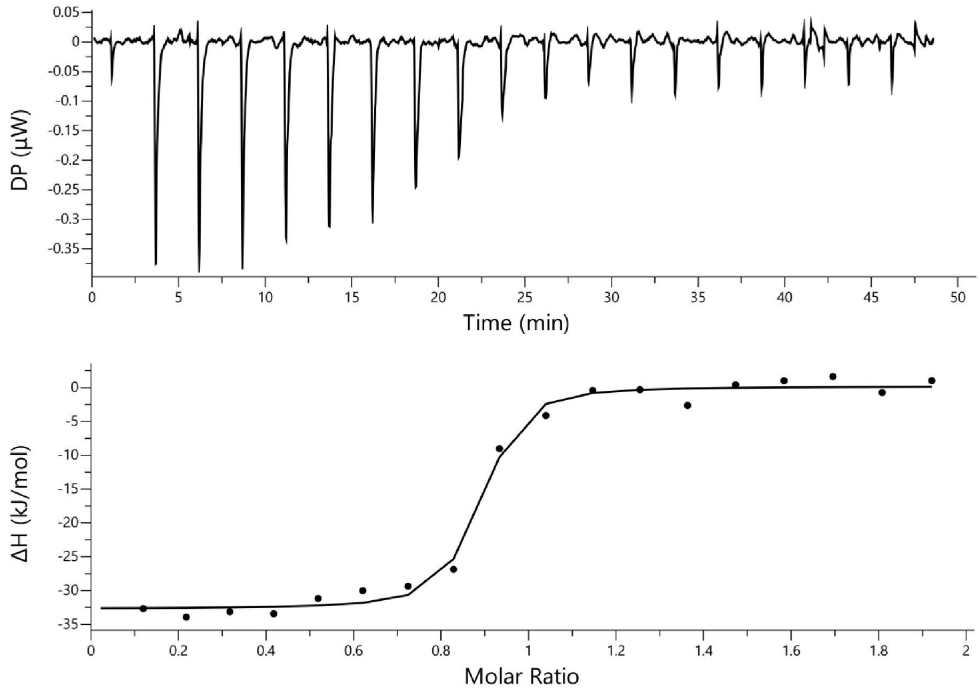

Fig. S6 Representative ITC data for the binding of SAHA to $HDAH_{pa}$ in HEPES buffer pH 8.0 at 30 °C.

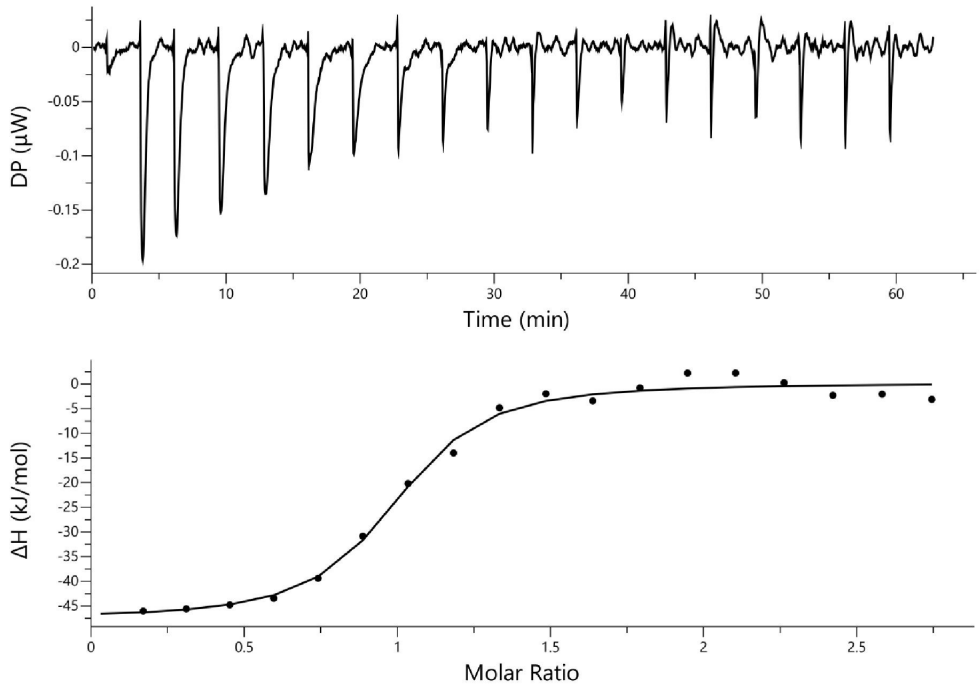

Fig. S7 Representative ITC data for the binding of PFSAHA to $HDAH_{pa}$ in HEPES buffer pH 8.0 at 30 °C.

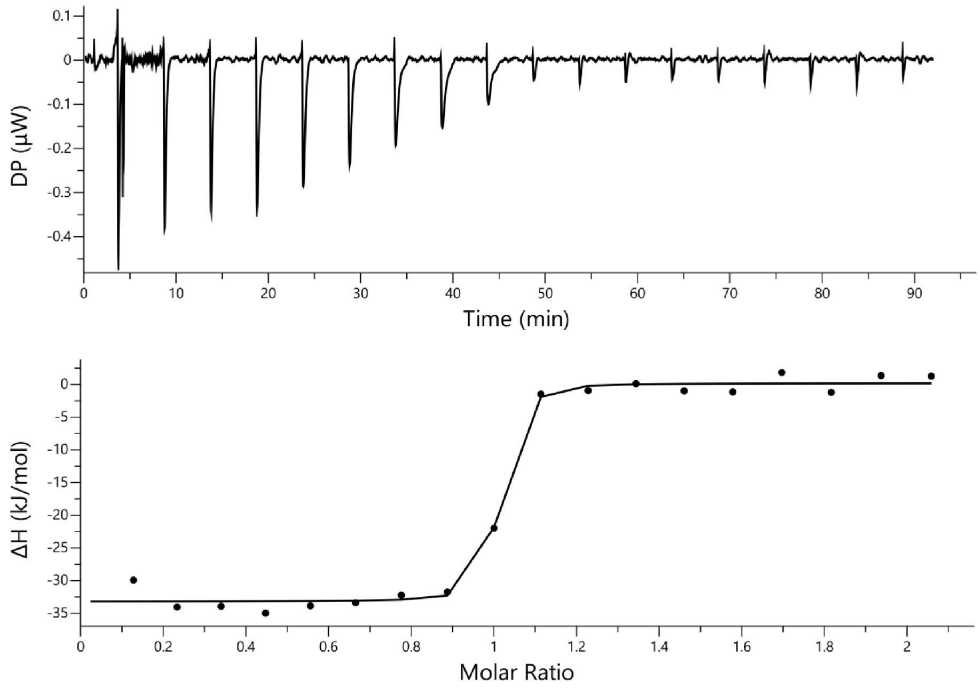

Fig. S8 Representative ITC data for the binding of SATFMK to $HDAH_{pa}$ in HEPES buffer pH 8.0 at 30 °C.

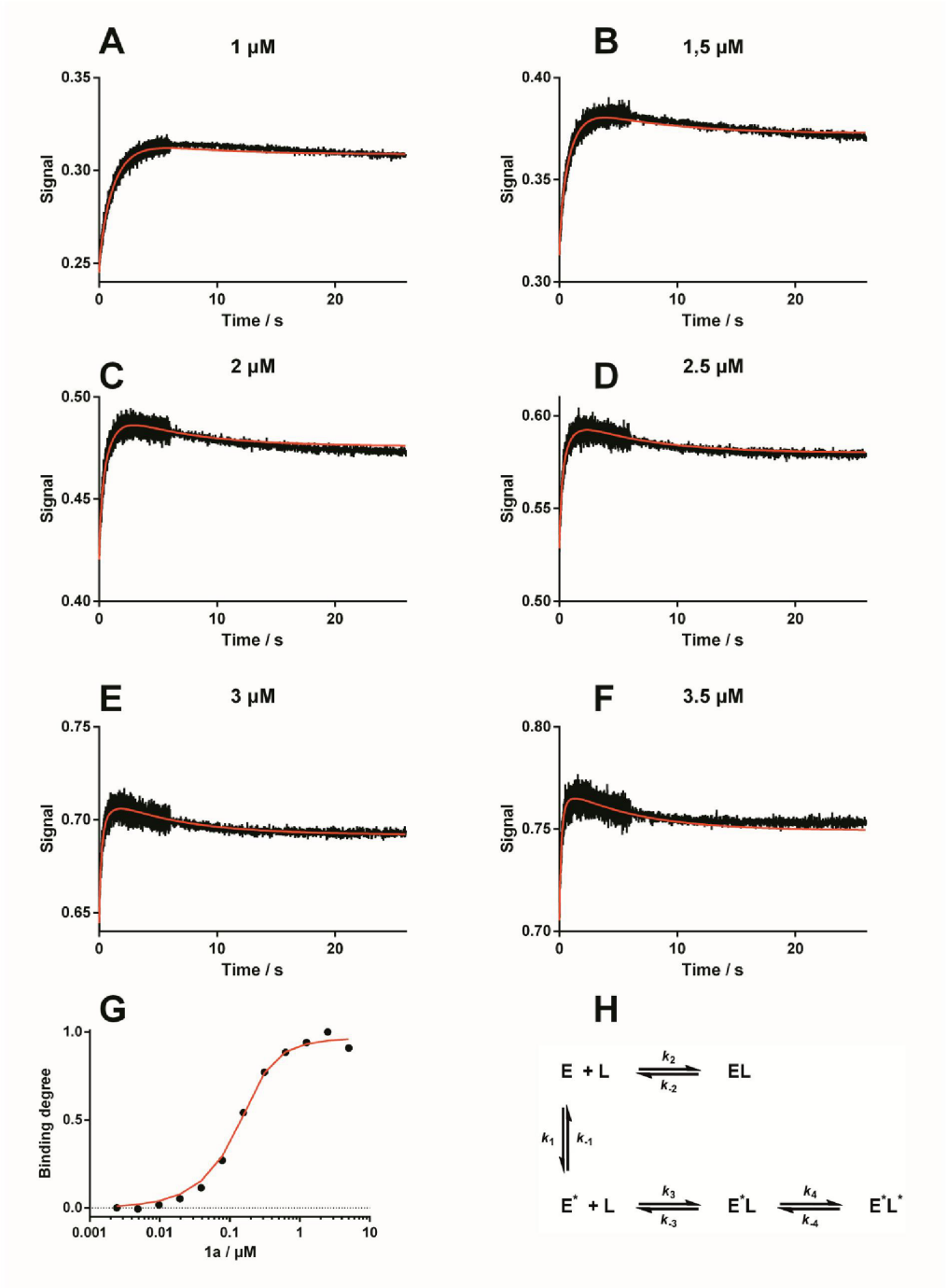

Fig. S9 Global fit analysis of the binding of 1a to HDAH$_{pa}$. Association kinetic traces of varying concentrations of **1a** to HDAH$_{pa}$ (**A-F**) as well as the equilibrium binding curve (**G**) were fitted simultaneously to the indicated binding model (**H**). The association kinetics were measured using a stopped-flow system and the equilibrium binding curve was determined by the FRET binding assay as described in the experimental section. The determined global fit curves are represented by the red lines.

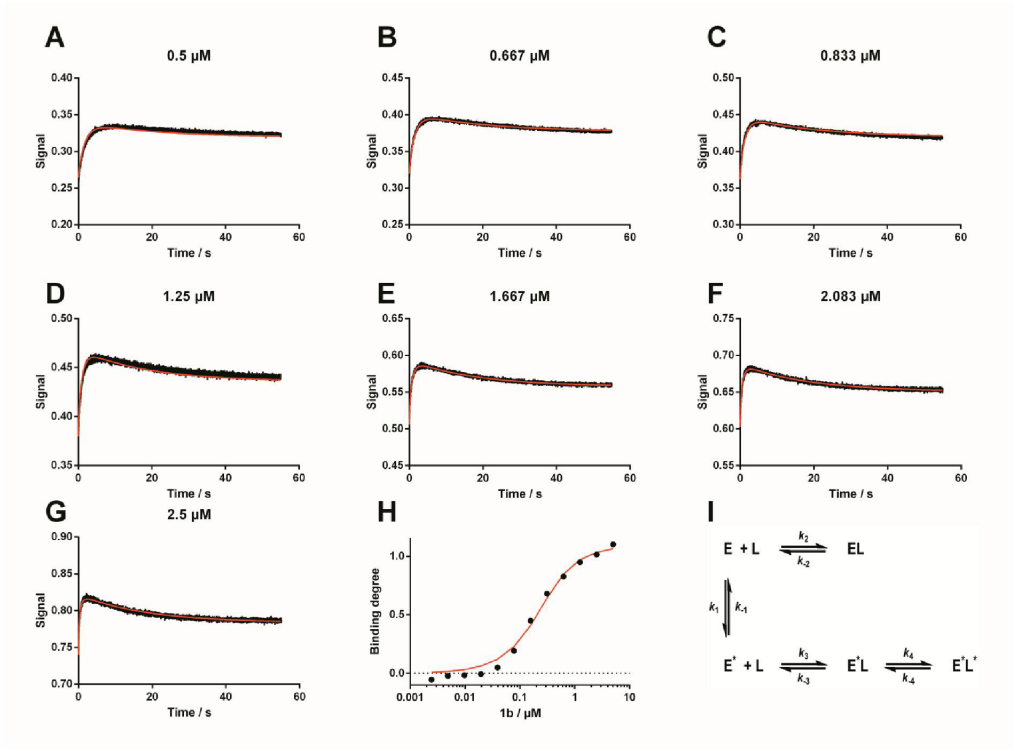

Fig. S10 Global fit analysis of the binding of 1b to HDAH$_{pa}$. Association kinetic traces of varying concentrations of **1b** to HDAH$_{pa}$ (**A**-**G**) as well as the equilibrium binding curve (**H**) were fitted simultaneously to the indicated binding model (**I**). The association kinetics were measured using a stopped-flow system and the equilibrium binding curve was determined by the FRET binding assay as described in the experimental section. The determined global fit curves are represented by the red lines.

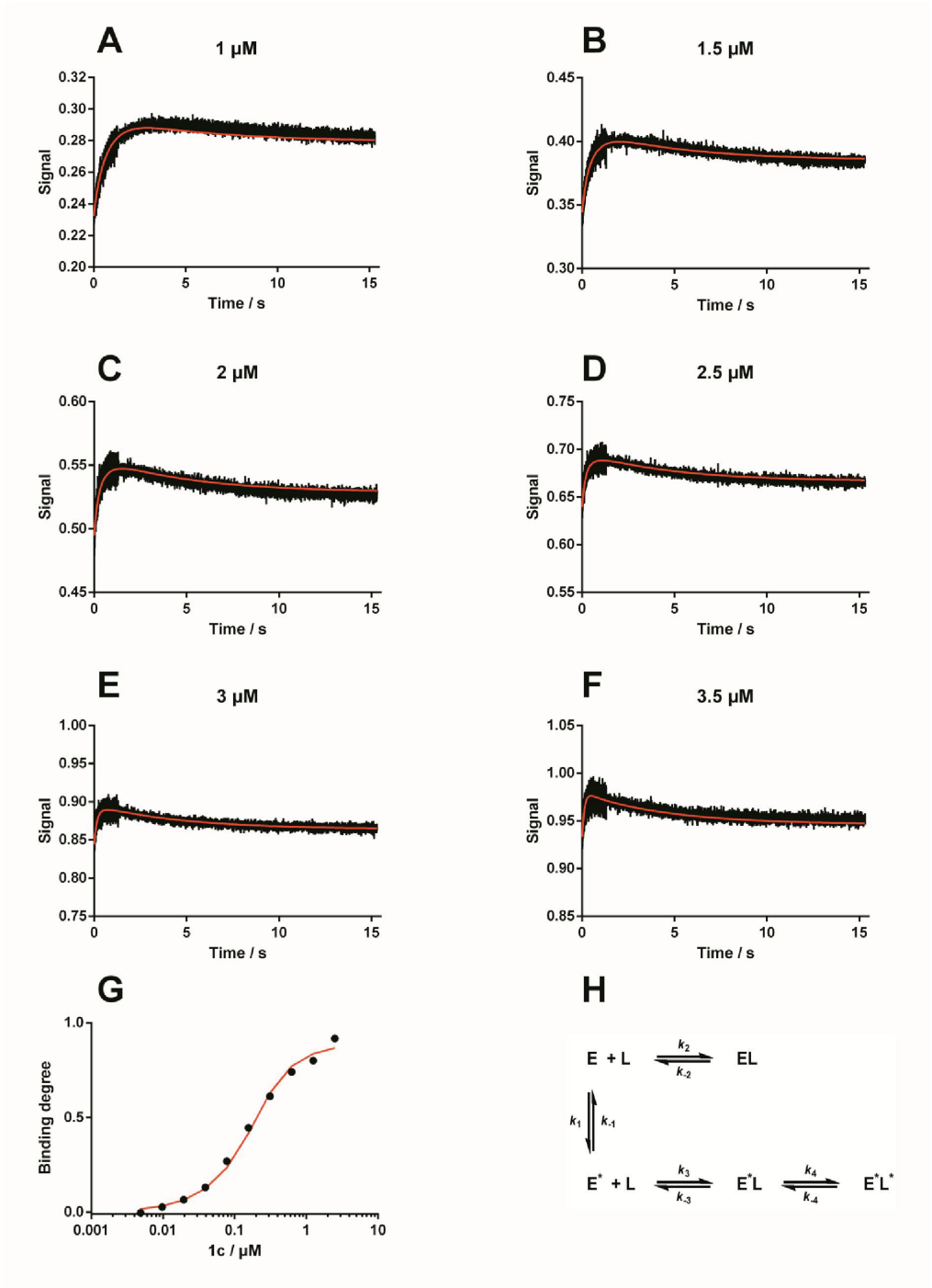

Fig. S11 Global fit analysis of the binding of 1c to HDAH$_{pa}$. Association kinetic traces of varying concentrations of **1c** to HDAH$_{pa}$ (**A-F**) as well as the equilibrium binding curve (**G**) were fitted simultaneously to the indicated binding model (**H**). The association kinetics were measured using a stopped-flow system and the equilibrium binding curve was determined by the FRET binding assay as described in the experimental section. The determined global fit curves are represented by the red lines.

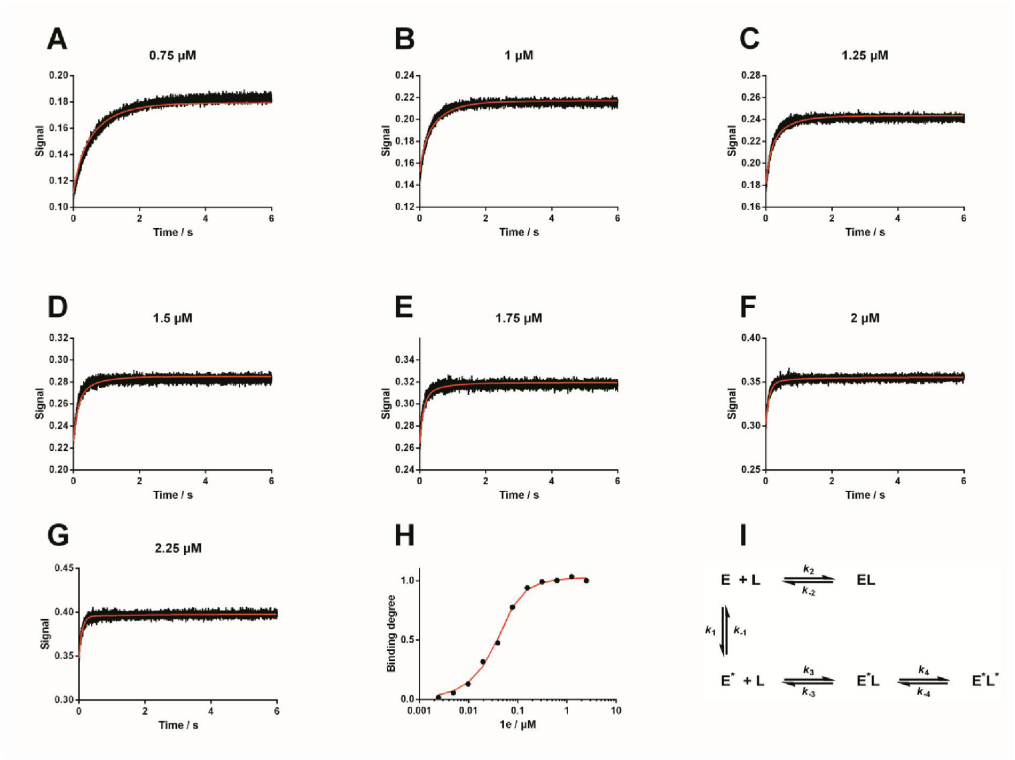

Fig. S12 Global fit analysis of the binding of 1e to HDAH$_{pa}$. Association kinetic traces of varying concentrations of **1e** to HDAH$_{pa}$ (**A**-**G**) as well as the equilibrium binding curve (**H**) were fitted simultaneously to the indicated binding model (**I**). The association kinetics were measured using a stopped-flow system and the equilibrium binding curve was determined by the FRET binding assay as described in the experimental section. The determined global fit curves are represented by the red lines.

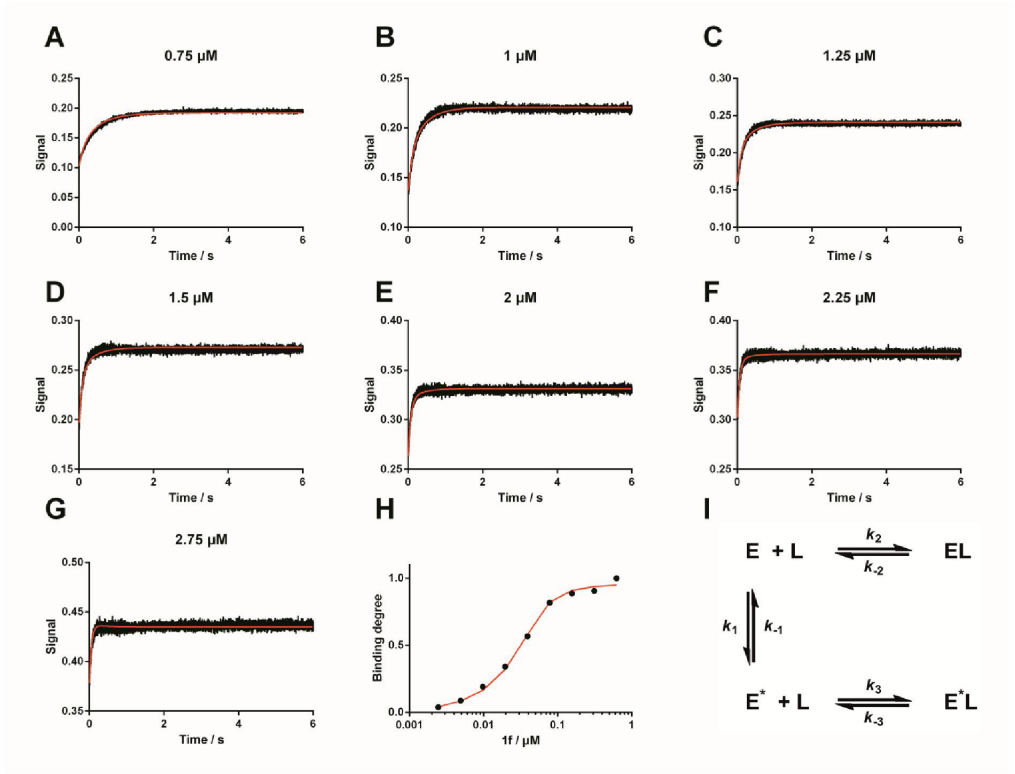

Fig. S13 Global fit analysis of the binding of 1f to HDAH$_{pa}$. Association kinetic traces of varying concentrations of **1f** to HDAH$_{pa}$ (**A-G**) as well as the equilibrium binding curve (**H**) were fitted simultaneously to the indicated binding model (**I**). The association kinetics were measured using a stopped-flow system and the equilibrium binding curve was determined by the FRET binding assay as described in the experimental section. The determined global fit curves are represented by the red lines.

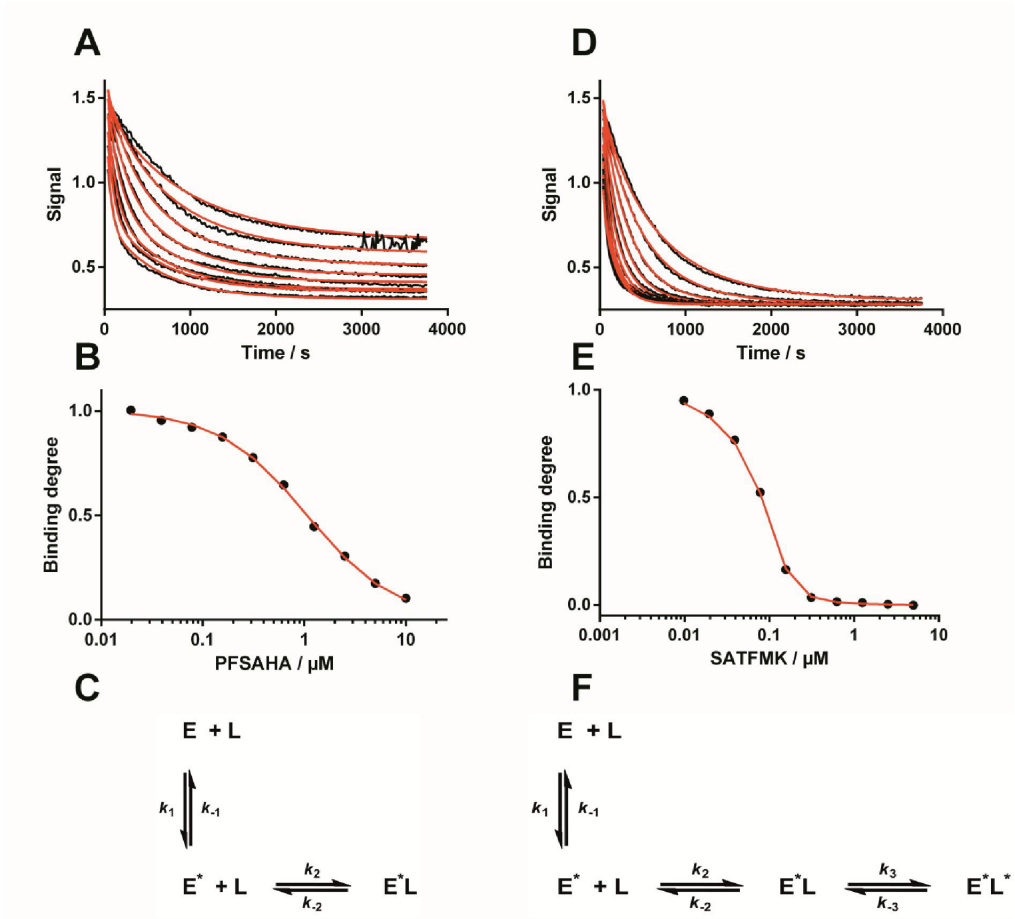

Fig. S14 Global fit analysis of the binding of PFSAHA (A-C) and SATFMK (D-F) to HDAH$_{pa}$. Association kinetic traces of varying concentrations of PFSAHA (**A**) and SATFMK (**B**) to HDAH$_{pa}$ as well as the equilibrium binding curves (**B** and **E**) were fitted simultaneously to the indicated binding models (**C** and **F**). The association kinetics and the equilibrium binding curves were determined by the FRET binding assay as described in the experimental section. The determined global fit curves are represented by the red lines.

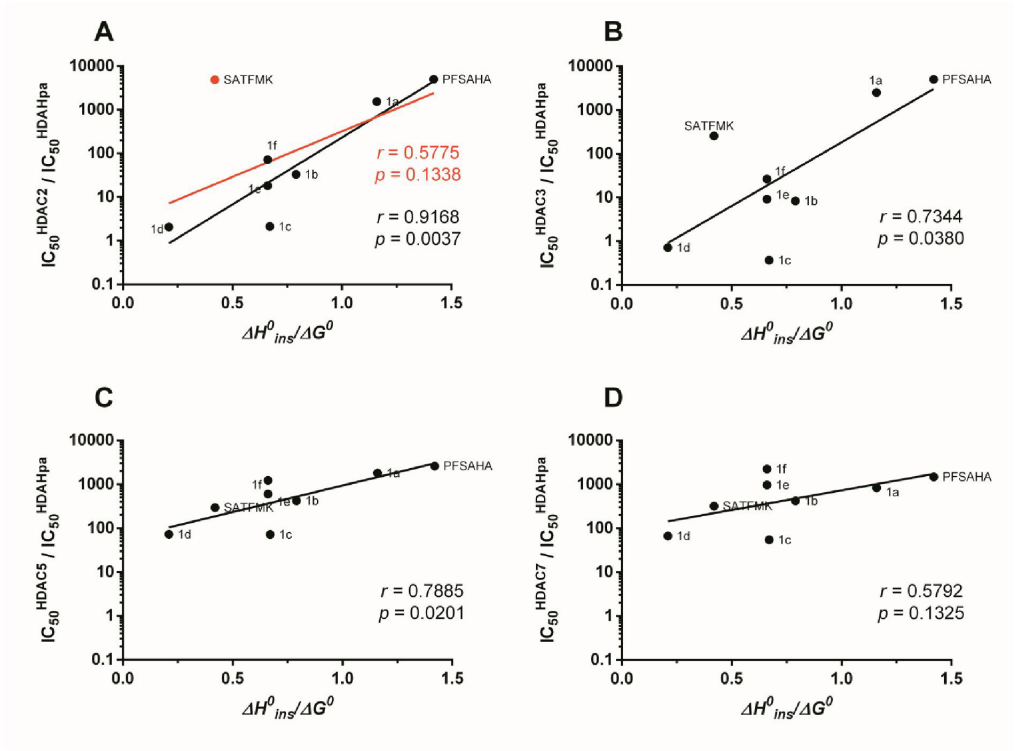

Fig. S15 Influence of thermodynamic parameters on the selectivity of $HDAH_{pa}$ inhibitors against human HDACs 2 (A), 3 (B), 5 (C) and 7 (D). The ratio of the IC_{50}-values was used as a measurement of selectivity and plotted against the ratio $\Delta H^0_{ins}/\Delta G^0$. The Pearson coefficient r indicates the correlation between selectivity versus the enthalpic contribution to binding. The correlation is significant if the p-value is < 0.05. For HDAC2 the data was evaluated twice: once with (red) and once without (black) SATFMK.

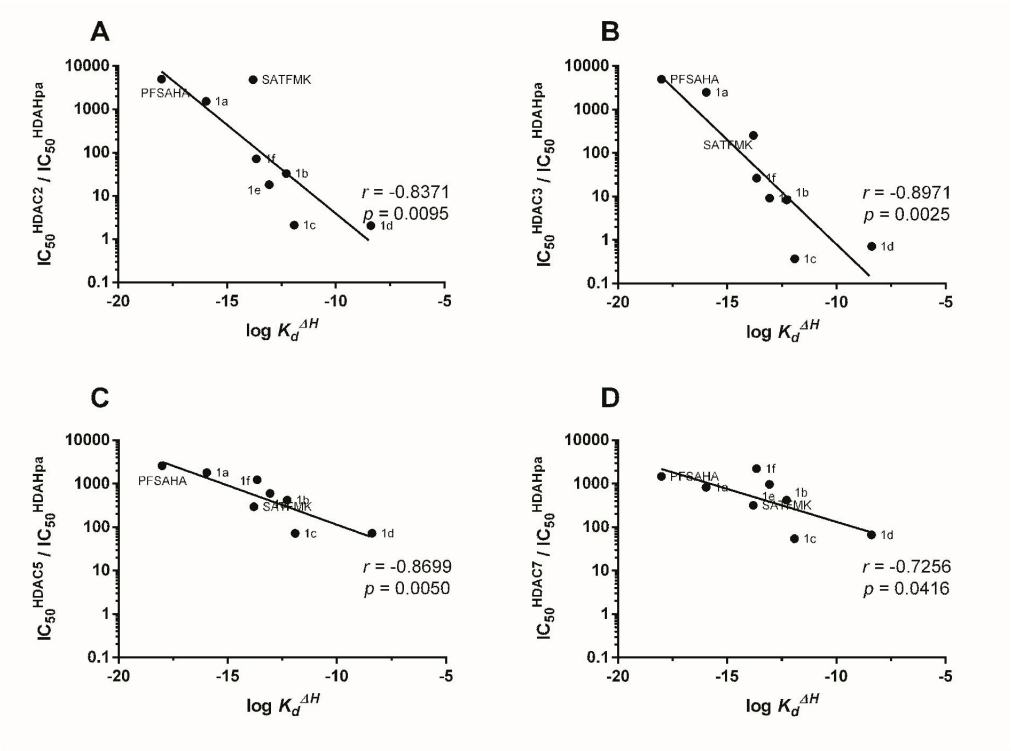

Fig. S16 Relationship between the enthalpy weighted binding constant $K_d^{\Delta H}$ and the selectivity of $HDAH_{pa}$ inhibitors against human HDACs 2 (A), 3 (B), 5 (C) and 7 (D). The enthalpy weighted binding constant $K_d^{\Delta H}$ was calculated from the affinity (K_d) and the ratio $\Delta H^0_{ins}/\Delta G^0$ by the following equation: $\log(K_d^{\Delta H}) = \log(K_d) * (1+ \Delta H^0_{ins}/\Delta G^0)$. The resulting values were plotted versus the ratio of the IC_{50}-values as a measurement for selectivity. The Pearson coefficient r indicates the correlation between both parameters and is significant if the p-value is below 0.05.

5.5. Supplemental information for: Perflourinated hydroxamic acids are potent and selective inhibitors of HDAC-like enzymes from *Pseudomonas aeruginosa*

Perfluorinated hydroxamic acids are potent and selective inhibitors of acetyl-polyamine-amidohydrolases from *Pseudomonas aeruginosa*

Christian Meyners[1], Benjamin Wolf[1], Alexander Kleinschek[1], Andreas Krämer[1] , Franz-Josef Meyer-Almes[1,*]

[1] Department of Chemical Engineering and Biotechnology, University of Applied Sciences, Haardtring 100, 64295 Darmstadt, Germany.

* Corresponding author:
Franz-Josef Meyer-Almes
Email : franz-josef.meyer-almes@h-da.de
Phone: +49 6151168406
Fax : +49 6151168404

Chemical Synthesis (New Compounds)

The general synthetic route is described in more detail in [1]:

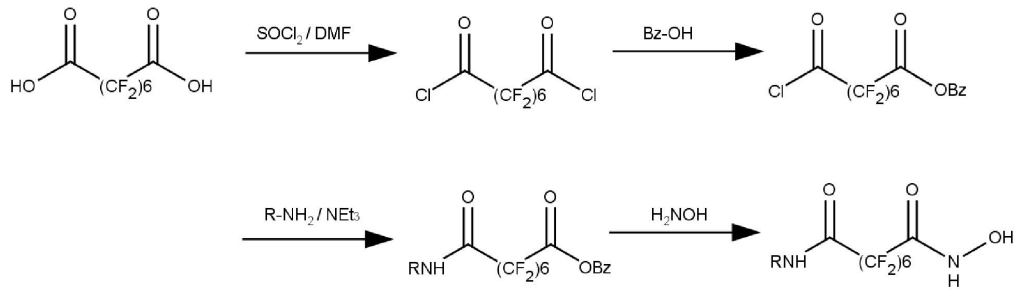

Introduction of new cap groups was accomplished by the following standard procedure

Benzyl-7-chlorocarbonyl-2,2,3,3,4,4,5,5,6,6,7,7-dodecafluoroheptanoate (0.50 g, 1.00 mmol) was dissolved in 10 ml THF and cooled in an ice bath. Within 30 min a solution of triethylamine (0.17 ml, 0.12 g, 1.19 mmol) and the particular aromatic amine or heteroaromatic amine (1.00 mmol), respectively in the required amount of THF (10–20 ml) was added via a dropping funnel, maintaining the reaction temperature below 5 °C. The reaction mixture was stirred for 2 h at 0 °C, then 3 h at 20 °C. After evaporation of the solvent the product was isolated by column chromatography.

Benzyl 8-((4-(dimethylamino)phenyl)amino)-2,2,3,3,4,4,5,5,6,6,7,7-dodecafluoro-8-oxooctanoate

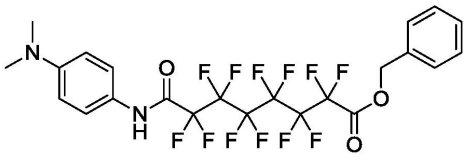

Yield: 80%, yellow crystals
^{1}H-NMR (500 MHz, $CDCl_3$): δ (ppm) = 7.85 (s, 1H), 7.48 – 7.33 (m, 7H), 6.79 – 6.64 (m, 2H), 5.38 (s, 2H), 2.95 (s, 6H).
^{19}F-NMR (282 MHz, $CDCl_3$): δ (ppm) = -116.15 – -117.28 (m), -117.86 (ddd, J = 15.9, 6.0, 3.9 Hz), -119.74 – -120.46 (m), -120.53 – -121.59 (m).
MS (70 eV, EI): *m/z* (%) = 598.4 (80), 508.3 (2), 463.2 (2), 135.2 (100)

Benzyl 2,2,3,3,4,4,5,5,6,6,7,7-dodecafluoro-8-((4-methoxyphenyl)amino)-8-oxooctanoate

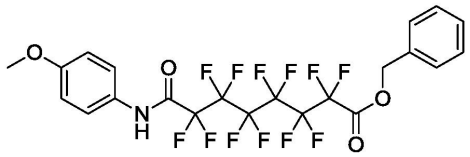

Yield: 90%, colourless solid
^{1}H-NMR (300 MHz, $CDCl_3$): δ (ppm) = 7.93 (s, 1H), 7.50 – 7.41 (m, 2H), 7.39 (s, 5H), 6.98 – 6.66 (m, 2H), 5.38 (s, 2H), 3.81 (s, 3H).
^{19}F-NMR (282 MHz, $CDCl_3$): δ (ppm) = -116.85 (t, J = 10.9 Hz), -117.85 (t, J = 11.5 Hz), -120.06 (dd, J = 14.5, 7.1 Hz), -120.80 (dd, J = 9.6, 6.2 Hz), -120.92 – -121.16 (m).
MS (70 eV, EI): *m/z* (%) = 585.3 (23), 91.1 (100)

Benzyl 2,2,3,3,4,4,5,5,6,6,7,7-dodecafluoro-8-((4-fluorophenyl)amino)-8-oxooctanoate

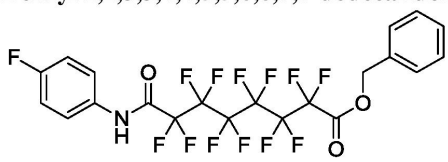

Yield: 87%, yellow solid
^{1}H-NMR (300 MHz, $CDCl_3$): δ (ppm) = 8.00 (s, 1H), 7.53 (ddd, J = 6.9, 5.2, 2.9 Hz, 2H), 7.47 – 7.32 (m, 5H), 7.17 – 7.01 (m, 2H), 5.38 (s, 2H).
^{19}F-NMR (282 MHz, $CDCl_3$): δ (ppm) = -118.36 (t, J = 11.5 Hz), -119.37 (t, J = 12.1 Hz), -120.89 – -121.98 (m), -122.06 – -122.42 (m), -122.42 – -122.75 (m).
MS (70 eV, EI): *m/z* (%) = 573.2 (15), 91.1 (100)

Benzyl 8-((3-chlorophenyl)amino)-2,2,3,3,4,4,5,5,6,6,7,7-dodecafluoro-8-oxooctanoate

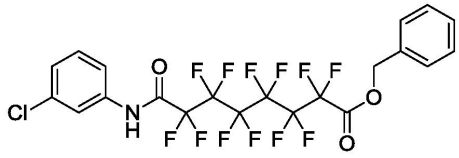

Yield: 90%, yellow solid
^{1}H-NMR (300 MHz, $CDCl_3$): δ (ppm) = 8.07 (s, 1H), 7.67 (t, J = 1.9 Hz, 1H), 7.52 – 7.29 (m, 7H), 7.27 – 7.19 (m, 1H), 5.38 (s, 2H).
^{19}F-NMR (282 MHz, $CDCl_3$): δ (ppm) = -116.84 (t, J = 11.5 Hz), -117.84 (t, J = 12.2 Hz), -120.04 (dd, J = 15.3, 7.5 Hz), -120.74 (dd, J = 9.5, 5.8 Hz), -121.00 (dd, J = 17.9, 10.8 Hz).

MS (70 eV, EI): *m/z* (%) = 589.1 (13), 91.1 (100)

Benzyl 8-((2-chlorophenyl)amino)-2,2,3,3,4,4,5,5,6,6,7,7-dodecafluoro-8-oxooctanoate

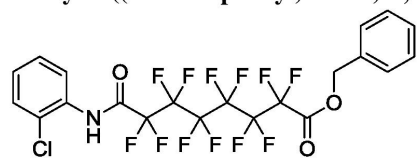

Yield: 86%, yellow solid
^{1}H-NMR (300 MHz, $CDCl_3$): δ (ppm) = 8.50 (s, 1H), 8.30 (dd, *J* = 8.2, 1.4 Hz, 1H), 7.51 – 7.29 (m, 7H), 7.20 (td, *J* = 7.8, 1.5 Hz, 1H), 5.38 (s, 2H).
^{19}F-NMR (282 MHz, $CDCl_3$): δ (ppm) = -116.82 (t, *J* = 11.7 Hz), -117.84 (t, *J* = 12.3 Hz), -119.99 (ddd, *J* = 16.8, 12.7, 8.1 Hz), -120.50 – -120.87 (m), -120.84 – -121.18 (m).
MS (70 eV, EI): *m/z* (%) = 589.1 (9), 91.1 (100)

Benzyl 2,2,3,3,4,4,5,5,6,6,7,7-dodecafluoro-8-oxo-8-(o-tolylamino)octanoate

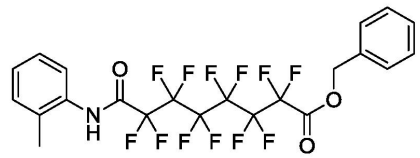

Yield: 90%, yellow solid
^{1}H-NMR (300 MHz, $CDCl_3$): δ (ppm) = 7.97 (s, 1H), 7.44 – 7.32 (m, 6H), 7.31 – 7.23 (m, 1H), 7.06 (d, *J* = 7.4 Hz, 1H), 5.38 (s, 2H), 2.37 (s, 3H).
^{19}F-NMR (282 MHz, $CDCl_3$): δ (ppm) = -116.86 (t, *J* = 11.5 Hz), -117.83 (t, *J* = 12.1 Hz), -119.76 – -120.35 (m), -120.60 – -120.92 (m), -120.92 – -121.23 (m).
MS (70 eV, EI): *m/z* (%) = 469.2 (22), 91.1 (100)

Benzyl 2,2,3,3,4,4,5,5,6,6,7,7-dodecafluoro-8-oxo-8-(m-tolylamino)octanoate

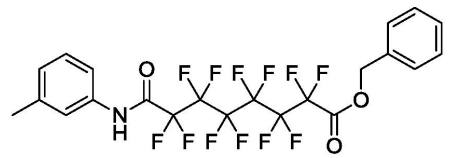

Yield: 93%, yellow solid
^{1}H-NMR (300 MHz, $CDCl_3$): δ (ppm) = 7.90 (s, 1H), 7.69 (dd, *J* = 6.4, 3.0 Hz, 1H), 7.44 – 7.36 (m, 5H), 7.31 – 7.18 (m, 4H), 5.39 (s, 2H), 2.28 (s, 4H).

^{19}F-NMR (282 MHz, $CDCl_3$): δ (ppm) = -116.84 (t, J = 11.9 Hz), -117.79 (t, J = 12.5 Hz), -119.72 – -120.23 (m), -120.64 – -120.90 (m), -120.91 – -121.18 (m).
MS (70 eV, EI): m/z (%) = 569.1 (4), 478.1 (33), 91.1 (100)

General procedure for the synthesis of the hydroxamic acids

To a solution of the benzylic ester in THF (c = 0.05 M) hydroxylamine hydrochloride (4 equivalents) and triethylamine (2 equivalents) were added. The solution was stirred for 24 h at 20 °C. The solvent was evaporated and the residue was dissolved in ethyl acetate. The organic solution was washed with saturated ammonium chloride solution and the aqueous layer was reextracted with ethyl acetate. The combined organic layers were dried and the solvent was evaporated. The product was purified by column chromatography.

N^1-(4-(Dimethylamino)phenyl)-2,2,3,3,4,4,5,5,6,6,7,7-dodecafluoro-N^8-hydroxyoctanediamide

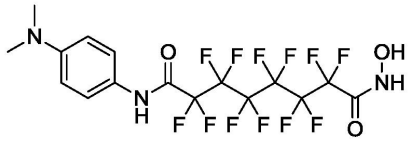

Yield: 70%, colourless solid
^{1}H-NMR (300 MHz, DMSO): δ (ppm) = 10.91 (s, 1H), 7.46 (d, J = 9.1 Hz, 3H), 7.31 (d, J = 4.4 Hz, 2H), 6.72 (d, J = 9.2 Hz, 3H), 3.36 (s, 2H), 2.88 (s, 8H).
^{19}F-NMR (282 MHz, DMSO): δ (ppm) = -115.22 (t, J = 10.7 Hz), -118.20 (t, J = 11.1 Hz), -121.67 (s), -121.88 – -122.13 (m), -122.35 (s).
MS (70 eV, EI): m/z (%) = 464.1 (63), 135.1 (100)

2,2,3,3,4,4,5,5,6,6,7,7-Dodecafluoro-N^1-hydroxy-N^8-(4-methoxyphenyl)octanediamide

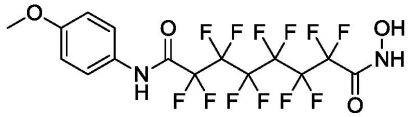

Yield: 56%, colourless solid
^{1}H-NMR (300 MHz, DMSO): δ (ppm) = 11.08 (s, 1H), 7.61 – 7.52 (m, 2H), 7.02 – 6.92 (m, 2H), 4.10 (q, J = 5.2 Hz, 1H), 3.75 (s, 3H).
^{19}F-NMR (282 MHz, DMSO): δ (ppm) = -116.85 (t, J = 11.3 Hz), -120.00 (t, J = 11.3 Hz), -123.35 (d, J = 7.4 Hz), -123.52 – -123.87 (m), -123.87 – -124.35 (m).
MS (70 eV, EI): m/z (%) = 451.1 (61), 122.1 (100)

2,2,3,3,4,4,5,5,6,6,7,7-Dodecafluoro-N^1-(4-fluorophenyl)-N^8-hydroxyoctanediamide

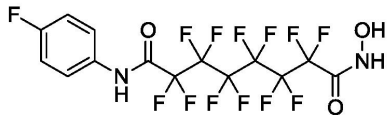

Yield: 42%, colourless solid
^{1}H-NMR (300 MHz, DMSO): δ (ppm) = 11.30 (s, 1H), 7.70 (dd, J = 9.2, 5.0 Hz, 2H), 7.24 (t, J = 8.9 Hz, 2H), 6.11 (t, J = 6.6 Hz, 1H), 4.34 (d, J = 4.1 Hz, 1H).
^{19}F-NMR (282 MHz, DMSO): δ (ppm) = -115.27 (t, J = 10.2 Hz), -116.26 (s), -118.40 (t, J = 11.0 Hz), -121.65 (d, J = 8.0 Hz), -121.86 – -122.19 (m), -122.35 (d, J = 5.3 Hz).
MS (70 eV, EI): m/z (%) = 439.0 (35), 110 (100)

N^1-(3-Chlorophenyl)-2,2,3,3,4,4,5,5,6,6,7,7-dodecafluoro-N^8-hydroxyoctanediamide

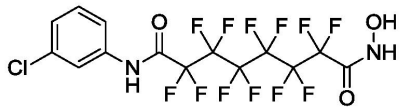

Yield: 50%, colourless solid
^{1}H-NMR (300 MHz, DMSO): δ (ppm) = 11.37 (s, 1H), 7.80 (t, J = 2.0 Hz, 1H), 7.65 (ddd, J = 8.2, 2.0, 0.8 Hz, 1H), 7.45 (t, J = 8.1 Hz, 1H), 7.35 – 7.28 (m, 1H).
^{19}F-NMR (282 MHz, DMSO): δ (ppm) = -115.20 (t, J = 10.9 Hz), -118.47 (t, J = 11.2 Hz), -121.68 (d, J = 8.0 Hz), -121.87 – -122.15 (m), -122.33 (d, J = 4.7 Hz).
MS (70 eV, EI): m/z (%) = 455.0 (36), 154 (100)

N^1-(2-Chlorophenyl)-2,2,3,3,4,4,5,5,6,6,7,7-dodecafluoro-N^8-hydroxyoctanediamide

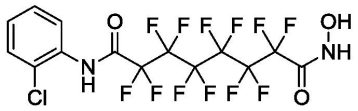

Yield: 68%, colourless solid
^{1}H-NMR (300 MHz, DMSO): δ (ppm) = 11.26 (s, 1H), 7.60 (dt, J = 10.9, 4.4 Hz, 1H), 7.46 – 7.38 (m, 3H).
^{19}F-NMR (282 MHz, DMSO): δ (ppm) = -114.67 – -115.66 (m), -118.59 (d, J = 8.4 Hz), -121.66 (d, J = 7.3 Hz), -121.96 (d, J = 7.9 Hz), -122.32 (s).

MS (70 eV, EI): *m/z* (%) = 455.0 (14), 420 (100)

2,2,3,3,4,4,5,5,6,6,7,7-Dodecafluoro-N^1-hydroxy-N^8-(o-tolyl)octanediamide

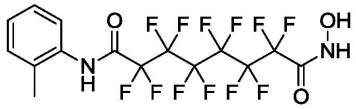

Yield: 81%, colourless solid
^{1}H-NMR (300 MHz, DMSO): δ (ppm) = 7.34 – 7.29 (m, 1H), 7.28 – 7.22 (m, 2H), 7.21 – 7.16 (m, 1H), 2.17 (s, 3H).
MS (70 eV, EI): *m/z* (%) = 435.1 (16), 91.1 (100)

2,2,3,3,4,4,5,5,6,6,7,7-Dodecafluoro-N^1-hydroxy-N^8-(m-tolyl)octanediamide

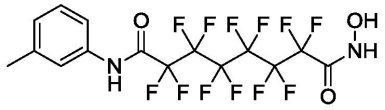

Yield: 90%, yellow solid
^{1}H-NMR (300 MHz, DMSO): δ (ppm) = 11.10 (s, 1H), 7.50 (s, 1H), 7.44 (d, J = 8.1 Hz, 1H), 7.33 – 7.25 (m, 2H), 7.05 (dd, J = 7.6, 0.6 Hz, 1H), 2.31 (s, 4H).
^{19}F-NMR (282 MHz, DMSO): δ (ppm) = -115.18 (t, J = 10.7 Hz), -118.33 (t, J = 11.0 Hz), -121.67 (s), -121.87 – -122.18 (m), -122.37 (d, J = 4.6 Hz).
MS (70 eV, EI): *m/z* (%) = 435.1 (9), 134.1 (100)

Enzyme activity assays:

All enzyme activity assays were run in 20 mM Tris–HCl pH 8, 50 mM NaCl and 0.001 % Pluronic at 30 °C.

194

195 For HDAC 1and 6:

196 The activity of HDACs 1 and 6 was determined by a fluorogenic assay as described by Wegener
197 et al. [2]. 1 nM of HDAC was incubated with increasing concentrations of the respective
198 compound for 30 minutes. The reaction was initiated by addition of 50 µM of the substrate Boc-
199 Lys(Ac)-AMC. After an incubation of 60 minutes the reaction was stopped by addition of 20 µM
200 SAHA and the deacetylated substrate was converted into a fluorescent product by the addition of
201 trypsin.

202 For HDAC 4, 5, 7 and 8:

203 The activity of HDACs 4,5,7 and 8 was determined by a fluorogenic assay using the same assay
204 principle as described above. 1 nM of the respective HDAC was incubated with increasing
205 concentrations of the respective compound for 30 minutes. The reaction was initiated by addition
206 of 20 µM of the substrate Boc-Lys(trifluoroacetyl)-AMC. After an incubation of 60 minutes the
207 reaction was stopped by addition of 20 µM 9,9,9-trifluoro-8,8-dihydroxy-N-phenylnonanamide
208 (SATFMK) and the deacetylated substrate was converted into a fluorescent product by the
209 addition of trypsin.

210 For HDAH, PA3774, PA1409 and PA0321:

211 The assay principle was the same as for the assays for human HDAC isoforms (see above). But
212 in contrast to the HDAC assays the kinetics of the bacterial enzymes was determined in a one-
213 step reaction: A mix of 20 µM Boc-Lys(trifluoroacetyl)-AMC substrate and 0.5 mg/ml trypsin
214 was added to 10 nM enzyme. For all enzymes the K_I values were calculated from IC_{50}-values
215 according to Cheng and Prusoff. The K_M values were 26 µM for PA0321, 16 µM for PA1409,

11 μM for PA3774, 14 μM for HDAH, 78 μM for HDAC1, 18 μM for HDAC4, 23 μM for HDAC5, 99 μM for HDAC6, 61 μM for HDAC7 and 30 μM for HDAC8.

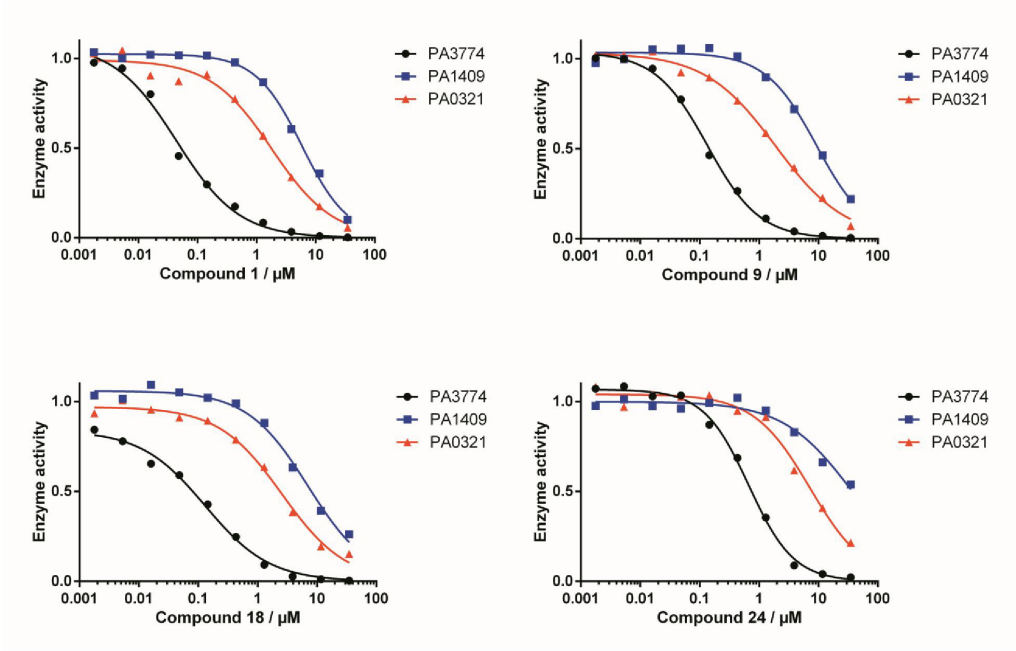

Fig. S1 Representative dose response curves for inhibition of PA3774, PA1409 and PA0321 by perfluoro compunds.

QSAR model:

A set of 15 chemical 2D descriptors with highest relative importance was used to build a QSAR model to summarize the experimental data and predict IC_{50} values of PA3774 inhibitors using MOE software (Chemical Computing Group, Canada). The corresponding fit report including the QSAR model with the explicit coefficients for all used chemical descriptors is shown below:

```
Activity Field          : lg_IC50
Weight Field            :
Condition Limit         : 1e+006
Component Limit         : 0

Observations            : 28
Descriptors             : 15
Components Used         : 14
Condition Number        : 965555.06

ROOT MEAN SQUARE ERROR (RMSE): 0.27305
CORRELATION COEFFICIENT (R2) : 0.84594

ESTIMATED LINEAR MODEL

lg_IC50 =
      -38.24354
       -0.02914 * PEOE_VSA+0
       +0.00912 * PEOE_VSA-1
       +0.01973 * PEOE_VSA_POS
       +0.01333 * SlogP_VSA1
       -0.02045 * SlogP_VSA7
       +0.00281 * SlogP_VSA9
       +0.03761 * SMR_VSA1
       -0.02782 * SMR_VSA7
       +0.02847 * vdw_vol
       +0.04138 * vsa_hyd
       -0.01205 * Weight
       -0.00376 * weinerPath
       -0.32980 * weinerPol
       +0.24979 * zagreb
       +0.00906 * PEOE_VSA-0
```

262 **References**
263
264 [1] L.M. Henkes, P. Haus, F. Jager, J. Ludwig, F.J. Meyer-Almes, Synthesis and biochemical
265 analysis of 2,2,3,3,4,4,5,5,6,6,7,7-dodecafluoro-N-hydroxy-octanediamides as inhibitors of
266 human histone deacetylases, Bioorg. Med. Chem., 20 (2012) 985-995.
267 [2] D. Wegener, C. Hildmann, D. Riester, A. Schwienhorst, Improved fluorogenic histone
268 deacetylase assay for high-throughput-screening applications, Anal. Biochem., 321 (2003) 202-
269 208.

270

5.6. Supplemental information for: The thermodynamic signature of ligand binding to histone deacetylase-like amidohydrolases is most sensitive to the flexibility in the L2-loop lining the active site pocket

The thermodynamic signature of ligand binding to histone deacetylase like amidohydrolases is most sensitive to the flexibility in the L2 loop lining the active site pocket

Christian Meyners[1], Andreas Krämer[1], Özkan Yildiz[2], Franz-Josef Meyer-Almes[1,*]

[1] Department of Chemical Engineering and Biotechnology, University of Applied Sciences, Schnittspahnstr. 12, 64287 Darmstadt, Germany.

[2] Department of Structural Biology, Max-Planck-Institute of Biophysics, 60438 Frankfurt, Germany.

* Corresponding author:

Franz-Josef Meyer-Almes

Email : franz-josef.meyer-almes@h-da.de

Phone: +49 6151168406

Fax : +49 6151168404

Content

$HDAH_{pa}$	100	44	34	35	21
$HDAH_{bo}$	44	100	32	35	21
$HDAC6_{CD1}$	34	32	100	49	23
$HDAC6_{CD2}$	35	35	49	100	26
HDAC8	21	21	23	26	100

Fig. S1: Percent identity matrix of indicated HDAC homologs.

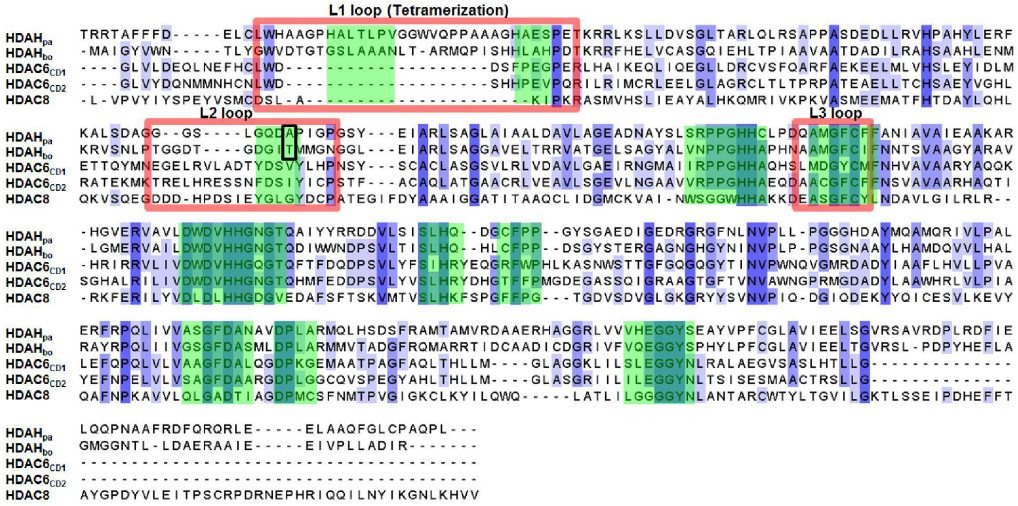

Fig. S2: Structure based multiple sequence alignment of indicated enzymes. Both catalytic domains (CD1 and CD2) of HDAC6 are shown. The red boxes mark loops 1-3 and the green shaded area denote regions within 10 Å of bound inhibitor in $HDAH_{pa}$-SATFMK complex (PDB ID: 5G1B) from a superimposition of $HDAH_{pa}$ (PDB ID: 5G1B), $HDAC6_{CD2}$ (PDB ID: 5EDU) and HDAC8 (PDB ID: 1T69). The location of the $HDAH_{bo}$ T101A mutation is indicated by a black frame.

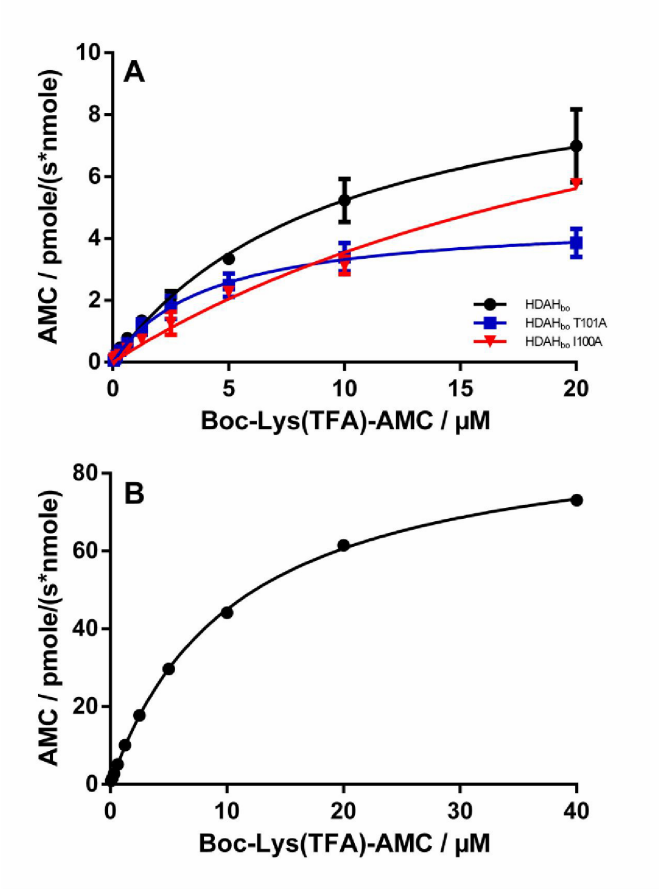

Fig. S3: Michaelis-Menten kinetics of A) $HDAH_{bo}$, indicated mutants and B) $HDAH_{pa}$ using the enzyme activity assay

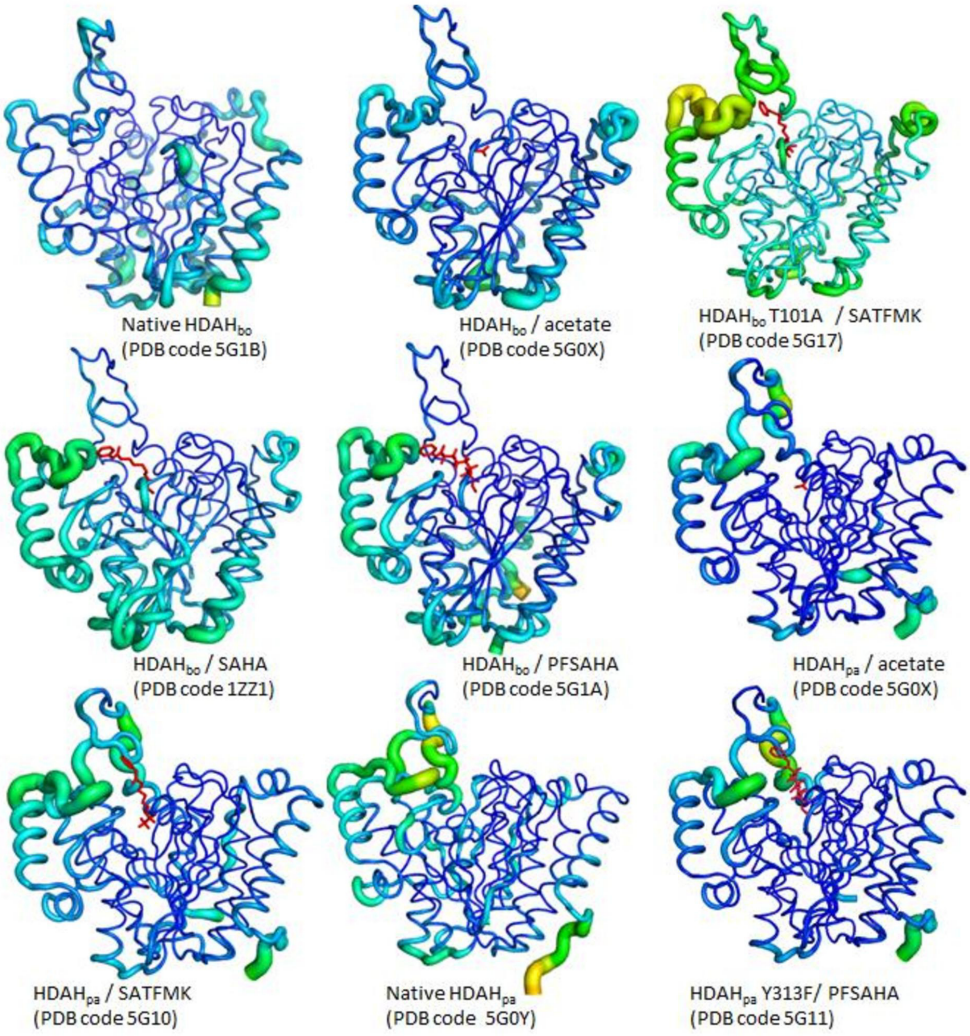

Fig. S4: Crystal structures of HDAH$_{bo}$ and HDAH$_{pa}$ unbound/native or in complex with indicated ligand. The tube thickness and color gradient indicate averaged B-factors from low (thin, dark blue) to high (thick, red). PDB ID's: 5G0Y, 5G10, 5G0X and 5G11 were described in [1]. PDB ID's: 5G1A, 5G1B, 5G17 are described in this study.

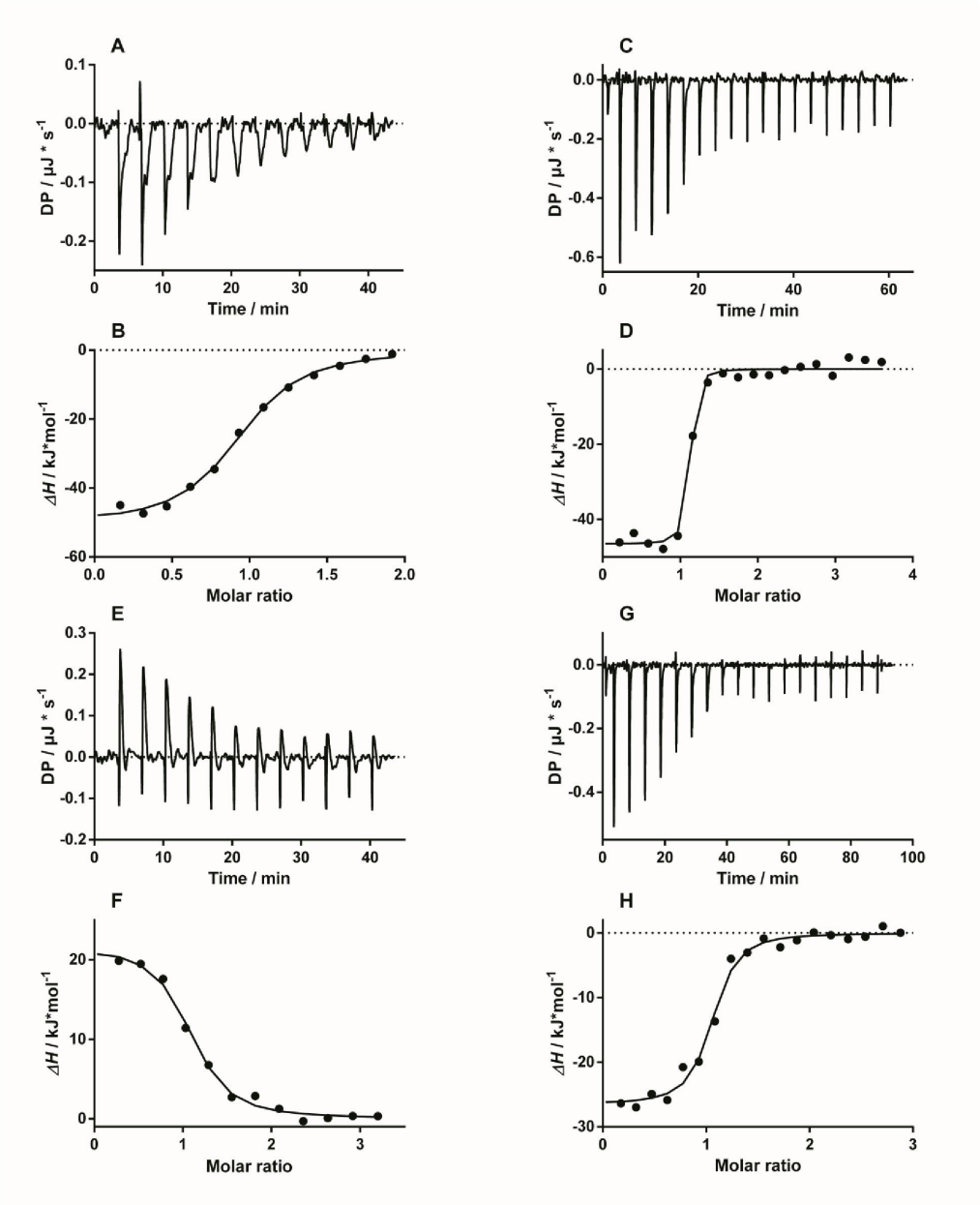

Fig. S5: Representative ITC data for the binding of SATFMK (A-D) and PFSAHA (E-H) to $HDAH_{bo}$ (A, B and E, F) and $HDAH_{pa}$ (C, D and G, H) in Tris buffer at pH 8.0 and 30 °C.

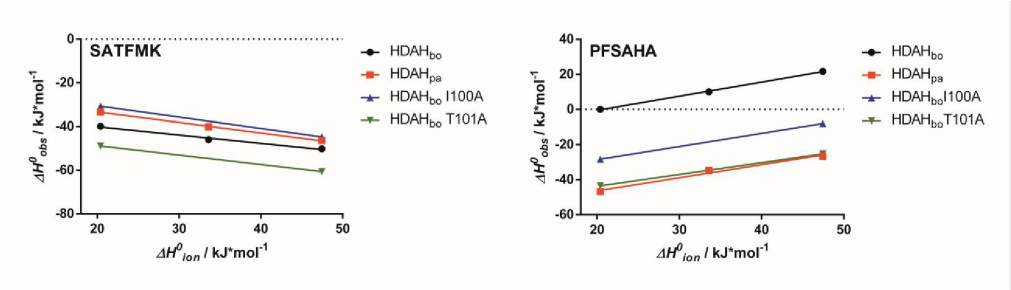

Fig. S6: Proton exchange with the bulk solution upon binding of SATFMK and PFSAHA to $HDAH_{bo}$, $HDAH_{bo}$ variants and $HDAH_{pa}$ at 30 °C. The observed binding enthalpy ΔH^0_{obs} is plotted against the buffer ionization enthalpy ΔH^0_{ion} of the used buffer substances (Tris, triethanolamine and HEPES). Data points represent the mean of two independent experiments with differences < 5%.

Reference:

[1] A. Kraemer, T. Wagner, Ö. Yildiz, F.J. Meyer-Almes, Crystal structure of a histone deacetylase homolog from Pseudomonas aeruginosa, Biochemistry, (2016) DOI 10.1021/acs.biochem.1026b00613.

6. Appendix

A Abrevations

APAH	Acetylpolyamine deactylase
CREB	Cyclic AMP-responsive element-binding protein
C-terminus	Carboxy-terminus
DAD	Deacetylase activating domain from N-CoR1/2
Dansyl	5-(Dimethylamino)naphthalene-1-sulfonyl
EC_{50}	Concentration at which the effect is half maximal
ERRα	Steroid hormone receptor ERR1
FAHA	(E)-3-(Furan-2-yl)-N-hydroxyacrylamide
FK228	Romidepsin
HAT	Histone acetyltransferase
Hda1	Histone deacetylase HDA1
HDAC	Histone deacetylase
HDAH	Histone deacetylase-like amidohydrolase
$HDAH_{bo}$	HDAH from *Bordetella/Alcaligenes*
$HDAH_{pa}$	HDAH from *Pseudomonas aeruginosa*
HDLP	Histone deacetylase-like protein
HSP90	Heat shock protein HSP 90
IC_{50}	Concentration at which the inhibition is half maximal
Ins(1,4,5,6)P4	Inositol 1,4,5,6-tetrakisphosphate
K_d	Equilibrium dissociation constant
k_{obs}	observed rate constant
k_{off}	dissociation rate constant
k_{on}	association rate constant
LBH589	Panobinostat
M344	4-(Dimethylamino)-*N*-(7-(hydroxyamino)-7-oxoheptyl)-benzamide
MTA1	Metastasis-associated proteins MTA1
N-CoR1/2	Nuclear receptor corepressor 1/2
NMR	Nuclear magnetic resonance spectroscopy
N-terminus	Amino-terminus
p53	Cellular tumor antigen p53
PFSAHA	2,2,3,3,4,4,5,5,6,6,7,7-Dodecafluoro-N^1-hydroxy-N^8-phenyloctanediamide

PXD101	Belinostat
Rpd3	Histone deacetylase RPD3
SAHA	Vorinostat
SATFMK	9,9,9-Trifluoro-8-oxo-*N*-phenylnonanamide
SIRT	NAD-dependent protein deacetylase sirtuin
SIN3	Paired amphipathic helix protein Sin3
TSA	Trichostatin A

B Danksagung

Zunächst möchte ich mich bei Herrn Prof. Dr. Franz-Josef Meyer-Almes für die Bereitstellung des Themas, die Betreuung und die äußerst angenehme Zusammenarbeit in den letzten Jahren bedanken.

Herrn Prof. Dr. Harald Kolmar danke ich für die Aufnahme als externen Doktoranden, sowie für die Übernahme des Referats dieser Arbeit.

Bei Herrn Prof. Dr. Michael Reggelin und Herrn Prof. Dr. Adam Bertl bedanke ich mich für Ihre Arbeit als Fachprüfer meiner Dissertation.

Ein großer Dank gilt auch unseren Kooperationspartnern Dr. Robert Wawrzinek, Monique Mertens, Prof. Dr. Pablo Wessig, Dr. Matthias Baud, Dr. Matthew Fuchter und Özkan Yildiz.

Frau Dr. Janina Fengel und der Graduiertenschule der Hochschule Darmstadt danke ich für die Finanzierung dieser Arbeit.

An alle ehemaligen und aktuellen Mitarbeiter der Arbeitsgruppen Meyer-Almes und Fuchsbauer geht ein besonderer Dank für die Unterstützung, die angenehme Atmosphäre und heiteren Unternehmungen auch abseits des Labors. Hervorzuheben sind hier die Doktoranden Stephan Zindel, Michael Korbus, Benjamin Horstmann, Andreas Krämer, Alexander Kleinschek, David Fiebig, Norbert Jüttner, Anita Anderl und Benjamin Wolff, unsere Laboringenieure Ulrike Becher und Michael Schröder, sowie meine Bacheloranden Martina Zimmermann, Sara Kalman, Patrick Streb, Nina Schumacher, Michelle Roth und Niklas Jänsch.

Ein herzlicher Dank gilt meinen Freunden und meiner Familie, allen voran meiner Frau Nina, für die bedingungslose und grenzenlose Unterstützung in allen Lagen meines Lebens.

C *Curriculum vitae*

Name:	Christian Meyners
Geburtsdatum:	09.09.1985
Geburtsort:	Norden

Ausbildung

04. 2014 – 05. 2017	Kooperative **Promotion** an der Hochschule Darmstadt und der Technischen Universität Darmstadt unter der Leitung von Prof. Dr. Franz-Josef Meyer-Almes und Prof. Dr. Harald Kolmar Dissertation: *Selectivity in histone deacetylase inhibition: A biophysical approach*
03. 2012 – 03. 2014	**Master of Science** in Biosystemtechnik an der Hochschule Darmstadt Masterarbeit: *Reaktionsmechanismus der Bindung von Dansyl-Hydroxamaten an eine Histondeacetylase-ähnliche Amidohydrolase*
09. 2007 – 02. 2012	**Bachelor of Science** in Biotechnologie an der Hochschule Darmstadt Bachelorarbeit: *Bestimmung der thermodynamischen Signatur der Bindung von Substanzen an HDAH mittels eines fluoreszenzspektroskopischen Bindungsassays*
07. 2006	**Fachhochschulreife** an der Viktoriaschule Darmstadt

7. Affirmations

Darmstadt, 09.05.2017

Christian Meyners
Ludwig-Büchner-Straße 9
64285 Darmstadt

Erklärung

Ich erkläre hiermit, dass ich meine Dissertation selbstständig und nur mit den angegebenen Hilfsmitteln angefertigt habe.

(Unterschrift)

Darmstadt, 09.05.2017

Christian Meyners
Ludwig-Büchner-Straße 9
64285 Darmstadt

Erklärung

Ich erkläre hiermit, noch keinen Promotionsversuch unternommen zu haben.

(Unterschrift)